UNIVERSITY OF KWAZULU-NATAL

OBSERVATIONAL PROBES OF MERGING GALAXY CLUSTERS

by

Kenda Leigh Knowles

Accepted in fulfillment of the
academic requirements for the degree of
Doctor of Philosophy (Applied Mathematics)
in the
School of Mathematics, Statistics, and Computer Science,
University of KwaZulu-Natal

Durban
February, 2016

For my grandpa, Richard Oates, whose pride in me and wish for me to complete this has kept me going.

For my parents.

ABSTRACT

Galaxy clusters, being at the intersection of astrophysics and cosmology, are important objects to study. Galaxy clusters allow us to study the global evolution of the Universe, and simultaneously investigate the complex astrophysical processes occurring in the intracluster medium. Clusters can be probed at multiple wavelengths, with each set of observations providing complementary information about the cluster environment. Cluster mergers, being the most energetic processes known, are of particular interest. In this thesis we investigate cluster merger signatures of diffuse radio synchrotron emission in clusters selected via the Sunyaev-Zel'dovich (SZ) effect, and gravitational lensing effects in massive merging galaxy clusters with the Hubble Space Telescope.

The first part of this thesis is focused on a low-frequency radio follow-up of a mass-selected subset of Atacama Cosmology Telescope (ACT) equatorial clusters with the Giant Metrewave Radio Telescope (GMRT), with the aim of finding evidence of diffuse centralised radio emission. This emission is predicted to be a signpost of merger activity. In chapter two we introduce the theory underlying diffuse radio emission in galaxy clusters. In chapter three we present new 610 MHz GMRT radio observations of a subset of eight clusters from the ACT equatorial cluster sample; 75% of the targets in our sample are high redshift ($z > 0.5$) clusters, and all but one have final SZ-derived masses of $M_{500,\mathrm{SZ}} > 5 \times 10^{14} M_{\odot}$. Our radio observations reveal faint diffuse emission in only one of the cluster targets, ACT-CL J0256.5+0006, a detection rate of 12.5%. This is below the 40% detection rate for high mass ($M_{500,\mathrm{SZ}} > 5 \times 10^{14} M_{\odot}$) SZ-selected clusters,

and towards the lower range of detection rates for X-ray selected samples. We determine radio power upper limits for the radio halo non-detections and present these on the radio power-mass scaling relation plot. Furthermore, we investigate the radio environments of our clusters with non-detections. A $\sim$ 500 kpc active radio galaxy and a high-metallicity, local starforming galaxy are present in two of the cluster fields.

In chapter four we present a multi-wavelength analysis of the cluster ACT-CL J0256.5+0006 which hosts the single observed radio halo. In addition to the 610 MHz data, we present new 325 MHz GMRT observations of the cluster and discuss the observed halo properties at both frequencies. The extrapolated 1.4 GHz radio power of the halo is within the scatter of the observed correlations from the literature. We use X-ray and optical spectroscopic data to investigate the dynamical substructure in the cluster and determine that ACT-CL J0256.5+0006 is comprised of two components with a 7:4 mass ratio. Furthermore, we set up a simple merger model to constrain the merger geometry and time-scale. Radio halo formation theory suggests that radio halo emission increases in power as the merger proceeds, and then decreases after the merger concludes. By comparing our results with simulations, we conclude that we are most likely viewing this cluster just before first core passage.

The second part of this thesis presents the gravitational lensing analysis of two of the Hubble Frontier Field (HFF) clusters to constrain the dark matter content in these systems to unprecedented precision. After introducing the theory of gravitational cluster lensing and mass modelling techniques in chapter five, the work presented in chapter six of this thesis details the gravitational lensing analysis of deep imaging data of two clusters observed with the HFF program: MACSJ0416.1-2403 and MACSJ1149.6+2223. The main focus of the work is the multiple image identification and strong lensing mass modelling of the clusters. In addition, we summarise the combined multiwavelength and strong- and weak-lensing analysis of MACSJ0416.1-2403 which leads to two possible scenarios proposed for the triple merger occurring in this cluster. We also determine time delays and future predictions for the lensed supernova observed in one of the background galaxies multiply imaged by MACSJ1149.6+2223. We predicted the next supernova image to appear some time between November 2015 and January 2016.

ACKNOWLEDGMENTS

There have been many people who have helped in some way towards the completion of my PhD. The most important of whom is my supervisor, Prof. Kavilan Moodley. I would like to thank him for his belief in me and his endless support, hard work, and guidance. His motivation and trust in my abilities, particularly when I didn't trust them myself, have encouraged me through the dark times that many postgraduate students go through over the course of their studies. I couldn't have asked for a better boss and mentor and I am extremely grateful that he accepted me as a Masters student five years ago. I am immensely proud to call him my supervisor.

Through Kavi's global network of colleagues and contacts, I have been lucky to travel overseas to attend workshops and enjoy research visits in several countries. Through these visits I have made a few good friends who help keep alive the joy of astronomy, and who have been wonderful in showing me their bits of the planet and broadening my horizons. In particular, I would like to thank Grégory Hellbourg and Jonathan Koo – two of the most wonderful human beings who went out of their way to make me feel welcome and who were happy to show me around when I was but a stranger. Thank you, too, to the astrophysics department at Princeton University, which I had the privilege to visit twice during my postgraduate career. The people were extremely helpful and always had suggestions for new things to try or places to go during my stays.

My work would not be the same without my collaborators. Firstly, an enormous thank you

to Dr. Huib Intema, who I initially met at a local conference, and who later became one of my primary collaborators on my radio-related work. His willingness to answer my endless questions and improve my knowledge of data reduction techniques and tricks has been greatly appreciated. Secondly, I thank Dr. Mathilde Jauzac, first and foremost a friend, and then collaborator and co-supervisor. I have really enjoyed working with her and am honoured to have been invited into the CATS lensing collaboration with her. The wine times in Durban and Durham have been wonderful and I am grateful for her caring and support, happy to be an ear for my problems, both personal and professional, and more often than not giving sage advice on both counts. I'd also like to thank Dr. Matt Hilton, my other co-supervisor, for always being available to discuss my work and to suggest ways around the problems that inevitably crop up.

None of my studies and travel would have been possible without the funding of the Square Kilometre Array South Africa project and their Human Capital Development program, in joint association with the National Research Foundation. They have funded me since my Honours year and have brought me into contact with esteemed scientists from all over the world during their annual conferences. Through their association, I have also been introduced to people who I now count among my closest friends. I'd like to thank them for their understanding and graciousness after I became gravely ill in my first year of Masters and had to make alternate plans for my studies.

I have been lucky, I think, in terms of the departments I have worked in during my academic career. Since undergraduate studies in Pietermaritzburg with the best Honours class imaginable and inspiring professors such as Dr. John Pierrus, I have been blessed with a great work environment fueled by camaraderie between all levels of academia. In particular, I'd like to thank the people of the Astrophysics and Cosmology Research Unit which has been my home for the past four and a half years. It makes a big difference to a student's growth when there is an environment in which they can approach professors, postdocs, and fellow students alike, for guidance and suggestions, as well as a bit of relaxing fun. From bottles of wine to making liquid nitrogen ice cream, and everything in between, I am happy to have been a part of the ACRU family.

On a more personal note, I'd like to thank my family for their patience and support, particularly during the stressful times when I know I was not the most pleasant company. In the last

few weeks of my PhD, and during the writing up, I want to thank them for their forbearance – knowing when to leave me be has been a godsend. I wouldn't have gotten this far without them.

Finally, I'd like to thank the other two quarks: Nikhita Madhanpall and Susan Wilson. We have come through academia together since the easy days of PMB and our postgraduate journeys are almost over. The friendship we've formed over the past six or more years is one of my most cherished and I thank them for their support, both work-related and in life in general. Being able to let off steam or celebrate our personal and academic victories together (even the small ones of finally finding the bug in the code!) has been a major factor in my PhD path leading me to this end point. I am eternally grateful for their presence in my life.

PREFACE

The work described in this thesis was carried out in the School of Mathematics, Statistics, and Computer Science, University of KwaZulu-Natal from August 2011 to December 2015. This dissertation was completed under the supervision of Prof. K. Moodley, with co-supervision by Dr M. Hilton and Dr M. Jauzac.

This study represents original work by the author and has not been submitted in any form for any degree or diploma to any other tertiary institution. Where use was made of the work of others it has been duly acknowledged in the text.

DECLARATION OF NON-PLAGIARISM

I, **Kenda Leigh Knowles** declare that

1. The research reported in this thesis, except where otherwise indicated, is my original research.

2. This thesis has not been submitted for any degree or examination at any other university.

3. This thesis does not contain other persons' data, pictures, graphs or other information, unless specifically acknowledged as being sourced from other persons.

4. This thesis does not contain other persons' writing, unless specifically acknowledged as being sourced from other researchers. Where other written sources have been quoted, then:

   (a) Their words have been re-written but the general information attributed to them has been referenced.

   (b) Where their exact words have been used, then their writing has been placed in italics and inside quotation marks, and referenced.

5. This thesis does not contain text, graphics or tables copied and pasted from the Internet, unless specifically acknowledged, and the source being detailed in the thesis and in the References sections.

Signed in Westville, KwaZulu-Natal: ..... Date: .....

DECLARATION OF PUBLICATIONS

Details of contribution to publications that form part of and/or include research presented in this thesis:

Chapter 3

GMRT observations of a subset of ACT Equatorial galaxy clusters
Knowles K., Intema H., Moodley K., et al. (2016), in preparation.

I am the main contributor to this work. I undertook the analysis and wrote up the results under the supervision of Prof. K. Moodley.

Chapter 4

A giant radio halo in a low-mass SZ-selected galaxy cluster: ACT-CL J0256.5+0006
Knowles K., Intema H.T., Baker A.J., Bond J.R., Cress C., Gupta N., Hajian A., Hilton M., Hincks A.D., Hlozek R., Hughes J.P., Lindner R.R., Marriage T.A, Menanteau F., Moodley K., Niemack M.D., Reese E.D., Sievers J., Sifón C., Srianand R. & Wollack E.J. (2015), arXiv:1506.01547 Submitted for publication to MNRAS.

I am the main contributor to this work. I undertook the analysis, coordinated the paper, and wrote up the results under the supervision of Prof. K. Moodley. The form of the publication has been altered slightly to adhere to the formatting requirements of this thesis.

Chapter 5

Hubble Frontier Fields: a high-precision strong-lensing analysis of galaxy cluster MACSJ0416.1-2403 using ∼200 multiple images

Jauzac M., Clment B., Limousin M., Richard J., Jullo E., Ebeling H., Atek H., Kneib J.-P., Knowles K., Natarajan P., Eckert D., Egami E., Massey R. & Rexroth M. (2014) MNRAS, 443, 1549

Hubble Frontier Fields: the geometry and dynamics of the massive galaxy cluster merger MACSJ0416.1-2403

Jauzac M., Jullo E., Eckert D., Ebeling H., Richard J., Limousin M., Atek H., Kneib J.-P., Clment, B., Egami, E., Harvey, D., Knowles K., Massey, R., Natarajan P., Neichel B. & Rexroth M. (2015) MNRAS, 446, 4132

For these papers I contributed to the identification and verification of multiple images for the strong lensing analysis. The form of the publications has been altered slightly to adhere to the formatting requirements of this thesis.

Hubble Frontier Fields: Predictions for the Return of SN Refsdal with the MUSE and GMOS Spectrographs

Jauzac M., Richard J., Limousin M., Knowles K., Mahler G., Smith G.P., Kneib J.-P., Jullo E., Natarajan P., Ebeling H., Atek H., Clment B., Eckert D., Egami E., Massey R. & Rexroth M. (2015), arXiv:1509.08914. Submitted for publication to MNRAS.

For this paper I contributed to the identification and verification of multiple images for the strong lensing analysis. The form of the publication has been altered slightly to adhere to the formatting requirements of this thesis.

Signed in Westville, KwaZulu-Natal: ..... Date: .....

CONTENTS

LIST OF TABLES

LIST OF FIGURES

CHAPTER 1

INTRODUCTION

Cosmology is the study of the Universe, including theories for its formation and evolution. The observable Universe can be described by a simple model with a number of cosmological parameters which in turn create a framework in which to study the observed structures in the Universe and the abundance of complex physical processes within them. Studies of the clustering of galaxies and the temperature fluctuations in the cosmic microwave background have shown that the Universe is almost homogeneous and isotropic on large scales (see e.g. Tago et al., 2006; Hinshaw et al., 2007; Komatsu et al., 2011; Tempel et al., 2012; Bennett et al., 2013; Planck Collaboration et al., 2014a; Alam et al., 2015). In addition, observations of Type Ia supernova indicate that the Universe is expanding at an accelerating rate which requires an exotic form of energy to dominate the Universe (Riess et al., 1998; Perlmutter et al., 1999; Riess et al., 2004, 2007; Wood-Vasey et al., 2007; Kowalski et al., 2008; Hicken et al., 2009; Conley et al., 2011; Campbell et al., 2013; Rest et al., 2014; Rigault et al., 2015; Friedman et al., 2015).

The widely accepted formation theory for the Universe is that of a hot Big Bang model in which the Universe, consisting of radiation, baryonic matter, and unknown (dark) forms of matter and energy, originated from a hot, dense plasma, beginning in an epoch of radiation dominance. In this model, the equation of state of the Universe is described by the densities of the above

components, each with their own equation of state, as well as a curvature parameter defining the Universal geometry. The inflationary scenario of Guth (1981) is the established model to explain the flatness and horizon problems inferred from observations of the matter density and temperature homogeneity of the Universe (see e.g. Rindler, 1956; Misner et al., 1973; Dicke and Peebles, 1979). Inflation postulates that the Universe underwent an exponential expansion during the radiation dominated phase of its history, seeding density perturbations which are the basis of the observed structures populating the Universe today.

1.1 Cosmological probes

During this radiation dominated epoch, photons and relativistic particles were closely coupled, with the photons having very short path lengths due to scattering off the baryons and leptons. As the Universe cooled, recombination occurred and the electrons and protons combined to form neutral hydrogen, and eventually heavier elements (helium, lithium). At this stage, the photons decoupled from the matter and were able to propagate freely. These free-streaming photons are observed as the Cosmic Microwave Background (CMB), aptly described as the oldest light in the Universe. The CMB was first detected by Penzias and Wilson (1965), and contains temperature fluctuations which are imprinted with the cosmological model which defines the Universe. Thus observations of these fluctuations can constrain the model and its parameter values.

There are several instruments which have observed the temperature fluctuations of this background radiation, i.e. space telescopes such as COBE (Boggess et al., 1992), WMAP (Bennett et al., 2003), and the Planck satellite (Bouchet, 2009), as well as ground-based instruments, the South Pole Telescope (SPT; Ruhl et al., 2004) and the Atacama Cosmology Telescope (ACT; Kosowsky, 2006). The cosmological information lies in the statistical properties of the temperature anisotropies. The location and amplitude of peaks in the power spectrum of the two-point correlation function are related to several cosmological parameters, such as the Universal curvature, Ω_k, the baryon fraction Ω_b/Ω_m, the spectral index of the primordial perturbations, n_S, and the optical depth of the Universe after decoupling, τ.

In the radiation-dominated epoch, the growth of primordial perturbations, traced by tempera-

ture fluctuations in the CMB, are retarded by the rapid expansion (the Mészáros effect; Meszaros, 1974). Once the Universe transitioned into a matter dominated epoch, after decoupling, the perturbations grew quickly via gravitational attraction, becoming the progenitors of large scale structure formation. As the perturbations evolve, regions of high density grow more, with low density regions becoming less dense. This leads to anisotropic clustering of matter which is observable in large scale galaxy surveys such as the 2dF galaxy redshift survey (2dFGRS; Percival et al., 2001). Observations of large scale clustering show a characteristic scale (Percival et al., 2001; Peacock et al., 2001), which is indicated by a peak in the real-space two-point correlation (Eisenstein et al., 2005). This signature is caused by baryonic acoustic oscillations (BAOs) which are the result of sound waves, produced by the primordial fluctuations, which propagate until decoupling when they are effectively "frozen", leaving a distinctive imprint on scales of $\sim$ 100 h^{-1} Mpc in the clustering of mass in the Universe. The power spectrum of the galaxy distribution two-point correlation function is directly related to the CMB power spectrum. Thus the location and amplitude of the BAO signature can also constrain cosmological parameters, for example the dark energy equation of state, w_X, and the baryon fraction, Ω_b/Ω_m.

Another constraint on the dark energy equation of state is provided by measurements of the cosmological luminosity distance, D_L, from the light curves of Type Ia supernovae. These sources are thought to be exploding white dwarfs which collapse after exceeding the Chandrasekhar mass (Chandrasekhar, 1939) while accreting matter from a nearby companion source. These sources have characteristic light curves which can be standardised and can thus be used to measure cosmological distances. Large numbers of Type Ia supernovae have been discovered with the Supernova Legacy Survey (SNLS; Astier et al., 2006), providing constraints on the matter density of the Universe, Ω_m, and w_X assuming a flat universe.

Combining the results of some or all of these complementary cosmological probes – BAO in the large scale clustering of galaxies (e.g. Percival et al., 2001; Tegmark et al., 2006; Blake et al., 2011; Anderson et al., 2012; Reid et al., 2016), supernova experiments (e.g. Amendola et al., 2007; Conley et al., 2011), and studies of anisotropies in the CMB (Spergel et al., 2007; Hinshaw et al., 2009; Shirokoff et al., 2011; Das et al., 2011, 2014; Planck Collaboration et al., 2014c) – breaks the degeneracies between cosmological parameters, leading to tighter constraints

on the equations of state of the Universe.

1.2 Cluster cosmology

The current "concordance" model describes the Universe as spatially flat, dominated by dark energy, with roughly a quarter of the mass/energy budget made up of dark matter. The presence of a significant dark matter component was first hypothesised due to observations of large line-of-sight radial velocities of galaxy clusters which could not be explained by the visible matter (Zwicky, 1933), and has since been confirmed by several studies of clusters and their member galaxies through observations of stellar dynamics (e.g. Treu and Koopmans, 2004; Bridges et al., 2006; Baumgardt and Mieske, 2008; Bradford et al., 2011; Tortora et al., 2014; Samurović, 2014; Sweet et al., 2016), distributions of intracluster gas (Sarazin, 1986; Loewenstein and Mathews, 1987; Meiksin, 1990), galaxy rotation curves (Rubin et al., 1980; Quillen and Frogel, 1997; Núñez et al., 2010; Hernandez-Jimenez et al., 2013; Brook and Shankar, 2016), and gravitational lensing (e.g. Mellier, 1999; Bartelmann and Schneider, 2001; Hamana et al., 2003; Mitchell et al., 2005; Benjamin et al., 2007; Coe and Moustakas, 2009; Jullo et al., 2010; Tinker et al., 2012; Kilbinger et al., 2013; Liu et al., 2015).

In the current cosmological paradigm, structure follows a hierarchical formation process (Davis et al., 1985), whereby small-scale, low-mass structures, for instance dwarf galaxies, are the first to form and evolve through gravitational interactions into progressively larger objects such as Milky Way-type galaxies, and eventually into galaxy groups and clusters. Galaxy clusters are the largest virialised structures in the Universe, typically $10^{14} - 10^{15}$ solar masses, and are composed of a dominant portion of dark matter, and baryonic matter in their member galaxies and in a hot gaseous plasma known as the intracluster medium (ICM). As clusters grow from primordial perturbations, the formation of their structure is sensitively dependent on the initial cosmological conditions. The observed number density of clusters as a function of redshift, $N(M, z)$, thus provides a powerful constraint on both the expansion history of the Universe, and the gravitational growth of structure within it (e.g. Holder et al., 2001; Haiman et al., 2001; Carlstrom et al., 2002; Rosati et al., 2002; Pierpaoli et al., 2003; Voit, 2005; Frieman et al., 2008;

Marian and Bernstein, 2006; Frieman et al., 2008; Vikhlinin et al., 2009; Sahlén et al., 2009; Planck Collaboration et al., 2014d).

Within the cluster regions, i.e. on scales less than ~ 1 Mpc, gravitational forces are accompanied by dynamical baryonic processes in the ICM which play a significant role in the structure formation process. Cluster mergers are the most energetic processes in the Universe, releasing $\sim 10^{64}$ ergs of energy into the intracluster medium (ICM). During these mergers, shocks and adiabatic compression heat the ICM gas to X-ray-emitting temperatures (Randall et al., 2002; Poole et al., 2006, 2007). As the merger processes dissipate, the ICM eventually cools to reach hydrostatic equilibrium. Star formation and accretion of the dense ICM gas onto galactic supermassive black holes can provide energy feedback via supernovae winds or active galactic nuclei (AGN) activity (see e.g. Sarazin and Boller, 1989), enriching the ICM with heavy elements (Loewenstein and Mushotzky, 1996).

Galaxy clusters thus lie at a unique position at the intersection of cosmology and astrophysics; a viable cosmological model has to explain both the large scale structure formation, as well as the physical dynamics occurring within the clusters themselves. As galaxy clusters are fundamentally rare objects, particularly the most massive ones, large survey areas are needed to obtain a significant cluster sample.

1.3 Cluster detection methods

1.3.1 Optical

The first extensive galaxy cluster catalogues were based on optical detections at low redshift (Abell, 1958; Zwicky et al., 1968; Abell et al., 1989), appearing a long time after Charles Messier and William Herschel first noted clustering of galaxies in the late 18th century, in the regions of what are now the Virgo and Coma clusters. These early catalogues had a relatively low redshift cut-off ($z \lesssim 0.1$, Bahcall and Soneira, 1983) and contained several biases such as photometric errors (Sutherland, 1988) and projection effects (Lucey, 1983; Katgert et al., 1996). More recently, improved detector technologies and automated cluster detection methods have produced galaxy

cluster catalogues of hundreds of sources out to redshifts of $z \sim 1$ (Postman et al., 1996; Stanford et al., 1997; Gal et al., 2000, 2003; Ebeling et al., 2001; Gladders and Yee, 2005; Koester et al., 2007; Gal et al., 2009).

Each cluster detection method has its own advantages and weaknesses. Optical methods have the benefit of being able to cover wide areas of sky relatively cheaply by putting large arrays of CCD detectors onto telescopes with a large field-of-view. However, optical cluster catalogs are flux- and therefore redshift-limited and have the added problem of projection effects due to contaminants along the line of sight. Moreover, measurements of the cluster mass, the main cosmological probe, are not as well-defined using optical properties. These disadvantages motivated cluster studies at other wavelengths, particularly in X-rays.

1.3.2 X-ray

In the 1970s the *UHURU* satellite found that galaxy clusters are second only to quasars (very energetic, distant, quasi-stellar radio sources) in terms of their X-ray brightness (Giacconi et al., 1972). About fifteen years later, Henriksen and Mushotzky (1986) determined that the X-ray brightness of clusters comes from thermal bremsstrahlung radiation in the hot ICM plasma. Due to these thermal properties, clusters in the X-ray band are bright extended sources with luminosities of the order of 10^{44} erg s^{-1}. These luminosities make it possible to use X-rays to detect clusters at high redshift, although bremsstrahlung radiation does suffer from redshift dimming. X-ray selection has since become the preferred method for cluster detection and there have subsequently been many cluster studies using X-ray information. With the advancement in telescope technology and software techniques there are now several extensive X-ray cluster surveys conducted by the *ROSAT*, *XMM*, and *Chandra* satellites, such as the MAssive Cluster Survey (MACS), ROSAT-ESO Flux Limited X-ray (REFLEX) survey, and the XMM Cluster Survey (Rosati et al., 2002; Ledlow et al., 2003; Böhringer et al., 2004; Ebeling et al., 2001; Šuhada et al., 2011; Lloyd-Davies et al., 2011; Willis et al., 2013).

X-ray observations of clusters provide information about the 2D cluster morphology, the electron density and surface brightness profiles, and cluster temperature. This makes the deter-

mination of cluster mass from X-ray observations simpler than from optical ones. Furthermore, other than extremely nearby galaxies or supernova remnants in the galactic plane, galaxy clusters are the only extended X-ray sources in the sky. This makes it easier to compute selection functions for X-ray cluster surveys (e.g. Burenin et al., 2007) compared to optical surveys. Moreover, cluster X-ray emission depends on the square of the gas density which means that clusters in the X-ray would stand out strongly from lower density regions. Combining this with the relatively low surface brightness of X-ray sources ensures that projection effects are not as serious in X-ray cluster detection than they are in the optical band. However, projection effects will impact the determination of a cluster's dynamical state from the 2D morphology and the determination of cluster mass from X-rays requires the assumption of spherical symmetry and hydrostatic equilibrium. Moreover, since X-ray probes are also flux- and redshift-limited, researchers turned to other regions of the electromagnetic spectrum.

1.3.3 Millimetre

With the discovery of the Sunyaev-Zeldovich (SZ) effect in the 1970s (Sunyaev and Zel'dovich, 1972), studies of the microwave regime became a novel possibility to detect and observe galaxy clusters. The SZ effect describes the process whereby low energy CMB photons are inverse-Compton (IC) scattered to higher energies whilst traversing the hot gas of the ICM. Observationally, this effect translates into a distortion of the thermal blackbody CMB spectrum in the direction of a cluster of galaxies. The cluster samples obtained are nearly independent of redshift as, although the CMB itself suffers from redshift dimming, the ratio of SZ signal to CMB does not. Moreover, since it is a scattering effect, the distance of the scattering medium does not matter. Due to this redshift-independence, this method produces mass-limited cluster samples, detecting all clusters above a certain mass threshold.

There are other important advantages to selecting clusters through their SZ signal, compared with other selection methods. Firstly, numerical simulations, analytical models and SZ observations have shown that scaling relation between the SZ flux the cluster mass is fairly robust, with low scatter (e.g. Reid and Spergel, 2006). This is due to the proportionality between the SZ

signal, gas mass, and total mass. Secondly, the simulated SZ signals are less affected by baryonic astrophysics. Thus an SZ-selected sample should provide more reliable cluster detections with a closer correlation with cluster mass (an important cosmological property), than X-ray or optical cluster surveys, particularly at high redshift. There are several large-area SZ surveys which are detecting large numbers of new galaxy clusters out to redshifts of $z \sim 1$: the *Planck* satellite (Planck Collaboration et al., 2011), the South Pole Telescope (SPT; Ruhl et al., 2004), and the Atacama Cosmology Telescope (ACT; Swetz et al., 2011).

1.4 Cluster probes

1.4.1 Diffuse radio emission

X-ray and SZ cluster detection methods probe the thermal component of the ICM. In recent years it has been realised that low frequency radio observations can be used to probe its non-thermal component through the detection of diffuse cluster-scale ($\sim$ 1 Mpc) synchrotron emission in the form of radio halos and relics (for reviews see Ferrari et al., 2008; Feretti et al., 2012). Due to their extended nature, *in situ* acceleration of cosmic rays is necessary for the formation of these diffuse sources. The leading formation theory explains the observed link with cluster mergers, whereby relativistic electrons, possibly seeded by previous large scale structure formation and AGN activity, are reaccelerated by merger-driven shocks and turbulent motions in the ICM (Schlickeiser et al., 1987; Ensslin et al., 1998; Sarazin, 1999; Petrosian, 2001; Fujita et al., 2003; Brunetti et al., 2004; Keshet et al., 2004; Xu et al., 2010; Brunetti and Lazarian, 2011).

Sensitive observations of this emission can provide constraints on the magnetic fields and cosmic ray processes in galaxy clusters (Cassano et al., 2006a; van Weeren et al., 2011a, 2012; Lindner et al., 2014), however, radio halos and relics are relatively rare phenomena with large samples ($\sim$ 30) of massive X-ray selected, and more recently SZ-selected, clusters showing a detection rate of $\sim 10 - 30\%$, with the more massive systems having a higher probability of hosting the emission (Venturi et al., 2008, 2013; Cassano et al., 2013). These cluster samples comprise mostly low-redshift ($z < 0.4$) systems and thus the observed correlations between

radio power and thermal cluster properties (Cassano et al., 2006b, 2007, 2013) are dominated by low-redshift statistics. Only a handful of radio halos in high-redshift clusters have been studied (Giovannini and Feretti, 2000; Bonafede et al., 2009, 2012; Lindner et al., 2014; van Weeren et al., 2014). Although the number of radio halo and relic studies has increased dramatically over the past decade, there are still a number of unanswered questions regarding the generation of diffuse radio emission (Brunetti and Jones, 2014). More clusters, over a wider range of redshift, need to be studied to address the theoretical issues and to gain insight into the evolution of the emission properties over the course of the merger, as well as over cosmic time.

1.4.2 Gravitational lensing

Massive cluster mergers can also be studied using probes of the cluster dark matter distribution. The massive nature of galaxy clusters causes them to distort light from distant galaxies through the process of gravitational lensing. Cluster-scale gravitational lensing thus serves as a powerful cosmological tool as it enables a direct measurement of the total (dark and baryonic) matter distribution within the cluster (the lens), as well as the imaging of extremely high redshift $z > 7$ galaxies through lensing magnification. Measurements of time delays between lensed images and their relative positions constrain the distance ratio, which depends on the Universe's matter density and dark energy equation of state (see e.g. Coe and Moustakas, 2009; Linder, 2011; Cao et al., 2015; Meng et al., 2015). Thus observations of gravitationally lensed systems add additional cosmological constraints to the existing universal model (for reviews see Schneider et al., 1992; Massey et al., 2010; Kneib and Natarajan, 2011; Hoekstra et al., 2013). The first object identified as being lensed by a cluster was the giant luminous arc observed in ground-based images of galaxy cluster Abell 370 (Soucail, 1987) taken with the Canada-France-Hawaii Telescope (CFHT; Racine, 1981). Since then multiple lensed sources have been found in many massive clusters, with lensing analyses of systems with a large number (> 10) of identifiable lensed images providing the most precise mass maps of cluster cores (e.g. Bradač et al., 2006, 2008; Jullo et al., 2007; Limousin et al., 2007; Jullo and Kneib, 2009; Coe et al., 2010).

Gravitational cluster lensing studies have been transformed in the past few decades by the

high quality images produced by the Hubble Space Telescope (HST). Multi-colour, high angular resolution images allow secure identifications of large numbers of lensed images (e.g Broadhurst et al., 2005; Limousin et al., 2007; Zitrin et al., 2011; Limousin et al., 2012). With the aim of using cluster gravitational lensing to investigate the distant Universe to unparalleled depth, the Hubble Frontier Fields (HFF) campaign is providing the community with ultra-deep multi-band Hubble images of six massive clusters. The first data indeed revealed detections of $z > 7$ lensed galaxies and provided lensing mass maps of unprecedented precision (Laporte et al., 2014; Atek et al., 2014; Jauzac et al., 2014, 2015a; Laporte et al., 2015; Diego et al., 2015c; Jauzac et al., 2015b; McLeod et al., 2015; Wang et al., 2015; Jauzac et al., 2015c; Atek et al., 2015b,a; Diego et al., 2015d).

1.5 Thesis outline

The work presented in this thesis is divided into two major topics: (1) observations of diffuse radio emission in clusters, and (2) the study of the gravitational lensing effect in massive cluster cores. In the first part of the dissertation, we extend the number of radio cluster observations focused on detecting diffuse cluster emission with a SZ mass-selected sample from ACT. In chapter 2 we present the observational properties of the three main types of diffuse radio emission found in clusters, and discuss the existing theoretical models for the formation mechanism responsible for the emission. In chapter 3 we present our cluster sample and discuss our new radio observations and data reduction process. Finally, we present the results of our radio observations in the context of the detection of diffuse radio emission.

In chapter 4, we discuss the radio properties of the known merging cluster in our sample, ACT-CL J0256.5+0006, which we found to host a faint giant radio halo. Furthermore, we present a multi-wavelength analysis of the cluster using X-ray and spectroscopic redshift data. Finally, we model the cluster merger as a two-body gravitational interaction and use the multi-wavelength data to constrain the merger geometry and merger time-scale. We compare our results with simulations to better understand the halo properties we observe.

The second part of this thesis presents high precision mass reconstructions through gravita-

tional lensing studies of two of the Hubble Frontier Field clusters. In chapter 5 we introduce gravitational lensing theory, and apply it to massive galaxy clusters, introducing both the strong and the weak regimes. Furthermore, we discuss lens modelling techniques and focus on the parametric approach implemented in the publicly available LENSTOOL software. In chapter 6 we detail the strong lensing analyses of MACSJ0416.1-2403 and MACSJ1149.6+2223 based on the new data from the Hubble Frontier Fields project, and present the resulting high-precision lensing mass maps. For MACSJ0416.1-2403 the strong lensing analysis is combined with weak lensing measurements to produce a lensing mass reconstruction out to larger radii. This combined lensing analysis is used in conjunction with multi-wavelength data to constrain the merger history and dynamics of this complex cluster. The strong lensing analysis of MACSJ1149.6+2223 allows us to estimate time delays and future appearance predictions for the lensed supernova observed in one of the multiply lensed images. Finally, in chapter 7 we summarise our results and describe future extensions to the work presented here.

We adopt a ΛCDM flat cosmology with $H_0 = 70$ km s^{-1}Mpc^{-1}throughout this thesis, however the assumed cosmological parameters differ slightly between the two parts of the thesis. For the radio portion we adopt values of Ω_m = 0.27 and Ω_Λ = 0.73. We assume $S_\nu \propto \nu^{-\alpha}$ throughout the radio analysis, where S_ν is the flux density at frequency ν and α is the spectral index. In the second part of the thesis, we adopt values of Ω_m = 0.3 and Ω_Λ = 0.7. All source magnitudes from the Hubble imaging are quoted in the AB system.

CHAPTER 2

DIFFUSE RADIO EMISSION IN GALAXY CLUSTERS

In the hierarchical model of structure formation, the formation of galaxy clusters through mergers is one of the most energetic processes in the Universe, dissipating large amounts of energy ($\sim 10^{64}$ erg) into the intracluster medium (ICM). The non-thermal processes in the ICM can be probed via observations of diffuse radio emission in the cluster environment of which there are several classes. In this chapter we discuss the observational properties of each type and the various models to explain the physical processes which drive them.

2.1 Synchrotron radiation in terms of diffuse radio emission

When electrons are radially accelerated to relativistic speeds (when the acceleration is perpendicular to the velocity) in a magnetic field, the particles emit synchrotron radiation (see Figure 2.1). The emitted power is given by the relativistic Larmor formula and thus depends on the Lorentz factor (which defines the electron energy) and the magnitude of the magnetic field. Large magnetic fields require less electron energy in order to produce emission at a given frequency

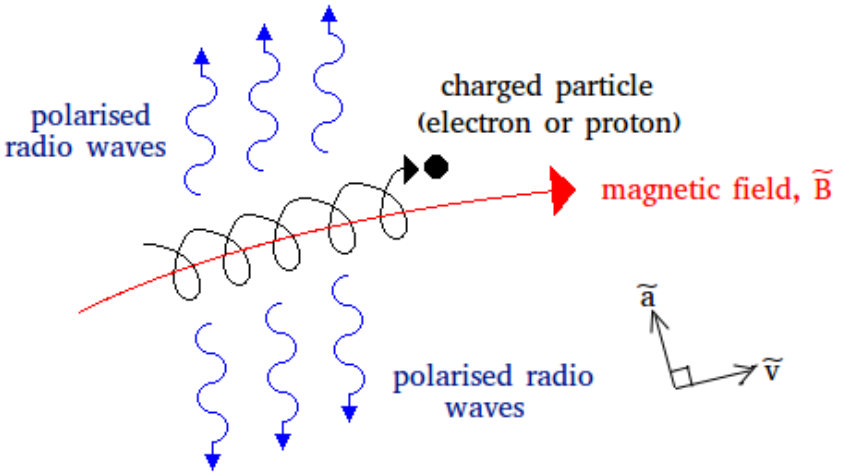

Figure 2.1: Schematic of synchrotron radiation emitted from an electron/proton spiraling in a magnetic field. In the case of synchrotron emission, the particle acceleration is perpendicular to its velocity. Source: adapted from `http://abyss.uoregon.edu`

compared to magnetic fields of lower strengths. Thus for a given electron energy, the stronger the magnetic field, the more powerful the synchrotron radiation will be.

Thorough treatments of radiation processes and synchrotron theory can be found in several textbooks (e.g. Rybicki and Lightman, 1986; Longair, 2011). Here we summarise the features of synchrotron emission in an astrophysical context. Consider a homogeneous and isotropic population of relativistic electrons (CRe) with a power-law energy distribution of index δ given by

$$N(E)dE \propto E^{-\delta}dE. \tag{2.1}$$

If this plasma is also optically thin, which is the case for diffuse radio emission, the radiated synchrotron emission will exhibit the following properties:

- At a particular frequency, the emissivity, which is related to the number density of CRe and the strength of the magnetic field, follows a power law with a spectral index, α, related to the CRe energy distribution index: $\alpha = (\delta - 1)/2$. Typical radio sources exhibit spectral indices of $\sim$ 0.7 - 0.8.

- Over time, CRe experience energy losses which leads to a change in the global energy

distribution of the particles, and therefore a change in the spectral profile. Strong energy losses produce a cut-off of the spectrum at frequencies higher than a critical frequency ν^*, which is linked to the particle lifetime. Therefore older radio sources exhibit curved spectra and generally have steeper spectral indices than the typical sources. The spectrum at lower frequencies indicates the original energy distribution of the CRe.

- If the CRe are spiraling in a uniform magnetic field, the emitted synchrotron radiation is linearly polarized with the electric vector perpendicular to the plane-of-the-sky projection of the magnetic field. The degree to which the emission is intrinsically polarized depends on the energy distribution. For typical spectral indices this is 75 - 80%. The degree of polarization is reduced when the magnetic fields involved have complex or tangled structures.

- As mentioned above, the total energy of a synchrotron source is defined by the energies of the relativistic particles as well as the magnetic field, taking into account the magnetic field filling factor (the fraction of the source volume occupied by the magnetic field). Observations of synchrotron radio sources enable a determination of the minimum total energy under the equipartition condition. This is when the energy contributions are more or less equally split between the accelerated particles and the magnetic field. The magnetic field in this case is generally called the equipartition field, B_{eq}.

Over the past two decades, observations of cluster-scale diffuse radio emission of synchrotron origin have been made. These sources can be separated into different classes but all of them exhibit low surface brightnesses and steep spectra, have no obvious link to the cluster galaxies, and are thus associated with the ICM (see the reviews by Ferrari et al., 2008; Feretti et al., 2012, and references therein). The prevailing theory for the origin and distribution of cluster magnetic fields is that they originate from cosmological fields or are injected by active galactic nuclei (AGN), and are then amplified through the hierarchical build up of structure (see Ryu et al., 2008; Roettiger et al., 1999; Dolag et al., 2002, 2005a; Subramanian et al., 2006; Xu et al., 2011, for more details).

As the diffuse radio emission is both extended and of low surface brightness, it can be difficult to detect. Successful observations require both excellent surface brightness sensitivity, typical of single dish telescopes, as well as good angular resolution to distinguish compact sources embedded in or projected along the line of sight of the emission. Interferometers are better suited to diffuse emission studies, as single dish instruments have large beams and often suffer from confusion. However, many interferometers do not have sufficient sensitivity to structures on large scales as they do not sample many short spacings. Another challenge to fully understanding diffuse synchrotron sources is that information about the age and energy of the specific population of CRe is encoded in the shape of the spectrum, with sensitive multi-frequency observations required to reproduce this shape for a single source. This is rarely available for large numbers of observed sources. Finally, since the diffuse emission in question exhibit steep spectra, they are best identified at low frequencies. Radio campaigns with instruments such as the Westerbork Synthesis Radio Telescope (WSRT), the Very Large Array (VLA), and the Giant Metrewave Radio Telescope (GMRT), with their low radio frequencies (< 1.4 GHz), good angular resolution, and low surface brightness sensitivities, have increased the knowledge of diffuse radio structures in clusters over a relatively short period of time (Venturi et al., 2007, 2008; Giacintucci, 2011; van Weeren et al., 2011d,b).

2.2 Types of diffuse cluster radio emission

Evidence for diffuse radio sources of synchrotron origin with no optical counterpart and no obvious connection to the cluster galaxies has been around since the 1960s and 1970s (Large et al., 1959; Willson, 1970; Miley and Perola, 1975; Ballarati et al., 1981; Giovannini et al., 1991). In the last decade, many diffuse radio sources with steep spectra ($\alpha \gtrsim 1$) and low surface brightness (~ 0.1 - 1 μJy arcsec^{-2} at 1.4 GHz) have been detected and these observations can be separated into three main classes of emission. These types have their own observational properties and thus are expected to originate from different mechanisms. Here we discuss the observational properties of each class in turn.

2.2.1 Radio Halos

The first example of cluster-scale diffuse radio emission to be detected was in the form of a *giant radio halo* (GRH). These are characterised by their central location in the cluster, relatively regular morphology, and large extents ($\gtrsim$ 1 Mpc). They are typically unpolarized down to a few percent due to internal or beam depolarization. The latter case occurs when the synthesised beam of the telescope is larger than the scale on which the intrinsic source polarization is coherent, effectively smoothing out the source polarization and reducing the observed polarization signal. This is an effect which cannot be corrected for once observations have been made. Notable exceptions of polarized GRHs have been found in A2255 (Govoni et al., 2005) and MACSJ0717.5+3745 (Bonafede et al., 2009).

The prototype of this class is the GRH found in the Coma cluster which has been extensively studied over the past forty years (e.g. Jaffe et al., 1976; Sastry and Shevgaonkar, 1983; Deiss et al., 1997; Kronberg et al., 2007; Brown and Rudnick, 2011) since its first detection by Large et al. (1959) and Willson (1970). Since then, with the improvement in observations and data reduction techniques, smaller radio halos and some with more irregular morphologies have been detected. The merging system of A399 and A401 is the only system currently known to host double radio halos (Murgia et al., 2010b). Examples of observed radio halos of different sizes and morphologies are provided in Figure 2.2. To date there are over 50 clusters hosting radio halos with halo sizes ranging from a few hundred kpc to 1.65 Mpc, all of which display indications of recent merger activity through X-ray or optical substructure. A recent exception is the GRH in CL1821+643, a cluster with an intact cool-core (Bonafede et al., 2014b); in this case Bonafede et al. suggest that if a merger is indeed responsible for the diffuse radio emission, it is either off-axis, in an early phase, or a minor one.

The rate of occurrence of radio halos appears to increase with cluster X-ray luminosity and Sunyaev-Zel'dovich (SZ) effect Compton-y parameter[1], with radio halos occurring in $\sim$30% of

[1]This characterises the amplitude of the SZ signal in a given direction: $y = \int n_e \sigma_T (kT_e/m_e c^2) dl$. The integrated Compton parameter, $Y = \int y d\Omega$, is proportional to the product of the cluster gas mass and mass-weighted temperature when integrated over the cluster region. A common choice is to integrate within R_{500}.

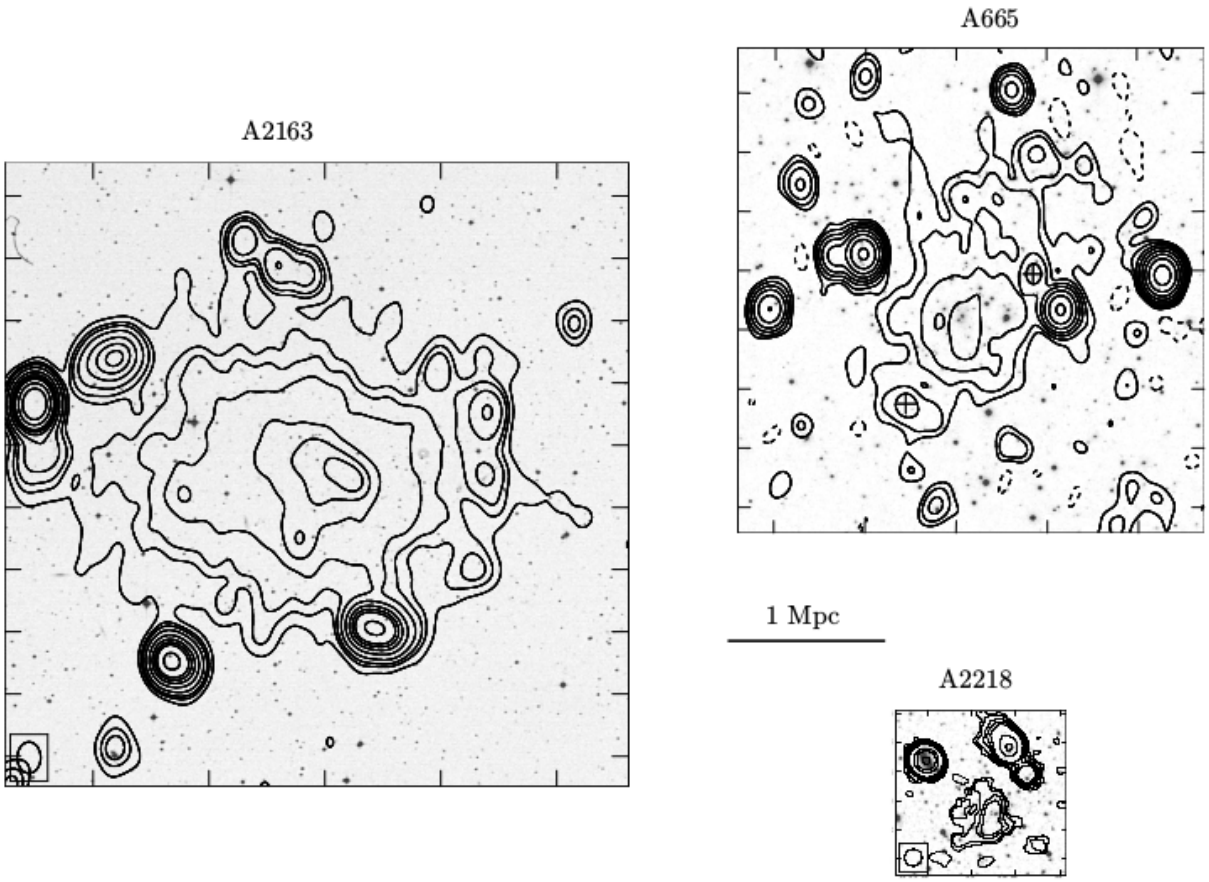

Figure 2.2: Images of the radio halos in A2163 (Feretti et al., 2001), A665, and A2218 (Giovannini and Feretti, 2000), showing the different sizes and morphologies that can be observed. In each case, the radio emission (contours) is overlaid on an optical image. For A2163, the contours start at 0.2 mJy beam^{-1} and increase in steps of 0.3 mJy beam^{-1}. The contour levels in A665 are -0.2, 0.2, 0.4, 0.8, 1.5, 3, 6, 12, 25 mJy/beam. For A2218, the contour levels are -0.2, 0.2, 0.3, 0.5, 0.7, 1, 3, 5, 10 mJy/beam. The maps have been scaled to the same linear scale. Source: Feretti et al. (2012).

clusters with $L_{\rm X} > 5 \times 10^{44}$ erg s^{-1} (Cassano et al., 2011). The redshift distribution of radio halos is fairly homogeneous for $z < 0.35$. The number of high redshift ($z > 0.4$) sources is small, probably due to selection effects and/or sensitivity limits although a true dearth of high redshift sources is not impossible. The highest redshift radio halo currently known is in the massive cluster "El Gordo" (z=0.87, Lindner et al., 2014), with the closest competitor being MACSJ0717.5+3745 at z=0.55 (Bonafede et al., 2009). Until a larger statistical sample of high redshift radio halos is obtained, the redshift evolution of this class of diffuse emission cannot be

reliably investigated. Here we discuss the main observational properties of radio halos to date.

2.2.1.1 Spectral properties

Integrated spectrum

In general, the integrated spectrum of radio halos in poorly known due to a lack of multi-frequency data. Only a few of the most thoroughly studied systems have more than three different frequency measurements and in general, the highest frequency is 1.4 GHz which is too low to detect spectral steepening – this is imperative in order to select a preference between the formation models discussed in 2.3.

All radio halos have a global spectral index of $\alpha \gtrsim 1$, where the halo flux density scales with frequency as $S_\nu \propto \nu^{-\alpha}$, typical of aged synchrotron sources (see §2.1). The most extensively studied integrated spectrum is that of the Coma cluster, with integrated flux density measurements at thirteen different frequencies between 30.9 MHz and 4.85 GHz (Hanisch, 1980; Hanisch and Erickson, 1980; Cordey, 1985; Schlickeiser et al., 1987; Henning, 1989; Venturi et al., 1990; Kim et al., 1990; Giovannini et al., 1993; Deiss et al., 1997), revealing a definite spectral steepening at high frequencies (Thierbach et al., 2003).

Studies of the scaling relation between a radio halo's integrated spectrum and the average cluster temperature (Feretti et al., 2004a; Giovannini et al., 2009) lead to the suggestion of a tentative link between mergers and radio halos, a relationship which also exists in the high-redshift cluster "El Gordo" (Lindner et al., 2014). Although the studies suffer from poor statistics due to inhomogeneous spectral index measurements and few data points, they provide marginal evidence that the two properties are anti-correlated, i.e. flatter spectrum halos exist in hot clusters. The results favour the reacceleration model discussed in §2.3.1 as a flatter spectrum implies there is more energy available to accelerate the CRe. This energy could presumably arise from violent mergers, which are expected to occur in hot clusters (Feretti et al., 2004a,b; Cassano and Brunetti, 2005; Cassano et al., 2008). The link between radio halos and mergers is discussed further in a following section.

Spectral index distribution

The radio halo spectral index map provides an effective way of probing the changes in spectral profile over the halo volume, and therefore the changes in shape of the CRe energy distribution and the strength of the magnetic field. Studies of the spatial distribution of radio halo spectral index are relatively rare. This is primarily due to the lack of sensitive data: a spectral index map requires excellent surface brightness sensitivity at two or more frequencies.

Since the first spectral index map of the Coma cluster (Giovannini et al., 1993), which showed a fairly smooth spectral distribution with radial steepening towards the outskirts, spectral index maps of other radio halos have shown a wide variety of distribution patterns (Liang et al., 2000; Feretti et al., 2004b; Giacintucci et al., 2005; Orrú et al., 2007; Pizzo and de Bruyn, 2009; Kale and Dwarakanath, 2010). These spectral variations potentially indicate energy losses and/or gains of the individual CRe populations. Feretti et al. (2004b) showed that in order to flatten a spectral index from 1.3 to 0.8, a factor of ~ 2.5 more energy must be injected into the CRe population. If CRe are not experiencing an injection of energy, a flatter spectrum indicates that the last energising event was more recent than for a steeper spectrum. Therefore the spectral index is expected to be flatter in regions currently or more recently affected by merger activity.

As in the case of the integrated spectrum, observed spectral index maps currently support the turbulent acceleration model, where the injected energy is supplied by a merger (Cassano, 2010). In particular, the radial steepening of the spectral index could be caused by the magnetic field strength decreasing further from the cluster centre, as well as the presence of a high energy break in the CRe energy distribution (Brunetti et al., 2001).

Ultra-steep spectrum sources

The majority of radio halo sources exhibit spectral indices of ~ 1 - 1.5. However a small population of radio halos with $\alpha \geq 1.6$ have been detected which are called ultra-steep spectrum radio halos (USSRH). To date there are seven USSRHs in the literature: A1914 (Bacchi et al., 2003), A521 (Dallacasa et al., 2009; Giovannini et al., 2009), A2255 (Feretti et al., 1997), A697 (van Weeren et al., 2011b), A1300 (Reid et al., 1999), MACSJ1149.5+2223 (Bonafede et al., 2012), and PLCKG171.9-40.7 (Giacintucci et al., 2013). Most of these clusters have relatively low temperatures, giving another weak link between radio halos and mergers.

2.2.1.2 Radio power correlations

With larger statistical samples of radio halos now available, studies of the 1.4 GHz radio halo power have shown it to be correlated with various other radio halo and cluster properties. Since the majority of radio halos have been detected at low redshift, $z < 0.4$, it is not yet clear whether the observed correlations hold for higher redshift sources as well.

Halo size, R_H

We mentioned at the beginning of this section that classical radio halos have physical sizes $\gtrsim 1$ Mpc (GRHs), but that there exist radio halos as small as a few hundred kpc. Giovannini et al. (2009) found a correlation between the largest linear size of the radio halo and its emitted power which is continuous over the range of sizes. The slope of this correlation is in agreement with that obtained using only GRH sources (Feretti et al., 2012). Moreover, Murgia et al. (2009) studied the range of emissivities in the radio halo samples and found that the variation among radio halos of different size was small, supporting the conclusion that halo size and power are correlated.

Although there are a handful of outliers, all of which have radio powers higher than expected from their observed size (MACSJ0717.5+3745, Bonafede et al. 2009; A1213, Giovannini et al. 2009; and A1351, Giacintucci et al. 2009), the correlation between these two halo properties is relatively tight. This confirms that GRHs and radio halos of smaller size are indeed members of the same class as they share the same properties. We thus expect them to have a common formation mechanisms, unlike radio mini-halos which are discussed in §2.2.3.

X-ray cluster properties: $L_{\rm X}, T, M_{\rm X}$

A link between the radio halo power and the cluster X-ray luminosity $L_{\rm X}$ was first discovered by Liang et al. (2000) using the ten most securely identified radio halos available at the time. This correlation has since been confirmed by several authors, and radio power scaling relations have been defined for X-ray temperature T, and mass M (Bacchi et al., 2003; Cassano et al., 2006b, 2007). Previous studies only considered clusters hosting radio halos. Using an X-ray selected

sample of *ROSAT* clusters, Brunetti et al. (2007) were the first to observe a bimodality in the $P_{1.4\mathrm{GHz}}$–L_{X} plane by determining radio power upper limits for those clusters with no evidence of a radio halo. They found the radio halos to have powers correlated with the L_{X} of the host cluster, however the non-detections lay roughly an order of magnitude below this correlation. This apparent dichotomy is expected to be related to the dynamical state of the cluster: disturbed systems host radio halos, whereas the upper limits belong to relaxed systems. However, this separation is not perfect and we will discuss the suspected merger connection in more detail in §2.2.1.3.

Within the population of radio halos, there is some scatter in the $P_{1.4\mathrm{GHz}}$–L_{X} correlation. A few outliers, generally at low L_{X}, host halos that are more powerful than their cluster X-ray luminosity would suggest. Conversely, the USSRHs all lie below the correlation, with radio powers somewhat lower than expected based on the cluster X-ray luminosity.

Finally, the non-thermal radio halo emission in well resolved systems has been found to be spatially correlated with the X-ray structure of the thermal bremsstrahlung emission (Govoni et al., 2001a; Feretti et al., 2001; Giacintucci et al., 2005), suggesting a link between the two plasmas (Govoni et al., 2001a). The slope of this relation is predicted by reacceleration models, however the correlation is not evident once halos with irregular or asymmetric morphologies are considered. From results of magnetic field modelling, Vacca et al. (2010) argue that this disparity may be caused by variations in the magnetic field on scales of $\sim$ hundreds of kpc.

SZ cluster properties: $Y_{\mathrm{SZ}}, M_{500,\mathrm{SZ}}$

The $P_{1.4\mathrm{GHz}}$–L_{X} relation is probably the most well studied of the radio power correlations owing to the fact that radio halo campaigns have historically been carried out on X-ray selected samples – X-ray emission has been used to detect galaxy clusters since the 1970's (Meekins et al., 1971; Gursky et al., 1971). However, the thermal ICM also radiates at mm-wavelengths via the SZ effect and Moffet and Birkinshaw (1989) were the first to suggest a link between a cluster's thermal SZ Compton-y parameter and the existence of a radio halo. This correlation has been confirmed (Basu, 2012) using clusters in the Planck 2013 SZ catalogue (Planck Collaboration et al., 2014b).

As in the case of $L_{\rm X}$, a bimodality is also observed in the $P_{1.4{\rm GHz}}$–$Y_{\rm SZ}$ domain (Cassano et al., 2013), although the separation appears to be slightly weaker than in X-ray selected samples (Sommer and Basu, 2014). In addition, Sommer and Basu (2014) find that SZ-selected samples appear to have a lower fall-out fraction of clusters without radio halos than that measured using X-ray clusters samples. They argue that this may be due to a combination of the fact that SZ and X-ray ICM emission evolve at different rates during cluster mergers, as well as a bias toward cool-core systems in X-ray selected samples.

One of the expected advantages of SZ-selected cluster samples is that the SZ effect is a more robust proxy for the cluster mass, as compared to the cluster X-ray luminosity (Carlstrom et al., 2002). From this one may expect a tighter correlation between the radio halo power and SZ-derived cluster properties, however, Cassano et al. (2013) find that the uncertainties in the best-fit parameters for the $P_{1.4{\rm GHz}} - Y_{\rm SZ}$ relation are comparable to those for the X-ray selected sample.

No spatial link between (giant) radio halo emission and SZ emission has been found as yet, possibly owing to the relative lack of high-resolution SZ cluster maps. Cluster surveys with the NIKA (Adam et al., 2015), MUSTANG-1.5 (Young et al., 2014) and forthcoming MUSTANG-2.0 instruments will provide the community with SZ cluster maps of sufficient angular resolution to make such a study possible.

Relaxation parameter, Γ

Wen and Han (2013) defined an optically-derived relaxation parameter, Γ, to quantify a cluster's dynamical state from photometric data. By smoothing the brightness distribution of cluster members, Γ is defined as the distance to the optimal plane defined by the distribution asymmetry, ridge flatness, and the normalised model-fitting residual. A negative value indicates a disturbed system, with positive values implying dynamical relaxation. They found an anti-correlation between Γ and the 1.4 GHz radio power, with the more powerful halos hosted in clusters with smaller relaxation parameters. The scatter in the observed scaling relations between $P_{1.4{\rm GHz}}$ and thermal cluster properties discussed above can be reduced by incorporating Γ to create a 3D correlation (Yuan et al., 2015).

2.2.1.3 Connection with mergers

The bimodality in the radio halo $P_{1.4\mathrm{GHz}}$ scaling relations indicates a connection between the on/off radio state of a cluster and its dynamical characterisation. Early radio halo studies provided circumstantial evidence for this as radio halos had only been found in clusters showing either X-ray (Feretti, 1999, 2002; Giovannini and Feretti, 2002; Schuecker et al., 2001; Böhringer and Schuecker, 2002) or optical substructure (Girardi and Biviano, 2002; Ferrari et al., 2003; Boschin et al., 2004, 2006). The link between radio halos and cluster mergers was quantitatively confirmed through comparisons with X-ray morphological parameters (Buote, 2001; Cassano et al., 2010): radio loud systems and systems with radio upper limits populated separate regions of the parameter space, linked with merging and relaxed morphologies respectively. Cassano et al. (2013) confirmed that the two populations found in SZ-selected samples also correlated in the same way with the cluster dynamics. This observed merger connection is in agreement with predictions from the turbulent reacceleration model discussed in §2.3.1.

Yet the radio loud/radio quiet dynamical separation is not perfect: some merging clusters have no observable diffuse emission (e.g. A141, A2631, MACSJ2228.5+2036,[2] Cassano et al. 2010; A119, Giovannini and Feretti 2000; A2146, Russell et al. 2011), and a GRH has been detected in a cluster with a cool-core, which is more commonly associated with relaxed systems (CL1821+643, Bonafede et al., 2014b). These observations raise questions about whether there is an extra observational dichotomy within merging clusters themselves, which is not yet well understood. As some of the radio quiet mergers are relatively low-mass clusters, the question to answer is whether lower energy mergers (as expected from low-mass clusters) lead to a physical lack of radio halo, or if the emission is merely below the sensitivity limits of current observations. Next generation telescopes such as LOFAR and the Square Kilometre Array, with their superior sensitivities, should be able to determine whether radio halos exist in all mergers, or only the most massive systems.

Another possible explanation for the discrepant observations is that radio halo emission is

[2]Cassano et al. (2010) quoted an upper limit in the merging cluster A781, but a GRH was observed at 325 MHz and 1.4 GHz in the following year (Govoni et al., 2011).

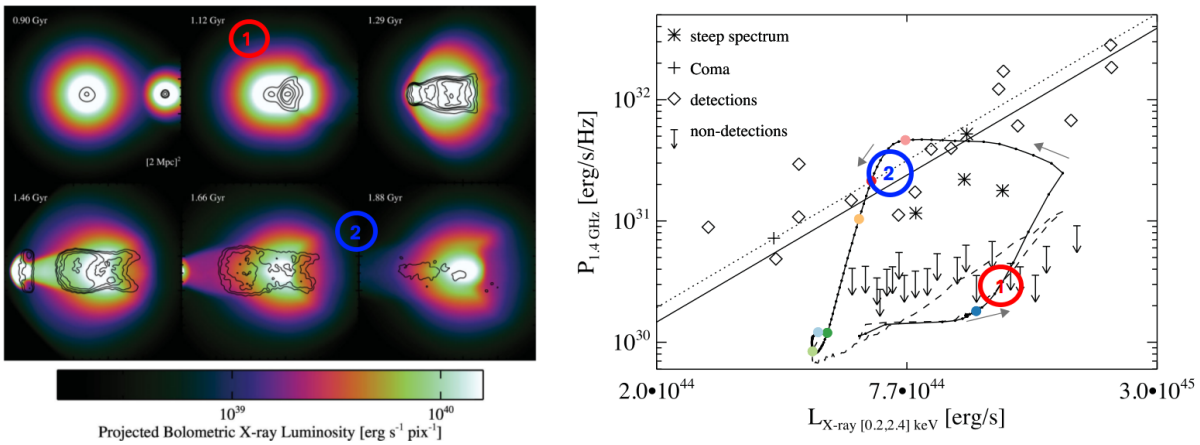

Figure 2.3: Results of the MHD simulations of Donnert et al. (2013) showing cluster properties at different stages of the cluster merger. *Left:* Projections of the bolometric X-ray luminosity overlaid with 1.4 GHz radio contours. The contours have the same levels throughout. *Right:* Evolution throughout the merger of the system's X-ray luminosity and radio power (black curve) overlaid on the observed radio halos and upper limits from Brunetti et al. (2009). The correlation is shown as the straight black line. Grey arrows indicate the time direction throughout the merger trace. Two main stages of the merger are indicated on both panels: (1) turbulent energy in the ICM has increased sufficiently for the radio halo to "switch on" and become observable; (2) the merger activity has lessened significantly and the radio halo begins to dissipate. Source: Adapted from Donnert et al. (2013).

linked to the stage of evolution of the merger at which the cluster is observed. Donnert et al. (2013) ran a magnetohydrodynamical (MHD) simulation of a massive ($10^{15} M_{\odot}$), high mass ratio merger between two subclusters and modelled both the power and morphology of the expected X-ray and radio emission from turbulent reacceleration at different times during the merger. Some of their results are shown in the left and right panels of Figure 2.3. They showed that radio halos are transient phenomena, with energy injected via turbulent motions in the ICM "switching on" the radio emission and moving the cluster from the region of upper limits onto the $P_{1.4\mathrm{GHz}} - L_{\mathrm{X}}$ correlation (region 1 in both panels). As the merger evolves, the spectrum of the synchrotron radiation steepens and the radio halo dissipates, moving the system back towards the radio quiet population (region 2 in both panels). This scenario explains the position of USSRHs in the $P_{1.4\mathrm{GHz}} - L_{\mathrm{X}}$ plane, where they appear to be bridging the gap between the two populations.

2.2.2 Radio Relics

When diffuse radio emission is located on the periphery of the cluster region, it is generally classified as a *radio relic*. Like radio halos, relics exhibit low surface brightnesses and steep spectra, however unlike their centralised counterparts, relics are significantly polarized up to 20 - 30%. Radio relics are excellent indicators that μG magnetic fields and relativistic particles exist in the outskirts of clusters. The prevailing theory is that giant radio relics trace relatively strong merger shocks in the outer regions of cluster cores, which drive the acceleration or reacceleration of the radiating CRe (Miniati et al., 2001a; Brüggen et al., 2012; Kang et al., 2012; Ensslin et al., 1998; Hoeft and Brüggen, 2007; Kang and Ryu, 2011; van Weeren et al., 2010; Bagchi et al., 2006; Roettiger et al., 1999; Enßlin and Gopal-Krishna, 2001; Hoeft et al., 2008; Skillman et al., 2011; Markevitch et al., 2005; Pinzke et al., 2013) in agreement with predictions from shock statistics from cosmological simulations (Skillman et al., 2008)

The first radio relic was detected in the Coma cluster (e.g. Giovannini et al., 1991, and references therein). It displays an elongated morphology, with the major axis roughly perpendicular to the direction towards the cluster centre. The majority of relic sources have this morphology, however variations have also been observed. Roundish radio relics have been detected, usually closer to the cluster centre but still offset from the X-ray emission, and these tend to be less expansive than their elongated counterparts. The different radio relic shapes are discussed below in §2.2.2.1.

To date there are over 70 known radio relics hosted in 53 clusters. Most detections occur at low redshift ($z < 0.4$), with high redshift detections made difficult due to instrument sensitivity limits. By far the highest redshift observation is the double radio relics in “El Gordo”, a massive cluster at z=0.87. As with radio halos, deeper surveys will probe further back in time and improve our insight as to whether there are intrinsically few diffuse radio sources in clusters at high redshifts.

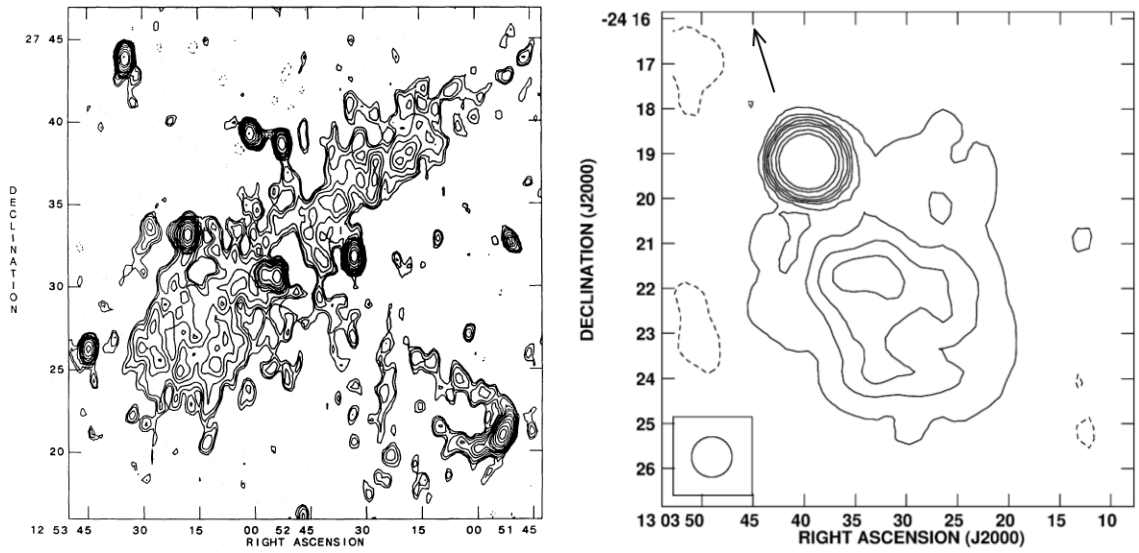

Figure 2.4: Examples of radio relics with different morphologies. *Left:* 608 MHz WSRT image of the elongated relic in the Coma cluster. Source: Giovannini et al. (1991). *Right:* NVSS 1.4 GHz contours of the roundish radio halo in A1664. Contour levels are -1.05, 1.05, 2.10, 3.15, 4.20, 5.25, 10.50, 21.00, 42.00 mJy beam^{-1}, with a synthesised beam of $45'' \times 45''$. The cluster centre is $\sim$ 500 kpc ($\sim 3.7'$) North of the compact source, in the direction of the arrow. Image adapted from Kale et al. (2012).

2.2.2.1 Observed structure

Radio relics can be split into two main categories based on their differing morphological properties, referred to as either elongated or roundish radio relics. Observations have also revealed different combinations of diffuse radio emission involving radio relics. Examples of the different morphologies and configurations are given in Figures 2.4, 2.5 and 2.6.

Elongated relics

The prototypical form of radio relics, *elongated relics* have high major- to minor-axis ratios, with the major axis tangential to the edge of the cluster region, and cover large distances ($\gtrsim 1$ Mpc). Elongated relics are highly polarized with polarization vectors orientated perpendicular to the major axis. An image of the Coma relic from Giovannini et al. (1991) is given in the left panel of Figure 2.4.

Not all elongated relics have the same morphologies; some elongated relics are exceptionally narrow with a few giant narrow relics such as the "Sausage" relic in CIZA J2242.8+5301 (van Weeren et al., 2011c, Figure 2.5) and the "Toothbrush" relic in 1RXS J0603.3+4214 (van Weeren et al., 2012, Figure 2.6) being extensively researched (van Weeren et al., 2011a; Röttgering et al., 2013; Ogrean et al., 2013a; Stroe et al., 2014c,b,a, 2015). The sausage relic is part of a double radio relic system shown in Figure 2.5 and is slightly curved with extremely regular polarization vectors. In certain cases projection effects may play a major role in explaining apparently odd orientations of elongated relics (e.g. A115, Govoni et al., 2001b), however the overall morphology and location of elongated relics are in line with models of merger shocks, discussed further in §2.2.2.4.

Roundish relics

The second morphological class of radio relics have a more symmetrical, circular structure and are therefore called *roundish relics*. Although these relics also lie on the periphery of clusters, they are found slightly closer to the cluster centre and tend to be smaller than elongated relics, with typical sizes of ∼100 - 350 kpc. To date, most roundish relics have been observed at quite low redshifts, $z < 0.2$, and have very steep curved spectra. An example of a roundish relic is that in A1664 (Govoni et al., 2001b) displayed in the right panel of Figure 2.4.

As they have different shapes and cluster locations compared to elongated relics, roundish relics have different models for their origin. High resolution imaging of roundish relics show a filamentary structure within the relic itself, and they are often located near the central first ranked galaxy (FRG) but not coinciding with it (Govoni et al., 2001b; Slee et al., 2001). Since these sources are often close to AGN they can be explained by the shock-wave re-energisation

of radio lobes from previous AGN activity. The radio lobes were previously unobservable due to synchrotron and IC losses. We note, however, that unlike the shock-driven elongated relics, roundish relics have not as yet been found in pairs. Mathews and Brighenti (2008) suggest a different scenario in which the relics are the result of radio bubbles interacting with the outer regions of the ICM. Due to their sometimes small size, the correct identification of roundish radio relics can be complicated by the presence of old radio galaxies with aged spectra (Randall et al., 2010). In some cases, a few roundish relics cannot be readily explained by models involving previous radio activity (Feretti et al., 2006; Solovyeva et al., 2008; Govoni et al., 2001b). More observations are required in order to fully understand the origin of these types of relics.

Double relics

We previously mentioned the link between elongated radio relics and shock fronts caused by cluster mergers, discussed in §2.2.1.3. In mergers with almost equal subcluster mass ratios and a low impact parameter, a pair of shocks, and hence radio relics, are expected on either side of the cluster, aligned with the merger axis. When this configuration is observed the cluster is said to host double radio relics. The first double relic system was observed in A3667 (Rottgering et al., 1997; Johnston-Hollitt et al., 2002; Johnston-Hollitt, 2003) but these configurations have since become quite common with almost 40% of relics belonging to double systems. Figure 2.5 shows examples of three double relic systems of different sizes. Most double relics have elongated structures, in line with the connection to plasma shocks.

Hydrodynamical simulations of CIZA J2242.8+5301 have shown that the observed double relic morphologies result routinely from plane-of-the-sky mergers involving the head-on collision of equal mass clusters (van Weeren et al., 2011c). Thus double relic systems should be found in low-ratio mergers, whereas single relic systems are expected to be in mergers with higher mass ratios or where the merger is occurring to some degree along the line of sight.

Relics and halos

In several cases, radio relics, both double and single, have been observed in clusters hosting a radio halo. These systems are significant indications of there being a link between radio relics,

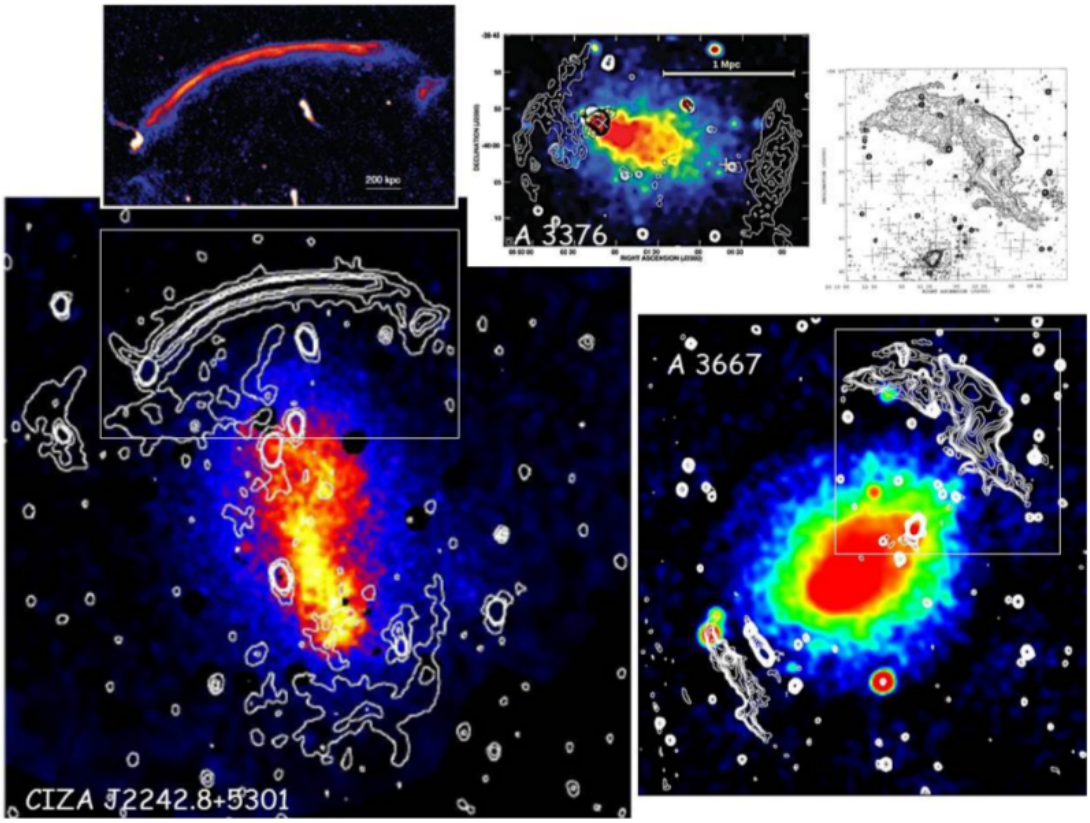

Figure 2.5: Images of giant radio relics (contours) overlaid on the X-ray emission from the host systems (colors). The three radio relics are reported with the same physical scale. Upper-left and upper-right panels highlight the high-resolution radio images of the northern relics in CIZA2242 and A3667, respectively (credits: van Weeren et al. (2010) and Ogrean et al. (2013a) for CIZA2242; Rottgering et al. (1997) for A3667; and Kale et al. (2012) for A3376). Source: Brunetti and Jones (2014).

radio halos and mergers, as the relics and halos may stem from the same merger event, although from different physical mechanisms. Figure 2.6 shows some examples of combined radio halo and relic systems. In some cases there is bridge emission between the halo and relic, as is the case for the "Toothbrush" relic and its associated halo in 1RXS J0603.3+4214 (right panel of Figure 2.6.

However the majority of relic systems do not host a radio halo, and in all relic-halo systems, the relic has a surface brightness significantly higher than that of the halo. The lack of radio halos in many relic systems may indicate that radio relics can be produced by weak/minor mergers which don't produce enough turbulent energy to drive an observable radio halo. This may also

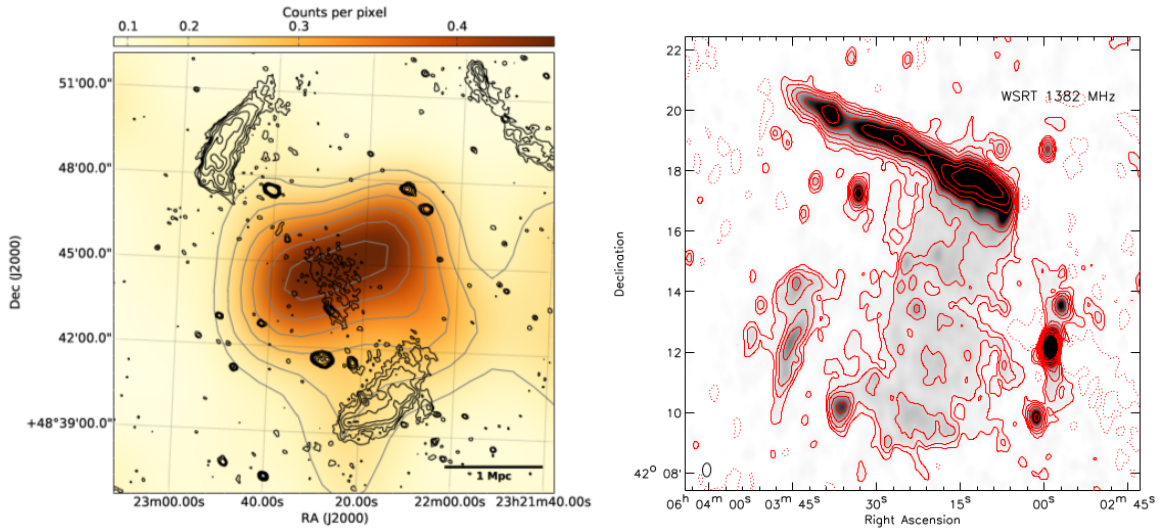

Figure 2.6: Examples of galaxy clusters hosting both radio halo and radio relic emission. *Left:* GMRT 323 MHz contours showing the radio halo and double relics in PSZ1 G108.18-11.53 at $(1, 2, 4, 8, 16, 32) \times 3\sigma$ with $\sigma = 86\mu$Jy beam^{-1} (beam: $11'' \times 8''$). The contours are overlaid on the smoothed 0.1 - 2.4 keV photon image from the ROSAT all sky survey. Source: de Gasperin et al. (2015). *Right:* 1.4 GHz WSRT emission of the radio halo and single straight radio relic in 1RXS J0603.3+4214. There is a bridge of radio emission joining the two structures. Source: van Weeren et al. (2012).

explain the observations of radio relics in cool-core clusters (e.g. A85, Slee et al., 2001): if a minor or off-axis merger were present, a shock wave to induce a relic can occur without disrupting the cluster core.

2.2.2.2 Spectral properties

Comprehensive radio spectral data is available for several radio relics, most of which have elongated structure as these are favoured by interferometric observations — the cluster periphery is less contaminated by compact radio sources which allows robust relic detections over a wider range of frequencies.

Integrated spectrum

As is seen for radio halos, all radio relics exhibit steep spectra, $\alpha \gtrsim 1$, however the two branches of relics have different ranges of spectral indices and indeed different spectral properties (Feretti

et al., 2012). Elongated relics have spectral indices $\alpha \sim 1.0 - 1.6$ with a fairly uniform distribution over that range. Roundish relics have spectral indices with similar values but on average they have a much steeper spectrum, $\langle\alpha\rangle \approx 2.0$. The observed range of spectral index for roundish relics extends to $\alpha = 2.9$.

When two or more frequency measurements are available, roundish radio relic spectra show spectral steepening at higher frequencies, whereas elongated relics generally have flat spectra. This reflects the involvement of strong shocks in the peripheral region of clusters, as shocks with large Mach numbers are responsible for producing flat-spectrum emission. In a few cases, such as A754 (Bacchi et al., 2003) and A2256 (Clarke and Ensslin, 2006), the integrated spectrum has a complex shape.

Spectral index distribution

Accurate spectral index maps are available for only a few well-studied relics (Lindner et al., 2014; Kale and Dwarakanath, 2012; Clarke and Ensslin, 2006; van Weeren et al., 2012; Stroe et al., 2015; Orrú et al., 2007). Elongated relics have distinct spectral index distributions. The spectral index steepens along the minor axis, with the flattest region at the outermost edge. This pattern is evident in the spectral map of the "Toothbrush" relic in 1RXS J0603.3+4214 shown in the left panel of Figure 2.7 (or A2744), and is in accordance with the brightness profile of the relics (van Weeren et al., 2012).

Only a small fraction of roundish radio relics have spectral index maps and there is little consensus on the distributions. The roundish relic in A2256 (Clarke and Ensslin, 2006) shows a spectral steepening towards the cluster centre, but it lacks the regular spectral index gradient found in elongated relics. In other systems, such as A1664, the roundish relic, shown in the right panel of Figure 2.7, displays no discernible pattern of the spectral index distribution (Kale and Dwarakanath, 2012). These relics have complex structures at high resolution which leads to the irregular spectral index distributions.

Ultra-steep spectrum sources

At the beginning of this section we mentioned that some roundish radio relics have extremely

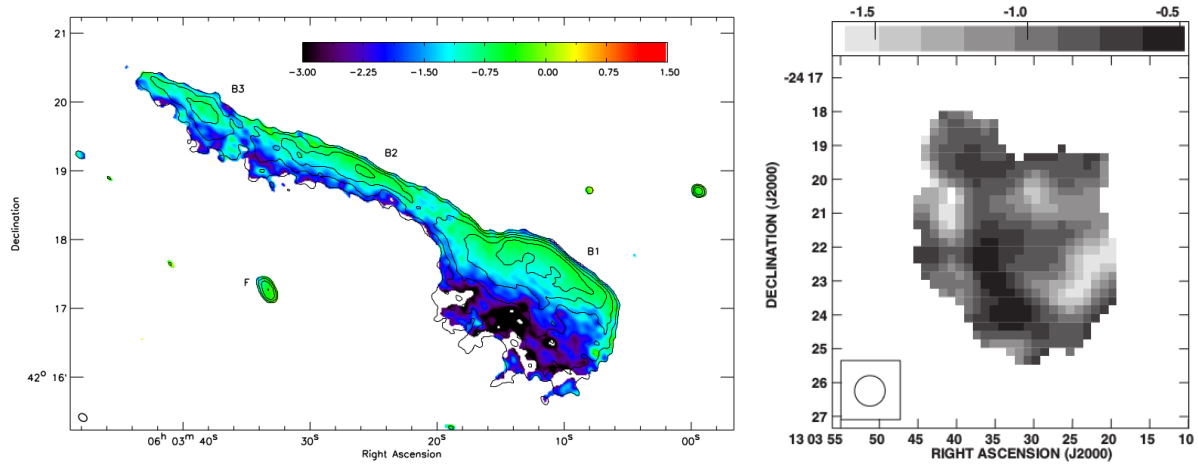

Figure 2.7: Radio relic spectral index maps. *Left:* "Toothbrush" relic in 1RXS J0603.3+4214 showing a spectral steepening towards the centre of the cluster. Source: van Weeren et al. (2012). *Right:* The roundish relic in A1164 with no indication of a regular spectral index distribution. Source: Kale and Dwarakanath (2012).

steep spectra ($\alpha \gtrsim 2$). These are considered as ultra-steep spectrum radio relics (USSRRs) and their spectra incorporate a cut-off at high frequencies. Very few of these sources exist (some examples are A13 from Slee et al. (2001) and A2443 from Cohen and Clarke (2011)) but the small number of detections may be due to selection effects, observing at too high a frequency considering the sensitivities of current telescopes, as well as incorrect classification as old radio galaxies. The data from low frequency surveys with LOFAR (Röttgering et al., 2011) and other next generation telescopes should reveal more of these objects. Considering the differences in spectral properties of the two types of radio relics, spectral index measurements may be a crucial factor in correctly classifying new relic sources.

2.2.2.3 Observed correlations

In §2.2.1.2 we discuss the various correlations found between observable radio halo properties and those of the host cluster. Similarly, Feretti et al. (2012) collated all the then known radio relic observations, consisting of 50 relics from 39 clusters, and found a variety of correlations between different parameters, although generally speaking they are weaker than those for radio halos.

Projected distance, size, and radio power

As radio relics exist on the periphery of clusters, they can be characterised by their projected distance from the centre of the cluster, $R_{\rm cc}$. As roundish relics are generally found closer to the centre than elongated relics, it is not surprising that in correlations involving $R_{\rm cc}$, the two populations are fairly separated with only a small overlap in parameter space. Roundish relics are clustered at an average distance of $\sim$ 0.4 Mpc from the cluster centre, whereas elongated relics populate distances between $\sim$ 0.5 - 1.5 Mpc, but can be found out to 3 Mpc.

Feretti et al. (2012) looked at the relationships between $R_{\rm cc}$, the largest linear size (LLS), and 1.4 GHz radio power $P_{1.4\rm GHz}$ of the relics. They found no clear correlation between $R_{\rm cc}$ and $P_{1.4\rm GHz}$, although they noted that almost no powerful relics ($P_{1.4\rm GHz} > 10^{24}$ W Hz^{-1}) are detected closer than 0.4 Mpc to the cluster centre. At larger distances, relics exhibit a wide range of radio power ($\sim 10^{23}$ - 10^{25}). It is likely that this trend is due to the low efficiency of shocks in cluster central regions (Vazza et al., 2012a).

In terms of the size of relics, big (elongated) and small (roundish) radio relics are well separated with R_{cc}, with only the largest roundish relics populating the same space as elongated relics. The two smallest relics in the sample, the roundish relics in A4038 and A2063, have the smallest projected distances ($\sim$ 0.04 Mpc) and lie far away from the main population of relics. Unlike radio halos, a comparison of relic LLS and radio power shows only a (marginal) correlation, and only when the full population of relics is considered as one. The most powerful relics ($P_{1.4\rm GHz} > 10^{25}$ W Hz^{-1}) are all elongated and have some of the largest extents. In general, however, for a given linear size, radio relics can exhibit almost the full range of radio power.

These comparisons show unequivocally that roundish and elongated radio relics have different properties, with roundish relics being on average smaller and fainter than their more elongated cousins. In general, the above relic properties are consistent with the current origin models, in which the more efficient shocks occur in the lower density regions on the outskirts of clusters, where they can spawn larger, more powerful emission.

Cluster X-ray luminosity, $L_{\rm X}$

A correlation between relic radio power and cluster X-ray luminosity was found that holds for both types of relics. The correlation is similar to that for radio halos, where the more powerful emission is detected in the brighter X-ray clusters. However the relic relation has more scatter and the overall slope is flatter. Although halos and relics occupy almost the same region of parameter space, more relics are found in low luminosity clusters ($L_{\rm X} < 10^{44}$ erg s^{-1}) possibly owing to their flatter spectra (elongated relics) or smaller size.

2.2.2.4 Connection with shocks

There are several indications that radio relics are associated with plasma shocks in the ICM. The first of these is the remarkable similarity of the shape and location of elongated relics to that of shock fronts observable in the X-rays (e.g. van Weeren et al., 2011c). This is strong evidence for a direct connection between shocks and the energisation of the synchrotron-emitting cosmic rays in the same region (Markevitch, 2010; Giacintucci et al., 2008; Finoguenov et al., 2010; Macario et al., 2011; Akamatsu et al., 2012; Ogrean et al., 2013b; Owers et al., 2014). In the cases where relic emission is offset from the location of X-ray shocks, cosmological hydrodynamical simulations by Hong et al. (2015) show that this can be explained by the occurrence of multiple shocks along the line of sight. Secondly, the existence of double relic systems with the relics oriented along the merger axis (see §2.2.2.1) is further evidence for shock involvement in relic production as emerging merger shocks are expected to form in pairs. Finally, the orientation of strong polarization in some elongated relics implies that the magnetic field is aligned along the relic's major axis. This in turn suggests that relics develop where the magnetic field is compressed in the shock plane (Clarke and Ensslin, 2006; van Weeren et al., 2010; Brüggen et al., 2012).

However some observational evidence is contrary to this picture. X-ray observations show that the shocks thought to be driving the relics are relatively weak with Mach numbers of $\mathcal{M} \sim$ 1.5 - 3, including those with locations matching precisely with radio relic emission (Markevitch and Vikhlinin, 2007). Weak shocks are presumed to be fairly inefficient in accelerating particles, particularly if those particles are initially non-relativistic, and produce steeper spectra based on diffuse shock acceleration (DSA) models than are observed. This means that weak shocks cannot

energise injected particles to the level required to create the observed synchrotron emissions.

This can theoretically be solved by the existence of a seed population of pre-existing cosmic rays which are reaccelerated to higher energies by weak merger shocks (Markevitch et al., 2005; Kang et al., 2012; Pinzke et al., 2013). In this scenario, a flat-spectrum seed population interacting with weak shocks can be energised by DSA by a factor of a few. This makes the DSA reacceleration a more efficient process (Kang and Ryu, 2011). Moreover the resulting spectrum of the reaccelerated particles will be similar to that of the pre-existing population rather than the typical DSA spectrum for shock injected cosmic rays (Kang and Jones, 2005; Kang and Ryu, 2011). The leading origin theory for radio relics, the shock-induced reacceleration model, addresses most of these issues and is discussed in §2.3.1.2.

2.2.3 Mini-Halos

The third type of diffuse radio emission to be found in galaxy clusters is the mini-halo, so called due to the relatively small volumes they cover ($\approx$ 500 kpc) compared to the radio halos discussed in §2.2.1. Mini-halos are found in some cool-core clusters but the number of detections is quite low. They are centred around the cluster's main radio galaxy, often the cD galaxy, which is usually located at or close to the centre of the cluster. Like regular radio halos, they have steep spectra and are very faint ($\sim$ 0.1 - 1 μJy arcsec^{-2} at 1.4 GHz). Some observations indicate radial spectral steepening (e.g. Sijbring, 1993; Gitti et al., 2002, 2004; Murgia et al., 2010a). An example of a mini-halo is shown in Figure 2.8.

2.2.3.1 Identification difficulties

The class prototype is hosted by the Perseus cluster (Miley and Perola, 1975; Noordam and de Bruyn, 1982; Burns et al., 1992). This mini-halo is actually slightly more difficult to classify than a typical mini-halo such as that in the Ophiuchus cluster (Govoni et al., 2009; Murgia et al., 2010a). Since the magnetic fields and relativistic particles responsible for the non-thermal radio emission are thought to be thoroughly mixed with the thermal ICM gas, a spatial link between the X-ray emitting gas and the mini-halo emission can be exploited to assist in mini-

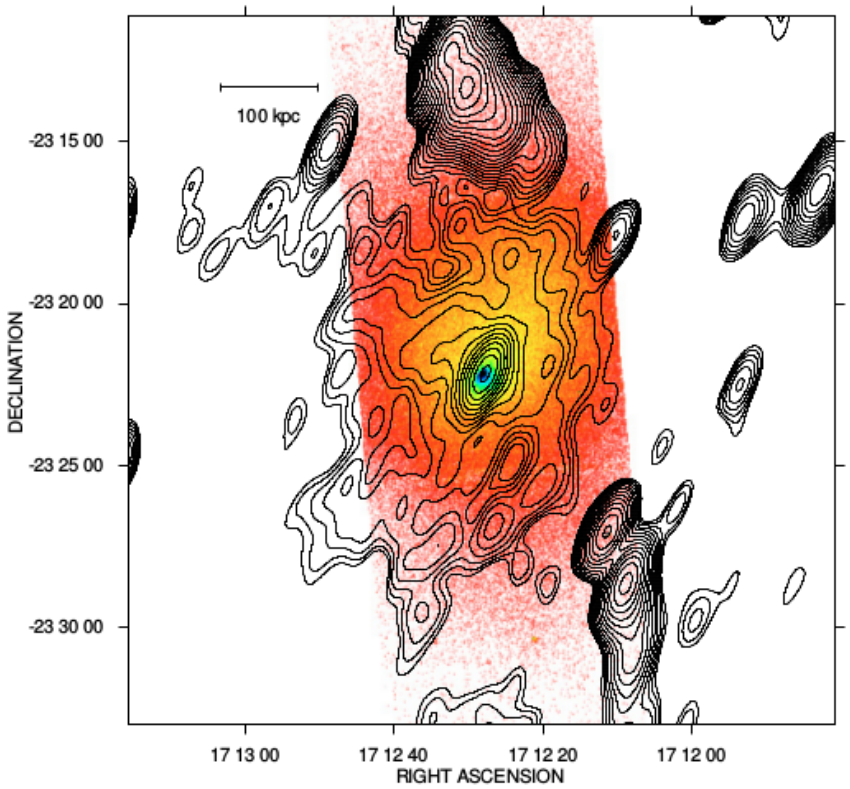

Figure 2.8: VLA 1.4 GHz contours of the mini-halo in the Ophiuchus cluster overlaid on the *Chandra* X-ray emission. The resolution of the radio image is $91.4'' \times 40.4''$. The first contour level is drawn at 0.3 mJy beam^{-1}, increasing in steps of a factor of $\sqrt{2}$. Source: Govoni et al. (2009).

halo identification and used to separate emission from old radio bubbles created by AGN activity.

If a small diffuse radio source in the centre of a cluster is off-set from cluster X-ray emission it is not classified as a mini-halo (e.g. emission in A2052 Blanton et al., 2011). Radio observations of the Perseus cluster show centralised diffuse emission coincident with X-ray cavities, however it is also host to similar emission at larger radii that overlaps the thermal X-ray gas and it is this portion of the radio emission which is identified as a radio mini-halo. The multitude of possible steep-spectrum sources in the central regions of clusters make mini-halo identification quite challenging if no X-ray observations are available.

Since mini-halos are centred around a dominant cluster radio galaxy, their detection becomes even more problematic if they have a small angular size and the diffuse emission is overwhelmed by the bright emission of the galaxy.

2.2.3.2 Formation theories

Due to the small number of detections, the origin of radio mini-halos is not yet certain. A correlation between the power emitted by the mini-halo and the host cluster's cooling power (Gitti et al., 2004) supports the argument that they evolved from a pre-existing population of CRe that are reaccelerated by MHD turbulence (Gitti et al., 2002). The reacceleration has also been suggested to occur via turbulence driven from gas sloshing in the cool cores of clusters (Mazzotta and Giacintucci, 2008; ZuHone et al., 2011a).

Recent high-resolution SZ observations of RXJ1347-1145 showed a similar mapping between the mini-halo emission and the SZ structure as previously found for X-rays (Ferrari et al., 2011). This provides evidence for CRe reacceleration from minor subcluster mergers which have not disturbed the cluster cool core and suggests that the synchrotron emission is driven by a small shock front moving through the ICM (Ferrari et al., 2011). More observations of radio mini-halos will be necessary to gain a more complete understanding of the mechanisms which cause the radio emission.

2.3 Formation models for cluster diffuse emission

In sections 2.2.1 and 2.2.2 we established a link between cluster merger activity and the presence of a radio halo and/or relic. Similarly, mini-halos have an observational connection to relaxed, cool-core clusters (see §2.2.3). Major cluster mergers that occur during the build-up of structure in the Universe are known to release large amounts of energy into the ICM, potentially providing energy for the radio-emitting cosmic rays and amplifying cluster magnetic fields to the observed μG levels (Roettiger et al., 1999; Dolag et al., 1999, 2002; Ryu et al., 2008).

With magnetic fields expected to pervade the entire Universe, relativistic electrons and/or protons are the pivotal element to explain the existence of diffuse synchrotron emission in clusters (see §2.1). Due to their large regular volumes, radio halos in particular are difficult to explain. The radiative lifetime of CRe, due to synchrotron and inverse Compton losses, is $\sim 10^8$ years (Sarazin, 1999). However, the expected diffusion velocity of the CRe population is close to

the Alfvén speed ($\sim$100 km s^{-1}). This leads to what is known as the *diffusion problem* where the radiative lifetime of the emitting particles is too short to explain the emission volume. The large scales covered by the emission thus require some *in situ* acceleration of the particles with an efficiency comparable to the electron losses (Petrosian, 2001), or relativistic particles to be continually injected into the cluster region (Jaffe, 1977).

There are currently two competing principal theories for how the GeV electrons get distributed in the cluster volume. These models have strong predictive power and their theories can therefore be tested with observations using scaling relations which provide links between the non-thermal and thermal properties of the ICM (e.g. X-ray or SZ observations, see sections 2.2.1.2 and 2.2.2.3). Here we introduce these models and discuss their observational predictions compared with the current data.

2.3.1 Reacceleration models

Also called primary electron models, reacceleration models are based on the notion that pre-existing populations of relativistic electrons exist in the cluster environment from previous or existing AGN activity from quasars and radio galaxies (Miley and Perola, 1975; Brunetti et al., 2001), or supernovae events and galactic winds during star formation in normal galaxies (Völk et al., 1996; Jones, 2011; Morlino and Caprioli, 2012), and that the seed CRe population undergoes second order Fermi acceleration processes (Fermi, 1949; Clarke et al., 2001) to reaccelerate the particles to the required energies. In the case of cool-core clusters, most of them contain a radio-loud central, dominant galaxy which can provide the necessary CRe (Burns, 1990; Best et al., 2007; Mittal et al., 2009). Certain models have also considered the possibility that the seed population is non-relativistic (e.g. Dogiel et al., 2007, and references therein).

There are two primary mechanisms to transfer energy from the ICM to the reaccelerated cosmic rays: cluster turbulence and cluster shocks, both of which occur during mergers.

2.3.1.1 Turbulence

During a cluster merger, ICM electrons can be reaccelerated to relativistic speeds via interactions with large scale ($\sim$ Mpc) MHD turbulence (e.g. Schlickeiser et al., 1987; Ensslin et al., 1998; Petrosian, 2001; Fujita et al., 2003; Brunetti et al., 2004; Xu et al., 2010; Brunetti and Lazarian, 2011). This turbulent energy is provided by gas sloshing in cluster cores, shearing instabilities, and from intricate interplay among structure formation and merger shocks which develop in the ICM (Vazza et al., 2010a, 2009b; Dolag et al., 2005b; Iapichino and Niemeyer, 2008; Keshet et al., 2010; Iapichino et al., 2011; Paul et al., 2011; ZuHone et al., 2011b; Hallman and Jeltema, 2011; Vazza et al., 2011a, 2012b; Nagai et al., 2013; Miniati, 2014). Numerical simulations show that a combination of these mechanisms can indeed drive MHD turbulence throughout the cluster region (Miniati, 2014; Beresnyak et al., 2013). These processes are the foundation for the turbulent reacceleration model for radio halos and radio mini-halos.

As a second-order Fermi process, turbulent acceleration is not very efficient and is only productive in re-energising CRe for a few hundred Myr. Any resulting observable radio emission is therefore expected to coincide with ongoing or very recent merger events (Brown et al., 2011a; Feretti et al., 2004a; Enßlin et al., 2011), which should leave observable traces in the thermal ICM. The turbulent reacceleration model thus successfully predicts the observed correlation between radio halos and cluster mergers as discussed in §2.2.1.3, as well as the existence of USS-RHs as discussed in §2.2.1.1. Once the turbulent energy loses efficiency, i.e. after a certain point in the merger, the spectrum of the reaccelerated particles will become dominated by synchrotron and IC energy losses and steepen accordingly. The observations that radio halos are not very common structures (e.g. Kuo et al., 2004), and the observed bimodality in the radio halo $P_{1.4GHz} - L_{\rm X}$ plane are also in line with MHD turbulence being the driving factor in radio halo formation (Brunetti et al., 2009).

Models of turbulence-driven particle acceleration predict that the resulting population of relativistic electrons will have an energy distribution with a maximum Lorentz factor of $\gamma \sim 10^5$ (Brunetti, 2004). This will cause a high-frequency cut-off in the population synchrotron spectrum and these models therefore anticipate a steepening of the radio halo spectrum at high frequencies.

Furthermore, since MHD turbulence is not uniform throughout the cluster region, with different turbulent processes being stronger or weaker in different parts of the cluster, the spectral index distribution of the radio emission will likely be of a complex and irregular nature. Observations of radio halo spectra agree with these predictions and thus support the turbulent reacceleration model for radio halos.

These models can also explain radio mini-halos. In this case MHD turbulence in the cool cores of clusters can drive the reacceleration of particles from a variety of potential seed populations in the central cluster region, as discussed in §2.2.3.2, which is consistent with the few observations of mini-halo spectra and the apparent correlation between their radio power and the cooling rate power of the host cluster (Gitti et al., 2004). Turbulent energy to form radio mini-halos may also be generated by gas sloshing (Mazzotta and Giacintucci, 2008; ZuHone et al., 2011a), a theory that is supported by spiral-shaped cold fronts in high resolution X-ray imaging of cluster cool-cores (Giacintucci et al., 2011).

Although MHD turbulence is a good fit to the radio halo and mini-halo data, the intricacies of the physical mechanisms involved are still not perfectly understood. Our knowledge will be improved once X-ray observations are deep enough to place tight constraints on the physics of turbulence in dynamically disturbed clusters (Schuecker et al., 2004; Sanders et al., 2013). The ASTRO-H satellite is expected to achieve this by observing, among other things, the Doppler broadening and shifting of metal lines in the ICM created by turbulent motions (Dolag et al., 2005b; Nagai et al., 2013; Sunyaev et al., 2003; Vazza et al., 2010b; Takahashi et al., 2010; Zhuravleva et al., 2012, 2013).

2.3.1.2 Shocks

Current observations of radio relics imply they are strongly connected with cluster shocks (Sarazin, 1999; Keshet et al., 2004). Shock acceleration, a first order Fermi process, has been identified as the process responsible for supernovae synchrotron emission (Jones, 2011; Morlino and Caprioli, 2012). In the cluster context, cosmological simulations have shown that out-going shock waves with moderate Mach numbers, $\mathcal{M} \sim 2$ - 3, occur on the peripheral regions of clusters due to

merger activity (Miniati et al., 2000; Ryu et al., 2003; Pfrommer et al., 2006; Skillman et al., 2008; Ryu et al., 2008; Vazza et al., 2009a, 2010a; Kang et al., 2007; Vazza et al., 2011b). The Mach number is the primary determinant of the shock acceleration efficiency. Strong shocks, $\mathcal{M} > 3$, are efficient particle accelerators, but only occur at very large distances (several Mpcs) from the cluster centre where the density is low and there is minimal energy available to interact with the shocks. Although weaker shocks are less efficient in accelerating particles, they are found closer to cluster cores where the density is higher and thus there is more accessible energy. In fact, a high percentage of the gravitational energy is dissipated at the relatively weak merger-driven shocks. If even a small amount of this energy is converted into non-thermal particles, then the ICM could host populations of non-thermal cosmic ray particles that have sufficient energy to create diffuse radio emission (Miniati et al., 2001b; Ryu et al., 2003; Blasi et al., 2007; Pfrommer et al., 2007; Vazza et al., 2012a). This is the basis of the shock-driven reacceleration model for radio relics, where the pre-existing relativistic electrons are thought to be from the thermal ICM itself (Ensslin et al., 1998), or remnants of previous AGN activity (Enßlin and Gopal-Krishna, 2001; Enßlin and Brüggen, 2002; Hoeft et al., 2004).

Diffuse shock acceleration (DSA) theory is commonly used to describe the energisation of cosmic rays at shock locations (Bell, 1978; Drury, 1983; Blandford and Eichler, 1987; Jones and Ellison, 1991). In this framework, if the seed particles have finite scattering lengths much larger than the width of the shock, they are trapped at the shock front until convection downstream of the shock allows them to escape. While the particles are held in this shock flow, they gain energy each time they are reflected back across the shock with a rate proportional to the energy itself.

Since electrons suffer from strong synchrotron and IC losses, their short radiative lifetimes limit visible radio emission to the region in the immediate vicinity of the shock fronts, causing fairly narrow widths. The downstream diffusion of particles once they are released from the shock-flow causes the oldest and least energetic population of cosmic rays to be the furthest away from the shock front, leading to a flatter radio spectrum at the shock edge. Moreover, DSA models predict that the magnetic field lines involved in the synchrotron emission are aligned with the shock front. These model predictions are consistent with the observed structures, relative locations, and polarization of elongated radio relics (§2.2.2.1).

DSA theories cannot exclude the possibility that shock acceleration could be effective at certain locations of radio halo emission (Markevitch, 2010). However, since radio halos cover large volumes of the ICM, it is unlikely that this emission is purely driven by localised shocks. Another possible link between shocks and radio halos is indicated by the spatial correlation between radio halo emission and the hot gas of the ICM (§2.2.1.2) that has been found for some clusters (e.g. Govoni et al., 2004). However this is not a strong link as the spatial correlation does not appear to be a generic feature of observed radio halos.

2.3.2 Hadronic/secondary electron model

It has been suggested that neutrino annihilation in the cluster dark matter halo can give rise to secondary products which can decay into the relativistic electrons necessary for the formation of diffuse radio emission (Colafrancesco and Mele, 2001), however the most popular hadronic models have relativistic electrons being continuously injected into the ICM through inelastic collisions between cosmic ray protons and particles in the thermal ICM. These secondary electrons interact with the cluster magnetic field to form radio halos and mini-halos (Dennison, 1980; Blasi and Colafrancesco, 1999; Dolag and Enßlin, 2000; Pfrommer and Enßlin, 2004; Keshet and Loeb, 2010; Zandanel et al., 2012). These hadronic models require a population of relativistic protons and thus cannot be used to explain radio relics, as the outer regions of clusters are too sparsely populated by cosmic ray protons (CRp). In the central cluster region, CRp can be injected into the ICM by AGN or structure formation shocks, among others. This means that the radio emission produced by secondary electrons may not be linked to cluster merger activity, but it should be ubiquitous for all clusters.

Hadronic models can replicate the main properties of radio halos as long as the magnetic field in the radiating volume is stronger than a few μG. They predict halo spectra to follow a simple power law, i.e. no spectral curvature or complex features, independent of the position within the cluster (Brunetti, 2004). Furthermore this model predicts spectra with indices ~ 1.5, and thus the existence of USSRHs is not easily explained. Another specific prediction of this model is the production of observable gamma rays from neutrinos.

Keshet and Loeb (2010) used *XMM-Newton* (Jansen et al., 2001) and VLA data of a sample of 18 radio-halos and mini-halos to measure the distribution of magnetic fields in the clusters. Assuming secondary electron formation models and relatively strong ICM magnetic fields ($> 3\mu$G), they found a linear relationship between the X-ray and radio surface brightness that holds for both radio halos and mini-halos. Their model was able to reproduce the spectral steepening observed in halo spectra but it required an unlikely high central magnetic field of $> 10\mu$G.

One of the predictions specific to the hadronic model is the production of γ-ray emission that is an unavoidable consequence of the proton collisions that create the relativistic electrons: these collisions also produce neutral pions which then decay into γ-rays. As yet, diffuse γ-ray emission has not been observed in clusters (Reimer et al., 2003; Ackermann et al., 2010), but the high-energy upper limits can theoretically constrain the density of CRe produced in secondary electron models (e.g. Blasi et al., 2007). The most recent Fermi Large Area Telescope (Atwood et al., 2009) upper limits imply a minimum magnetic field strength to replicate observed radio halo emission without over producing γ-rays, which for some clusters is of the order of several μG (Jeltema and Profumo, 2011). A problem for hadronic models is that these implied magnetic field strengths are close to or higher than the largest cluster magnetic fields measured from Faraday rotation measures (Clarke et al., 2001; Carilli and Taylor, 2002; Bonafede et al., 2010). However, although the current γ-ray limits predict potentially unreasonably strong magnetic fields, the uncertainties on the measurements are too large to rule out the hadronic model completely.

2.3.3 Hybrid models

Neither of the above models perfectly explain all the observational characteristics of diffuse radio emission in galaxy clusters, particularly radio halos and mini-halos. Additional models have been proposed that combine aspects from each of the above models. These are accordingly called *hybrid* models and suggest that the observed radio halos can evolve from the reacceleration of both primary and secondary electrons by MHD turbulence, with the secondary electrons being produced by relativistic protons as they are in hadronic models (Miniati et al., 2001a).

The relative contributions of primary and secondary electrons to the total reaccelerated parti-

cle population are constrained by the observed properties of the radio emission. Some constraints have been derived by Brunetti and Blasi (2005) and more generally by Brunetti and Lazarian (2011). They suggest that hybrid models can produce large scale radio halos that are fainter than the detection thresholds of current instruments but which should be detected by the next generation instruments such as LOFAR and the SKA. Hybrid models also predict radio emission from secondary particles in relaxed systems which is just below the current upper limits (Brown et al., 2011b).

CHAPTER 3

OBSERVING ACT GALAXY CLUSTERS WITH THE GMRT

Although the number of radio halo detections has increased over the years, they are still a relatively rare phenomenon, with only $\sim$30% of high X-ray luminosity clusters found to host this emission thus far (Feretti et al., 2012). In particular, the majority of radio halo observing programmes use X-ray selected clusters, focusing on high luminosity clusters which are expected to be massive, increasing the chances of hosting observable diffuse radio emission. However the selection criteria bias these samples to bright cool-core clusters.

With the discovery of the Sunyaev-Zeldovich (SZ) effect in the 1970s (Sunyaev and Zel'dovich, 1972), wide area, untargeted SZ surveys are detecting large numbers of galaxy clusters via inverse Compton scattering of cosmic microwave background (CMB) photons by electrons within the hot ICM, which causes a distortion of the CMB spectrum in the direction of clusters. The cluster samples obtained are nearly independent of redshift as, although the CMB itself suffers from redshift dimming, the ratio of SZ signal to CMB does not. Moreover, since it is a scattering effect, the distance of the scattering medium does not matter. Due to this redshift-independence, this method produces mass-limited cluster samples, detecting all clusters above a certain mass

threshold. Numerical simulations, analytical models, and SZ observations also show that the SZ flux is tightly correlated with the cluster mass with low scatter (e.g. Reid and Spergel, 2006) and the simulated signals are more robust to baryonic astrophysics. There are currently three instruments producing large-area cosmological SZ galaxy cluster surveys: the PLANCK satellite (Planck Collaboration et al., 2011), the South Pole Telescope (SPT; Ruhl et al., 2004), and the Atacama Cosmology Telescope (ACT; Kosowsky, 2006).

Only in the last three years has the correlation between radio halos and SZ-selected clusters been investigated, and then only in a reverse manner, taking a sample of X-ray selected clusters from previous radio halo studies and determining SZ correlations based on their Compton y value from the Planck satellite (Basu, 2012; Cassano et al., 2013; Sommer and Basu, 2014). Although these studies have shown the occurrence of radio halos in an SZ-selected sample to be slightly higher than through X-ray selection, there are no blind SZ-selected samples that have been probed for diffuse radio emission. To this end we embarked on an observing programme to search for diffuse radio emission, particularly focusing on radio halo emission, in clusters detected by ACT using the Giant Metrewave Radio Telescope (GMRT).

3.1 An SZ-selected cluster sample

ACT is a 6 m telescope that observes the millimetre sky with arcminute resolution (Swetz et al., 2011). Between 2008 and 2011, ACT surveyed a 455 deg^2 strip centred at δ = -55°, as well as a 504 deg^2 strip centred at δ = 0° overlapping the Sloan Digital Sky Survey (SDSS) Stripe 82, at 148, 218, and 277 GHz. ACT has reported cluster detections to redshifts beyond $z \sim 1$, in a cosmologically significant volume, $\sim$ Gpc^3 (Marriage et al., 2011; Menanteau et al., 2012; Hasselfield et al., 2013).

ACT has detected over ninety clusters via the SZ effect, some of which are the rarest, most massive systems ($M \sim 10^{15} M_{\odot}$; Sifón et al., 2013). As the GMRT has a declination cutoff of -50°, we focused our cluster selection on the Equatorial cluster sample (ACT-E hereafter; Hasselfield et al., 2013) and submitted two observing proposals on the GMRT: one for the pilot project, and one for a high redshift sample.

3.1.1 Pilot project

In January 2012 we applied for GMRT time to observe four clusters from the, then preliminary, ACT-E cluster sample over a range of redshift (GMRT proposal ID: 22_044, PI: Knowles). The masses for this cluster sample were estimated from the preliminary SZ Compton parameter using the mass scaling relation from Sifón et al. (2013). We selected all clusters with a preliminary SZ-derived mass of $M_{200} > 10^{15} M_{\odot}$ and excluded those for which there was existing radio data of sufficient depth to search for diffuse emission (ACT-CL J2337.6+0016, ACT-CL J0152.6+0100, ACT-CL J2129.6+0005, ACT-CL J0326.8-0044; Venturi et al. (2008)). We were left with four clusters covering a redshift range $0.117 < z < 0.535$ and estimated mass range of $(1.09 < M_{200} < 1.33) \times 10^{15} M_{\odot}$, which we proposed for GMRT time. Only one of these clusters had existing X-ray imaging, ACT-CL J0256.5+0006, which showed it to be a merging cluster (Majerowicz et al., 2004).

The radio observations of these clusters were taken in late August 2012 (see §3.1.3 for observation details). The full ACT-E SZ cluster parameters were finalised after this date and the mass estimates were revised after a full processing of the ACT-E data using the UPP[1] mass profile. The clusters observed were subsequently found, following a revised mass-SZ observable scaling relation analysis in Hasselfield et al. (2013), to have lower SZ-derived masses than originally expected, with only one cluster having a new B12-derived mass[2] greater than $M_{500} = 5 \times 10^{14} M_{\odot}$. The cluster parameters from the published ACT-E sample (Hasselfield et al., 2013) are given in the first four rows of Table 3.1.

3.1.2 High redshift sample

The evolution of radio halo power is expected to have a strong redshift dependence due to inverse Compton (IC) losses off the cosmic microwave background (CMB) becoming more significant relative to synchrotron cooling at high redshift (e.g. Cassano et al., 2006a). However, there are only a few known radio halos at high redshift ($z > 0.5$): CL0016+16 (Giovannini and Fer-

[1] Universal Pressure Profile from Arnaud et al. (2010).

[2] Using the scaling relation from Bode et al. (2012).

Table 3.1: Cluster parameters and predicted radio halo physical parameters for our pilot cluster sample (top four) and the high redshift sample (bottom four). The total on-source time applied for per cluster is given in the last column. The SZ masses are the published masses from Hasselfield et al. (2013), using the universal pressure profile.

Cluster Name	z	Y_{500} (10^{-4} arcmin^2)	$M_{500,\mathrm{SZ}}$ ($10^{14} M_\odot$)	$\log P_{1.4\mathrm{GHz}}$ (W Hz^{-1})	$S_{610\mathrm{MHz}}$ (mJy)	R_H (Mpc)	θ_H (arcmin)	$SB_{610\mathrm{MHz}}$ (mJy arcmin^{-2})	t_{int} (hrs)
ACT-CL J0014.9−0056	0.535	5.0 ± 0.9	5.7 ± 1.1	25.29	3.43	0.28	0.73	1.23	7.5
ACT-CL J0256.5+0006	0.375	3.4 ± 1.0	3.8 ± 0.9	25.08	5.11	0.30	0.98	1.71	7.5
ACT-CL J2135.7+0009	0.117	10.8 ± 6.3	2.6 ± 1.1	25.16	96.15	0.47	3.72	0.72	7.5
ACT-CL J2154.5−0049	0.488	3.4 ± 0.9	4.3 ± 0.9	25.05	2.48	0.25	0.69	0.94	7.5
ACT-CL J0022.2−0036	0.805	3.8 ± 0.6	5.5 ± 1.1	23.9	0.54	0.327	0.719	0.330	10.0
ACT-CL J0045.2−0152	0.545	4.8 ± 0.9	5.6 ± 1.1	23.9	1.62	0.483	1.261	0.325	10.0
ACT-CL J0059.1−0049	0.786	3.5 ± 0.6	5.2 ± 0.9	23.8	0.46	0.319	0.709	0.295	10.0
ACT-CL J2327.4−0204	0.705	10.1 ± 1.0	9.4 ± 1.5	24.8	5.67	0.603	1.397	0.924	10.0

etti, 2000), MACSJ0717.5+3745 (Bonafede et al., 2009), MACSJ1149.5+2223 (Bonafede et al., 2012), ACT-CL J0102-49 El Gordo (Lindner et al., 2014), and PLCKG147.3-16.6 (van Weeren et al., 2014). This means that the radio halo scaling relations with X-ray (e.g. Cassano et al., 2007; Cassano, 2010) or SZ luminosity (e.g. Cassano et al., 2013) are dominated by lower redshift clusters.

Since the GRHs in clusters such as El Gordo ($z = 0.87$, $P_{1.4} = 4.57 \times 10^{25}$ W Hz^{-1}) and PLCKG147.3-16.6 ($z = 0.65$, $P_{1.4} = 5.1 \times 10^{24}$ W Hz^{-1}) are so powerful at such high redshifts, for the given scaling relations this indicates that the inverse Compton losses are not as significant as expected, possibly due to the strength of the magnetic field in these clusters. Building a larger sample of high-redshift massive clusters that host radio halos will help to settle these open questions and allow us to better understand the evolution of radio halos over cosmic time.

In January 2014 we applied for GMRT time to observe a high-redshift sample of ACT-E clusters (GMRT proposal ID: 26_031, PI: Knowles). Using the published SZ masses from Hasselfield et al. (2013), we selected all clusters above a redshift of $z = 0.5$ that had a SZ mass $M_{500} > 5.0 \times 10^{14} M_{\odot}$. This left us with a uniformly selected subset of five clusters, one of which was observed in August 2012 as part of our pilot program (ACT-CL J0014.9−0056). The other four clusters comprised our final high-redshift observing sample. The cluster parameters are provided in the bottom four rows of Table 3.1.

3.1.3 Radio observations

Since we were searching for steep-spectrum radio sources, we selected the GMRT's low-frequency 610 MHz band for our observations, which is the same frequency at which previous radio halo surveys with the GMRT have been undertaken (Venturi et al., 2007, 2008).

To determine integration times for each of the clusters in our sample, we assumed that each cluster hosted a radio halo with a radius R_H estimated from the R_H–R_{vir} correlation presented in Cassano et al. (2007). However, this scaling relation is determined from observations at 1.4 GHz and radio halos with observations at multiple frequencies indicate that many GRH are not only brighter, but also larger in physical extent at lower frequencies. There is, however, no self-similar

scaling for R_H with frequency. Again to be conservative, we increased R_H relative to the scaling relation by adjusting it by a factor of 2, as inferred from the literature (e.g. RXJ1347-1145: Ferrari et al. 2011, MACSJ0717: Bonafede et al. 2009).

We then used the SZ-derived cluster masses and the $P_{1.4\mathrm{GHz}}$–M_{500} scaling relation presented in Cassano et al. (2013) to estimate the rest-frame 1.4 GHz radio halo power $P_{1.4\mathrm{GHz}}$ for each cluster, which gave us a theoretical 1.4 GHz flux density. We then extrapolated this value to our chosen observing frequency of 610 MHz given the cluster redshift and adopting, to be conservative, a value towards the lower end of the fiducial spectral index, α = 1.2 ($S_\nu \propto \nu^{-\alpha}$; see Ferrari et al., 2008). To estimate the expected brightness of a halo we spread this flux density over the estimated circular area of the halo using a Gaussian profile.

We used the GMRTs default continuum mode at 610 MHz, i.e. 32 MHz bandwidth, to observe each of the clusters in our sample and acquired data in two polarizations, RR and LL. To determine an integration time for each cluster, we set a signal-to-noise threshold of 15 and used the ideal radiometer equation below:

$$\sigma = \frac{\mathcal{F} T_{\mathrm{sys}}/A_{\mathrm{eff}}}{\sqrt{N(N-1)t_{int}\Delta\nu}}, \tag{3.1}$$

where σ is the theoretical map noise that can be achieved when observing a source for a time of t_{int} using an N-element interferometer with system temperature T_{sys}, effective antenna gain A_{eff}, and bandwidth $\Delta\nu$. $\mathcal{F}$ is an additional "fudge factor" which is determined by comparing ideal results to the integration times and sensitivities reported by Venturi et al. (2007). Although the GMRT has 30 antennas, during each of our observing cycles there was a minimum of 26 antennas expected to be available during array upgrades. From the GMRT System Parameters and Current Status reports, the best achieved array parameter values at 610 MHz were $A_{\mathrm{eff}} = 0.32$ K Jy^{-1}and $T_{\mathrm{sys}} = 102$. We used these values to calculate an initial integration time per cluster which were checked using a Matlab-based simulation code, which ensured that we would recover the extended halo structure. The predicted radio halo parameters and final integration times for each cluster in our samples are provided in Table 3.1.

For our pilot proposal (PI: Knowles, ID: 22_044) we were awarded 100% of our proposed

time of 34 hours. The observations took place between the 25th and 29th of August 2012. For our high-redshift sample (PI: Knowles, ID: 26_031) we were awarded 75% of our proposed 54 hours. Although we did not receive all the requested time, we determined that we could still observe all four clusters and get down to the required 0.04 mJy beam^{-1} noise level. The observations took place between the 7th and 13th of August 2014. The final proposed times included overheads for calibrator observations.

3.2 Data reduction & Analysis

Radio interferometers record information about the intensity distribution from the true sky $I(l, m)$ as Fourier transformed complex *visibilities* $\mathcal{V}(u, v, w)$ described by amplitude and phase components. However, the true sky intensity is modified by the antenna responses and other corrupting effects such as the ionosphere, pointing errors, system noise and radio frequency interference (RFI). In order to reconstruct the true sky, the modifications to the true visibilities must be corrected for and then Fourier transformed from the *uv*-plane back into the image plane. This is the principle behind radio data reduction and a full examination of the theory underlying radio interferometry and aperture synthesis is covered exhaustively in Thompson et al. (2001).

Several software programs are available to reduce radio interferometric data that all work on the same core principles of radio interferometry. For our main reduction steps we use the Source Peeling and Atmospheric Modelling package (SPAM; Intema et al., 2009; Intema, 2014), which is a python-based package that uses the Astronomical Image Processing System software (AIPS; Wells, 1985), and Obit tools (Cotton, 2008) via the ParselTongue (Kettenis et al., 2006) interface. The SPAM package uses standard reduction procedures for main calibration (§3.2.1) and self-calibration (§3.2.2), and then uses direction-dependent calibration techniques to correct for ionospheric phase fluctuations (§3.2.3). If higher level imaging steps were required, we used the Common Analysis Software for Astronomy package (CASA; McMullin et al., 2007).

Here we will discuss the reduction process that we followed in order to reduce our 610 MHz GMRT data. We completed the same basic steps for each cluster dataset. To explain some of the steps and assist the reader in visualising the data reduction process, we use our reduction of

ACT-CL J0014.9−0056 as an example.

3.2.1 Main Calibration

As an array of N antennas can be broken down into $N(N-1)/2$ antenna pairs, the simplest case is that of a 2-element array with components separated by a distance (baseline) b. A schematic of this setup is given in Figure 3.1. The signal recorded by antenna one, V_1, experiences a phase shift τ_g compared to that from the second antenna, V_2, that is dependent on the baseline b and the viewing direction. The two signals are then multiplied and averaged to produce a single amplitude and phase measurement at a point in the *uv*-plane determined by the projected baseline through a Fourier relationship. Aperture synthesis is the process by which a single physical baseline can fill in more than one point in the *uv*-plane using the rotation of the Earth to produce multiple projected baselines during an observation. A well sampled *uv*-plane is crucial to obtain an accurate reproduction of the true sky. If an observation is badly corrupted by RFI, many *uv* points may need to be removed, jeopardising one's ability to obtain a reliable skymap.

The relationship between the true sky intensity distribution $\mathcal{I}(l,m)$ in the image plane and the complex visibilities $\mathcal{V}(u,v,w)$ recorded by the interferometer (array hereafter) in the *uv*-plane is given by the *measurement equation*, which for a non-coplanar array like the GMRT is given by

$$\mathcal{V}(u,v,w) = \int_{-\infty}^{\infty}\int_{-\infty}^{\infty} \mathcal{A}(l,m)\mathcal{I}(l,m)\mathrm{e}^{i2\pi\left[ul+vm+w\left(\sqrt{1-l^2-m^2}-1\right)\right]}\frac{dldm}{\sqrt{1-l^2-m^2}} \tag{3.2}$$

where all of the antenna-dependent modifications to the true sky intensity can be encoded into the antenna gain factor $\mathcal{A}(l,m)$. Here w is the vertical positional component that is necessary when the array elements (antennas) are not on a level plane.

In order to Fourier Transform the measured visibilities back into the image plane and recover the sky intensity, the effects that modify the intensities need to be modelled and corrected for. As most astronomical science targets are complex and potentially faint sources, a model for the antenna response to the sky is achieved by observing bright compact calibrator sources for which the fluxes are known. In this way one can determine a flux scale for the otherwise uncalibrated

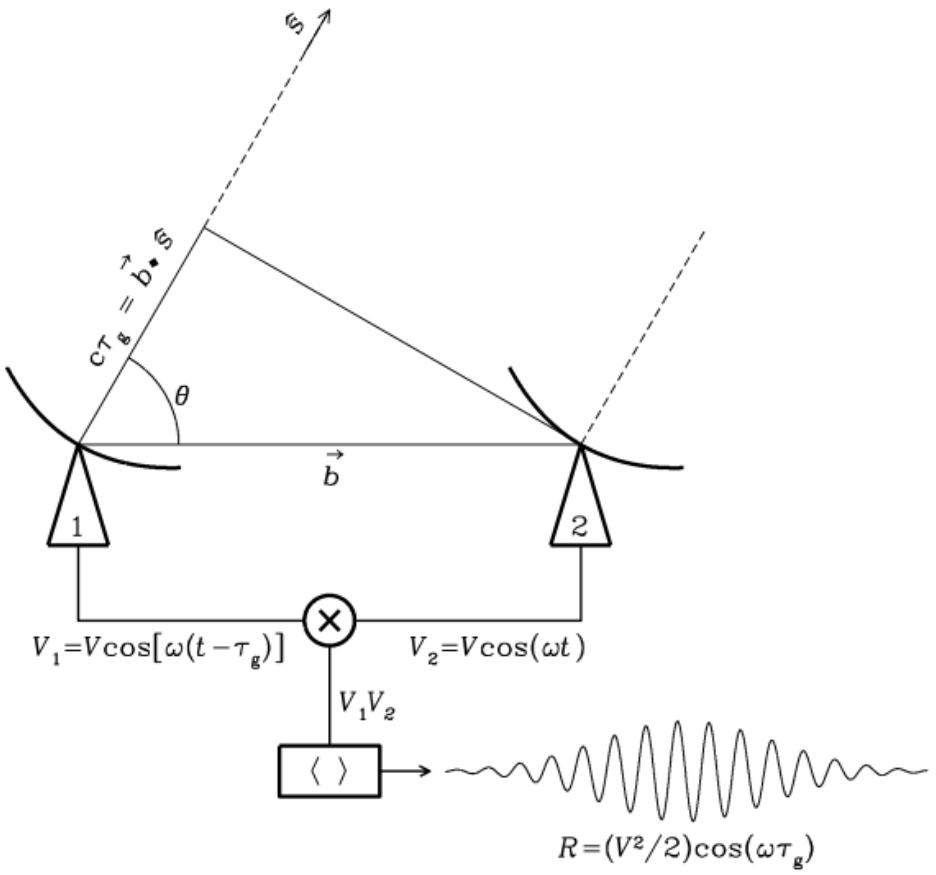

Figure 3.1: Schematic of a 2-element interferometer observing a source in direction $\hat{s}$. The signal V_1 experiences a phase shift τ_g compared to that from the second antenna, V_2, that is dependent on the distance between the antennas, b. Source: NRAO Essential Radio Astronomy online course `http://www.cv.nrao.edu/course/astr534/ERA.shtml`.

numbers recorded by the array, as well as determine phase solutions which can be applied to the main science target. This process of correcting the science target using information from another source is called *main calibration* and is the first step in our data reduction process.

Common reduction software requires two types of calibrators: a primary bright source which is well studied that can provide the flux scale for the observation and initial phase solutions, and a secondary source which is usually fainter than the primary calibrator but closer on the sky to the science target. The theory behind this is that there are few well-studied bright sources in the sky and it is therefore unlikely that the primary calibrator will be close enough to the science

target to provide accurate phase solutions which apply well enough to the viewing direction of the science source. The secondary calibrator is still relatively well-studied but it is closer to the target and therefore its phase solutions are more applicable. Although we observe a secondary calibrator in each of our observations, we do not use that data in our final data reduction process with SPAM — the flux calibrator observations are sufficient to provide an initial level of phase calibration for our target data.

Semi-automatic reduction recipes are available for SPAM in the form of python scripts. The user is required to carry out manual flagging at several stages of the reduction, although much of the RFI identification and excision is carried out by automatic routines. SPAM also uses classical outlier removal techniques which make cuts based on excessive visibility amplitudes and statistical outlier rejection methods in the time and frequency domain. In the following descriptions, manual tasks are indicated by italics.

At the beginning of a reduction, the user is required to select an antenna to serve as the reference antenna for calibration. This antenna needs to be stable for most of the observation. GMRT reductions usually use one of the central antennas for this purpose. For most of our datasets, we used antenna C09 or C02 as our reference antenna. Once this and the other reduction environment variables have been set up, the SPAM recipe for the main calibration is as follows:

1. Data from the beginning of each scan is removed and existing flags applied for the entire dataset. The existing flags are compiled by the telescope operators during each observing run and log events such as an antenna losing phase coherence, or servo errors on some antennas.

2. The flux scale, based on the calibrator data, is applied and a short interval calibration against this model is performed. This sets the initial flux scale for the observation and we compare the resulting calibrator flux value with the known literature value to check for consistency.

3. Based on the calibrator amplitudes/phases, *we manually identify and flag bad antennas for the entire observation* and re-calculate the flux scale. The *uv*-data for the calibrator

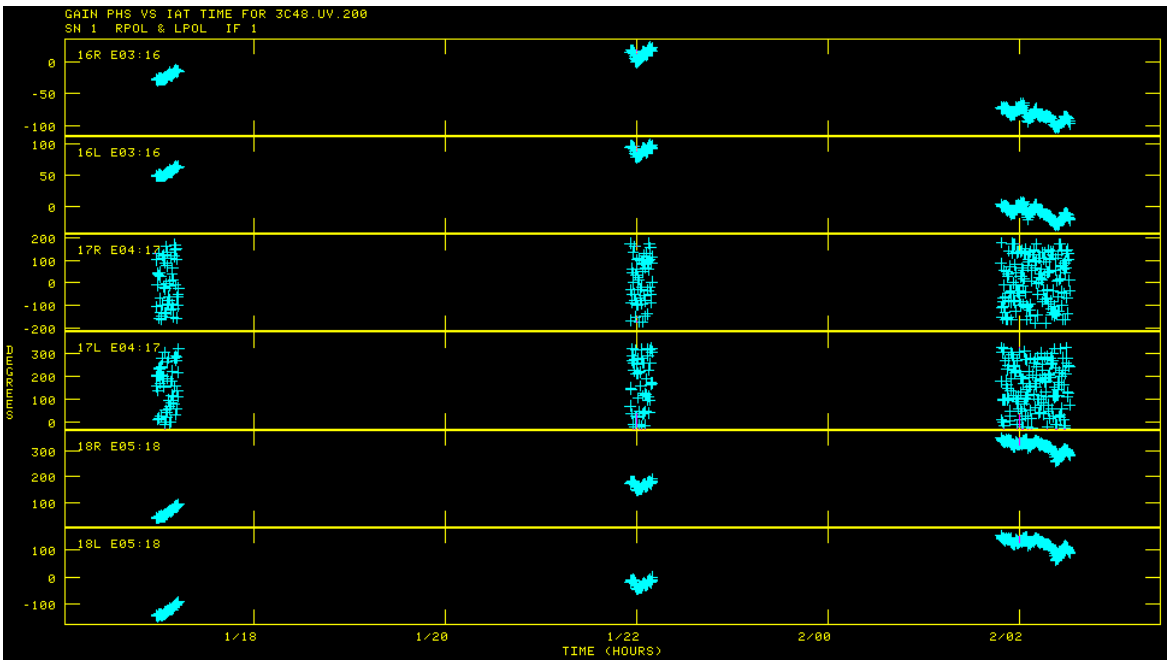

Figure 3.2: *uv*-data of the calibrator source 3C48 in the ACT-CL J0014.9−0056 dataset showing phase vs time for each polarization on antennas 16, 17, and 18. The random phases for antenna 17 identify it as a bad antenna which should be removed.

is checked using the AIPS task SNPLT. Bad antennas show random phases or excessive phase or amplitude jumps over the course of the scan — an example is shown in Figure 3.2 which shows the 3C48 calibrator data for both polarizations for antennas 16, 17 and 18 from the ACT-CL J0014.9−0056 observation. Antenna 17 shows random phases for both polarizations, for all scans, and is thus flagged as a malfunctioning antenna. For all of our datasets, we completely flagged at least one antenna at this stage, with antenna C06:7 not working for five of our observations.

4. We then perform *manual flagging of the calibrator data*, looking for amplitude spikes and discontinuous phases using the AIPS task EDITA. An example screen for flagging on the calibrator data is given in Figure 3.3. This step is not always necessary but the manual flagging can improve the quality of the initial primary calibration steps which follow.

5. Bandpass and baseline calibrations on the calibrator are performed and the solutions, along with the amplitude solutions from the flux scale, are applied. Excessive *uv*-data values are

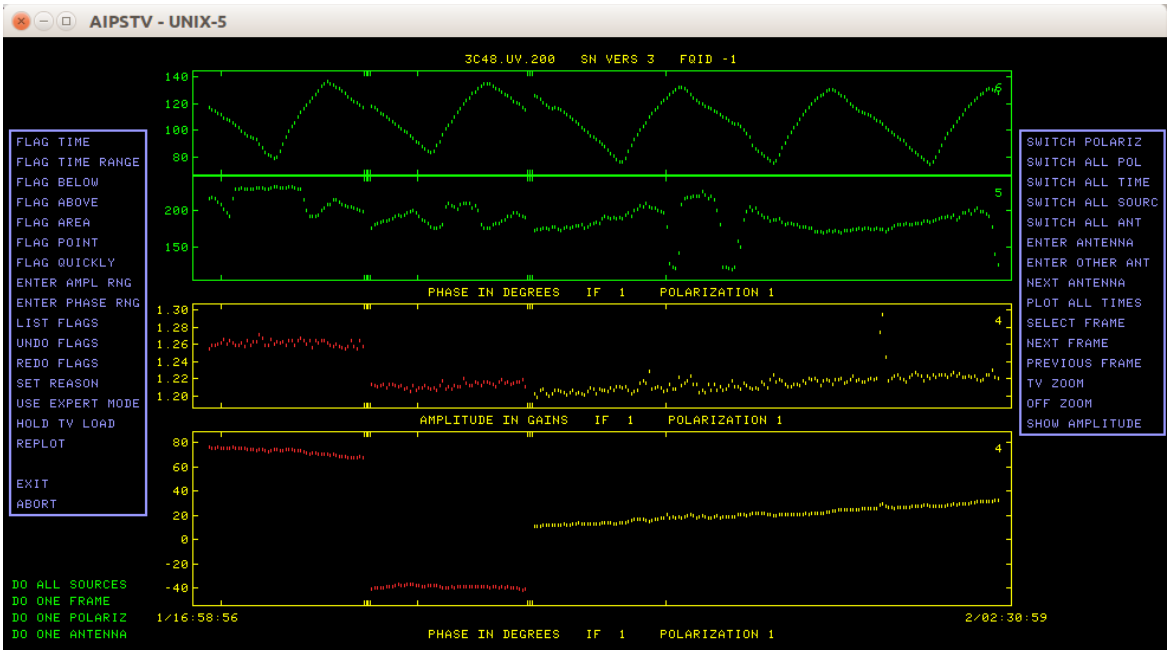

Figure 3.3: Interactive flagging environment for the *uv*-data of the calibrator source 3C48 in the ACT-CL J0014.9−0056 dataset showing phase and amplitude vs time for antenna 4 (yellow, bottom two panels), and phase vs time for the next two antennas (green, top two panels). The red points show the bad data for antenna 4, identified by the phase and amplitude jump in the second scan, which has been flagged manually in the window. Phase jumps and dropouts can be seen for antenna 5 at a different time range.

flagged using statistical tests. The calibrator data is then averaged, with final instrumental phase calibration applied. We checked the calibrated *uv*-data using SNPLT to ensure the calibration was successful, before applying the amplitude, bandpass, baseline and instrumental phase calibration solutions to the target data.

6. The calibrated target data is then averaged in time and frequency to reduce the computational expense, before *manual flagging with* EDITA, looking for amplitude spikes and discontinuous phases. This is the first look at the science target data. Data affected by time-dependent, strong RFI or scintillation effects is excised manually — less than 0.2% of the target data was flagged in this step for each of our datasets.

Once the target data has been calibrated, averaged, and obvious bad data has been removed, the target data is imaged to produce a "main calibration image", designated `MC1`. SPAM uses

a wide-field, faceting approach to imaging. Using archival data from the VLA Low-frequency Sky Survey (VLSS; Cohen et al., 2007) and the NRAO VLA Sky Survey (NVSS; Condon et al., 1998), the primary beam is covered with facets and outlier facets are added at positions of bright interfering sources outside of the primary beam. These facets are imaged using a Cotton-Schwab CLEAN deconvolution using an iterative, automatic clean-boxing algorithm.

The MC1 image RMS is $\sim 62 - 170\mu$Jy beam^{-1} for the range of our datasets. The MC1 image of ACT-CL J0014.9−0056 is shown in the top left panel of Figure 3.4. The image has prominent artifacts such as strong North-South sidelobes and amplitude errors around bright sources, indicative that further processing of the data is required.

3.2.2 Self-calibration

The imaging results of the main calibration clearly show residual problems in the data. One of the main sources of the artifacts is residual phase errors that were unable to be addressed by the calibrator solutions. In standard reduction procedures, the image is improved by *self-calibration* where the target data is used to calibrate itself, rather than data from a separate source. In the SPAM recipe three rounds of self-calibration are applied, interspersed with both manual and automatic flagging. The self-calibration steps taken during our data reduction are as follows:

1. The CLEANed target *uv*-data is calibrated against the true sky model from NVSS and VLSS.

2. We then use the AIPS task SNPLT to *manually identify a stable phase period for all, or at least most, antennas in the target data.* This time range is used to calibrate the instrumental phases. For most of our datasets we were able to identify an entire scan period that suited the criteria. However, for ACT-CL J2327−0204 we selected two independent time intervals of approximately 20 minutes each for the calibration, as there was no single full scan that remained unaffected by RFI or other phase errors.

3. The primary beam source model is then subtracted from the data and the *uv*-data is flagged baseline-by-baseline on different times scales to mitigate RFI. Less than 0.1% of the data

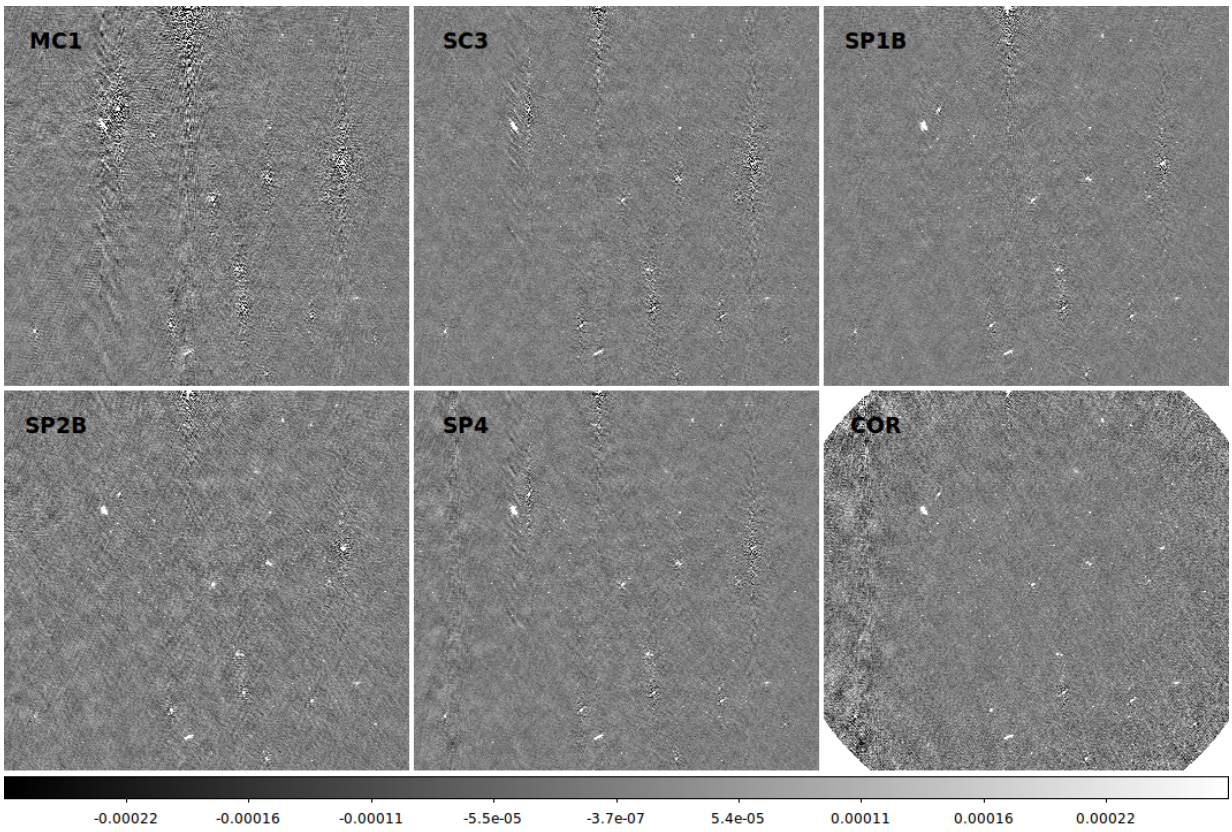

Figure 3.4: Images of ACT-CL J0014.9-0056 at different stages of the data reduction with SPAM, showing the same inner 0.165 square degrees. *Top left:* First image after the main calibration has been applied. *Top middle:* After the third and final round of self-calibration has been applied. *Top right:* After the first round of peeling. *Bottom left:* After the second round of peeling. *Bottom middle:* After an extra few rounds of flagging and peeling to improve the overall image. *Bottom right:* After primary beam calibration and astrometric corrections have been applied. This is the final full-resolution image of the reduction. All images have the same colour scale, given in Jy beam^{-1}.

is removed for all datasets.

4. The primary beam is then re-imaged to get the first self-calibration image (`SC1`). The phase errors are visibly reduced compared to the `MC1` image, however there are still strong sidelobes and amplitude errors around bright sources. The improvement in map noise varies over the image, but in every case the noise is lower by at least 20%.

5. Amplitude self-calibration solutions are determined and applied to the *uv*-data before re-calibrating against the sky model and re-imaging to produce the second self-calibration

image, SC2. Again, there is visible improvement in image quality, with the map noise being reduced by up to 35% in the areas of the image affected by artifacts.

6. We repeat step 3, also clipping visibility amplitudes above a designated threshold, before calibrating the bandpass on the target field and applying the solutions.

7. A final calibration against the updated sky model is performed before re-imaging to produce the third and last self-calibration image, SC3. The improvement in image quality over the previous SC2 image is visible but not as large as between the first two self-calibration images. The SC3 images in our sample have a rms noise in the range $36-100\mu$Jy beam^{-1}, an improvement of at least 40% on the corresponding MC1 images.

The SC3 image for ACT-CL J0014.9−0056 is shown in the top middle panel of Figure 3.4. There is a marked improvement in image artifacts compared to the MC1 image, although lower level issues are revealed around the extended bright source to the North-East, and there are still phase and amplitude problems visible around the bright sources.

In the initial attempts at reducing the GMRT data from the pilot project, we successfully used the CASA software to complete the main and self-calibration steps, however we were unable to improve the quality of the images past this point where the image plane was still plagued by long North-South sidelobes of bright sources which often ran through the pointing centre –the cluster region we are interested in. To move forward with improving the images we turned to the SPAM software with its direction-dependent phase calibration in the form of source peeling and ionospheric modelling. Since the SPAM software also included the standard calibration steps, we ran the data reduction starting from the raw telescope data, rather than our previous CASA results.

3.2.3 Peeling and Atmospheric Modelling

Although self-calibration greatly improved on the main calibration imaging results, the final image still suffers from artifacts around bright sources which inflate the noise level of the image and restrict the quality of the resulting scientific analysis. One of the major sources of visibility phase

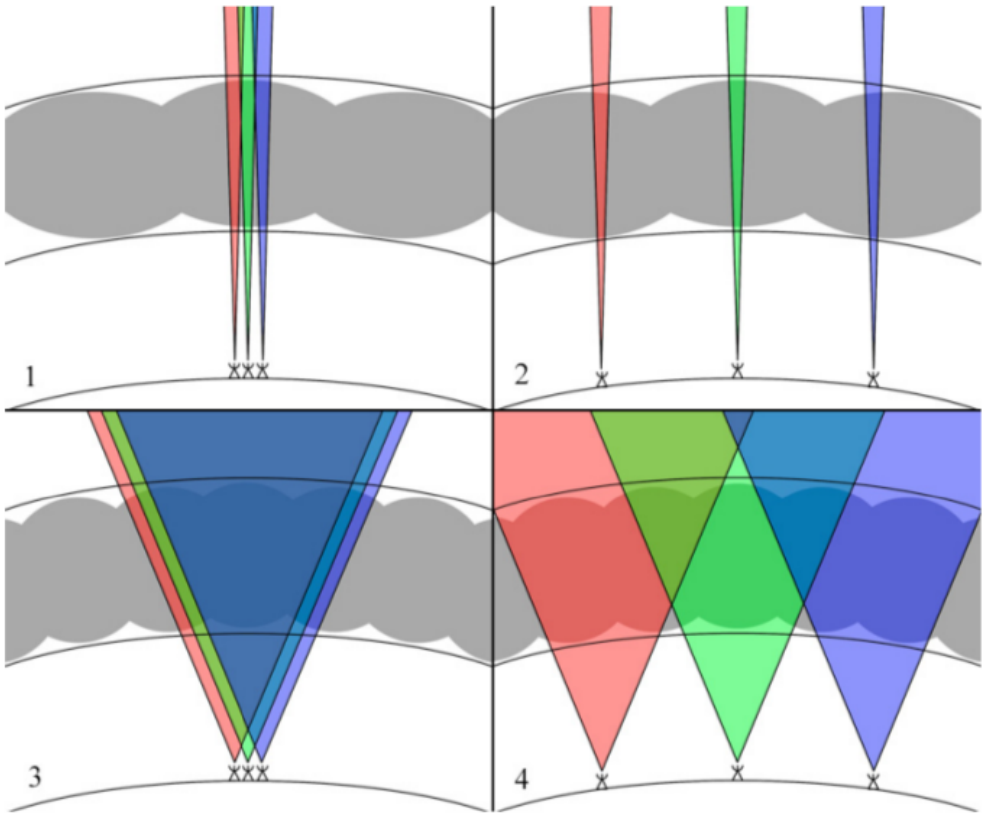

Figure 3.5: 2D schematic showing the four calibration regimes discussed by Lonsdale (2005) that depend on the field-of-view of the telescope and the antenna spacings. The array is represented by three antennas at ground level, each with their own field-of-view (red, green, and blue regions, respectively). The antennas observe the same source through the ionosphere which is shown by the grey bubbles. *Top left (regime 1):* Compact array of small antennas with narrow primary beams. *Top right (regime 2):* Extended array of small antennas with narrow primary beams. *Bottom left (regime 3):* Compact array of large antennas with wide fields-of-view. *Bottom right (regime 4):* Extended array of large antennas with wide fields-of-view. See text for details. Source: Intema et al. (2009).

errors is the ionosphere, with severe atmospheric conditions potentially causing amplitude errors as well (Jacobson and Erickson, 1992). Lonsdale (2005) identified four ionospheric calibration regimes defined by the size of the array and the individual fields-of-view of the antennas. These regimes are schematically outlined in Figure 3.5. In regimes 1 and 2 (top left and right panels respectively) the antennas have a narrow primary beam compared to the large scale ionospheric structure and thus they probe a fairly constant ionospheric electron density. In regimes 3 and 4 (bottom left and right panels respectively), the antennas have a large primary beam and therefore

experience variations in ionosphere structure across their fields-of-view. For the compact arrays in regimes 1 and 3, the ionospheric variations across the antennas can be approximated by a gradient. However, these variations across the array differ significantly from a gradient and can in fact be quite complex in the case of the extended arrays in regimes 2 and 4, where each antenna views the source through a wholly different portion of the ionosphere. The phase variations introduced to the visibilities become more complex as one moves from regime 1 to regime 4, with the latter being the most complicated case where each antenna requires its own phase correction that changes across its primary beam, i.e. in this case the ionosphere is a *direction-dependent* effect. Self-calibration cannot account for this as it produces only a single phase correction per antenna (Pearson and Readhead, 1984).

There are several proposed and existing methods to deal with direction-dependent ionospheric calibration in radio data reductions, e.g. direction-dependent modifications to the standard self-calibration schemes (Schwab, 1984; Subrahmanya, 1991), field-based calibration (Cotton et al., 2004), RIME-based mathematical schemes (Smirnov, 2011), clustered calibration (Kazemi et al., 2013), non-linear Kalman filters (Tasse, 2014), and Bayesian techniques (Lochner et al., 2015). Solving for atmospheric phase errors in a direction-dependent way is the main purpose of the SPAM package, which is designed to work in the fourth Lonsdale regime. It uses source peeling of bright sources within the target field (e.g. Noordam, 2004) and use of a single or multi-layered phase screen to model the phase errors (see Intema et al., 2009, for full details on the algorithms involved).

SPAM's peeling process is fully automated. In essence, bright sources in the field-of-view are identified and a measurement for the atmospheric phase structure is made by phase calibrating on these sources over short time intervals. A virtual phase screen (or multiple screens) is imposed at a set height above the Earth's surface and all peeled source–antenna pair phase measurements from the peeling process are mapped onto this screen. This is then fit with a set of optimised Karhunen-Loéve base functions which represents the stochastic ionosphere as a linear combination of orthogonal functions. The fitted ionospheric model will reproduce the phases in the measured directions, but when applied on-the-fly during imaging, will also predict the direction-dependent phase corrections for arbitrary viewing directions.

After self-calibration is complete, we completed the following direction-dependent SPAM recipe:

1. First bright sources in the model-subtracted self-calibrated data are identified using the primary beam facets, and peeled. Depending on the quality of the preceding `SC3` image, sources with fluxes above 0.02–0.04 Jy are identified as peeling candidates in our reductions. Each source is *visually checked to ensure they are suitable candidates for further peeling processing.* Sources that are too extended or appear to be heavily influenced by artifacts are excluded from the fitting procedure.

2. An ionospheric model is then fit to the selected peeled source phases. For our datasets, the model used between four and ten peeled sources for this initial ionospheric fit.

3. Instrumental phase effects are then removed and the ionospheric model is re-fit before automatic flagging procedures are applied.

4. The model phase solutions, peeling amplitude solutions, and delays are combined to produce a set of peeling solutions which replace the model solutions. The *uv*-data is then imaged to produce the first peeling result, `SP1`. Our images show a major improvement in phase errors around the more extended, bright sources in the field, compared to the `SC3` images, with the map noise being reduced by up to 25% in areas affected by strong sidelobes.

5. Bandpass phase solutions and amplitude calibration solutions are determined before outlier flagging is performed. Once the solutions are applied, the data is re-imaged to produce image `SP1A`. Small improvements in amplitude errors around bright sources are evident, although the map noise is largely unchanged.

6. Automatic flagging of baseline-dependent problems, which appear in the image as striping, is performed before subtracting the primary beam sources and applying baseline- and residual amplitude-based flagging. The data is then re-calibrated against the peeling solutions and re-imaged to produce image `SP1B`. For some of our datasets, this image appeared

marginally worse than the previous SP1A image in terms of the noise level, however amplitude errors were slightly reduced around the brightest sources.

7. Steps 1 to 6 are then repeated to create images SP2, SP2A, and SP2B. This second round of peeling improves on the first round by fitting ionospheric phase solutions to between 12 and 20 sources for each of our datasets, with identified source fluxes as low as 10 mJy. For the brightest sources the second round of peeling shows a flux measurement change of up to 2%.

The SP1B and SP2B images for ACT-CL J0014.9−0056 are shown in the top right and bottom left panels of Figure 3.4, respectively. The first round of peeling reduces the visible sidelobes of most of the bright sources, in particular the extended source to the North-East. For the majority of our clusters, the second round of peeling produced a good image with which to finalise the reduction process. However for clusters ACT-CL J0014.9−0056 and ACT-CL J0045−0152, additional rounds of self-calibration and peeling were performed due to source shape errors introduced during the final round of peeling and in an attempt to further reduce sidelobes that affected the central part of the image. In the case of ACT-CL J0014.9−0056, the final post-peeling image that lead to the best quality image after primary beam and flux scale corrections (see §3.2.4), SP4, is shown in the bottom middle panel of Figure 3.4. The final post-peeling images for our cluster sample have a rms noise in the range $30 - 87\mu$Jy beam^{-1}. The target rms from our observing proposal was 40 μJy for each of our clusters.

3.2.4 Primary beam correction and astrometry

Once all the necessary calibration steps have been completed, i.e. main calibration (§3.2.1), self-calibration (§3.2.2), and direction-dependent ionospheric calibration (§3.2.3), the final steps in the main data reduction process are to correct for the effect of the primary beam and to check for astrometric accuracy.

The positions of sources can appear to have shifted if the time-average of the residual phase errors in the direction of the sources has a non-zero spatial gradient (Intema et al., 2009). This effect can be introduced during any of the calibration processes, but particularly if during peeling,

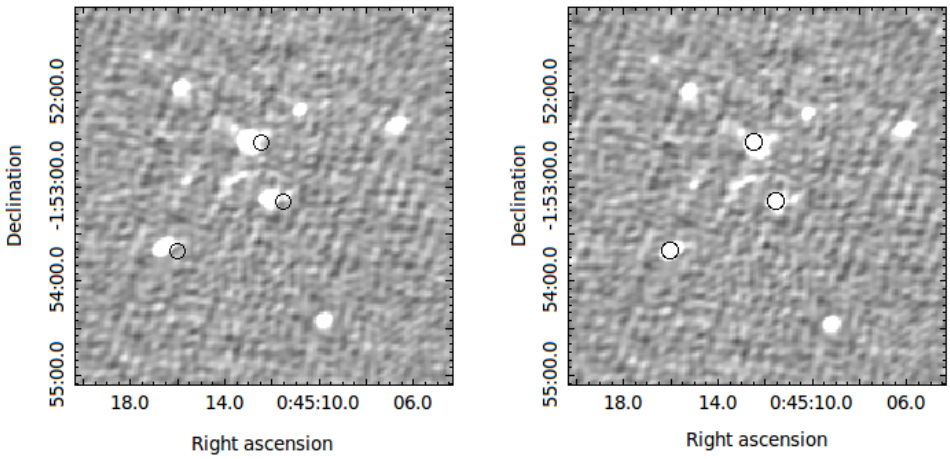

Figure 3.6: Fully calibrated images of the inner portion of the ACT-CL J0045.2−0152 field-of-view before (left panel) and after (right panel) astrometric corrections are applied. After calibration, ACT-CL J0045.2−0152 has a $\sim 10''$ positional offset from the FIRST source peak positions, shown in both panels by the black circles.

a source is centred on the incorrect catalogue position. To correct the final images for astrometric errors, SPAM compares peak source positions in the final image with that of counterparts in the input sky model from survey data. The peak source position catalogue from the final image is created manually using the source extraction tool PyBDSM (Mohan and Rafferty, 2015). If a systematic source position shift is identified during the comparison, SPAM corrects the astrometry in the final image. Not all of our datasets incurred an astrometric error, but those that did (ACT-CL J0045.2−0152, ACT-CL J0022.2−0036, ACT-CL J2154.5−0049) had positional offsets of between $10''$ and $18''$. As an example, we show the inner 3 square arcminutes of the `SP2B` and corrected images of ACT-CL J0045.2−0152 in the left and right panels of Figure 3.6, respectively. The circles show the positions of sources detected in the FIRST survey. In the `SP2B` image, there is a positional peak offset of $\sim 10''$, which has been corrected in the right panel image with SPAM.

In addition to checking, and fixing if necessary, the astrometry of the post-peeling image, the SPAM recipe corrects for the primary beam and the flux scale, the latter using a system temperature measurement from the 408 MHz Haslam sky survey (Haslam et al., 1981). With these corrections applied, we have a final full-resolution image of the dataset, designated `COR`.

The COR image for ACT-CL J0014.9-0056 is shown in the bottom right panel of Figure 3.4. Although the background is noisy close to the edge of the primary beam, the noise within the FWHM is quite stable and many faint point sources can be detected. The rms noise of our final maps for each dataset are given in Table 3.2, with the COR image for each cluster given in Appendix A. For most datasets we achieve a central map noise close to or better than the GMRT's 610 MHz "best" map noise of 40 μJy beam^{-1}, from their most recent System Parameters document. ACT-CL J2135+0009 has the highest final map noise, well above that achieved by our other dataset reductions. This is partly due to strong confusing sources in the field of view for which we could not derive more accurate phase solutions, but mainly a result of the dataset being heavily corrupted by RFI. By the end of the reduction, over 50% of the target data had to be excised. In the case of ACT-CL J2327−0204, the central map noise has an average value of 57.2 μJy beam^{-1}, similar to that achieved in the ACT-CL J0022.2−0036 dataset. However, unlike the former case, the field for the ACT-CL J2327−0204 observation is dominated by a bright, extended source (the active radio galaxy PKS 2324-02, see §3.3.1.2) and thus the noise fluctuations in the central region of the map are larger than for some of the other clusters. In areas closest to PKS 2324-02, the noise level can be as high as 100 μJy beam^{-1}.

3.2.5 Low-resolution imaging

By definition, radio halos are low surface brightness structures of large angular extent, and thus they may not be immediately observable in the final maps due to confusing bright sources in the cluster region. One of the things that makes the GMRT such a powerful instrument for searching for diffuse radio emission is its variety of baseline lengths. Due to the Fourier relationship between visibilities and the image plane, short baselines provide sensitivity to extended structures, and long baselines provide the angular resolution to resolve compact sources. To complete the search for faint diffuse cluster emission, we remove the point source emission by imaging at high-resolution, using only baselines above 2 kλ. This high-resolution point source model is then subtracted from the *uv*-data, which is then re-imaged at low resolution using an upper baseline cutoff of 8 kλ and an inner Gaussian *uv*-taper of 5kλ.

Table 3.2: Full-resolution imaging results for the full cluster sample. The third column gives the dimensions (major and minor axes, and position angle) of the synthesised beam. The final column indicates whether there is any diffuse emission present. * Due to a bright interfering source to the West of the cluster region, the central map noise is as high as 0.1 mJy beam^{-1}.

Cluster name	rms noise (μJy beam^{-1})	$\theta_{\rm synth}$, p.a. ($''\times''$, $^\circ$)	Diffuse emission?
ACT-CL J0014.9−0056	34.9	6.2 × 4.2, 72.3	No
ACT-CL J0022.2−0036	57.9	6.8 × 5.2, -56.9	No
ACT-CL J0045.2−0152	40.8	5.9 × 4.6, -68.0	No
ACT-CL J0059.1−0049	49.7	5.2 × 4.3, 76.0	No
ACT-CL J0256.5+0006	28.1	5.7 × 4.1, 72.2	Yes
ACT-CL J2135.7+0009	89.1	5.1 × 4.5, 59.4	No
ACT-CL J2154.5−0049	45.8	6.1 × 4.0, 68.3	No
ACT-CL J2327.4−0204	57.2*	5.4 × 5.0, 63.1	No

Any diffuse central emission should become visible in the low resolution images, although any structural features will be lost. For the range of our datasets, the low-resolution synthesised beam is 28″–32″, showing that the short-baseline *uv*-coverage is fairly consistent over all datasets. The rms noise of the final low-resolution image is in the range $85 - 200\mu$Jy beam^{-1}.

3.3 Results

The imaging results for the full cluster sample are given in Table 3.2. The full-resolution images can be found in Appendix A. Low-resolution imaging revealed diffuse emission in only one of our eight clusters, which we then studied in more detail (§3.3.2, Chapter 4). For all the other clusters, we calculate a halo radio power upper limit (§3.3.1.1) and comment on the radio environment of each cluster (§3.3.1.2). Figure 3.7 shows our results on the $P_{1.4\rm GHz}$–Y_{500} and $P_{1.4\rm GHz}$–$M_{500,\rm SZ}$ scaling relations from the literature. Our single halo detection in ACT-CL J0256.5+0006 is shown by a star and our upper limits as filled triangles. Radio halos (USSRHs) from the literature are shown as filled (empty) circles, and the upper limits from the literature as empty triangles. The measurements are coloured according to the redshift of the host cluster.

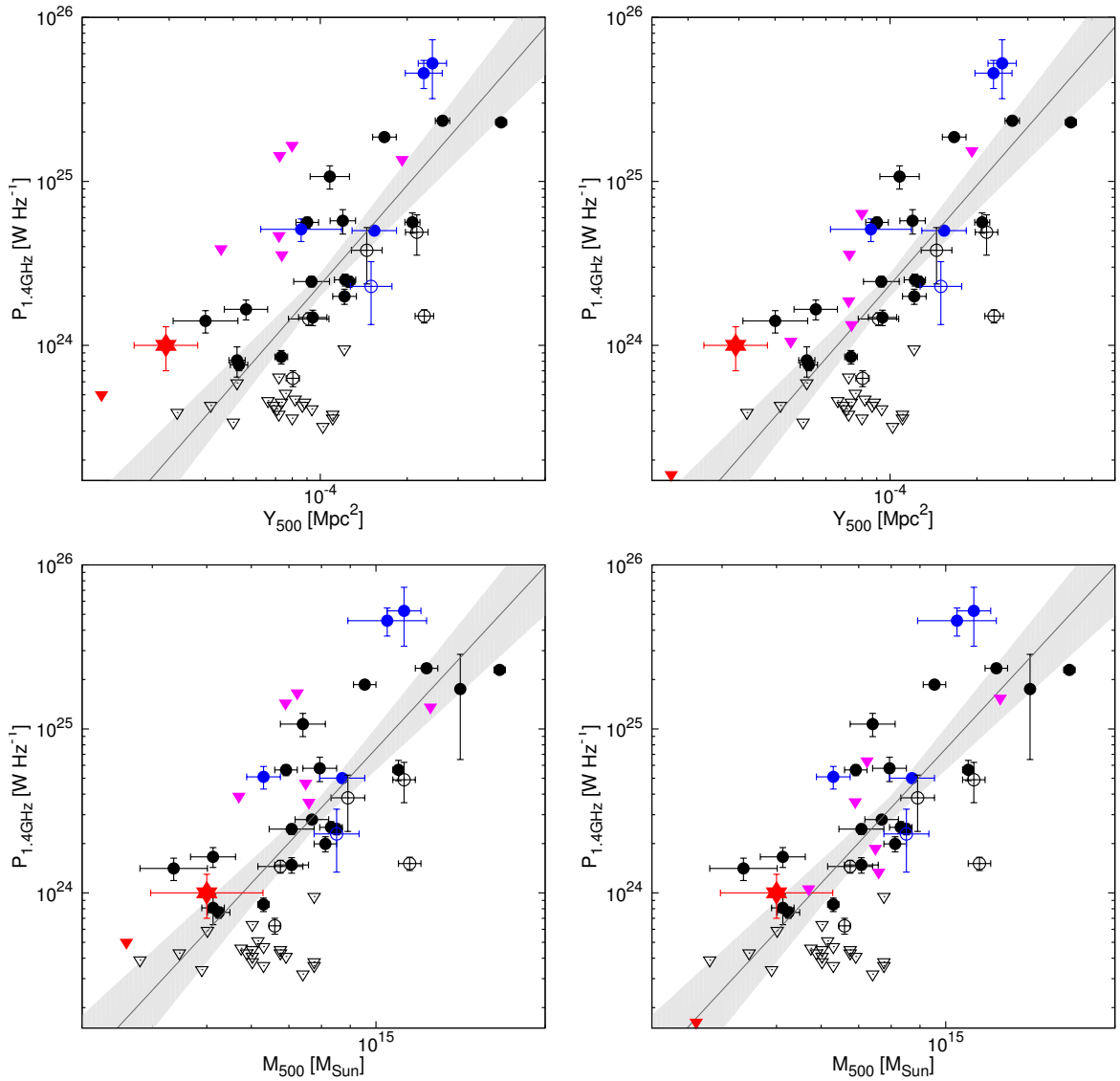

Figure 3.7: Scaling relations between 1.4 GHz radio power versus SZ Compton-y parameter (*top row*) and versus SZ-derived mass (*bottom row*). Radio halos (USSRHs) from the literature are shown as filled (empty) circles, and the literature upper limits as empty triangles. Large, filled triangles are upper limits on the clusters we observed with GMRT. The radio halo in ACT-CL J0256.5+0006 is indicated by a star. The measurements are coloured according to the redshift of the host cluster: $z < 0.45$ (black/red) and $z > 0.45$ (blue/magenta). *Left panel:* Upper limits determined using 1 Mpc simulated halos as per the literature. *Right panel:* Upper limits determined using cluster-defined simulated halo radii. See text for details.

3.3.1 Clusters without diffuse emission

3.3.1.1 Upper limits

The final low resolution maps of seven of our clusters showed no diffuse radio emission at the cluster location. In order to obtain secure radio power upper limits for each cluster we followed the method of Brunetti et al. (2007); Venturi et al. (2008) and Kale et al. (2013) by injecting simulated radio halos into the *uv*-data and re-imaging at various resolutions.

We assume a maximum halo diameter of 1 Mpc, typical of giant radio halos, and model the average brightness profile of well-studied halos (Brunetti et al., 2007) with seven concentric, optically thin spheres with diameters ranging from 400 kpc to 1 Mpc. For each model, approximately 50% of the flux is in the largest sphere. For each cluster we inject several simulated halos with total flux densities in the range $S_{\rm sim} \sim 3 - 300$ mJy and image the altered *uv*-data at several resolutions. The angular size of the injected halo varies between 130″ - 470″ over the redshift range of our cluster sample.

An example of a 300 mJy simulated halo injected into the ACT-CL J0014.9−0056 dataset is given in Figure 3.8. The left panel shows an image of only the simulated halo, with no real data. The seven concentric spheres are schematically indicated by the black circles. For the highest flux density and no noise, the imaging recovers $\sim 98\%$ of the total flux, and a largest linear size of 0.94 Mpc. The middle panel shows the same simulated halo injected into the real ACT-CL J0014.9−0056 dataset, and re-imaged. The white contours start at 160 μJy, $\sim 3\sigma$ above the map noise, and increase by a factor of 2. With the real data, the halo is detected out to only $\sim$50% of the injected halo's radius. As the halo region is embedded with compact sources, an accurate measurement of the recovered flux is difficult. The right panel shows the low-resolution ($\sim$30″), point source subtracted version of the middle panel. The white contours start at 6 mJy, $\sim 3\sigma$ above the map noise, and increase by a factor of 2. In the low-resolution image, the linear extent of the recovered halo is 58% of the input model, based on the 3σ detection threshold. In this region, 84% of the halo flux is recovered.

Figure 3.9 shows a gallery of injected radio halos of constant size (1 Mpc) but varying flux densities, injected into the ACT-CL J0014.9−0056 dataset. The injected halo flux density $S_{\rm sim}$

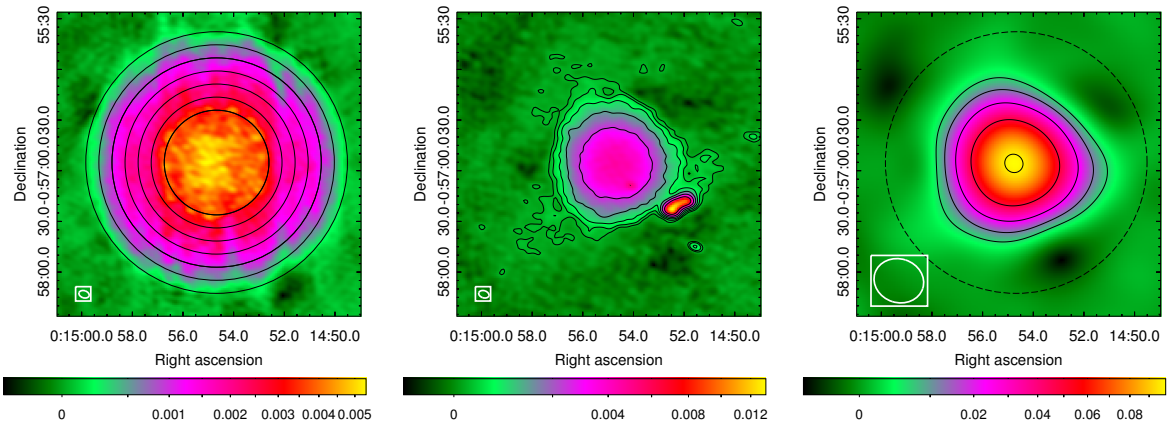

Figure 3.8: Example of a 300 mJy simulated radio halo in ACT-CL J0014.9−0056. *Left:* Image of the model halo components injected into an empty *uv*-dataset. The black circles indicate the seven concentric spheres used to model the halo brightness profile. *Middle:* Full resolution re-imaging of the ACT-CL J0014.9−0056 dataset with the injected halo model from the left panel. The white contours start at 160 μJy, $\sim 3\sigma$ above the map noise, and increase by a factor of 2 with each contour. *Right:* Low-resolution ($\sim$30″ beam) image of the middle panel after point source subtraction. The white contours start at 6 mJy, $\sim 3\sigma$ above the map noise, and increase by a factor of 2. The largest model sphere is indicated in the middle and right panels by the black circle. The colour scale is not the same over the three panels.

increases from left to right as 3, 10, 15, and 30 mJy respectively. The top panel shows the full resolution images and the bottom panel shows the low-resolution ($\sim$30″) imaging after subtracting the point sources, the peak positions of which are indicated by the red crosses. The first contour is at the 3σ and 4σ level for the full- and low-resolution images, respectively. In the case of ACT-CL J0014.9−0056, the simulated halo is directly observed in the full resolution image for an injected flux density of 30 mJy. The recovered portion of the halo decreases as the injected flux density decreases. The 10 mJy halo is visible in the low resolution image, although residual point source emission is also apparent. The 3 mJy injected halo is undetected in both the full- and low-resolution images, since the emission in the latter image is consistent with compact source residuals due to imperfect source subtraction.

We find that extended emission is securely established for fluxes above a value of $S_{\rm sim} = 15$ mJy for all but the lowest redshift cluster, ACT-CL J2135.7+0009, which has an upper limit of 40 mJy owing to the large angular size of the injected halo in this case. For the other six clusters, all of which lie at redshifts higher than 0.48, injected halo fluxes in the range 10–15 mJy result

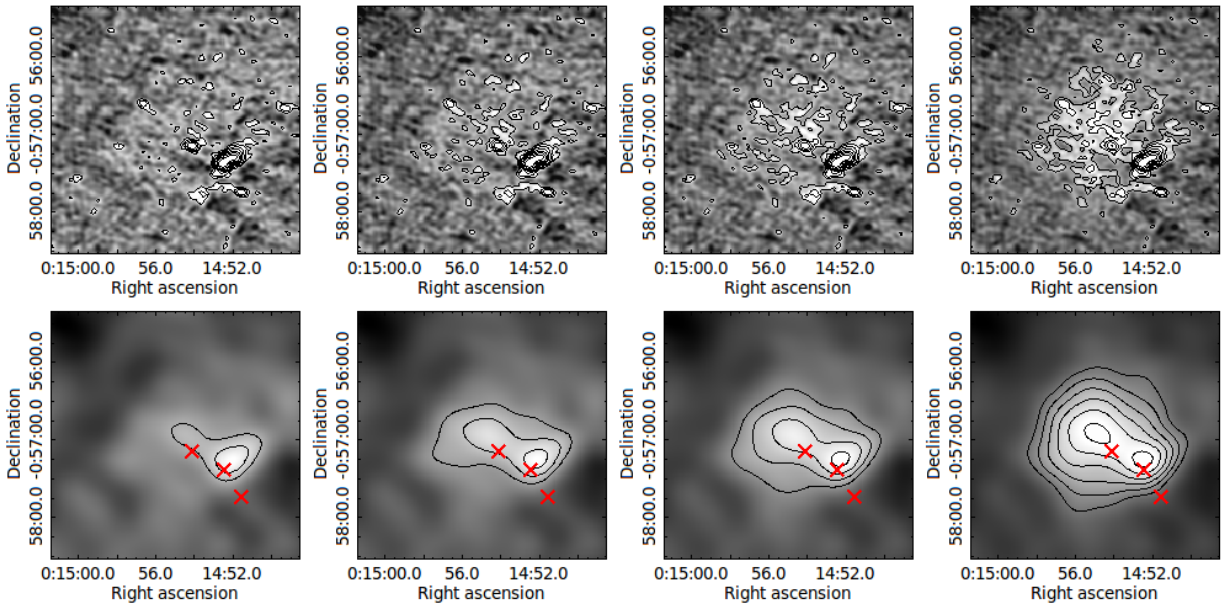

Figure 3.9: Examples of re-imaged ACT-CL J0014.9−0056 data with injected simulated radio halos. The simulated halos have a constant angular size and varying flux density, from left to right, of 3, 10, 15, and 30 mJy. *Top:* Full-resolution radio images of the adjusted data. Contours start at the 3σ level, corresponding to 108 μJy, and increase by a factor of 2. *Bottom:* Low-resolution radio images of the adjusted data after high-resolution point source subtraction. Contours start at the 4σ level, corresponding to 1.2 mJy, and increase by a factor of 2. Red crosses show the positions of the compact sources in the cluster region. In these panels, the the injected halo is securely detected in the low-resolution image for halo fluxes of 10 mJy and above. For the 3 mJy halo, the emission in the low-resolution image is consistent with residual point source contamination.

in positive residuals in the full-resolution image with integrated flux density $\sim 4\sigma$ above the noise level with indications of extended emission in the low-resolution image. For each cluster, the upper limit is taken to be the flux for which the halo is just undetected in the low-resolution image. Table 3.3 lists the 610 MHz radio halo upper limit fluxes for the clusters in which no evidence of central residual emission is found. Using a spectral index of 1.3, we extrapolate the fluxes to 1.4 GHz to produce a k-corrected, 1.4 GHz radio power upper limit for each cluster using the following equation:

$$\left(\frac{P_{1.4\mathrm{GHz}}}{\mathrm{WHz}^{-1}}\right) = 4\pi \left(\frac{D_\mathrm{L}}{\mathrm{m}}\right)^2 \left(\frac{S_{610\mathrm{MHz}}}{\mathrm{m}^{-2}\mathrm{WHz}^{-1}}\right) \left(\frac{1400\mathrm{MHz}}{610\mathrm{MHz}}\right)^{-1.3} (1+z)^{-1+1.3}, \tag{3.3}$$

where D_L is the luminosity distance at the cluster redshift z. These upper limits are shown as

Table 3.3: Radio halo power upper limits for clusters with non-detections. We use a maximum physical diameter of 1 Mpc for the simulated halo at the redshift of the cluster. We use a generic spectral index of 1.3 to scale the 610 MHz upper limit to 1.4 GHz.

Name	z	θ_{max} (arcsec)	S_{610MHz} (mJy beam^{-1})	$\log(P_{1.4GHz})$ (W Hz^{-1})
ACT-CL J0014.9−0056	0.535	78.3	8	24.55
ACT-CL J0022.2−0036	0.805	65.5	13	25.22
ACT-CL J0045.2−0152	0.545	77.5	10	24.67
ACT-CL J0059.1−0049	0.786	66.0	12	25.16
ACT-CL J2135.7+0009	0.117	233.8	40	23.70
ACT-CL J2154.5−0049	0.488	82.2	11	24.59
ACT-CL J2327.4−0204	0.705	68.8	15	25.13

filled triangles in the $P_{1.4\mathrm{GHz}}$–Y_{500} and $P_{1.4\mathrm{GHz}}$–M_{500} planes shown in the top left and bottom left panels of Figure 3.7, respectively. The upper limits for the high redshift clusters (shown in magenta) are larger than the existing upper limits from the literature which are shown as empty triangles — instead of lying in the existing region of upper limits, they are above the correlation in most cases. This indicates that we did not reach the predicted halo fluxes from the observing proposals. There are several effects which contribute to this. Firstly, the noise in some of our final maps are up to a factor of two higher than the target noise in the proposal. For ACT-CL J2327.4−0204 and ACT-CL J2135.7+0009, this could cause a factor of two increase in the expected upper limit. Secondly, the cluster masses used in the pilot proposal are larger than the final published masses, and the UPP masses used in the high-redshift proposal are slightly different to the final B12 masses. The B12 masses were considered to be the most accurate masses from the SZ-mass scaling relation at the time of this work[3]. A lower cluster mass implies a less powerful halo, which would require a longer integration time to detect. The most significant factor is that in our prediction of halo fluxes in the proposals, we estimated a radio halo size using the Cassano et al. (2007) correlation between radio power and halo size. This means that some of

[3]Recent results of weak lensing mass calibration of the ACT-E cluster sample tentatively indicate that this reverts to the UPP masses (Battaglia et al., 2015). As these results are as yet unpublished, we use the B12 masses for our analysis.

Table 3.4: Radio halo power upper limits for clusters with non-detections. We use scaling relations to convert the B12 M_{500} cluster masses from Hasselfield et al. (2013) to simulated radio halo sizes. We use a generic spectral index of 1.3 to scale the 610 MHz upper limit to 1.4 GHz.

Name	z	θ_{max} (arcsec)	R_H (Mpc)	S_{610MHz} (mJy beam^{-1})	$\log(P_{1.4GHz})$ (W Hz^{-1})
ACT-CL J0014.9−0056	0.535	78.3	0.843	3	24.13
ACT-CL J0022.2−0036	0.805	65.5	0.813	5	24.81
ACT-CL J0045.2−0152	0.545	77.5	0.833	4	24.27
ACT-CL J0059.1−0049	0.786	66.0	0.774	3	24.56
ACT-CL J2135.7+0009	0.117	233.8	0.435	13	23.21
ACT-CL J2154.5−0049	0.488	82.2	0.653	3	24.03
ACT-CL J2327.4−0204	0.705	68.8	1.309	17	25.19

the predicted radio halos differed, at times significantly, from 1 Mpc.

To investigate this we re-compute upper limits for our clusters, injecting simulated halos with sizes determined by extrapolating a 1.4 GHz radio power from the cluster B12 mass, and then using the Cassano et al. (2007) scaling relation to get the halo size. The halo size and new upper limit fluxes and radio powers are given in Table 3.4. These revised upper limits are shown in the right top and bottom panels of Figure 3.7. For all but our highest redshift clusters, ACT-CL J0022.2−0036 and ACT-CL J0059.1−0049, the revised upper limits fall on or below the $P_{1.4\mathrm{GHz}}$–M_{500} correlation. The higher upper limits for these two clusters may be explained by the similarity in angular size of the injected halos compared to the low resolution synthesised beam of the images ($\sim 28''$). In this case the map noise has a greater effect on the detection limit, than for clusters with larger, and therefore more resolved, injected halos. However, in the $P_{1.4\mathrm{GHz}}$–Y_{500} plane, the revised upper limits are still above the correlation, although they are now well within the scatter produced by the literature values. This indicates that the lack of flux sensitivity is a major problem when observing high-redshift systems of intermediate SZ-signal and mass, and that correcting the size of the simulated halos is insufficient on its own.

In order to check whether or not our upper limits could belong to the population of detections, we performed a bivariate, non-parametric survival analysis on the data using the Astronomy Sur-

Table 3.5: Results of the survival analysis for the $P_{1.4\mathrm{GHz}}$ vs Y_{500} relation, on three combinations of the data.

Statistic	Literature only	Lit. + original UL	Lit. + revised UL
CI	$< 0.1\%$	$< 0.1\%$	$< 0.1\%$
χ^2	14.496	11.884	11.884
intercept	30.626 ± 1.134	30.626 ± 1.134	30.626 ± 1.134
slope	1.561 ± 0.289	1.561 ± 0.289	1.561 ± 0.289
standard deviation	0.367	0.367	0.367

vival Analysis Package (ASURV Lavalley et al., 1992). We implemented the Cox Proportional Hazard Model and the EM algorithm to test for a correlation and perform linear regression to determine the fit parameters, respectively. We used three sets of data: (0) the previous detections from the literature only, (1) the literature detections with our original upper limits, and finally (2) the literature detections with our revised upper limits. The correlation statistics are the confidence level at which a correlation is found and the chi-squared value. The linear regression determines the slope, intercept, and standard deviation of the fit.

The results of the analysis are shown in Tables 3.5 and 3.6. A strong correlation is found in all datasets, at a confidence level of $P < 0.1\%$, for both the $P_{1.4\mathrm{GHz}}$–Y_{500} and $P_{1.4\mathrm{GHz}}$–M_{500} relations. In the case of the $P_{1.4\mathrm{GHz}}$–Y_{500} relation, there is no significant difference in the determined fit parameters between the three datasets. This indicates that the correlation is unaffected by our upper limits, in either form. In the $P_{1.4\mathrm{GHz}}$–M_{500} plane, the significance of the correlation, based on the chi squared statistic, degrades as we move from the data with detections only to data that also includes the revised upper limits, with the latter giving a marginally less constrained fit than when the original upper limits are used. However, the standard deviation of the fit is relatively stable over the three datasets and is consistent within the error bars, as are all other statistics. From this we conclude that our upper limits do affect the $P_{1.4\mathrm{GHz}}$–M_{500} correlation, leading to a flatter slope, but that they are not in contention with the literature-only result and therefore do not necessarily belong to a second population.

Table 3.6: Results of the survival analysis for the $P_{1.4\mathrm{GHz}}$ vs M_{500} relation, on three combinations of the data.

Statistic	Literature only	Lit. + original UL	Lit. + revised UL
CI	$< 0.1\%$	$< 0.1\%$	$< 0.1\%$
χ^2	13.531	17.134	18.050
intercept	-16.202 $\pm$ 7.693	-17.870 $\pm$ 6.959	-21.455 $\pm$ 7.062
slope	2.732 $\pm$ 0.516	2.842 $\pm$ 0.467	3.080 $\pm$ 0.474
standard deviation	0.375	0.370	0.383

Table 3.7: Compact sources in the ACT-CL J0014.9−0056 cluster region. The spectral index is determined using the FIRST source flux when available.

ID	R.A. (hms)	Dec. (hms)	$S_{610\mathrm{MHz}}$ (mJy)	α_{610}^{1400}	Optical counterpart
S1	00 14 52.23	−00 57 20.11	35.73 $\pm$ 0.12	1.04	CM
S2	00 14 54.08	−00 57 09.70	1.53 $\pm$ 0.07	–	CM (BCG)
S3	00 14 51.54	−00 57 45.11	0.87 $\pm$ 0.06	–	CM

3.3.1.2 Radio environments

The 610 MHz primary beam of the GMRT is $\sim$45′, and as such each of our cluster datasets has a very large field-of-view. We investigate the compact radio emission in the cluster region for each dataset, as well as comment on interesting sources in the wider field-of-view. A full investigation into the nature of these sources will be part of the upcoming paper on the radio results of the full cluster sample (Knowles et al., in prep).

ACT-CL J0014.9−0056

There are three sources in the cluster region, only the brightest of which (S1) is detected in the NVSS and FIRST catalogues. S1 is a possible tailed radio galaxy, however the resolution of our 610 MHz map is not high enough to provide any further details on the nature of this source. All three sources have optical counterparts in the 12th SDSS Data Release (DR12; Alam et al., 2015) image linking them to possible cluster members. The 610 MHz properties for all three sources

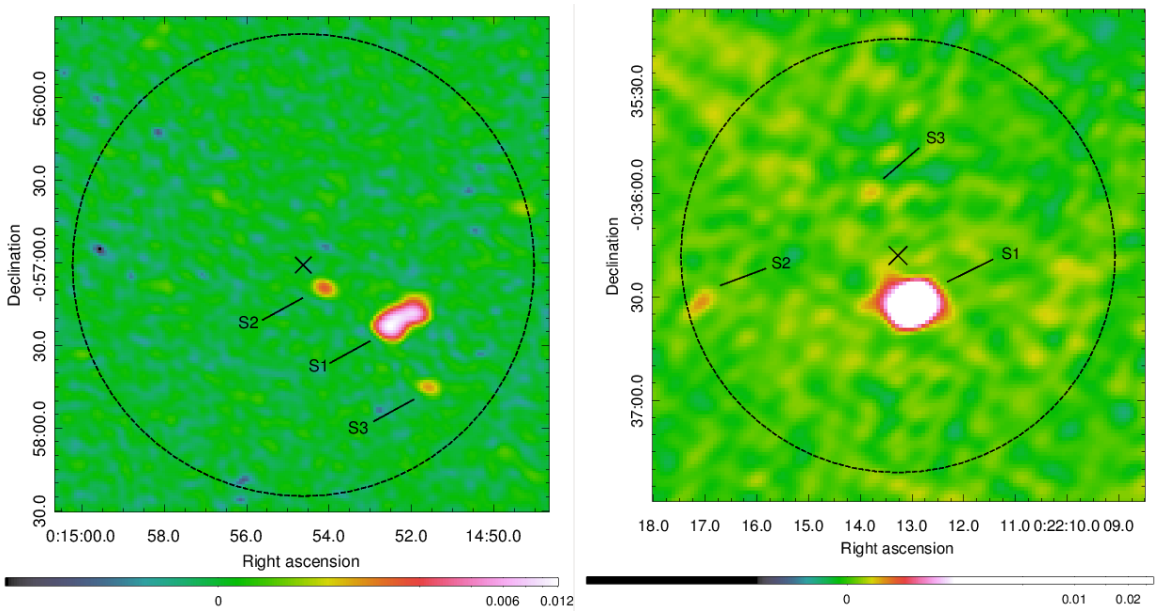

Figure 3.10: GMRT 610 MHz maps of the cluster regions for ACT-CL J0014.9−0056 (*left*) and ACT-CL J0022.2−0036 (*right*). In each panel, the dashed circle indicates the R_{500} cluster scale, with the cross showing the SZ peak.

are provided in Table 3.7, with the GMRT radio map of the cluster region given in the left panel of Figure 3.10.

ACT-CL J0022.2−0036

There are three sources detected at 610 MHz in the cluster region, shown in the right panel of Figure 3.10. Their details are given in Table 3.8. Only the brightest source is detected in FIRST, which is also matched with the cluster BCG in the SDSS DR12 image. S2 has a foreground optical counterpart.

ACT-CL J0045.2−0152

The cluster region at 610 MHz is host to three compact sources, the details of which are given in Table 3.9. All three sources are detected in FIRST and all are matched with potential cluster members in the SDSS DR12 image. The 610 MHz radio map of the cluster region is shown in the left panel of Figure 3.11.

Table 3.8: Compact sources in the ACT-CL J0022.2−0036 cluster region. The spectral index is determined using the FIRST source flux when available.

ID	R.A. (hms)	Dec. (hms)	$S_{610\mathrm{MHz}}$ (mJy)	α_{610}^{1400}	Optical component
S1	00 22 12.96	−00 36 31.95	33.59 ± 0.16	0.68	CM (BCG)
S2	00 22 17.04	−00 36 31.75	0.29 ± 0.06	–	FG
S3	00 22 13.79	−00 35 59.21	0.17 ± 0.06	–	–

Table 3.9: Compact sources in the ACT-CL J0045.2−0152 cluster region. The spectral index is determined using the FIRST source flux when available. Optical counterparts are defined as being a foreground (FG) source or a possible cluster member (CM) based on optical colours in the SDSS DR12 image.

ID	R.A. (hms)	Dec. (hms)	$S_{610\mathrm{MHz}}$ (mJy)	α_{610}^{1400}	Optical counterpart
S1	00 45 12.28	−01 52 33.55	13.72 ± 0.11	1.32	CM (BCG)
S2	00 45 11.45	−01 53 10.22	4.83 ± 0.08	1.01	CM
S3	00 45 15.95	−01 53 41.05	4.69 ± 0.09	1.06	CM

The radio galaxy NGC 0245 (J2000 R.A. = 00h46m05.35s, Dec. = −01d43m24.35s) lies within the GMRT field-of-view of ACT-CL J0045.2−0152. NGC 0245 is a nearly face-on spiral galaxy at z = 0.0136. It has been identified as a metal-rich starburst galaxy, with recent star formation occurring in the galaxy nucleus as well as in regions of the spiral arms (Pérez-González et al., 2003). It is part of several galaxy samples studied in the infrared and near and far ultraviolet wave bands (Moshir et al., 1990; Rego et al., 1993; Moustakas and Kennicutt, 2006; Hao et al., 2011).

In our 610 MHz map, we detect the bright core of NGC 0245, $S_{610,\mathrm{core}} = 7.83 \pm 0.05$ mJy, surrounded by a halo of faint diffuse emission of radius 0.57′ (9.5 kpc at the galaxy redshift of z = 0.0136). The right panel of Figure 3.11 shows our 610 MHz radio contours for this galaxy, overlaid on the 3-colour *gri* image from SDSS Data Release 12 (Alam et al., 2015). The diffuse emission traces the spiral arms, with radio hot spots roughly coinciding with the regions of star forming activity. The flux of the entire object is $S_{610} = 65.17 \pm 0.42$ mJy. The galaxy features

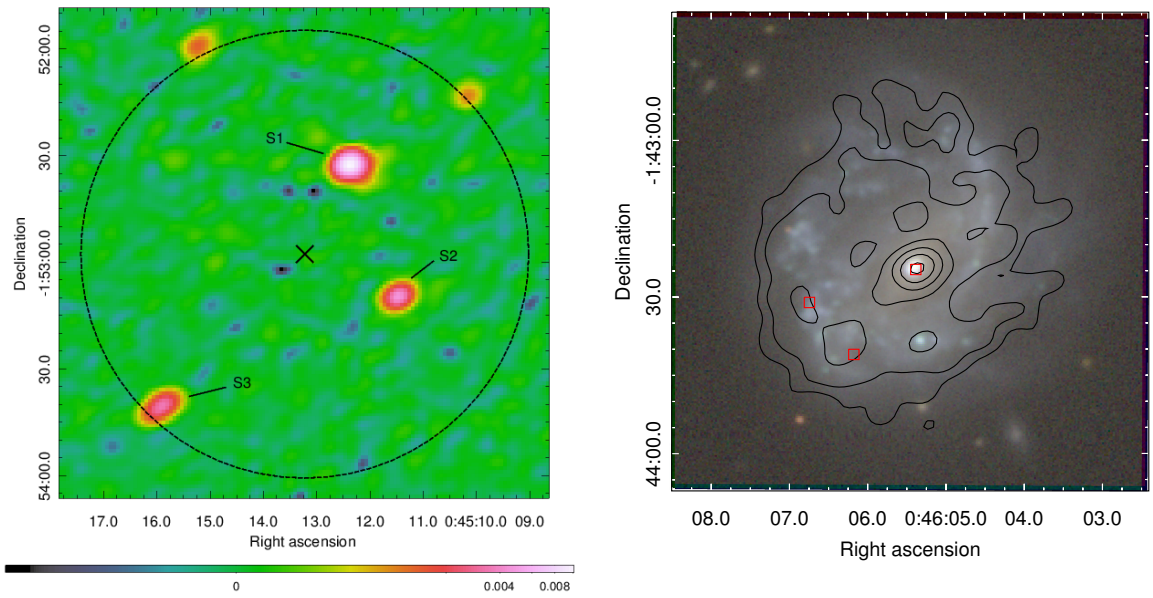

Figure 3.11: *Left:* GMRT 610 MHz map of the cluster region of ACT-CL J0045.2−0152. The dashed circle indicates the R_{500} cluster scale, with the cross showing the SZ peak. *Right:* GMRT 610 MHz image of the radio galaxy NGC0245 which lies within the field of view of our J0045 observation.

are unresolved in NVSS, with the entire object having a flux of $S_{\rm NVSS} = 38.2 \pm 1.9$ mJy. This gives a global source spectral index of $\alpha_{610}^{\rm NVSS} = 0.64$. The diffuse emission surrounding the radio galaxy is not detected in FIRST, although two hotspots in the spiral arms are detected, with FIRST fluxes of 5.6 ± 0.3 mJy and 4.9 ± 0.2 mJy respectively. With its smaller synthesised beam, FIRST also resolves the central core, but it has a higher flux of $S_{\rm FIRST,core} = 8.16 \pm 0.4$ mJy compared to the GMRT 610 MHz flux, leading to a spectral index of $\alpha_{610,\rm core}^{\rm FIRST} = -0.05$. An inverted radio spectrum has been found in the nucleus of another star forming galaxy, NGC 4418 ($\alpha_{1.4\rm GHz}^{5\rm GHz} = -0.7$, Varenius et al., 2014). The authors suggest that the inversion could be due to flux attenuation from AGN activity at the lower frequency (in their case 1.4 GHz), in the form of synchrotron self-absorption, or thermal free-free absorption in the foreground. If a similar scenario is present in NGC 0245, high resolution imaging with Very Long Baseline Interferometry (VLBI) would be necessary to reveal AGN activity within its nucleus. The FIRST source positions are indicated by red squares in the right panel of Figure 3.11.

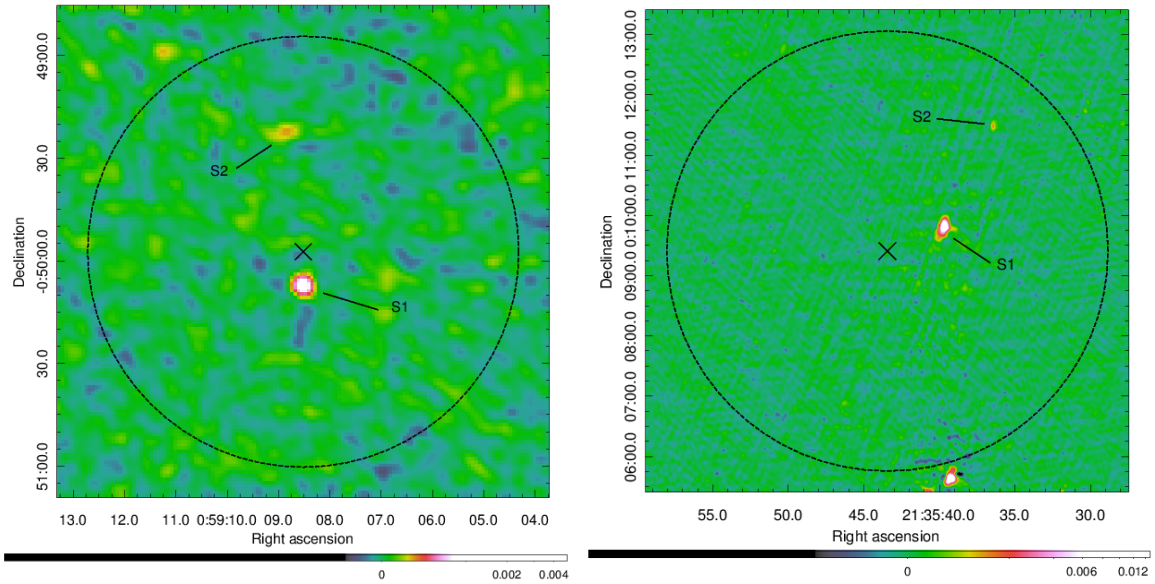

Figure 3.12: GMRT 610 MHz maps of the cluster regions for ACT-CL J0059.1−0049 (*left*) and ACT-CL J2135.7+0009 (*right*). In each panel, the dashed circle indicates the R_{500} cluster scale, with the cross showing the SZ peak.

ACT-CL J0059.1−0049

There are only two compact sources in the cluster region, neither of which is detected in FIRST or NVSS. S1 appears to be the cluster BCG based on optical matching in the SDSS DR12 image. The 610 MHz source details are provided in Table 3.10, with the 610 MHz radio image of this region shown in the left panel of Figure 3.12.

The field-of-view is dominated by a bright source to the East of the cluster region, positioned at R.A. = 00h59m30.10s, Dec. = −00d46m12.74s, as can be seen in Figure A.4. The 610 MHz flux of this source is 465.18 ± 0.11 mJy. It is detected in both NVSS and FIRST, providing a spectral index measurement of α = 0.92.

ACT-CL J2135.7+0009

This is a low redshift cluster (z = 0.117) and it hence has a large angular size of 7.3′($R_{500} = 930$ kpc), shown in the right panel of Figure 3.12. However, there are only two sources in this region, only one of which is above the detection threshold of FIRST. Both sources have optical coun-

Table 3.10: Compact sources in the ACT-CL J0059.1−0049 cluster region. Neither of the sources is detected in FIRST or NVSS. Optical counterparts are defined as being a foreground (FG) source or a possible cluster member (CM) based on optical colours in the SDSS DR12 image.

ID	R.A. (hms)	Dec. (hms)	$S_{610\mathrm{MHz}}$ (mJy)	Optical counterpart
S1	00 59 08.52	−00 50 07.01	0.94 ± 0.06	CM (BCG)
S2	00 59 08.90	−00 49 22.80	0.34 ± 0.06	–

Table 3.11: Compact sources in the ACT-CL J2135.7+0009 cluster region. The spectral index is determined using the FIRST source flux when available. Optical counterparts are defined as being a foreground (FG) source or a possible cluster member (CM) based on optical colours in the SDSS DR12 image.

ID	R.A. (hms)	Dec. (hms)	$S_{610\mathrm{MHz}}$ (mJy)	α_{610}^{1400}	Optical counterpart
S1	21 35 39.71	00 09 48.36	33.14 ± 0.29	1.01	CM (BCG)
S2	21 35 36.43	00 11 29.16	1.77 ± 0.17	–	FG

terparts in the SDSS DR12 image, one of which appears to be the cluster BCG. The 610 MHz source details are given in Table 3.11.

ACT-CL J2154.5−0049

The 610 MHz field-of-view, shown in Figure A.7, is dominated by a 826.50 ± 0.12 mJy source at α = 21h55m36.79s, $\delta = -$00d47m55.96s. This source has a 1.4 GHz flux of 485.37 mJy and 465.6 ± 14.0 mJy from FIRST and NVSS maps respectively, giving a source spectral index of $\alpha \sim 0.64 - 0.69$.

The 610 MHz radio map of the cluster region is given in the left panel of Figure 3.13. There are only two sources detected in this region, neither of which are detected in FIRST or NVSS. The brighter source has an optical counterpart in the SDSS DR12 image. The source details are given in Table 3.12.

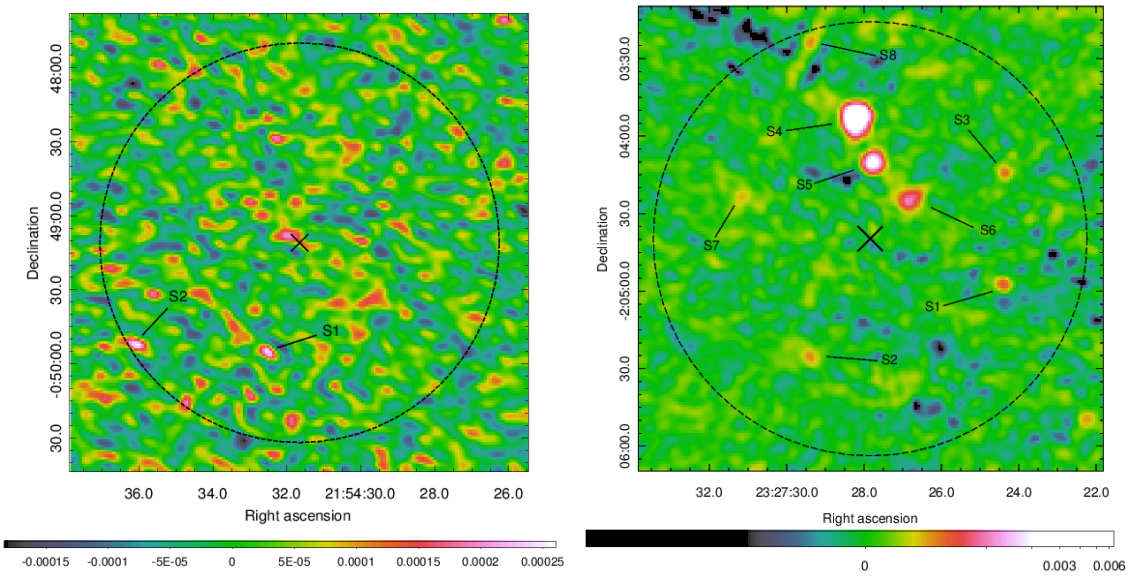

Figure 3.13: GMRT 610 MHz maps of the cluster regions for ACT-CL J2154.5−0049 (*left*) and ACT-CL J2327.4−0204 (*right*). In each panel, the dashed circle indicates the R_{500} cluster scale, with the cross showing the SZ peak.

ACT-CL J2327.4−0204

There are several compact radio sources in the 610 MHz map of the cluster region shown in the right panel of Figure 3.13. Their properties are given in Table 3.13. Only the brightest source (S4) is detected in FIRST. Most of the sources have an optical counterpart in the SDSS DR12 image.

The dominating source in the field-of-view is a bright, extended source identified as the active radio galaxy PKS 2324-02 at $z = 0.188$[4]. Figure 3.14 shows our 610 MHz radio map of PKS 2324-02 (top). The galaxy core is situated at a J2000 position of R.A = 23h26m53.843s, Dec. = −02d02m13.09s and has a flux of $S_{610,\mathrm{core}}$ = 180.0 ± 0.1 mJy in our 610 MHz GMRT, primary beam corrected map. Diffuse structures surrounding the galaxy core are oriented roughly NE to SW and have a largest angular extent of 2.4′, corresponding to 454.5 kpc at the redshift of this source. This places this source below the size threshold of the rare giant radio galaxies (> 700 kpc, see e.g. Molina et al., 2014). The 610 MHz flux of the entire object is $S_{610} = 4.439 \pm 0.003$ Jy. There is bright compact emission within the NE lobe with a bridge of compact emission

[4]Using the NASA/IPAC Extragalactic Database: `https://ned.ipac.caltech.edu/`

Table 3.12: Compact sources in the ACT-CL J2154.5−0049 cluster region. None of the sources are identified in FIRST or NVSS, but there are several sources in the cluster region detected in the survey data that are not visible in the 610MHz map. Optical counterparts are defined as being a foreground (FG) source or a possible cluster member (CM) based on optical colours in the SDSS DR12 image.

ID	R.A. (hms)	Dec. (hms)	$S_{610\mathrm{MHz}}$ (mJy)	Optical counterpart
S1	21 54 32.51	−00 49 55.51	0.11 ± 0.04	FG
S2	21 54 36.06	−00 49 52.44	0.13 ± 0.04	–

Table 3.13: Compact sources in the ACT-CL J2327.4−0204 cluster region. The spectral index is determined using the NVSS source flux when available. Optical counterparts are defined as being a foreground (FG) source or a possible cluster member (CM) based on optical colours in the SDSS DR12 image.

ID	R.A. (hms)	Dec. (hms)	$S_{610\mathrm{MHz}}$ (mJy)	α_{610}^{1400}	Optical counterpart
S1	23 27 24.37	−02 04 57.77	0.30 ± 0.05	–	–
S2	23 27 29.38	−02 05 25.90	0.22 ± 0.05	–	FG
S3	23 27 24.34	−02 04 14.37	0.25 ± 0.05	–	FG
S4	23 27 28.15	−02 03 54.68	8.82 ± 0.08	0.52	CM (BCG)
S5	23 27 27.72	−02 04 11.15	2.24 ± 0.06	–	CM
S6	23 27 26.81	−02 04 25.22	1.00 ± 0.06	–	CM
S7	23 27 31.16	−02 04 23.72	0.20 ± 0.06	–	–
S8	23 27 29.40	−02 03 23.71	0.29 ± 0.07	–	FG

joining it to the galaxy core. This bridge-like feature is also detected in the 1.4 GHz FIRST radio image of this galaxy, shown in the bottom left panel of Figure 3.14. The FIRST data shows similar structures within the diffuse emission as found in our 610 MHz map. The FIRST core flux is $S_{\mathrm{core,FIRST}} = 144.3 \pm 0.3$ mJy, giving a relatively flat spectral index of $\alpha_{610}^{1400} = 0.27$.

The radio images of PKS 2324-02 from NVSS and VLSS are shown in the bottom middle and right panels of Figure 3.14, respectively. None of the source structure can be resolved with the large beams of these surveys. Determining the NVSS and VLSS flux in a 2.4′ circular aperture centred on the 610 MHz core gives $S_{\mathrm{NVSS}} = 2.171 \pm 0.001$ Jy and $S_{\mathrm{VLSS}} = 16.85 \pm 0.13$ Jy,

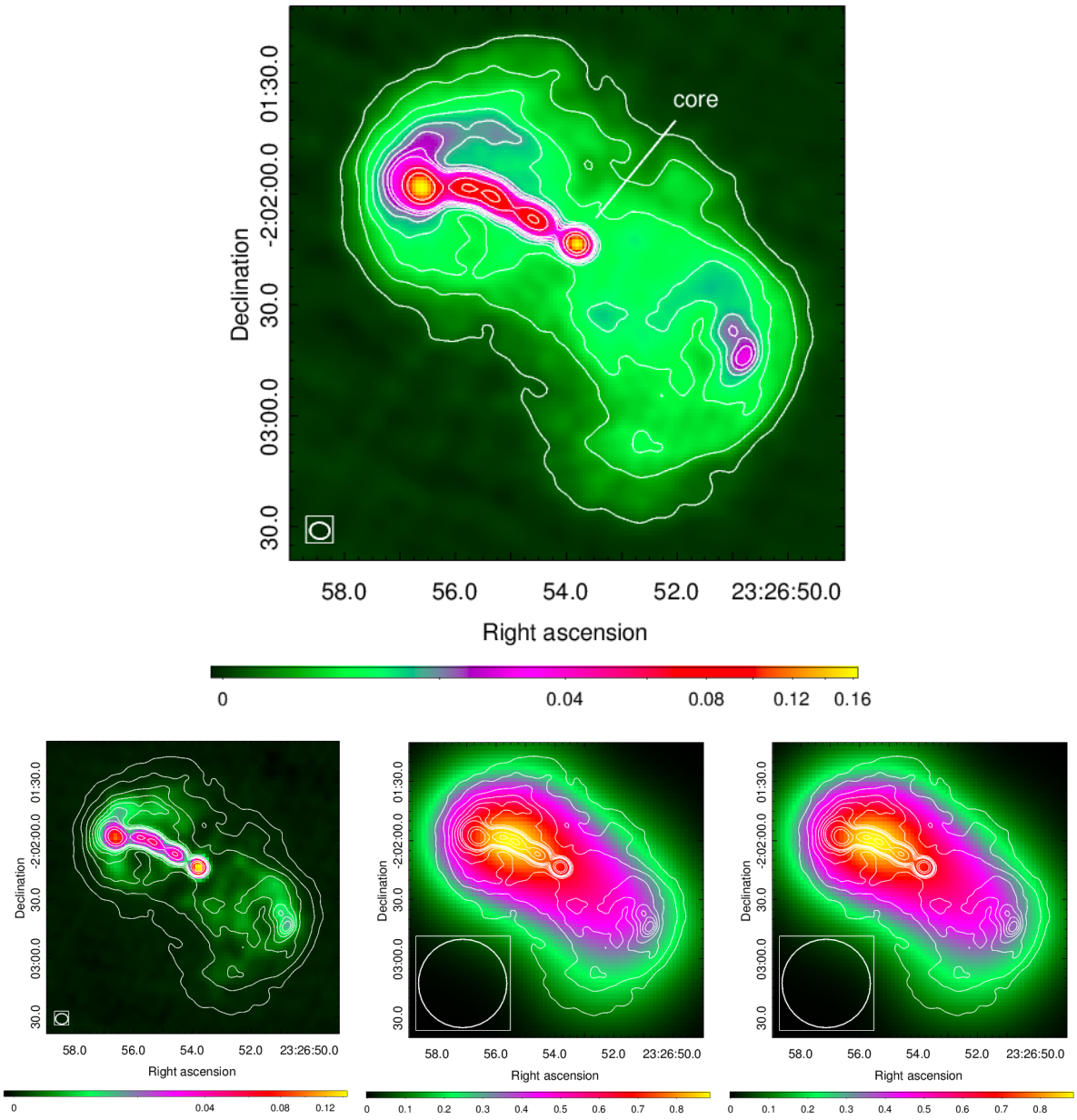

Figure 3.14: Radio maps of active radio galaxy PKS 2324-02 which lies in the field of view of our ACT-CL J2327−0204 observations. *Top:* GMRT 610 MHz image with the presumed galaxy core indicated. *Bottom:* Archival radio images from FIRST (*left*, 1.4 GHz), NVSS (*middle*, 1.4 GHz), and VLSS (*right*, 74 MHz), with GMRT 610 MHz radio contours overlaid. Contours start at 2 mJy beam^{-1} and increase in steps of 4 mJy beam^{-1} until 30 mJy beam^{-1}, after which they increase in steps of 30 mJy beam^{-1}. The synthesised beam is shown as the boxed ellipse in the bottom left corner of each image.

respectively. We therefore have the following global spectral indices for PKS 2324-02: $\alpha_{610}^{1400} = 0.86$ and $\alpha_{74}^{610} = 0.63$. A multiwavelength study of this source will form part of a future paper on the GMRT cluster sample.

3.3.2 Clusters with diffuse emission

Only one of the observed clusters, ACT-CL J0256.5+0006, was found to host diffuse radio emission in the cluster region in the form of a faint ($S_{610} = 5.6 \pm 1.4$ mJy) giant radio halo with a $P_{1.4\mathrm{GHz}}$ radio power of $(1.0 \pm 0.3) \times 10^{24}$ W Hz^{-1}. The position of this new detection on the $P_{1.4\mathrm{GHz}}$–Y_{500} plane is shown as a star in Figure 3.7. Additional observations at 325 MHz were obtained through GMRT's Director's Discretionary Time during July 2014 in order to measure a spectral index for the radio halo. A multi-wavelength analysis of this cluster was undertaken, the main goal of which was to estimate a merger time scale for the cluster. A detailed discussion of the multi-wavelength analysis of ACT-CL J0256.5+0006 is given in chapter §4.

3.4 Discussion and conclusion

We have observed eight ACT clusters with the GMRT, with the goal of detecting diffuse cluster emission. The radio halo detection rate is 12.5% in our cluster sample, which is within the expected range predicted by theory (Cassano and Brunetti, 2005) when considering X-ray luminous clusters. However, it is well below the 40% detection rate when considering high mass ($M_{500,\mathrm{SZ}} > 5 \times 10^{14} M_{\odot}$) SZ-selected samples (Cassano et al., 2013). We note, however, that one of our clusters has a final SZ mass lower than this threshold, which slightly biases the comparison of our detection rate with that from the literature. Our detection rate decreases to 9% if we include the three literature upper limits for previously studied clusters which are members of the ACT-E cluster sample (ACT-CL J0152.7+0100, ACT-CL J0228.5+0030, and ACT-CL J2337.6+0016). The low detection rate may be explained by the dynamical state of the clusters.

As we performed a blind search for radio halos, with no information about the dynamical state of the clusters prior to observing, the lack of visible diffuse emission in the majority of our

cluster sample can be be explained if the clusters are relaxed systems. This indeed appears to be the case based on the dynamical studies of the ACT-E sample from optical redshift information (Sifón et al., 2015). The only cluster in our observed sub-sample with an indication of merging activity from dynamical information is ACT-CL J0256.5+0006, which is also the only target to host observable diffuse emission. As low-resolution SZ cluster detections, such as those provided by ACT, SPT, and Planck, provide no dynamical information on the cluster state, this means that blind SZ-selected radio halo or relic observing samples may have a high fraction of non-detections.

The $P_{1.4\mathrm{GHz}}$ upper limits for our non-detections are higher than the upper limits quoted in the literature, for all but our lowest redshift cluster (§3.3.1.1) which is also the only cluster in our sample below a redshift of $z = 0.48$ with a non-detection. The upper limits from the literature are for clusters below a redshift of $z = 0.4$. We note, however, that our upper limit fluxes are fairly consistent with those from the literature (see e.g. Kale et al., 2013). Since the angular size of a 1 Mpc halo decreases with increasing redshift, the radio power relating to a given flux will increase with increasing redshift. For example, an upper limit 610 MHz flux of 8 mJy gives a 1.4 GHz log radio power (in W Hz^{-1}) of 23.9 at $z = 0.3$, but produces a value of 24.5 at a higher redshift of $z = 0.5$. After compensating for varying radio halo sizes over the range of masses in our cluster sample, most of the high-redshift upper limits are below the radio power/mass correlation. Only our two highest redshift clusters, ACT-CL J0022.2−0036 and ACT-CL J0059.1−0049, are still slightly above this scaling relation. However, the upper limits are still above the $P_{1.4\mathrm{GHz}}$–Y_{500} correlation, although well within the scatter. We performed a survival analysis for both relations and found that the upper limits could belong to the population of detected radio halos without significantly changing the correlation found using only the true detections.

High-redshift clusters would need to be observed for much longer than their closer counterparts in order to achieve upper limit powers of the same order of magnitude. However, the rms noise of an observation, and thus the upper limit flux, is limited by the telescope properties. The theoretical noise level for an image cannot be improved on by increased integration time, but only by using a more sensitive instrument. We therefore note that our cluster upper limits which lie above or on the radio power correlation don't exclude the existence of radio halos in

these clusters. Longer integration times with better sensitivity may yet reveal diffuse emission in these clusters. With that in mind, studies of diffuse emission in high redshift cluster samples will become more feasible with the new generation instruments such as the SKA and its precursor telescopes.

Finally, as the masses used for the pilot project sample (§3.1.1) were preliminary values, and the mass selection for the high-redshift sample was based on the UPP-profile masses from Hasselfield et al. (2013) (§3.1.2), we do not have a complete mass-selected sample when considering the published B12 scaling relation masses, which were the final SZ-inferred mass values at the time of this work. Using these published B12 cluster masses, there are an additional 16 clusters which satisfy the $M_{500} > 5 \times 10^{14} M_{\odot}$ criterion over a redshift range of $0.15-0.7$. Observations of these remaining clusters are necessary in order to infer any reliable diffuse radio emission statistics on a SZ-selected ACT cluster sample.

CHAPTER 4

A GIANT RADIO HALO IN LOW-MASS SZ-SELECTED CLUSTER: ACT-CL J0256.5+0006

4.1 Introduction

Multiwavelength observations of galaxy clusters provide a wealth of information about the physics of the intracluster medium (ICM) and its relationship with cluster galaxies. The optical and X-ray bands have historically been used to identify merger activity via optical substructure (Carter and Metcalfe, 1980; Geller and Beers, 1982; Rhee and Katgert, 1987; Dressler and Shectman, 1988; Rhee et al., 1991; Wen and Han, 2013) and morphological parameters determined from X-ray images (Mohr et al., 1993; Jeltema et al., 2005; O'Hara et al., 2006; Santos et al., 2008). In the last decade, a link has been found between a cluster's merger status and the presence of large-scale diffuse synchrotron emission (see Brunetti and Jones, 2014, and references therein). This cluster-scale radio emission, dubbed a giant radio halo (GRH) if $\sim$Mpc in size, exhibits a steep spectrum and has no obvious link to the individual cluster galaxies (Buote, 2001; Feretti and

Giovannini, 2008; Ferrari et al., 2008; Feretti et al., 2012). Radio halos appear to trace the non-thermal ICM and typically have spectral indices of $\alpha \sim 1.1$–1.5. However, ultra-steep spectrum radio halos (USSRHs, $\alpha \sim 1.6$–1.9), presumably associated with more pronounced synchrotron ageing, have also been detected within the population (Brunetti et al., 2008; Dallacasa et al., 2009; Venturi et al., 2013).

The existence of USSRHs is predicted by one of the current leading theories for the origin of GRHs (Brunetti et al., 2008), namely the *turbulent re-acceleration* model in which the synchrotron emission is powered by turbulence generated during cluster mergers (Schlickeiser et al., 1987; Ensslin et al., 1998; Brunetti and Lazarian, 2011; Beresnyak et al., 2013). In this model one expects an USSRH to be seen when the turbulent energy in the cluster has decreased sufficiently for it to be less efficient in accelerating high energy electrons in the cluster. This scenario can also explain the observed bimodality in scaling relations between the 1.4 GHz GRH power and thermal cluster properties, in which clusters are either radio loud or radio quiet. This dichotomy has been observed in cluster samples selected via X-ray luminosity (Brunetti et al., 2007; Cassano et al., 2008) and the Sunyaev-Zel'dovich (SZ) effect (Sunyaev and Zel'dovich, 1972), although it is less pronounced in the latter case (Sommer and Basu, 2014). In practice, one anticipates a population of clusters in transition between these two states that will have intermediate radio power.

The observed bimodality could be due to selection effects in the cluster sample (Sommer and Basu, 2014) or a physical effect related to the cluster evolutionary state. Magnetohydrodynamic (MHD) simulations by Donnert et al. (2013) show that a GRH is a transient phenomenon that exhibits a rise and fall in radio halo emission over the course of a merger. This evolutionary model suggests that for a merging cluster, the observable diffuse radio emission depends strongly on the phase of the merger in which the cluster is being observed, which likely contributes to the scatter in the observed $P_{1.4\mathrm{GHz}}$ scaling relations with thermal cluster properties.

Moreover, one would expect to find two separate types of systems that populate the intermediate region of radio power: late-stage mergers with old GRHs that are in the process of switching off, and early-stage mergers in which the radio halo emission has recently switched on but not yet reached its maximum radio power. The former scenario is indeed the case for the

USSRHs, which are starting to fill in the intermediate region of GRH power. Clusters that are in the early stages of merging would also be interesting systems to identify and study as they would complete the evolutionary picture.

Cassano et al. (2010) find that the observed dichotomy is strongly related to cluster dynamical state, with morphologically disturbed systems hosting GRHs. However, several GRH non-detections in merging clusters are seemingly incongruent with this trend (A141, A2631, MACSJ2228: Cassano et al. 2010; A119: Giovannini and Feretti 2000; and A2146: Russell et al. 2011). In the case of A2146, Russell et al. postulate that the lack of a GRH in this strongly-merging system is due to the relatively low mass of the cluster. Low-mass systems are expected to generate less turbulent energy during their mergers, yielding weaker synchrotron emission, and hence GRHs that are too faint to observe with current telescopes. The era of LOFAR (Vermeulen, 2012), SKA precursors such as MeerKAT (Booth and Jonas, 2012) and ASKAP (DeBoer et al., 2009), and the SKA itself (Taylor, 2013) will bring with it highly sensitive observations of these systems, and should reveal the underlying GRH emission.

In this chapter we present the detection of a GRH in a low-mass system that we argue is in the early stages of merging. As discussed, such early-stage merging systems are interesting because they allow us to probe the full evolutionary cycle of GRHs and are expected to fill in the intermediate region in radio halo power.

The structure of the chapter is as follows. We present existing multiwavelength data on ACT-CL J0256.5+0006 in §4.2, and we describe the radio observations and data reduction process in §4.3, with the radio results presented in §4.4. X-ray and optical morphological analyses are discussed in sections 4.5.1 and 4.5.2, respectively. We construct a model for the merger geometry in §4.6 and infer merger time-scales from this model in §4.7. We conclude with a discussion in §4.8. We adopt a ΛCDM flat cosmology with $H_0 = 70$ km s^{-1}Mpc^{-1}, Ω_m = 0.27 and Ω_Λ = 0.73. In this cosmology, at the redshift of our cluster (z=0.363), one arcminute corresponds to 305.8 kpc. We assume $S_\nu \propto \nu^{-\alpha}$ throughout, where S_ν is the flux density at frequency ν and α is the spectral index.

Table 4.1: Published properties of J0256. [a] R.A. and Dec. (J2000) of the SZ peak of the cluster, with an astrometric accuracy of 5-10″. [b] Cluster redshift as per Menanteau et al. (2013). [c] Integrated 0.1–2.4 keV X-ray luminosity and X-ray mass from Majerowicz et al. (2004), corrected for the cosmology in this paper. This band luminosity is obtained from integrating the spectrum obtained by M04. [d] Integrated Compton y-parameter and B12 SZ mass from Hasselfield et al. (2013).

R.A. (hh mm ss.s)	02 56 33.0 [a]
Dec. (dd mm ss.s)	+00 06 26.3 [a]
redshift	0.363 [b]
$L_{\rm X}$ (10^{44} ergs s^{-1})	3.01 ± 0.20 [c]
Y_{500} (10^{-4} arcmin^2)	3.4 ± 1.0 [d]
$M_{500,\rm X}$ (10^{14} M$_\odot$)	5.5 ± 1.1 [c]
$M_{500,\rm SZ}$ (10^{14} M$_\odot$)	5.0 ± 1.2 [d]

4.2 ACT-CL J0256.5+0006

ACT-CL J0256.5+0006 (hereafter J0256) lies at z=0.363 and was detected by the Atacama Cosmology Telescope (ACT; Kosowsky, 2006) equatorial SZ cluster survey with a 148 GHz decrement signal-to-noise ratio of 5.4 (Hasselfield et al., 2013). It was first identified in *ROSAT* PSPC data and is included in the Bright SHARC catalogue (RX J0256.5+0006; Burke et al., 1997). Majerowicz et al. (2004) identify J0256 as undergoing a major merger based on observations carried out with *XMM-Newton*.

In the following sub-sections we describe the existing multiwavelength data for J0256 in the X-ray (*XMM-Newton*), optical (Gemini), millimetre (ACT), and radio (VLA) bands. The relevant cluster properties are given in Table 4.1.

4.2.1 X-ray

Majerowicz et al. (2004), hereafter M04, carry out a comprehensive X-ray study of J0256 based on their 25.3 ks *XMM-Newton* observations (obs ID: 005602301). The X-ray image shows two components in the direction of the cluster: a bright main component and a less luminous structure to the west. To investigate whether these are physically connected or serendipitously aligned,

M04 fit an elliptical β-model to the hot gas distribution of the main component, excluding point sources and the western component. After subtraction of the best-fit model from the data, the residuals reveal that the western component is a small galaxy cluster exhibiting a comet-like morphology, with the tail to the west (see Figure 2 in M04). This orientation indicates that gas in the subcluster is undergoing ram pressure stripping as it interacts with the main cluster component. Based on the orientation of the subcluster isophots away from the main component and numerical simulations by Ricker and Sarazin (2001), M04 conclude that the subcluster has not yet passed through the main cluster centre and thus that J0256 is in the pre-core crossing stage of its merger.

For the full cluster, M04 determine a temperature of $T = 4.9^{+0.5}_{-0.4}$ keV and a bolometric X-ray luminosity[1] of $L_{\rm X} = (7.88 \pm 0.53) \times 10^{44}$ erg s^{-1}, which is over-luminous compared to the $L_{\rm X}$–T relation measured by Arnaud and Evrard (1999). M04 conclude that this discrepancy between observed and predicted luminosity, coupled with their evidence for ram pressure stripping of the subcluster, suggests J0256 is not in dynamical equilibrium. Using count rates in the residual map in the region of the subcluster and translating into a luminosity, M04 determine a merger mass ratio of 3:1. However, this calculation requires several broad assumptions due to a lack of ancillary data, making the result somewhat uncertain.

In order to compare this cluster with observations in the literature, we need to convert the bolometric X-ray luminosity found by M04 into a band-limited luminosity within R_{500}. To this end, we use the XSPEC tool to correct the spectrum obtained by M04 for our cosmology and integrate it between 0.1 and 2.4 keV (the common band used in the literature) to determine a band luminosity $L_{0.1-2.4keV}$. The X-ray emission for J0256 is only detected out to a radius of 0.55 of the virial radius, which corresponds to $\sim$1.5 Mpc in our cosmology. Based on the SZ R_{500} value from Hasselfield et al. (2013), this is $\sim 1.1 R_{500}$. However the region from which M04 extract their spectrum is approximately 2.5′ across which corresponds to $\sim 0.8 R_{500}$. We thus conclude that the band luminosity we infer is comparable to the luminosity one would obtain within R_{500}.

[1] Corrected for the cosmology used in this paper.

4.2.2 Millimetre

J0256 was identified in the ACT equatorial 148 GHz map, with a decrement signal-to-noise ratio of 5.4 for a filter scale of θ_{500} = 7.06′ (see Hasselfield et al., 2013, hereafter H13, for details). H13 investigated prescriptions for the Y_{500}—M_{500} scaling relation, where Y_{500} is the integrated Compton parameter. H13 investigated several scaling relations computed from simulations (e.g., Bode et al., 2012) or empirical models (e.g., Arnaud et al., 2010), leading to a SZ mass range of $2.9 \times 10^{14} M_{\odot} < M_{500} < 7.5 \times 10^{14} M_{\odot}$ for J0256, taking into account the range of uncertainties on all mass estimates. The pressure profile scaling relation from Bode et al. (2012) is currently preferred, and in this chapter we use the corresponding SZ mass estimate of $M_{500,\mathrm{SZ}} = (5.0 \pm 1.2) \times 10^{14} M_{\odot}$.

4.2.3 Optical

The ACT collaboration has completed spectroscopic observations of J0256 using Gemini and identified 78 cluster members (Sifón et al., 2015). The cluster members are shown in Figure 4.1 where red circles (blue boxes) denote members that are at lower (higher) redshifts than the cluster redshift of z = 0.363. We identify these two sets of galaxies as separate kinematic components (§4.5.2), each of which has a brightest cluster galaxy (BCG) that is indicated by a large, bold symbol. If the cluster is not in the core passage phase of its merger, the superposition of the two populations in the plane of the sky indicates that the merger is occurring at least partially along the line-of-sight.

In §4.5.2 we use the peculiar velocities of the cluster members, with $v = 0$ at the cluster/component median redshift, to determine velocity dispersions for each kinematic component, as well as the cluster as a whole. We estimate a dynamical mass from each velocity dispersion using the relation from Munari et al. (2013). The redshifts can also be used to re-examine the merger geometry proposed by M04 by determing the velocity difference between the two populations (§4.6).

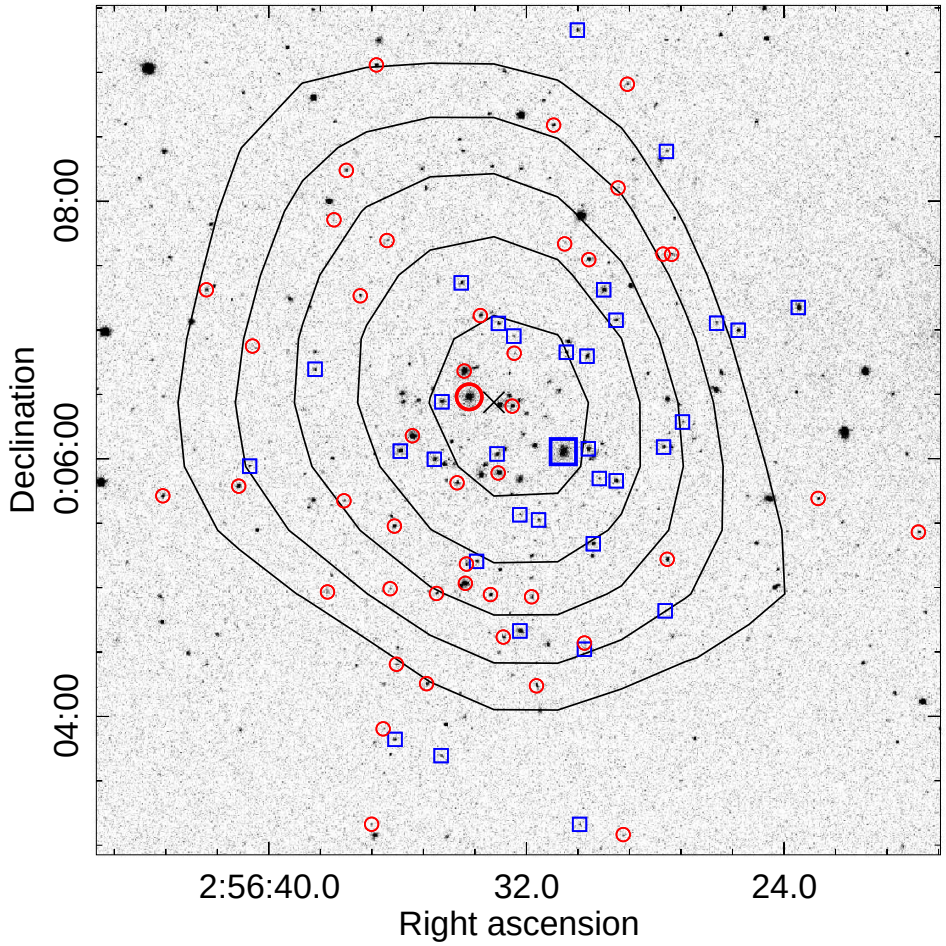

Figure 4.1: Cluster member galaxies with spectroscopic redshifts from Gemini identified on an SDSS r-band image. Blue boxes (red circles) denote members with higher (lower) redshifts than the systemic cluster redshift of $z = 0.363$. Large, bold symbols mark the BCGs of both kinematic components. The 148 GHz Compton y SZ contours are superposed. The contours start at a level of 2.0×10^{-5}, increasing towards the centre in steps of 1.25×10^{-5}. The black X marks the cluster SZ peak.

4.2.4 Radio

J0256 has been mapped at 1.4 GHz in the NRAO VLA Sky Survey (NVSS; Condon et al., 1998) and the Faint Images of the Radio Sky at Twenty-Centimetres (FIRST; Becker et al., 1995) survey, and at 74 MHz in the VLA Low-Frequency Sky Survey (VLSS; Cohen et al., 2007). Figure 4.2 shows the cluster region in each of the three sky surveys. Only one point source is detected in the 1.4 GHz survey data at R.A. and Dec. (J2000) of 02h56m34s and +00d065m03.

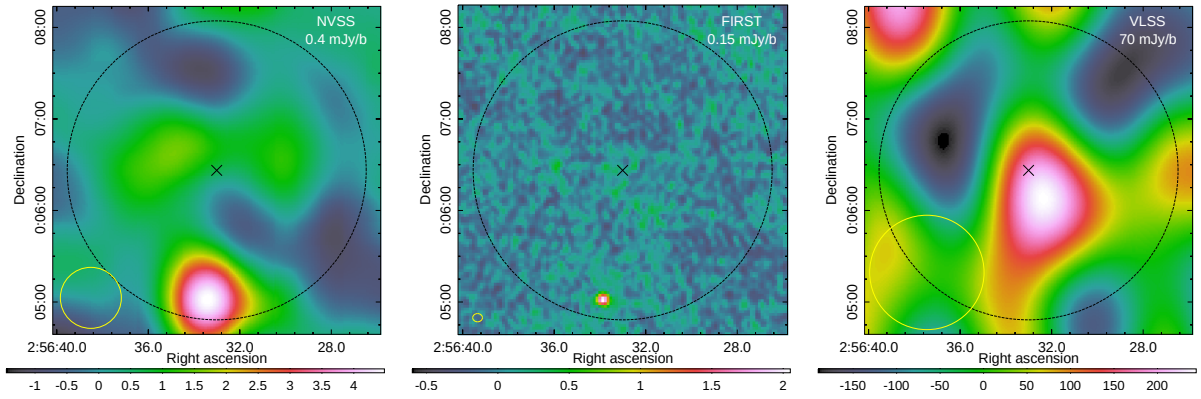

Figure 4.2: Postage stamp images of the J0256 cluster region at 1.4 GHz from NVSS (left) and FIRST (middle), and at 74 MHz from VLSS (right). The dashed black circle denotes R_{500} centred on the SZ peak, which is marked by a black X. The image resolutions, from left to right, are $40'' \times 40''$, $6.4'' \times 5.4''$, and $75'' \times 75''$. The rms is given in the upper right corner and the beam is indicated by the yellow ellipse at lower left in each image. The colour scales are all in units of mJy beam^{-1}.

Its NVSS and FIRST fluxes are 4.8 ± 0.4 mJy and 3.66 ± 0.27 mJy, respectively. This source is not detected in the VLSS data; however, there is a source $1.16'$ away, closer to the SZ peak of the cluster, detected 3σ above the map noise. The rms and resolution of each image is given in the caption for Figure 4.2.

4.3 New Radio Observations

We observed J0256 with the Giant Metrewave Radio Telescope (GMRT) as part of radio follow-up project of ACT equatorial clusters. Initial observations were carried out at 610 MHz in August 2012 as part of the pilot proposal (PI: Knowles; ID: 22_044) discussed in §3.1.1. A second set of 8-hour observations was carried out at 325 MHz on the GMRT using Director's Discretionary Time (PI: Knowles; ID: ddtb132) in July 2014. This dataset has a central frequency of 323 MHz with a total bandwidth of 33 MHz made up of 256 channels and an integration time of 8s. The total on-source time was 6.5 hrs. As with the 610 MHz observations, 3C48 was used as the sole calibrator. Observational details are given in Table 4.2. The pointing centre for both sets of observations was the same and was defined to be that of the SZ peak, given in Table 4.1.

Table 4.2: GMRT observations. Column descriptions: [1] Observing frequency. [2] Observing date. [3] Total time on source. [4] Observation integration time. [5] Usable bandwidth. [6] Synthesised beam of the full-resolution image. [7] RMS noise of the full-resolution image, where p.a. denotes the beam position angle. [8] Half-power beam width of the primary beam. [9] Maximum recovered scale relating to the minimum baseline.

ν (MHz)	Date	$t_{\rm src}$ (hrs)	$t_{\rm int}$ (s)	$\Delta\nu$ (MHz)	$\theta_{\rm synth}$, p.a. ($''\times''$, $^\circ$)	$\sigma_{\rm rms}$ (μJy beam^{-1})	HPBW (arcmin)	$\theta_{\rm max}$ (arcmin)
610	Aug 2012	7.5	16.1	29.1	5.7×4.3, 71.3	26	43 ± 3	17
325	Jul 2014	6.5	8.1	31.2	9.8×8.2, 76.1	72	81 ± 4	32

The 610 MHz and 325 MHz data were subjected to the same calibration procedure based on AIPS (NRAO Astronomical Image Processing System), SPAM (Intema et al., 2009), and Obit (Cotton, 2008) tools. The main calibration steps are outlined here. First, strong radio frequency interference (RFI) is removed by statistical outlier flagging tools. As a compromise between imaging speed and spectral resolution losses due to bandwidth smearing, the datasets are then averaged down to 28 channels. Phase calibration starts from a model derived from the VLSS (Cohen et al., 2007) and the NVSS (Condon et al., 1998), followed by a succession of self-calibration loops. To compensate for the non-coplanarity of the array, we use the polyhedron (facet-based) wide-field imaging technique available in AIPS. We perform several rounds of imaging and self-calibration, inspecting the residual visibilities for more accurate removal of low-level RFI using Obit. To correct for ionospheric effects, we then apply SPAM calibration and imaging. The presence of strong sources in the field of view enables one to derive direction-dependent (DD) gains for each source and to use these gains to fit a time variable phase screen over the entire array. The phase screen was used during imaging to correct the full field of view for ionospheric phase effects. More details on the SPAM recipe we followed can be found in Chapter 3.

Once an indication of low-level diffuse emission was identified, we imported the data into Common Astronomy Software Applications package (CASA; McMullin et al., 2007) for further imaging. Once imported into CASA, the on-the-fly peeling solutions from SPAM are no longer available during imaging. As J0256 lies at close to zero declination, bright sources in the field

are subject to strong north-south sidelobes that interfere with emission in the cluster region. To reduce the impact of these bright sources during the CASA imaging, in AIPS we modeled and subtracted all sources in the field outside of a 13 arcminute radius centred on the cluster, leaving a dataset with only the inner portion of the field. This is the uv-dataset that we worked with in CASA.

For each dataset we created several target field images in CASA, all with Briggs robust $R = 0$ weighting (Briggs, 1995). Briggs weighting is a visibility weighting scheme which is a function of a single real parameter, the robustness R. The weighting can vary smoothly between the two most common forms of weighting: natural ($R = +2$) which provides good sensitivity but poor angular resolution, and uniform ($R = -2$) which gives good resolution but at the expense of high thermal noise. Any value of R between these two limits is permitted, allowing a smooth variation between the two extremes. A value of $R = 0$ gives the best balance between thermal map noise and resolution for our datasets. We first made full resolution (FR) images, shown in Figures 4.15 (610 MHz) and 4.17 (325 MHz) at the end of this chapter, using all of the uv-data, cleaning until the residuals were noise-like. We then created high-resolution (HR) images in the following way. As the 610 MHz data have more long baselines than the 325 MHz data, we matched the uv-coverage of the two datasets by selecting a uv-range from 4 kλ ($\sim$52$''$) to 30 kλ ($\sim$6$''$), and imaging using a 25 kλ outer taper. The HR images were cleaned until their residuals showed no indication of emission in the cluster region. The clean components from the HR images were used as compact source models and were subtracted from the uv-data to create point source-subtracted datasets. Using these datasets, we imaged at full resolution (PSSUB-FR) to visually check that the point source subtraction was successful. 610 MHz HR and PSSUB-FR images of the cluster region are compared in the left and right panels of Figure 4.3, respectively. The PSSUB-FR image shows no visual indication of residual emission from the compact sources; however, we nevertheless investigate contamination from the source removal process in §4.4.2. Once satisfied, we re-imaged with a uv-cut of < 4 kλ and an outer taper of 3 kλ to gain sensitivity to diffuse emission on scales of $\sim$1 Mpc, creating point source subtracted, low-resolution (PSSUB-LR) images. We convolved each PSSUB-LR image with a $1'$ Gaussian, providing better sensitivity to extended features while retaining useful data, to create our final

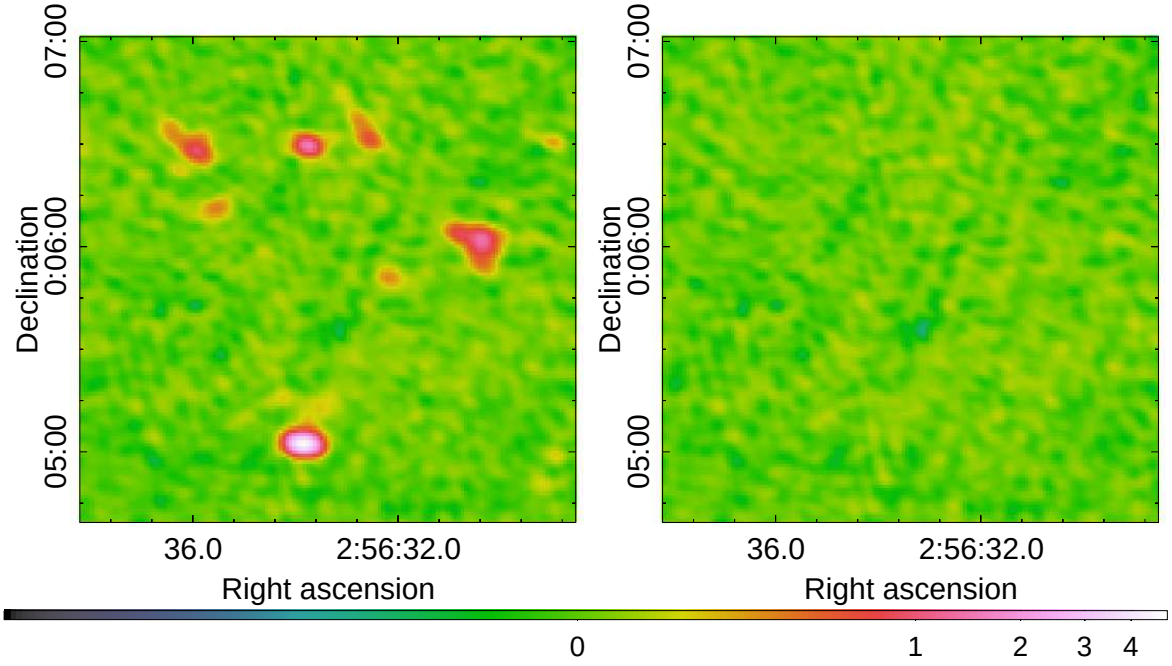

Figure 4.3: $Left$: 610 MHz full-resolution (FR) image of the cluster region showing seven radio sources. $Right$: 610 MHz full resolution image of the same region after subtracting the point source model from the uv-data (PSSUB-FR). The colour scale is in units of mJy beam^{-1} and is the same for both panels.

smoothed, point source subtracted, low-resolution (LR) maps shown in Figures 4.16 (610 MHz) and 4.18 (325 MHz) at the end of this chapter. The final LR 610 MHz (325 MHz) map has a maximum angular resolution of 17′ (32′). A summary of the different images created is given in Table 4.3.

4.4 Radio results

With the angular resolution and short baselines of the GMRT, we are able to investigate emission from both compact sources and extended diffuse structures. In the following, we discuss our results from both the 610 MHz and the 325 MHz datasets.

Table 4.3: Properties of the different radio images created. Values in brackets are for the 325 MHz images when different from the corresponding 610 MHz images. * The highest resolution available, defined by the synthesised beam. † The largest scale to which the image is sensitive, defined by the shortest baseline/uv-wavelength. ‡ PSSUB-LR convolved with a $1'$ Gaussian. $1'$ corresponds to $\sim$3.5 kλ.

Image ID	$\theta_{\rm min}{}^\star$ (arcmin)	$\theta_{\rm max}{}^\dagger$ (arcmin)	Point sources removed
FR	0.08 (0.13)	17 (32)	No
HR	0.13	0.86	No
PSSUB-FR	0.08 (0.13)	17 (32)	Yes
PSSUB-LR	0.84	17 (32)	Yes
LR‡	1.30 (1.26)	17 (32)	Yes

Table 4.4: Properties of cluster region radio sources. Columns: [1] Source labels, shown in the left panel of Figure 4.5. [2] R.A. and Dec. of the peak source emission in the 610 MHz map. [3] Source type. C: compact; T: resolved with tailed emission. [4], [5] 610 MHz and 325 MHz source fluxes, respectively. Flux errors include 10% measurement uncertainties. [6] Spectral index between 325 MHz and 610 MHz ($S_\nu \propto \nu^{-\alpha}$). Errors are determined via Monte Carlo methods (see text for details). ^{a} Associated with BCG of main component. ^{b} Associated with BCG of subcluster. ^{c} Foreground source. ^{d} Detected in NVSS and FIRST. Extrapolating S_{610} to 1.4 GHz using $\alpha_{_{S7}}$ gives $S_{1400} = 4.61 \pm 0.64$ mJy, which is consistent with the values quoted in §4.2.4.

Source	RA (hms)	DEC (dms)	Type^a	S_{610} (mJy)	S_{325} (mJy)	α^b
S1	02 56 35.5	00 06 11.0	C	0.56 ± 0.08	0.69 ± 0.12	0.33 ± 0.31
S2	02 56 35.9	00 06 27.9	T	2.17 ± 0.24	3.32 ± 0.37	0.67 ± 0.21
S3^a	02 56 33.8	00 06 28.8	C	2.17 ± 0.24	3.76 ± 0.41	0.87 ± 0.21
S4	02 56 32.6	00 06 30.9	T	1.20 ± 0.15	1.93 ± 0.23	0.75 ± 0.24
S5^b	02 56 30.4	00 06 01.8	T	4.14 ± 0.43	9.71 ± 0.98	1.35 ± 0.19
S6^c	02 56 32.2	00 05 50.8	C	0.42 ± 0.08	0.59 ± 0.12	0.54 ± 0.38
S7^d	02 56 33.8	00 05 02.0	T	7.71 ± 0.78	11.39 ± 1.15	0.62 ± 0.20

4.4.1 Compact radio sources

There are seven bright radio sources in the cluster region identified in both 325 MHz and 610 MHz full-resolution maps, five of which are associated with spectroscopically confirmed cluster members. The 610 MHz HR contours can be seen in the left panel of Figure 4.5, along with source labels. The only source detected in NVSS and FIRST, as discussed in §4.2.4, is detected in our maps as S7. The flux densities and spectral index we measure for this source, provided in Table 4.4, imply a consistent 1.4 GHz flux density of 4.61 ± 0.64 mJy.

Several of these sources exhibit resolved tail emission, possibly due to merging activity in the cluster. The BCG of the subcluster is associated with the radio source S5. This source has a wide extension to the west of the galaxy, and although our highest resolution image cannot resolve finer structure within the extended tail, it may be a bent narrow angle tail (NAT) radio galaxy contorted by ram pressure stripping due to the merger (Bliton et al., 1998). When a lobed radio galaxy has a high enough relative velocity, v_{gal}, compared to the high-density cluster gas, ram pressure proportional to $\rho_{gas} v_{gal}$ is exerted on the radio lobes forcing them to point away from the direction of movement. This leads to wide- and narrow-angled tailed radio sources O'Dea (1985). The multi-frequency radio properties of all seven sources are given in Table 4.4. Here and in §4.4.3.2, the spectral indices are determined using a Monte-Carlo simulation, in which we draw from Gaussian flux density distributions with means and widths represented by the flux densities and their uncertainties, respectively. The spectral index and uncertainties are then determined from the median and 68th percentiles of the resulting spectral index distribution.

4.4.2 Point source contamination

To unveil any low surface brightness extended cluster emission, the HR radio sources, particularly in the cluster region, have to be removed from the uv-data as described in §4.3. Although the point source removal is reasonably successful, as is clear from the right panel of Figure 4.3, it is not exact. In order to quantify the residual (low) level of contamination, we perform a statistical analysis of the LR image using both radio source and random off-source positions in the following way:

1. In the HR image, we select a large number (>100) of random off-source positions.

2. For each position, we calculate the LR map flux density in a LR beam-sized area centred on that position.

3. From this set of flux densities we calculate the mean, $\mu_{\rm rand}$, and standard deviation, $\sigma_{\rm rand}$, of the distribution. We expect $\mu_{\rm rand}$ to be close to zero for Gaussian white noise.

4. We then select all sources outside of the cluster region that are detected above 5σ in the HR map; we find 28 resolved and 53 unresolved sources, where resolved sources are those that are at least 1.2 times as large as the synthesised beam.

5. We repeat steps (2)–(3), now using the point source positions. $\mu_{\rm ptsrcs}$ quantifies the bias in subtraction of point source emission. $\sigma_{\rm ptsrcs}$ contains both the map uncertainty and a measure of the noise added by the subtraction process, $\sigma_{\rm syst}$, i.e. $\sigma^2_{\rm ptsrcs} = \sigma^2_{\rm rand} + \sigma^2_{\rm syst}$.

The results of this analysis are given in Table 4.5. We find that we are systematically over-subtracting a small quantity of point source emission, more so when the sources are resolved. Moreover, the subtraction process does add a small but non-negligible amount of noise into the LR image, as expected. Using the relation in step (5) above, this systematic noise is $\sigma_{\rm syst,610}$ = 0.3 mJy beam$^{-1}_{\rm LR}$ in the 610 MHz map and $\sigma_{\rm syst,325}$ = 1.0 mJy beam$^{-1}_{\rm LR}$ in the 325 MHz map. We incorporate these systematic and random residuals into our final flux density measurements (see §4.4.3.1).

A graphical representation of this process is shown in Figure 4.4. In the HR and LR maps, we stack on the source and random off-source positions separately. The left panels of Figure 4.4 show the stacked results from the HR map. As expected, the random positions produce a noise-like result and the stacked source positions produce a clear compact source at the centre.

Repeating this process in the LR image, we find a negative stacked signal slightly off-centre from the source position, in agreement with the over-subtraction implied by the values in Table 4.5. The shifted peak is due to the varying noise in the map, shown by the random stacked result (middle panels of Figure 4.4). We note that the rms of the LR source and off-source stacked maps are comparable.

Table 4.5: Results of the systematic and statistical tests to quantify the residual point source contamination in the low-resolution maps. All values are in units of mJy beam$_{\rm LR}^{-1}$.

ν	Quantity	Source Positions			Random
(MHz)		Compact	Resolved	All	Positions
Number of sources		53	28	81	116
610	μ	-0.075	-0.082	-0.077	0.013
	σ	0.547	0.822	0.655	0.586
325	μ	-1.073	-1.920	-0.971	0.273
	σ	3.109	2.470	2.693	2.503

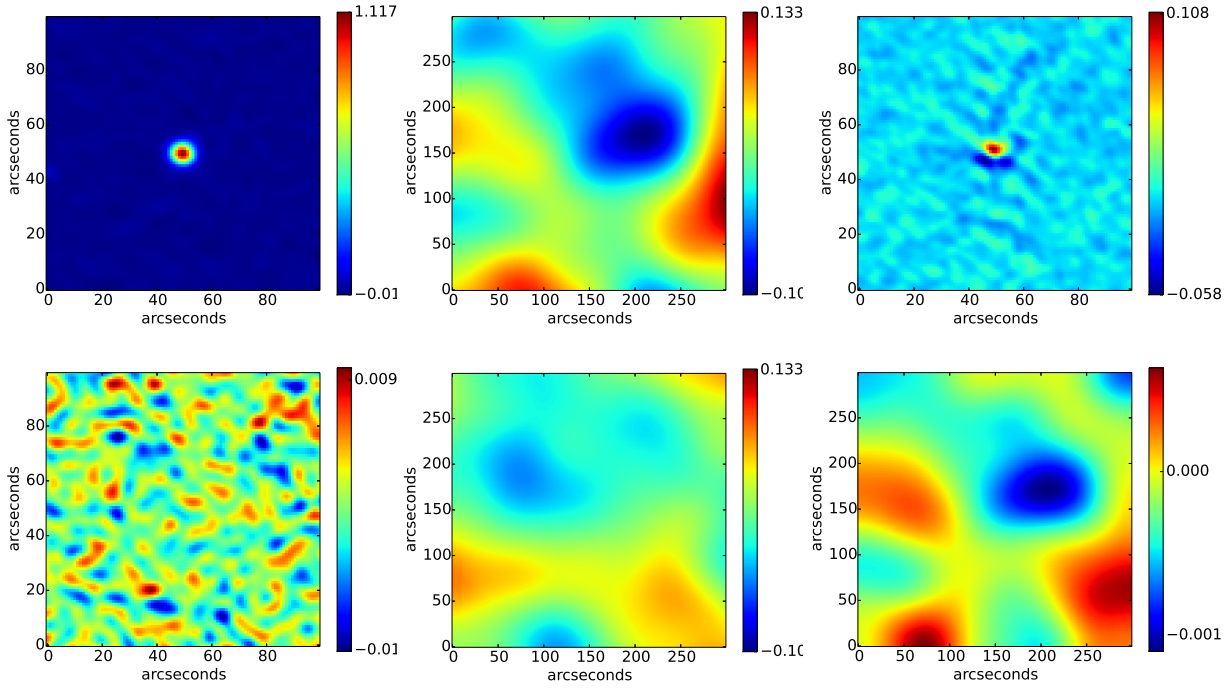

Figure 4.4: Results from stacking on radio source and random off-source positions in the 610 MHz maps, where all colour scales are in units of mJy beam^{-1} and the map axes are in arcseconds. All maps are centred on source positions. *Left panels:* Stacked images in the HR map using radio source (upper) and off-source (lower) positions. The elliptical beam is $6'' \times 5''$. *Middle panels:* Same as the left panels, but for the smoothed, source-subtracted, low-resolution (LR) map. The beam here is $80'' \times 70''$. *Right panels:* Radio source stacked maps from the PSSUB-FR image (upper) smoothed to the LR beam (lower).

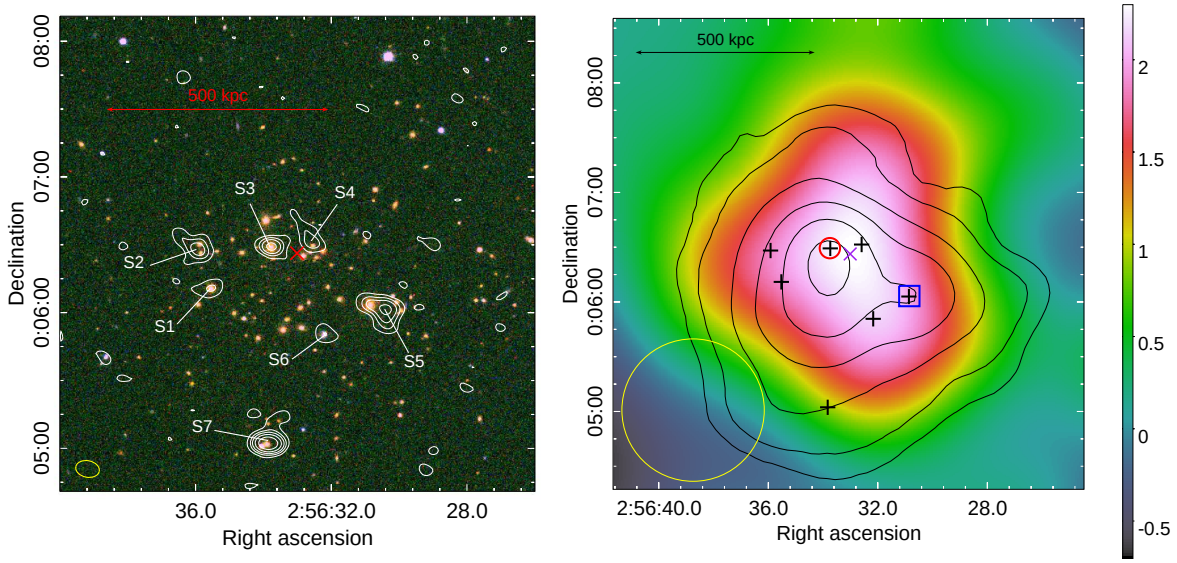

Figure 4.5: *Left*: GMRT 610 MHz high-resolution (6.5″ × 5.0″, p.a. 78.9°) contours of the J0256 emission, overlaid on the SDSS *gri*-band image. The high-resolution (HR) image 1σ noise level is 31 μJy beam^{-1}and the contours are [3,10,20,40,80]$\times 1\sigma$. The HR beam is shown as the yellow ellipse in the lower left corner. Individual radio galaxies are labelled from S1 to S7. Flux densities for these sources can be found in Table 4.4. The red X marks the position of the SZ peak. *Right*: Smoothed *XMM-Newton* MOS X-ray contours (arbitrary levels) overlaid on the smoothed low-resolution (LR) 610 MHz image of the GRH in J0256. The LR radio image is obtained after subtracting the compact source emission from sources S1 to S7 (positions marked by black crosses). The red circle (blue square) indicates the BCG of the main (subcluster) component. The positions of the BCGs coincide with the X-ray peaks of each component. The LR synthesised beam (79.6″ × 76.8″, p.a. -86.9°) is shown as the yellow ellipse. The purple X marks the position of the SZ peak.

As a final check, we stack on the radio source positions in the PSSUB-FR map and smooth this result to the same resolution as the LR map. These results are shown in the right panels of Figure 4.4. There is a net residual after source subtraction mostly caused by imperfect subtraction of resolved sources, the peak of which is $\sim$10% of the peak brightness of the average source in the stacked HR map. When we smooth to the same beam as the LR map (bottom, right panel), we largely recover the structure of the LR stacked source result (top, middle panel).

Table 4.6: GRH properties. Subscripts denote frequencies in MHz unless otherwise stated. † Extrapolated from S_{610} using a spectral index of $\alpha = 1.2 \pm 0.2$. ⋆ Largest linear size of the GRH, corresponding to 2.6′.

S_{610} (mJy)	5.6 ± 1.4
S_{325} (mJy)	10.3 ± 5.3
α_{325}^{610}	$1.0^{+0.7}_{-0.9}$
$P_{1.4\mathrm{GHz}}$ (10^{24} W Hz^{-1})†	1.0 ± 0.3
LLS_{610} (Mpc)⋆	0.8

4.4.3 Diffuse emission

After removal of the radio sources in the field, the LR 610 MHz map, shown in Figure 4.16, reveals distinct extended emission in the cluster region with a 6σ peak above the map noise. The 3σ angular extent of the emission is 2.6′, corresponding to a physical scale and largest linear size (LLS) of 0.8 Mpc at the cluster redshift. Due to the centralised position and size of this emission, we classify it as a giant radio halo, making J0256 one of the lowest-mass clusters to host one known to date. The right panel of Figure 4.5 shows the 610 MHz GRH overlaid with smoothed X-ray contours from the XMM EPIC image. The GRH roughly follows the X-ray emission and is centred on the cluster SZ peak. The GRH radio properties are listed in Table 4.6. Our LR 325 MHz map is shown in Figure 4.18. The radio peak of the GRH lies to the west of the cluster SZ peak and is only marginally detected in the 325 MHz map, being only 3σ above the map noise. We note that this radio peak is at the same position as the emission in the VLSS image of the cluster shown in the right panel of Figure 4.2.

4.4.3.1 Flux measurements

The flux density is measured within an aperture of radius 90″, centred on the 610 MHz emission such that all 610 MHz halo flux is captured. From the results of the point source contamination analysis in §4.4.2, the bias at 610 MHz is only at the 1σ level, i.e., $\mu_{610,\mathrm{ptsrcs}} = -0.077 \pm 0.073$ mJy beam$_{\mathrm{LR}}^{-1}$, leading to a 5% larger corrected flux density for the halo. However at 325 MHz, $\mu_{325,\mathrm{ptsrcs}} = -0.971 \pm 0.299$ mJy beam$_{\mathrm{LR}}^{-1}$, which is a bias measured at a significance of

3σ that leads to a fractional flux density increase of over 50%. We thus correct the measured flux densities and incorporate the systematic uncertainties introduced by the point source removal into the flux density uncertainties. We also include $\sim$10% absolute flux calibration and residual amplitude errors (Chandra et al., 2004). The final flux density, S_ν, and corresponding uncertainty, ΔS_ν, are calculated as follows:

$$S_\nu = S_{\nu,\mathrm{meas}} - (\mu_{\nu,\mathrm{ptsrcs}} \times N_S) \tag{4.1}$$

$$\Delta S_\nu^2 = (0.1 S_\nu)^2 + \left(\sigma_{\mathrm{rms}}^2 + \sigma_{\mathrm{syst}}^2\right) \times (N_S) \tag{4.2}$$

where σ_{rms} is the central map noise, σ_{syst} is the systematic error due to point source removal, and N_S is the number of independent beams within the flux aperture. We measure integrated halo flux densities of S_{610} = 5.6 $\pm$ 1.4 mJy and S_{325} = 10.3 $\pm$ 5.3 mJy. The additional contributions to the flux density uncertainty lower the significance of the 610 MHz detection to 4σ which is low, but still reliable. The 325 MHz flux, however, now has a signal-to-noise of less than 2. Higher sensitivity observations at 325 MHz are required to reliably confirm our detection at this frequency.

4.4.3.2 Spectral index

We can estimate a theoretical spectral index for the GRH in J0256 from the distribution of measured radio halo spectral indices from the literature, shown in Figure 4.6. Assuming this cluster is in the early stages of merging, based on the X-ray morphology determined by M04 (see §4.2.1 above), we expect J0256 to host a young, and therefore flatter spectrum, radio halo. We therefore exclude the USSRHs ($\alpha \geq 1.6$) from the literature and use the mean and rms of the remaining 17 radio halo spectral indices to determine our theoretical value and error respectively. We determine a spectral index for the typical radio halo population of α = 1.2 $\pm$ 0.2.

Our measured spectral index, $\alpha_{325}^{610} = 1.0^{+0.7}_{-0.9}$, obtained using S_{610} and the noisy S_{325} measurement, is consistent with the above value. However, given the large uncertainties on α_{325}^{610}, driven by the large error on S_{325}, we choose to adopt the spectral index of the regular radio halo population, α = 1.2 $\pm$ 0.2, to extrapolate our measured GRH flux density to other frequencies.

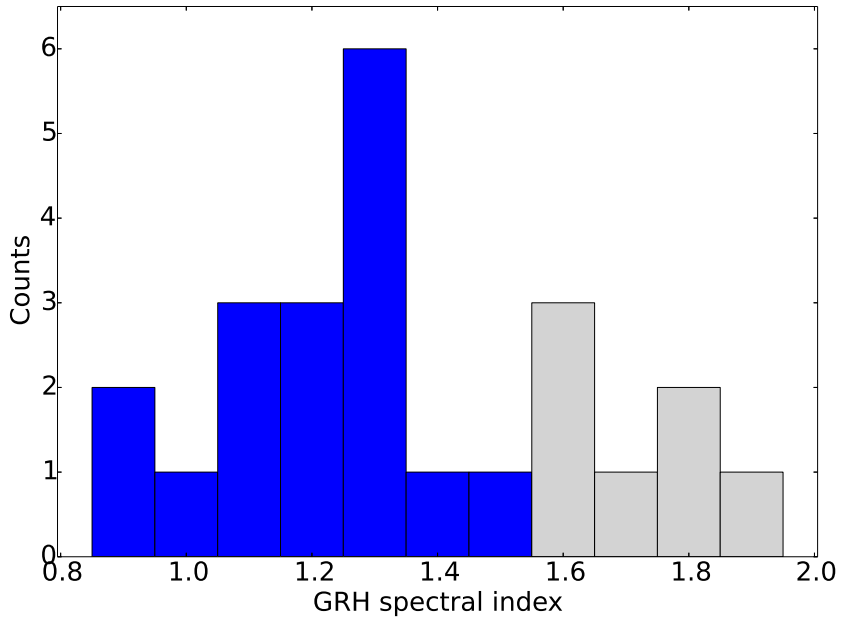

Figure 4.6: Distribution of all measured GRH spectral indices in the literature. The bulk of the values are taken from Feretti et al. (2012) with three updated measurements from Venturi et al. (2013) and new GRHs from Bonafede et al. (2014a) and Bonafede et al. (2014b). USSRHs ($\alpha \geq 1.6$) are shown in light grey.

4.4.3.3 Radio power

The 1.4 GHz GRH radio power, $P_{1.4\mathrm{GHz}}$ is correlated with thermal cluster properties and cluster mass (Cassano et al., 2013). To constrain $P_{1.4\mathrm{GHz}}$, we use our 610 MHz flux density measurement and the assumed spectral index from the previous section to extrapolate a flux density at 1.4 GHz. We correct for bandwidth shrinking and apply a k-correction in order to calculate a halo radio power of $P_{1.4\,\mathrm{GHz}}$ = (1.0 $\pm$ 0.3) $\times 10^{24}$ W Hz^{-1}. The error on $P_{1.4\,\mathrm{GHz}}$ is propagated from the spectral index uncertainties. We note that the radio power is consistent with the non-detections in NVSS, FIRST, and VLSS, as it corresponds to a GRH surface brightness far below the noise levels of these surveys.

J0256 is shown as the red star on the radio power correlations in Figure 4.7. The cluster lies within the scatter of the $P_{1.4\mathrm{GHz}}$–L_{X}, $P_{1.4\mathrm{GHz}}$–Y_{500}, and $P_{1.4\mathrm{GHz}}$–M_{500} correlations. However, J0256 appears to lie further away from the $P_{1.4\mathrm{GHz}}$–Y_{500} correlation, compared to its position

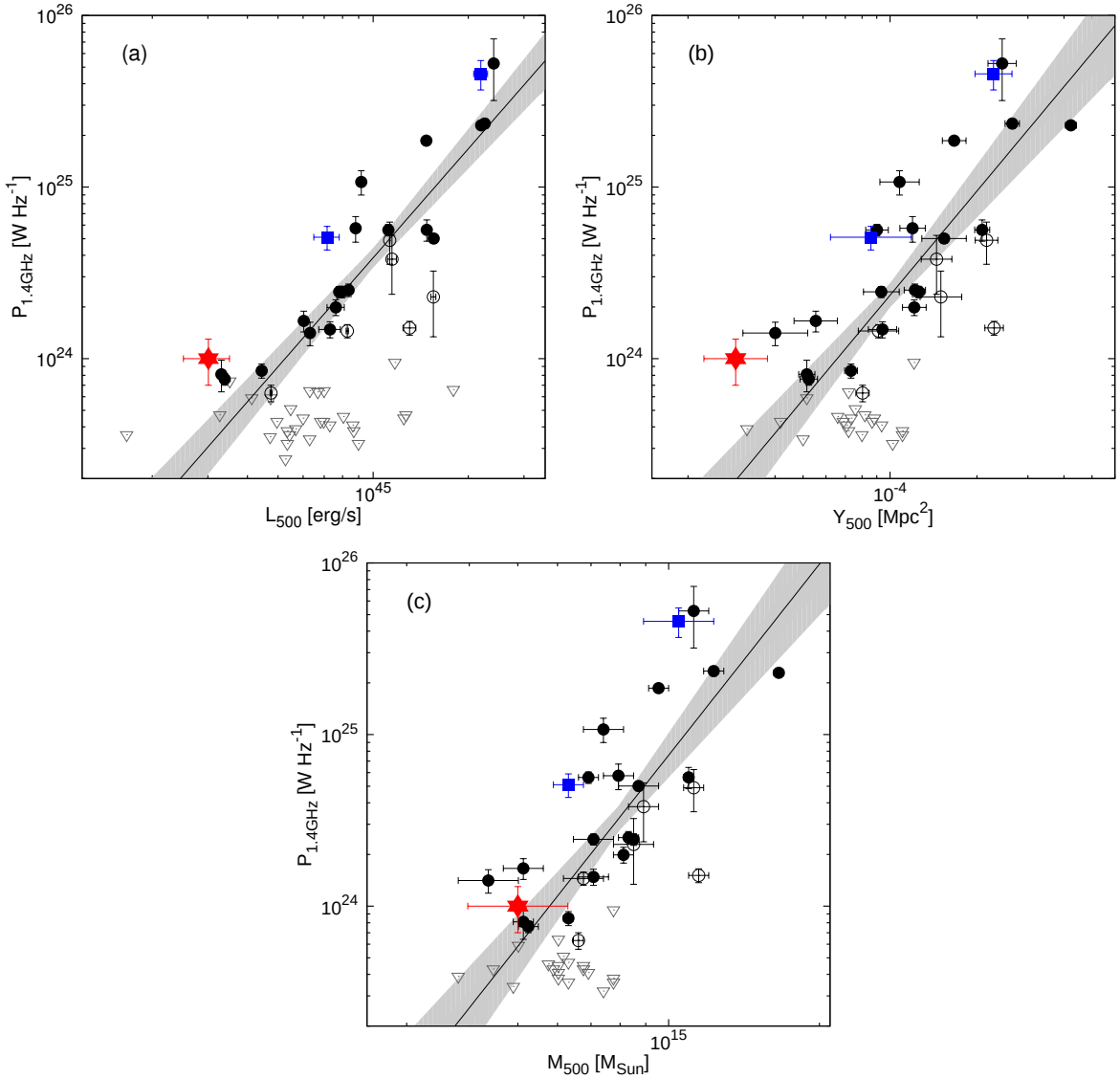

Figure 4.7: Radio halo detections and upper limits from the literature showing correlations between the 1.4 GHz radio power and cluster thermal parameters — (a) $P_{1.4}$ vs $L_{\rm X}$, (b) $P_{1.4}$ vs Y_{500}, and (c) $P_{1.4}$ vs $M_{500,\rm SZ}$. Black solid (open) circles and grey open triangles are giant radio halos (USSRHs) and upper limits, respectively, from Cassano et al. (2013), with recent GRHs in PLCK147.3-16.6 (van Weeren et al., 2014) and El Gordo (Lindner et al., 2014) shown as blue squares. The position of J0256 is shown as a red star. The best fit to the GRH detections and associated 95% confidence interval is from Cassano et al. (2013) and are shown by the black line and grey shaded region, respectively.

relative to the other relations. A possible reason for this is the difference in Y_{500}–M_{500} scaling relation used compared to the literature values. The literature Y_{500} and M_{500} values are taken

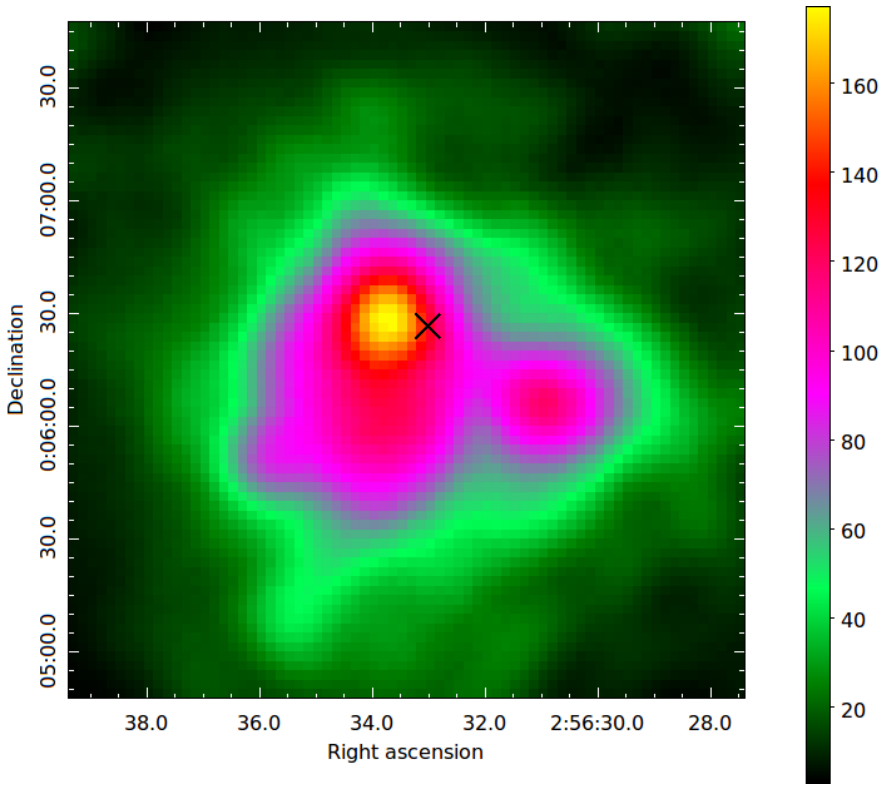

Figure 4.8: Smoothed exposure-corrected and background-subtracted combined *XMM-Newton* EPIC image of ACT-CL J0256.5+0006. The black cross shows the position of the SZ peak.

from the Planck catalog (Planck Collaboration et al., 2014b), which uses the universal pressure profile (UPP; Arnaud et al., 2010) relation. The corresponding values for J0256 are from the ACT-E catalog (Hasselfield et al., 2013), using the B12 scaling relation (Bode et al., 2012) which generally gives a higher mass for a given Y_{500} value than the UPP relation. Therefore, rather than being further away from the Y_{500} relation, J0256 may be closer to the M_{500} relation. We note that the ACT-E UPP mass of $M_{500}^{UPP} = 3.6 \times 10^{14} M_{\odot}$ places J0256 at a similar distance from the M_{500} relation as it currently sits relative to the Y_{500} correlation.

4.5 Cluster morphology

As current observations favour a theory of merger-driven radio halo formation, it is important to understand the dynamical state of J0256. With the X-ray and optical redshift information

available to us, we can perform a morphological analysis of J0256.

4.5.1 X-ray morphology

Following the work of Cassano et al. (2010), we use three parameters to estimate the level of substructure in J0256 from the *XMM-Newton* combined EPIC image shown in Figure 4.8. This image is produced by following the ESA reduction thread for extended X-ray sources[2] and is both exposure-corrected and background-subtracted. To determine the measurement uncertainty on each of our parameters, we adopt the simulation method of Böhringer et al. (2010) whereby a Poisson resampled X-ray image is used to compute the standard deviation of a parameter measurement, which is then used to estimate the measurement uncertainty.

4.5.1.1 Concentration parameter, c_{SB}

The concentration parameter, proposed by Santos et al. (2008) as a probe of cluster substructure, is the ratio of the cluster core and the larger-scale X-ray surface brightnesses. We calculate the concentration parameter as

$$c_{SB} = \frac{S(< 100 \text{ kpc})}{S(< 500 \text{ kpc})}, \tag{4.3}$$

where S is the X-ray surface brightness within a particular radius, centred on the X-ray peak. Before calculating c_{SB}, we smooth the X-ray image using a Gaussian filter with a standard deviation of σ = 3. We determine a value of $c_{SB} = 0.16 \pm 0.12$ for J0256.

4.5.1.2 Centroid shift, w

Poole et al. (2006) show that, compared to other X-ray morphological estimators, the centroid shift is the most sensitive to cluster dynamical state and least sensitive to cluster image noise. It is defined as the rms deviation of the projected separation between the X-ray peak and the centre of mass in units of the aperture radius, R_{ap}, computed in a series of concentric circular apertures centred on the cluster X-ray peak (Mohr et al., 1993; O'Hara et al., 2006; Maughan et al., 2008).

[2] `http://xmm.esac.esa.int/sas/current/documentation/threads/esasimage_thread.shtml`

Following Cassano et al. (2010), the aperture radius is decreased in steps of 5% from a maximum aperture of radius $R_{ap} = 500$ kpc to 0.05 R_{ap}. We compute the centroid shift as

$$w = \left[\frac{1}{N-1} \sum_i \left(\Delta_i - \langle \Delta \rangle \right)^2 \right]^{1/2} \times \frac{1}{R_{ap}}, \tag{4.4}$$

where Δ_i is the distance between the X-ray peak and the centroid of the ith aperture. Following Poole et al. (2006) we excise the central 30 kpc around the X-ray peak when determining the centroid so as to reduce the bias towards a central core. We measure a value of $w = 0.054 \pm 0.005$ for J0256.

4.5.1.3 Power ratio, P_3/P_0

The power ratio of a cluster is calculated using a multipole decomposition of the potential of the two-dimensional projected mass distribution. The idea of using the power ratio of the X-ray surface brightness to probe the underlying mass distribution was first introduced by Buote and Tsai (1995) and has since been widely used as an indication of substructure within a cluster (Jeltema et al., 2005; Ventimiglia et al., 2008; Böhringer et al., 2010; Cassano et al., 2010).

The multipole moments are determined as follows:

$$P_0 = \left[a_0 \ln \left(R_{ap} \right) \right]^2, \tag{4.5}$$

$$P_m = \frac{1}{2m^2 R_{ap}^{2m}} \left(a_m^2 + b_m^2 \right), \tag{4.6}$$

where R_{ap} is the radius of the aperture within which the moments are computed. We use an aperture of radius $R_{ap} = 500$ kpc centred on the X-ray cluster centroid. The parameters a_m and b_m are determined using:

$$a_m(R) = \int_{R' \leqslant R_{ap}} S(x') R'^m \cos m\phi' d^2x' \tag{4.7}$$

and

$$b_m(R) = \int_{R' \leqslant R_{ap}} S(x') R'^m \sin m\phi' d^2x'. \tag{4.8}$$

As X-ray images are pixelised, the integral in equations 4.7 and 4.8 becomes a sum over all pixels, labelled by (x, y), within the radius R_{ap}, where $S(x, y)$ is the surface brightness in that pixel. The zeroth moment a_0 given in equation 4.5 is thus the total X-ray intensity inside R_{ap}.

We use the normalised hexapole moment, P_3/P_0, which is the lowest power ratio moment providing a clear measure of substructure (Böhringer et al., 2010). For J0256, we calculate a value of $P_3/P_0 = (10.0 \pm 11.7) \times 10^{-6}$.

4.5.1.4 Comparison with the literature

Using the methods described in sections 4.5.1.1–4.5.1.3, Cassano et al. (2010) study the morphological parameters for all clusters in the GMRT Radio Halo Survey (Venturi et al., 2007, 2008) and find a link between cluster dynamical state and the presence of a radio halo. They define a cluster to be dynamically disturbed if its morphological parameters satisfy the following conditions: $c_{SB} < 0.2$, $w > 0.012$ and $P_3/P_0 > 1.2 \times 10^{-7}$. The majority of dynamically disturbed clusters are found to show radio halo emission. All of the parameter values we determine in our analysis of J0256 ($c_{SB} = 0.16 \pm 0.12$, $w = 0.054 \pm 0.005$ and $P_3/P_0 = (10.0 \pm 11.7) \times 10^{-6}$) satisfy the above conditions for a merging cluster.

However, the X-ray parameters in the literature are calculated using images from *Chandra*, which has a significantly higher resolution compared to *XMM-Newton*. To investigate the effect of the different telescope properties on the morphological parameters, we select a cluster, A2631, with archival data from both instruments and create exposure-corrected, background subtracted images from each telescope. We compute the morphological parameters for each image over a range of resolutions and find that the power ratio from the *XMM-Newton* image is up to five times larger than that from the *Chandra* image, whereas the other two parameters are comparable between images. By convolving the images to the same resolution, all parameters are now consistent within the error bars. We thus conclude that our power ratio measurement for J0256 should be taken as an upper limit, as we'd expect the result to decrease if we viewed the cluster with Chandra resolution. Nevertheless, a visual inspection of the X-ray image does suggest distinct substructure and if we reduce the measured J0256 P_3/P_0 value by the maximal factor of

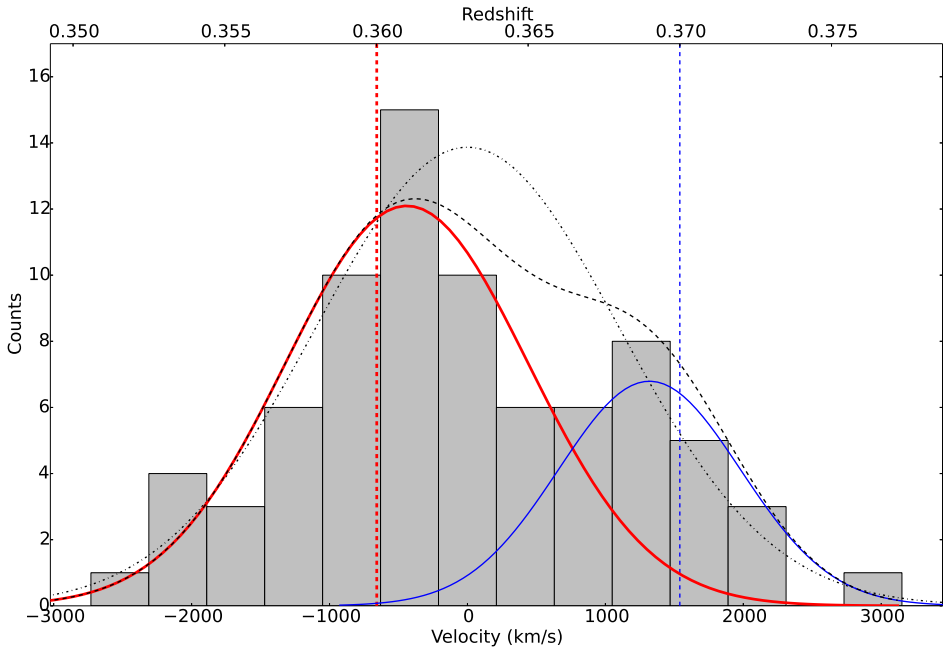

Figure 4.9: Histogram showing the redshift distribution for 78 spectroscopically confirmed cluster members. Here $v = 0$ is defined as the cluster systemic redshift of $z = 0.363$, and the bin width is 420 km s^{-1}. A bimodal fit of two Gaussians, defined by the thick red (main component; $\mu = 0.361 \pm 0.001, \sigma = 0.004 \pm 0.001$) and thin blue (subcluster; $\mu = 0.369 \pm 0.002, \sigma = 0.003 \pm 0.001$) curves, is shown as the dotted black curve. A single Gaussian fit ($\mu = 0.363 \pm 0.002, \sigma = 0.005 \pm 0.001$) is shown by the dot-dashed black curve. The vertical thick red (thin blue) dashed line shows the velocity of the BCG for the main (subcluster) component.

five, as found with our test cluster, the value is still in the "disturbed" region of the parameter space.

4.5.2 Optical redshift distribution

X-ray morphological parameters are largely insensitive to substructure along the line of sight. To gauge any disturbed morphology in this direction, we use the redshift distribution of 78 spectroscopically confirmed cluster member galaxies (see §4.2.3 above). This distribution is shown in Figure 4.9; there is an indication of bimodal structure in the histogram.

Table 4.7: GMM statistics from the redshift distribution of 78 cluster members. All errors are at the 1σ level. † The maximum log likelihood to which the fit converges. The difference in $\log L$ values defines a χ^2 proxy. ‡ Measure of how likely it is that the same statistic can be drawn from a unimodal model.

kurtosis, K	-0.260
peak sep., D	2.64 ± 0.82

Distribution	Statistics				Bootstrapping (%)‡		
	n	μ	σ^2	$\log L$†	K	D	χ^2
Unimodal	78	0.363 ± 0.001	0.005 ± 0.000	299.6	-	-	-
Bimodal	53.9 ± 15.9	0.360 ± 0.002	0.004 ± 0.001	300.7	49.0	46.6	69.4
(multi-variance)	24.1 ± 15.9	0.369 ± 0.003	0.003 ± 0.001				

4.5.2.1 Statistical analysis using GMM

To gauge its significance, we perform a Gaussian mixture model (GMM) analysis of the member galaxy redshifts. We use the GMM code developed by Muratov and Gnedin (2010) to fit a 2-mode Gaussian mixture to our data and compare it to a unimodal fit. The code calculates the kurtosis of the distribution, K, and the maximum log likelihood, $\log L$, to which each model converges. For a bimodal fit, the peak separation of the modes relative to their widths, D, is also calculated. A statistically significant bimodality would have $K < 0$, $D > 2$, and a log-likelihood value greater than that for a unimodal fit. Parametric bootstrapping of the unimodal distribution is performed to determine the probabilities of the observed K, D, and $\log L$ difference values being sampled from a unimodal distribution. The latter probability defines the confidence interval at which a unimodal fit can be rejected. The analysis also assigns a probability of being in each mode to every member galaxy.

The results of our analysis are given in Table 4.7. The multi-variance bimodal mixture model and unimodal Gaussian fits are superposed on the distribution in Figure 4.9, shown by the dotted and dot-dashed black curves respectively. The data satisfy the $K < 0$ and $D > 2$ criteria for bimodality, with the largest $\log L$ value coming from the multi-variance bimodal fit. The improvement in the $\log L$ value for the multi-variance bimodal model relative to the unimodal

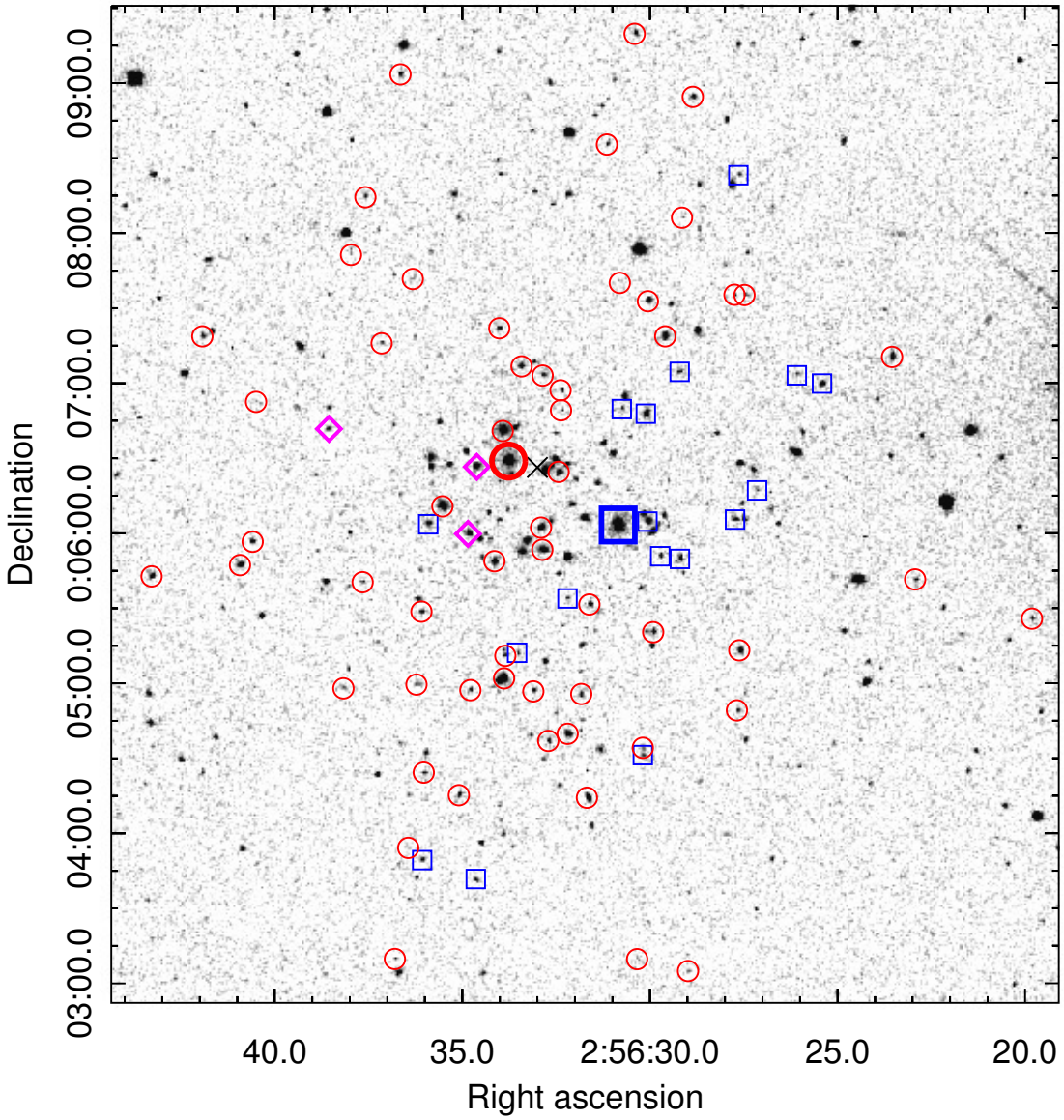

Figure 4.10: Distribution of cluster member galaxies overlaid on an SDSS r-band image. The member galaxies have been divided into their parent populations according to the probabilities determined via the GMM code. Red circles (blue boxes) denote members in the main (subcluster) component. Magenta diamonds identify those galaxies that have a comparable probability for being in either population, in this cae taken to be when both probabilities are greater than 40%. Large, bold symbols mark the BCGs of both kinematic components. The black X marks the cluster SZ peak.

model is not significant due to the difference in degrees of freedom —a likelihood-ratio test indicates that the bimodal fit is rejected in favour of the unimodal fit at 53%. According to the parametric bootstrapping, the unimodal distribution is consistent with the data at the 70% level when only the $\log(L)$ probability is considered, and at the 56% level when the bootstrapped probabilities of K = 49%, D = 47%, and $\log L$ are combined in quadrature. Figure 4.10 shows the distribution of member galaxies with a colour split determined by the probabilities from the GMM analysis. Red circles denote members with a higher than 50% probability of belonging to the main component. Similarly, blue squares denote the same but for the subcluster component. The galaxies with a greater than 40% probability for *both* populations, indicating the overlap between the two modes, are shown by magenta diamonds. Although not a completely plane-of-the-sky merger, there is indication of the two populations being spatially separated.

Although the GMM analysis finds a consistency with a unimodal model, statistical tests run on mock datasets reveal that a bimodal distribution cannot be reliably recovered when the distributions are small, i.e. less than 100 members, as is the case for J0256. Thus, although the multi-variance bimodal fit is not statistically preferred, we choose this fit over a unimodal one taking into account the small number statistics and the population distribution in the plane of the sky, as well as based on the following additional evidence. Firstly, there are two BCGs (cluster members with the lowest SDSS magnitudes) separated spatially, as seen from the SDSS image in Figures 4.1 and 4.10, and in velocity space as shown in Figure 4.9, providing support for the existence of two distinct galaxy populations. Moreover, the BCGs coincide with the peaks in the *XMM-Newton* X-ray emission (see Figure 4.5). Secondly, the cluster mass estimated using the unimodal fit (see §4.5.2.2) is inconsistent with the X-ray and SZ mass estimates at greater than a 2.0σ level, whereas the sum of the component masses from the multi-variance bimodal fit are consistent with X-ray and SZ mass estimates within 0.5σ. Finally, the DS-test of the redshift distribution results in a small enough statistic to indicate the presence of substructure (Sifón et al., 2015).

In the following section we use the GMM probabilities for the galaxy belonging to each of the kinematic components, in the multi-variance bimodal case, to calculate physical properties for the cluster and its components.

4.5.2.2 Velocity dispersions and dynamical masses

By fitting a 2-mode GMM to our data, each cluster member is assigned a probability of belonging to each of the modes. These probabilities can be used to determine the mean and variance for each mode by integrating over all members and weighting by the probabilities. Since we have a discrete number of member galaxies, the mean and variance for component n are given by

$$\bar{z}_n = \langle z \rangle_n = \frac{\sum_i p_n(z_i) z_i}{\sum_i p_n(z_i)} \tag{4.9}$$

$$\sigma^2_{z,n} = \left\langle (z - \bar{z})^2 \right\rangle_n = \frac{\sum_i p_n(z_i) z_i^2}{\sum_i p_n(z_i)} - \langle z \rangle_n^2 \tag{4.10}$$

where $n \in \{1, 2\}$, z_i is the redshift of the i-th member galaxy, and $p_n(z_i)$ is the probability that this member belongs to the n-th component. The mean and variance of each mode in the redshift distribution correspond to the peak redshift and velocity dispersion for each kinematic component, respectively. We use the velocity dispersion and the galaxies-based scaling relation from Munari et al. (2013) to determine M_{200} and R_{200} for each component[3]. Using the concentration parameter from Duffy et al. (2008), we integrate a NFW profile (Navarro et al., 1997) and interpolate to determine M_{500} and R_{500}. The results are given in Table 4.8, with all errors determined via bootstrapping. We follow the same process using the unimodal fit, the difference being that the probability for every member is 1.

From the mean redshifts of the components, we find a line-of-sight velocity difference of $v_\perp = 1880 \pm 210$ km s^{-1}. We also calculate individual component masses of $M_{500,\mathrm{main}} = (3.23 \pm 0.66) \times 10^{14} M_\odot$ and $M_{500,\mathrm{subcl.}} = (1.83 \pm 0.74) \times 10^{14} M_\odot$, leading to a merger mass ratio of 7:4, consistent within the mass uncertainties with the 3:1 ratio determined by M04. Combining the component masses, we calculate a cluster dynamical mass of $M_{500,\mathrm{opt}} = (5.06 \pm 0.99) \times 10^{14} M_\odot$, which agrees with the X-ray and SZ cluster masses given in Table 4.1 to better than 0.5σ. However, if we model the cluster as a single component, we estimate a total mass $M_{500,\mathrm{tot}} = (7.74 \pm 0.02) \times 10^{14} M_\odot$, which is 2.1σ and 2.3σ away from the X-ray and SZ masses, respectively.

[3] $M_{200} = (4\pi/3)\rho_{200} R_{200}^3$

Table 4.8: Optically derived properties of the two cluster components from 78 spectroscopic galaxy redshifts. $v_{\rm pec}$ is relative to z = 0.363.

	Main cluster	Subcluster
N	59	19
$z_{\rm mean}$	0.361 ± 0.001	0.369 ± 0.002
$v_{\rm pec}$ (km s^{-1})	-490 ± 100	1390 ± 180
σ (km s^{-1})	850 ± 70	690 ± 120
M_{200} ($10^{14} M_{\odot}$)	4.90 ± 1.03	2.76 ± 1.14
M_{500} ($10^{14} M_{\odot}$)	3.23 ± 0.66	1.83 ± 0.74
R_{200} (Mpc)	1.45 ± 0.11	1.20 ± 0.19
R_{500} (Mpc)	0.92 ± 0.06	0.76 ± 0.12

4.6 Merger geometry

M04 construct a simple merger model for J0256 using projected distances and the line-of-sight velocity difference between the main and subcluster components. We adopt a similar approach but update two aspects: we use a more current cosmology and the increased number of galaxy spectroscopic redshifts (78 vs. 4) discussed in §4.2.3. The optical galaxy redshift distribution also allows us to determine dynamical masses for the main and subcluster components.

For simplicity, we assume the same merger geometry as in M04, schematically outlined in Figure 4.11. Working in the rest frame of the main component, we assume the same simplification of a point mass subcluster and ignore dynamical friction. However, rather than using a β-model, we assume the mass distribution of the main component is defined by a NFW profile (Navarro et al., 1997):

$$M(< R) = 4\pi\rho_0 R_s^3 \left[\ln(1+c) - \frac{c}{1+c}\right] \tag{4.11}$$

where $R_s = R/c$ is a characteristic scale radius, c is the concentration parameter for radius R, and ρ_0 is the typical NFW dark matter density for the cluster. Using the $c(M, z)$ relation from Duffy et al. (2008) to determine c for our cluster, we have $c = 3.018$ and $\rho_0 = 5.497 \times 10^{14} M_{\odot}\mathrm{Mpc}^{-3}$.

Using the above mass profile and modelling the gravitational infall of the subcluster, we obtain the following relation between subcluster infall velocity, v, and physical separation, d,

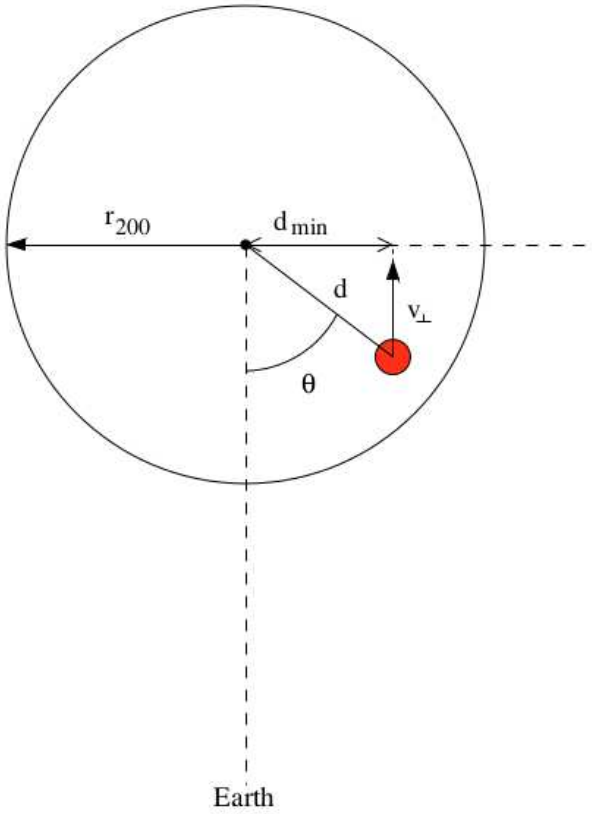

Figure 4.11: Merger geometry of J0256 as per Majerowicz et al. (2004). The small black dot represents the centre of the main cluster component and the red circle represents the centre of the subcluster. $d_{\rm min}$ and d are the projected distance and physical distance between the two component centres, respectively. $v_\perp$ is the line-of-sight infall velocity and θ is the impact angle.

between the centres of the subcluster and the main component:

$$v^2(d) = \frac{2GM_{200}}{R_{200}} + \frac{2GM_0}{R_s}\left[\frac{\ln(1+d/R_s)}{d/R_s} - \frac{\ln(1+c)}{c}\right], \tag{4.12}$$

where $M_0 = 4\pi\rho_0 R_s^3$. The derivation of this relation is discussed in Appendix B. The subcluster redshift $z_{\rm sub}$ is greater than that of the main cluster component, $z_{\rm main}$. As argued in §4.2.1, the X-ray emission pattern indicates that the subcluster is moving towards the main component. This implies that the impact angle must be less than 90°. Using simple trigonometry, it follows from the merger geometry in Figure 4.11 that

$$\left(\frac{d_{\rm min}}{d}\right)^2 + \left(\frac{v_\perp}{v}\right)^2 = 1. \tag{4.13}$$

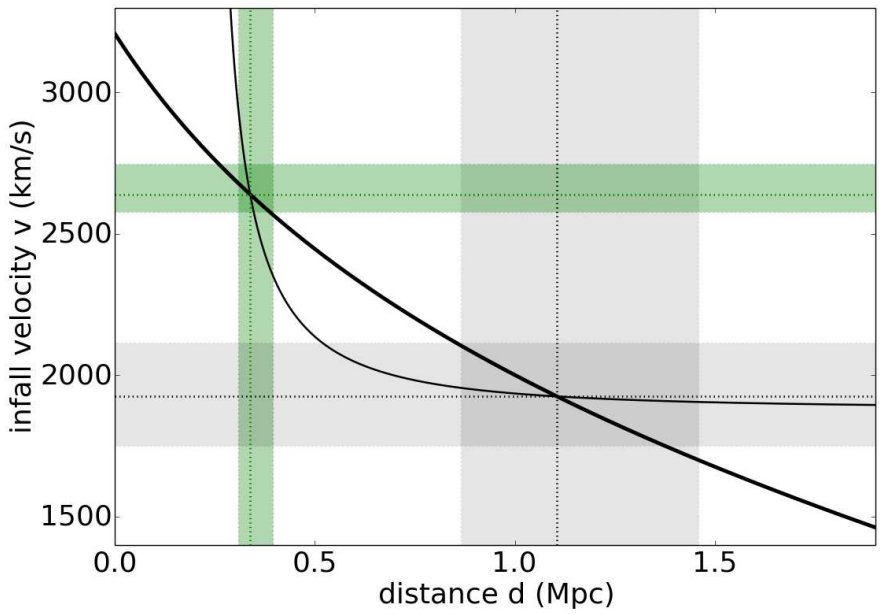

Figure 4.12: Trigonometric (solid, thick; eqn. 4.13) and integrated NFW profile (solid, thin; eqn. 4.12) relations between infall velocity v and cluster component separation d. The intersections of the two relations give the two possible solutions for v and d. The grey dotted lines and shaded areas indicate the solution for case one, $v_1 = 2640^{+110}_{-60}$ km s^{-1} and $d_1 = 0.338^{+0.056}_{-0.020}$ Mpc. The green dotted lines and shaded regions indicate the solution for case two: $v_2 = 1930^{+190}_{-170}$ km s^{-1} and $d_2 = 1.105^{+0.353}_{0.241}$ Mpc.

where $d_{\rm min}$ is the projected separation between the main component and the subcluster, and $v_\perp$ is the velocity difference along the line-of-sight.

Using the X-ray peaks of each component, the projected separation between cluster components is $\sim$0.78′, which corresponds to a physical projected distance of $d_{\rm min} = 237.6$ kpc (as compared to 350 kpc in M04). In §4.5.2.1 we found $v_\perp = 1880 \pm 210$ km s^{-1} which is consistent with the value estimated by M04. Based on the X-ray arguments in §4.2.1, the two cluster components have begun interacting and we can place the following limits on the physical separation and the infall velocity: $d_{\rm min} < d < R_{200}$ and $v > v_\perp$, where R_{200} is the cluster radius for the main component.

Simultaneously solving equations 4.12 and 4.13 with these constraints provides two sets of solutions for the merger model. These are listed in Table 4.9, with the graphical solutions given in Figures 4.12 and 4.13. The uncertainties on v, d, and θ are are shown in Figures 4.12 (v and d)

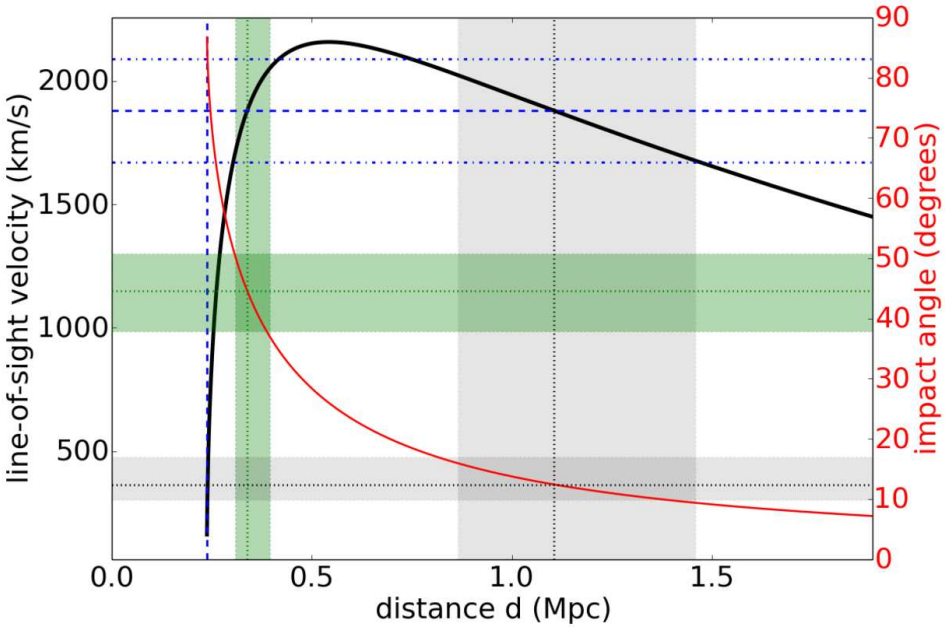

Figure 4.13: The line-of-sight velocity $v_\perp$ versus the component separation d (black, thick, solid) using the relation in equation 4.13 with the infall velocity $v(d)$ given by equation 4.12. The solid thin red curve is the impact angle θ as a function of d. The vertical and horizontal blue dashed lines indicate the values of $d_{\rm min} = 237.6$ kpc and $v_\perp = 1880 \pm 210$ km s^{-1} respectively, with the horizontal blue dot-dashed lines indicating the lower and upper limits for $v_\perp$. Figure 4.12 showed the two merger geometry solutions. Here the green dotted lines and shaded areas indicate the d and θ values and uncertainties for case one, $d_1 = 0.338^{+0.056}_{-0.020}$ Mpc and $\theta_1 = 44.6^{\circ}{}^{+6.2}_{-6.8}$. The grey dotted lines and shaded regions indicate the same, but for case two: $d_2 = 1.105^{+0.353}_{0.241}$ Mpc and $\theta_2 = 12.4^{\circ}{}^{+4.6}_{-2.5}$.

and 4.13 (d and θ), and are propagated from the uncertainties on the R_{200} mass and radius of the main cluster component, the R_{200} radius of the subcluster, and measured line-of-sight velocity difference. We consider these solutions in the next section to estimate relevant time-scales in the merger.

4.7 Merger and radio halo time-scales

To better understand the formation history and mechanism(s) of GRHs, we would like to relate the GRH formation time-scale to the merger time-scale. It is possible to model the physics of

Table 4.9: Merger geometry and time-scales from today for two possible cases with $d_{\rm min}$ = 237.6 kpc and $v_\perp$ = 1880 $\pm$ 210 km s^{-1}. Columns: [2] Infall velocity of the subcluster. [3] Physical separation between components. [4] Impact angle from the line-of-sight. [5] Time since first virial crossing. [6] Time until core passage. [7] Time until second virial crossing. [8] Measure of how far along in the merger the cluster currently is, $\Gamma = |t_{\rm A}/t_{\rm tot}| = |t_{\rm A}/(t_{\rm C} - t_{\rm A})|$.

	v (km s^{-1})	d (kpc)	θ (degrees)	$-t_{\rm A}$ [a] (Gyr)	$t_{\rm B}$ [b] (Gyr)	$t_{\rm C}$ [c] (Gyr)	Γ [d] (%)
case 1	2640^{+110}_{-60}	338^{+56}_{-20}	$44.6^{+6.2}_{-6.8}$	$1.61^{+0.01}_{-0.02}$	$0.10^{+0.02}_{-0.01}$	$1.81^{+0.02}_{-0.01}$	47 ± 1
case 2	1930^{+190}_{-170}	1105^{+353}_{-241}	$12.4^{+4.6}_{-2.5}$	$1.29^{+0.11}_{-0.19}$	$0.41^{+0.19}_{-0.11}$	$2.12^{+0.19}_{-0.11}$	38^{+3}_{-6}

turbulent re-acceleration using simulations. Donnert et al. (2013) (hereafter D13) used MHD simulations of a $10^{15} M_\odot$ and 8:1 merger to study the strength and pattern of diffuse radio emission at various merger stages. They found that the cluster needs to have been actively merging for a minimum amount of time, approximately 15% into the merger, such that there is sufficient turbulence generated, before the radio emission switches on.

4.7.1 Estimates for merger time-scales

To estimate the merger time-scales for J0256 we assume a simple merger taking place in a linear fashion along the merger axis determined by the impact angle, θ, schematically outlined in Figure 4.14. In §4.2.1, we ruled out a scenario in which the subcluster has already passed through the core. In Figure 4.14, we isolate three distinct times during the merger: (A) first virial crossing; (B) core passage; and (C) second virial crossing. Even though we refer to virial crossing, we use R_{200} as a proxy for the virial radius.

From the optical analysis in §4.5.2, $R_{200}^{\rm main}$ = 1.45 Mpc and $R_{200}^{\rm subcl}$ = 1.20 Mpc. First virial crossing thus occurs when the centres of the two components are initially 2.65 Mpc apart. The distances associated with the three merger stages are $R_A = 2.65$ Mpc $- d$, $R_B = d$, and $R_C = 2.65$ Mpc $+ d$, where d is the current physical separation for the two model solutions listed in Table 4.9.

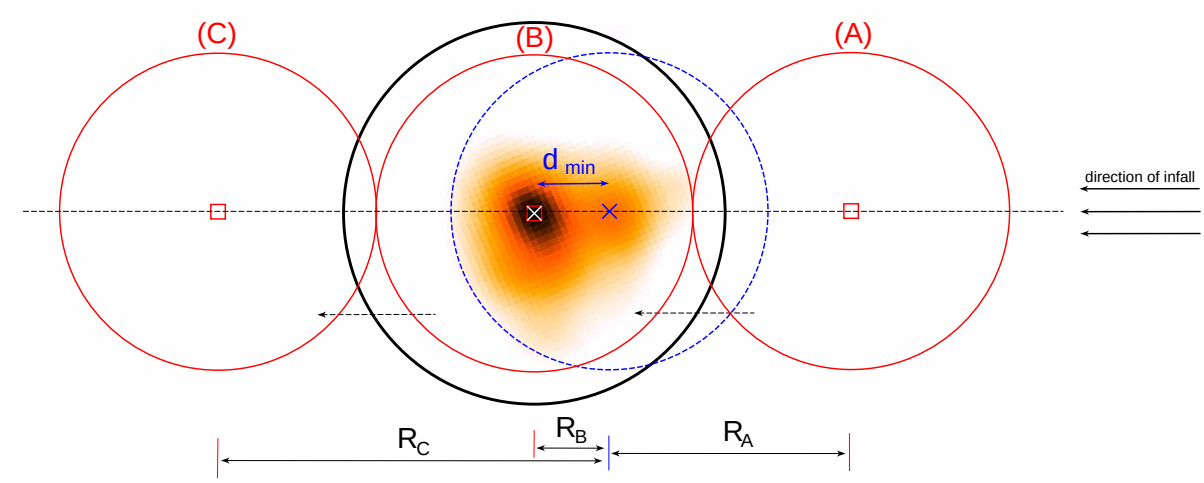

Figure 4.14: Schematic showing the relative position of the subcluster (red circles) to the main cluster (black circle) overlaid on the X-ray image at three different times during the merger: (A) first virial crossing; (B) core passage; and (C) second virial crossing. The centre of the main cluster is marked with a white cross while the centre of the subcluster at each interval of the merger is shown by a red diamond. The blue cross and dashed circle denotes the current position of the subcluster. The dashed black line represents the merger axis and $d_{\rm min}$ is the projected distance between the two cluster components. All circles denote R_{200} of the respective components. Even though we refer to virial crossing, we use R_{200} as a proxy for the virial radius.

For each merger model solution found in the previous section, we compute the merger times

$$t_n = \int_{R_0}^{R_n} \frac{\mathrm{d}R'}{v_{\rm NFW}(R')} \tag{4.14}$$

where $n \in \{\mathrm{A}, \mathrm{B}, \mathrm{C}\}$, R_0 is the observed position of the subcluster, and $v_{\rm NFW}$ is the velocity function given in equation 4.12. The total time of the merger, at least for the first passage, is given by $t_{\rm tot} = t_{\rm C} - t_{\rm A}$. We define the relative time phase of the merger as the ratio $\Gamma = |t_{\rm A}/t_{\rm tot}|$. The results for each model solution are given in Table 4.9.

For case 1, we find that J0256 would have completed first virial crossing 1.61 Gyr ago with $\sim$100 Myr until first core passage occurs. This puts the cluster $\Gamma_1 = 47 \pm 1\%$ of the way into its merger. In case 2, J0256 is closer to the beginning of its merger with 410 Myr until first core passage. The time-scales for case 2 result in J0256 having a relative time phase of

$\Gamma_2 = 38^{+3}_{-6}\%$. According to D13, these conclusions lead to very different theoretical predictions for the observed strength and morphology of the radio emission. In the following section we compare our time-scale results with the D13 simulations.

4.7.2 Comparison with MHD simulations

The simulated radio powers and morphologies in D13 are for observations at 1.4 GHz of a massive $10^{15} M_{\odot}$ cluster undergoing a 8:1 mass ratio, plane-of-the-sky merger. J0256 is about 50% of the total simulated mass but has a much smaller mass ratio of 2:1. As the strength, and hence observability, of the radio emission is related to cluster mass and the amount of turbulent energy created during a merger, we caution that, for the specific case of J0256, the following comparison with the D13 results can at best be qualitative due to the above differences between J0256 and the simulated cluster. MHD simulations of the particular case of J0256 would be required for a more accurate comparison.

To compare our merger time-scales with the MHD simulations of D13 we need to convert our values into their time frame. From the X-ray snapshots of their simulated merger (see their Figure 3), we estimate first and second virial crossings to occur at 0 Gyr and 2.56 Gyr respectively, giving $t_{\rm tot,D13} = 2.56$ Gyr, similar to the total merger time of 3.41 Gyr for J0256. Scaling our Γ values to this time-scale allows us to extrapolate expected radio power and general emission morphology for each case in Table 4.9 using the D13 simulation.

In case 1 we have $\Gamma_1 = 47 \pm 1\%$, corresponding to $t_{\rm A,D13} = 1.20^{0.03}_{0.02}$ Gyr. Here the GRH is in the early stages of having switched on and is gaining power. Case 2 gives $\Gamma_2 = 38^{+3}_{-6}\%$, corresponding to $t_{\rm A,D13} = 0.97^{0.08}_{0.15}$ Gyr. Here, not enough turbulence is being generated to drive the diffuse radio emission and only compact radio source emission is observable. Thus our case 1 appears to be the more likely of the two merger geometry solutions for J0256: we observe what could be a young radio halo and the X-ray image of J0256 shown in Figure 4.8 is a close visual match with the second panel of Figure 3 in D13, which has a relative time-scale similar to that of case 1. This consistency is in contrast to case 2, where no diffuse radio emission is observable and the expected radio power lies in the realm of the upper limits on the $P_{1.4\rm GHz}$–$L_{\rm X}$

scaling relation.

4.8 Summary and Conclusion

We have detected a low surface brightness giant radio halo (∼0.8 Mpc) in ACT-CL J0256.5+0006 with the GMRT at 610 MHz, and obtained a marginal detection at 325 MHz. With an SZ mass of $M_{500} = (5.0 \pm 1.2) \times 10^{14} M_{\odot}$, J0256 is one of the lowest mass clusters currently known to host such emission.

We measure halo flux densities of $S_{610} = 5.6 \pm 1.4$ mJy and $S_{325} = 10.3 \pm 5.3$ mJy, giving a measured spectral index of $\alpha_{325}^{610} = 1.0^{+0.7}_{-0.9}$. Due to the unreliability of the 325 MHz measurements, we calculate a bandwidth- and k-corrected 1.4 GHz radio power of $P_{1.4\mathrm{GHz}} = (1.0 \pm 0.3) \times 10^{24}$ W Hz^{-1} by extrapolating our 610 MHz flux density to 1.4 GHz using a theoretically motivated spectral index of $\alpha = 1.2 \pm 0.2$. As the detection at 610 MHz is not highly significant, we do not draw strong conclusions about the radio morphology, but we do note that it roughly follows the thermal gas as seen in the X-rays and is centred on the cluster SZ peak. More data at 325 MHz would be required to confirm our detection at this frequency and obtain a more accurate measured spectral index.

Using the X-ray and optical information available to us, we have investigated the morphology of J0256, concluding that this system consists of a main cluster component with an in-falling subcluster slightly in front and to the west of it. The merger mass ratio determined via new spectroscopic galaxy member redshifts is roughly 7:4, making it a major merger event. We estimate a line-of-sight velocity difference between the two components of $v_{\perp} = 1880 \pm 210$ km s^{-1}.

Using this information and assuming an NFW mass profile and a simple merger geometry defined by v, d, and θ, we find two possible solutions for the merger time-scale. Defining the merger time phase, Γ, to be the percentage of the first passage (between first and second virial crossings) already completed, we find that J0256 has a merger time phase of $\Gamma_1 = 47 \pm 1\%$ or $\Gamma_2 = 38^{+3}_{-6}\%$. We compare these values with MHD simulations from Donnert et al. (2013) and conclude that J0256 is most likely ∼47% of the way into its merger, with only ∼100 Myr

until first core passage. As the strength of the synchrotron emission is related to the amount of turbulent energy produced during a merger, a population of simulations varying in cluster mass and merger ratio would be useful in investigating the GRH formation rate for a wider range of models.

Our discovery of a GRH in J0256 may help to provide some insight into whether GRHs exist in all merging clusters and whether the non-detections in known merging systems are due to a combination of a low-mass cluster and insufficient sensitivity to diffuse emission, rather than to a complete lack of GRHs. More systems like J0256 will probe the full evolving population of GRHs, in particular the early-stage mergers, and potentially fill in the gap between radio upper limits and USSRHs in the $P_{1.4\mathrm{GHz}}$–L_{X} plane. It would be interesting to carry out a similar merger time-scale analysis for existing GRHs to probe the scatter in the radio power scaling relations.

4.9 Full-resolution and Low-Resolution ACT-CL J0256.5+0006 Radio Maps

Here we provide the inner $30' \times 30'$ of the full resolution and smoothed low resolution maps for both 610 MHz and 325 MHz. In each image, the dashed circle indicates the cluster scale $\theta_{500} = 3.1'$ from Hasselfield et al. (2013), centred on the SZ cluster peak, which is shown as a red or white X. The solid circle shows the $13'$ radius outside of which we removed all compact emission before further imaging in CASA, as described in §4.3.

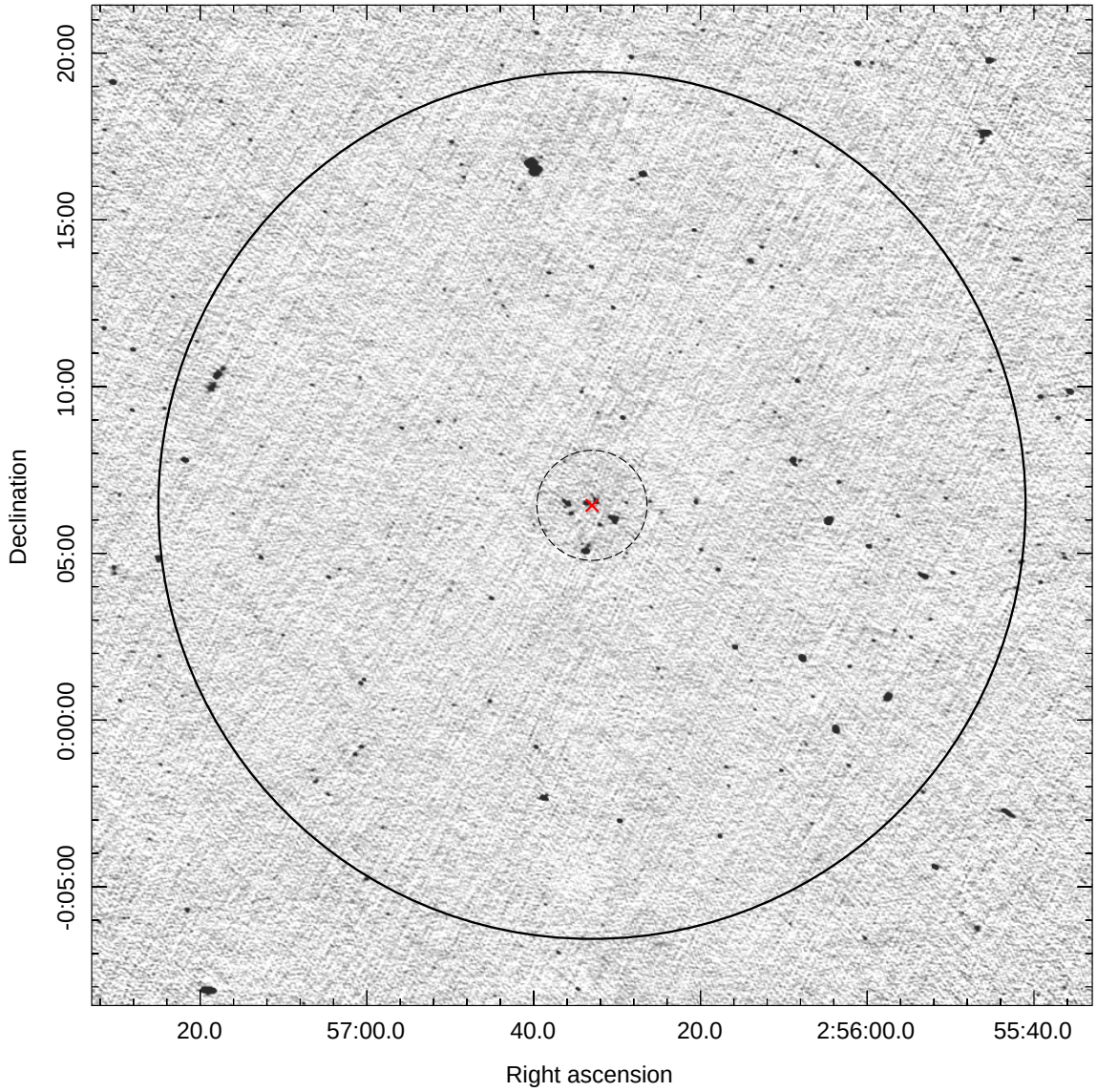

Figure 4.15: Inner $30' \times 30'$ of the full-resolution (FR) 610 MHz map. The beam is $5.7'' \times 4.1''$ at p.a. 71.3°, and the map noise is σ = 26 μJy beam^{-1}. The dashed black circle represents $\theta_{500} = 3.1'$, centred on the cluster SZ peak shown by the red X. The $13'$ radius is shown by the solid black circle.

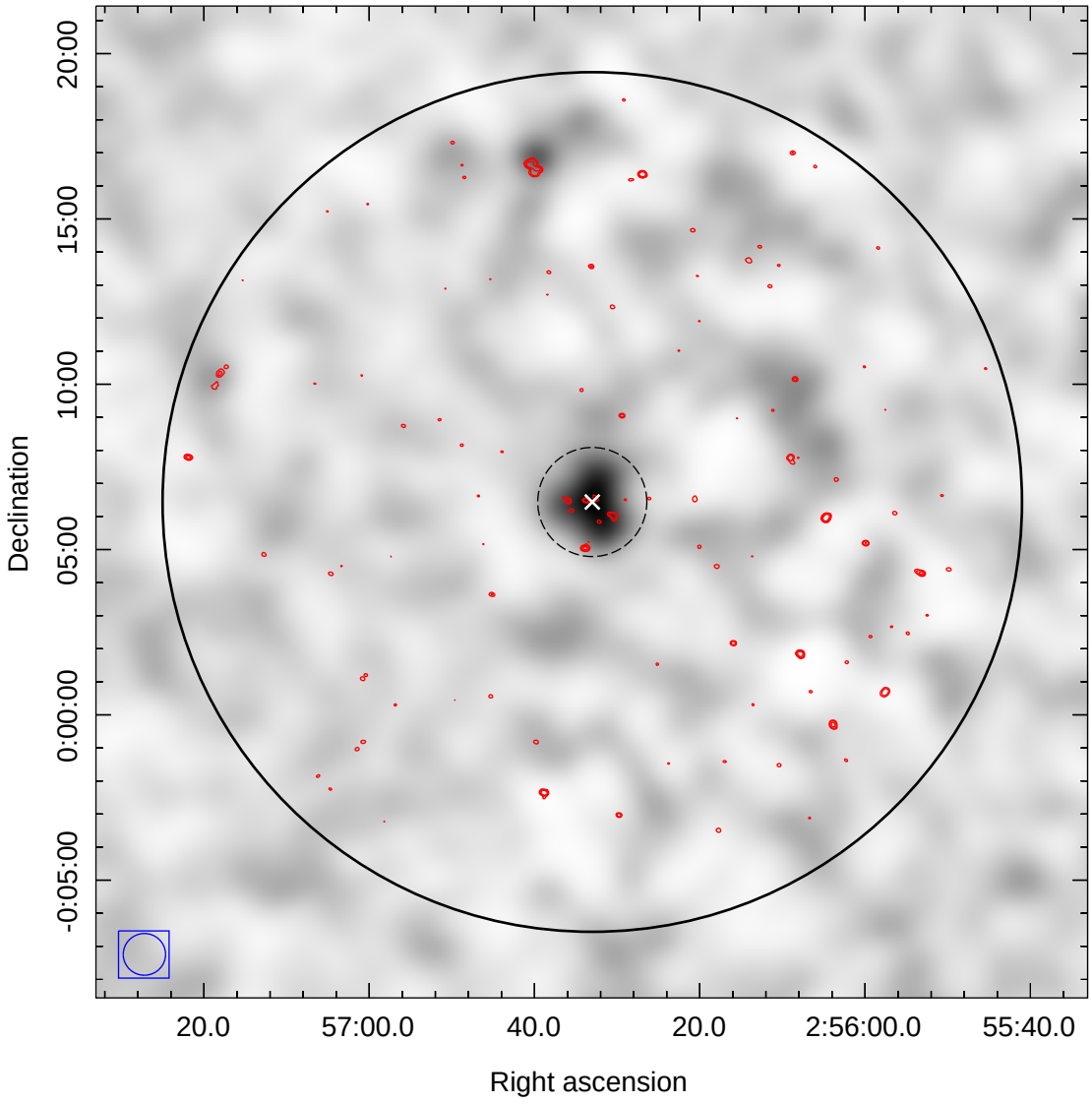

Figure 4.16: Inner 30′ × 30′ of the 610 MHz map. Greyscale is the low-resolution (LR), 1′-smoothed image. Red contours are the high-resolution (HR) [6, 20, 80]×1σ contours where 1σ = 31 μJy beam^{-1}. The X and black solid and dashed circles are as in Figure 4.15. The LR beam is 79.6″ × 76.8″ at p.a. -86.9° and is shown by the blue ellipse in the lower left corner. The 1σ noise in the LR greyscale image is 0.36 mJy beam^{-1}.

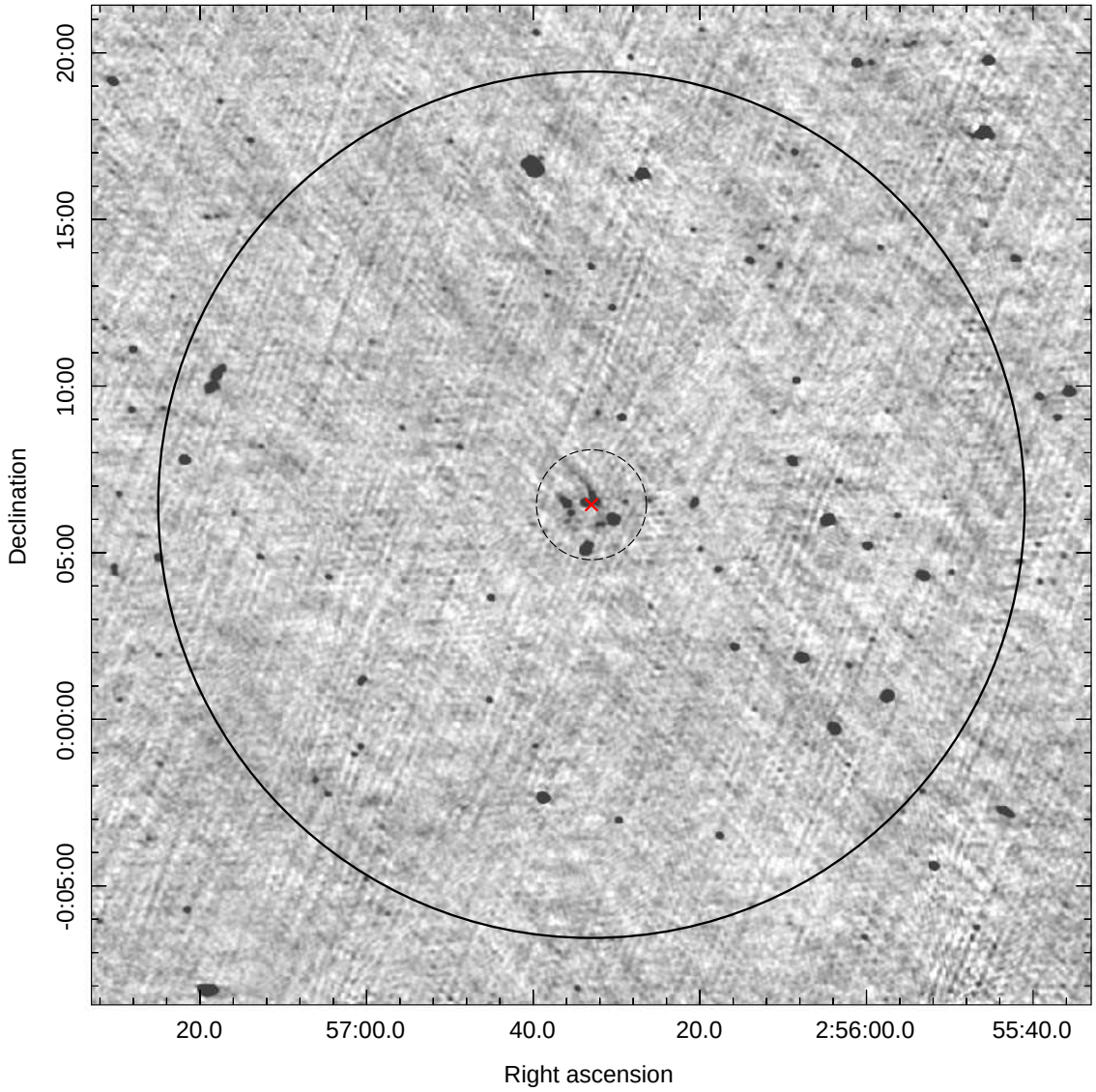

Figure 4.17: Inner $30' \times 30'$ of the full-resolution (FR) 325 MHz map. The beam is $9.7'' \times 7.9''$ at p.a. 74.1° and the map noise is $\sigma = 77$ μJy beam^{-1}. The X and black solid and dashed circles are as in Figure 4.15.

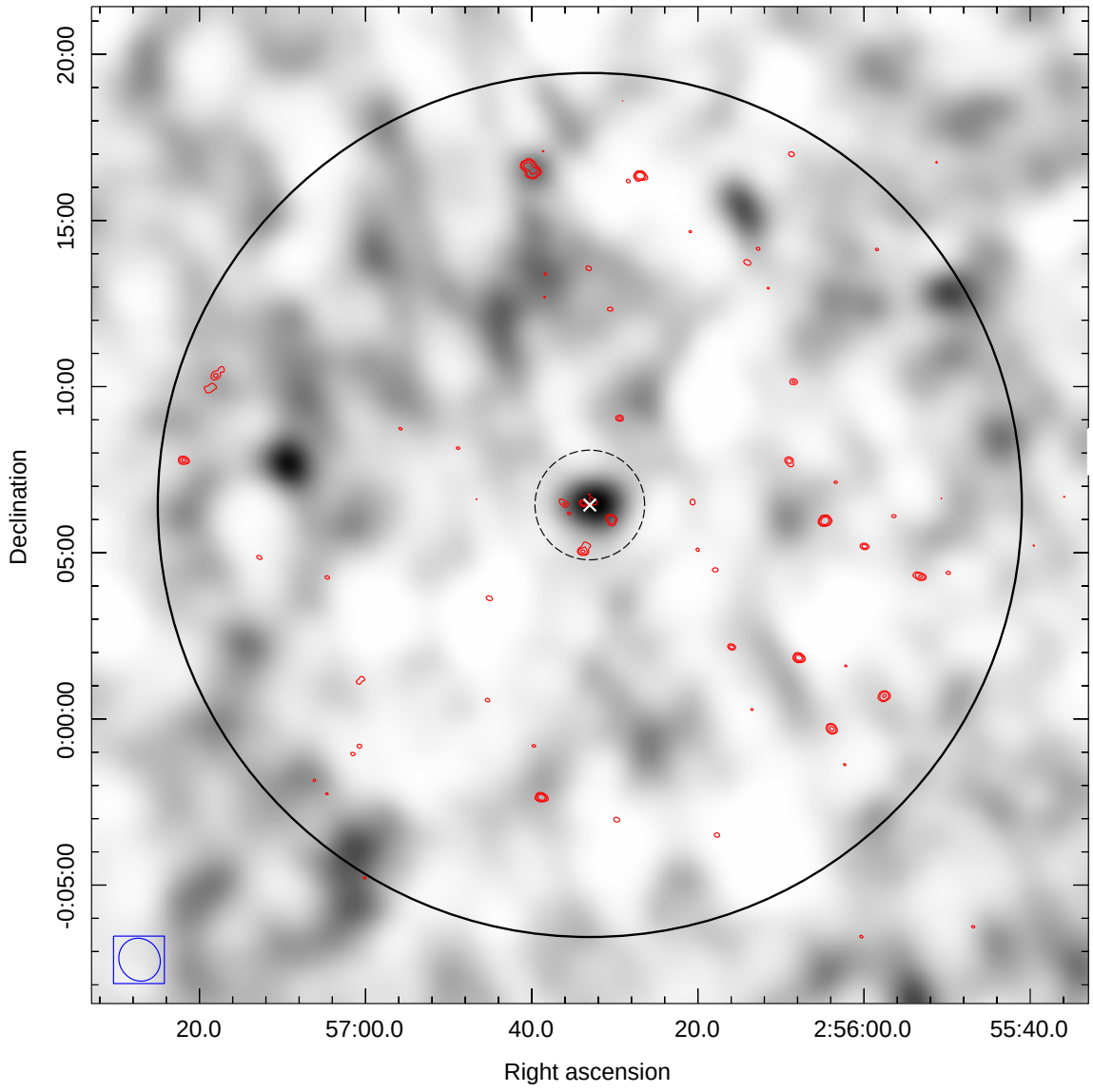

Figure 4.18: Inner $30' \times 30'$ of the 325 MHz map. Greyscale is the low-resolution (LR), $1'$-smoothed image. Red contours are the high-resolution (HR) [6, 20, 80]$\times 1\sigma$ contours where 1σ = 71 μJy beam^{-1}. The X and black solid and dashed circles are as in Figure 4.15. The LR beam is $79.4'' \times 73.1''$ at p.a. 56.7° and is shown by the blue ellipse in the lower left corner. The 1σ noise in the LR greyscale image is 1.18 mJy beam^{-1}.

CHAPTER 5

CLUSTER GRAVITATIONAL LENSING AND MASS MODELLING

General relativity predicts the local distortion of space-time around a large mass density. This leads to a geometric effect called gravitational lensing whereby light rays experience a local deformation along geodesics due to the distorted space-time. The first observational evidence of this phenomenon was in 1919 when Eddington measured the deviation of star positions by the Sun during an eclipse, however it wasn't until 1979 when Walsh et al. (1979) observed the double-quasar Q0957+561 at a redshift of z=1.4 that the first lensed object was documented. Gravitational lensing in clusters of galaxies was first observed in the mid- to late-80's when giant gravitational arcs were detected in Abell 370, Abell 2218, and CL2244-02 (Soucail, 1987; Lynds and Petrosian, 1986). These arcs were hypothesised to be gravitationally lensed images of background galaxies (Paczynski, 1987). This was confirmed by a redshift measurement of z=0.724 for the arc in Abell 370 which lies at a redshift of z=0.394 (Soucail et al., 1988). Following these discoveries, cluster gravitational lensing gained momentum as a field and is now used to trace the mass distribution of the lens (Mellier et al., 1993; Kneib et al., 1996) and to constrain cosmological parameters (Jullo et al., 2010). In the following I will discuss the theory of gravitational

lensing in the case of galaxy clusters and explain the lensing mass modelling techniques that I further used in the analysis of two *Hubble Frontier Fields* (HFF) clusters.

5.1 Gravitational lens equation

When a galaxy cluster of sufficient mass lies between an observer and a background source, the light from this source is deviated from the line-of-sight path causing distorted and sometimes multiple images of this source. Cluster gravitational lensing occurs in two regimes, categorised by the strength of the lensing effect on the background sources. *Strong lensing* effects are visible in the high density region of the cluster core. Background sources that are approximately aligned along the line-of-sight with the cluster core will be strongly lensed. Background galaxies further away from this line-of-sight also experience the gravitational effect of the lens but the effect is weak, requiring a statistical detection. This is the *weak lensing* regime.

The gravitational lensing phenomenon links true positions of background sources in the source plane to observed source positions in the image plane. In order to describe the gravitational lensing formalism, several assumptions have to be made, the foremost being that the cosmological principle, namely that the Universe is isotropic and homogeneous, is true on large scales. Here large refers to the scales L involved with the long-range gravitational force, i.e.

$$L \sim \frac{c}{\sqrt{G\bar{\rho}}} \sim 2 \text{ Gpc}, \tag{5.1}$$

where c is the speed of light, G is the gravitational constant, and $\bar{\rho}$ is the mean density of the Universe. The assumption of the cosmological principle imposes severe symmetries on the space-time metric. In highly concentrated regions, the metric will be locally perturbed, leading to the Schwarzschild metric (Weinberg, 1992) which describes a space-time near a point mass. In the stationary weak field limit $\Phi \ll c^2$, and generalising for a continuous mass distribution, the metric becomes

$$ds^2 = \left(1 + \frac{2\Phi}{c^2}\right) c^2 dt^2 - \left(1 - \frac{2\Phi}{c^2}\right) dr^2 \tag{5.2}$$

where Φ is the 3D gravitational potential of the mass distribution involved.

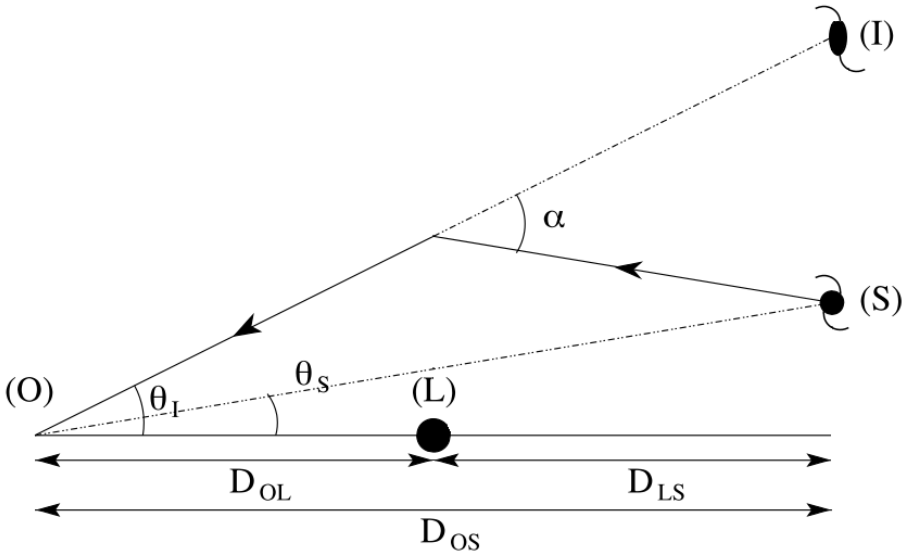

Figure 5.1: Schematic of a single thin lens setup with observer O, lens L, background source S, and observed image I, showing the distances and angles relevant to the lens equation. Source: adapted from Kneib and Natarajan (2011).

Consider the schematic in Figure 5.1 which depicts a simple single thin lens configuration in which an observer O views a source S through a lens L, observing an image I. Without an intervening lens, the observer would view the source at an angle θ_S. With the lens in place, the image of the source is instead observed at an angle θ_I, due to the deflection of the photon path coming from S, described by the deflection angle α, which itself depends on the local space-time deformation at θ_I. Since the local metric perturbation due to the lens, and thus the distortion angle, is minimal, the small-angle approximation of $\tan\theta \approx \theta$ is valid. Using this in conjunction with Thales theorem on the triangle OSI, the geometric equation in the thin lens regime relating the position of the background galaxy in the source to image planes is

$$d\theta_S = \theta_I - \frac{D_{\mathrm{LS}}}{D_{\mathrm{OS}}}\alpha(\theta_I) = \theta_I - \varepsilon\alpha(\theta_I). \tag{5.3}$$

The approximation of a thin lens is valid so long as the distances from the observer to the lens and to the source (D_{OL} and D_{OS} respectively) are far greater than the physical extent of the lens. This is always true in the case of galaxy and cluster lenses. The distance ratio $\varepsilon = D_{\mathrm{LS}}/D_{\mathrm{OS}}$ is a function of the source redshift z_S such that the higher the source redshift, the greater the

deflection and distortion. This ratio is used in the definition of the Einstein radius, defined as $\theta_{\rm E} = \varepsilon\alpha$ when there is perfect alignment between the observer, lens, and source. The Einstein radius is used to quantify the strength of the lens. For a point mass the Einstein radius becomes

$$\theta_{\rm E} = \sqrt{\frac{4GM}{c^2}\frac{\varepsilon}{D_{\rm OL}}}, \tag{5.4}$$

where the more massive the lens, the larger the geometric disruption will be.

Since photons follow null geodesics, $ds^2 = 0$, one can determine the travel time t_T for a given path length, which is a function of the deflection angle, α. Using Fermat's principle, which states that light follows a path with a stationary travel time, we have $dt_T/d\theta_I = 0$ and subsequently derive a formula for the deflection angle:

$$\alpha(\theta_I) = \frac{2\varepsilon}{c^2}\nabla_{\theta_I}\phi^{2D}_{\rm N}(\theta_I) \tag{5.5}$$

where $\phi^{2D}_{\rm N}(\theta_I)$ is the Newtonian gravitational potential projected into the lens plane. Incorporating this into equation 5.3 gives the *lens equation* in the thin lens approximation (for a detailed derivation see Schneider et al., 1992):

$$\theta_S = \theta_I - \nabla_{\theta_I}\varphi(\theta_I), \tag{5.6}$$

where $\varphi(\theta_I)$ is the *lensing potential* and is defined as

$$\varphi(\theta_I) = \frac{2\varepsilon}{c^2}\phi^{2D}_{\rm N}(\theta_I). \tag{5.7}$$

5.2 Gravitational lens mapping

The lens equation 5.6 relates positions in the source plane, S, to that in the image plane, I. However this position offset is also accompanied by a shape deformation. Thus in order to model the full effect of gravitational lensing, a mathematical transformation of source shapes into observed image shapes needs to be incorporated.

5.2.1 The amplification matrix

The deformation and magnification of a source in the image plane can be mathematically modelled by locally relating a source element of the image, $d\theta_I$, to its corresponding element in the source plane, $d\theta_S$:

$$d\theta_S = \mathcal{A}^{-1} d\theta_I \tag{5.8}$$

where $\mathcal{A}^{-1}$ is the Hessian of the lensing equation, commonly referred to as the *amplification* or *magnification matrix*. In Cartesian coordinates, where the z axis is normal to the sky-plane, it takes the following form:

$$\mathcal{A}^{-1} = \begin{pmatrix} 1 - \partial_{xx}\varphi & -\partial_{yx}\varphi \\ -\partial_{xy}\varphi & 1 - \partial_{yy}\varphi \end{pmatrix} \tag{5.9}$$

where $\partial_{ij}\varphi = \dfrac{\partial^2 \varphi(\theta_I)}{\partial\theta_i \partial\theta_j}$ is the second derivative of the lensing potential given in equation 5.7, measured at the image position, θ_I. The magnification at θ_I is characterised by the inverse of the determinant of the amplification matrix, namely the image magnification μ:

$$\mu \equiv \frac{1}{\det \mathcal{A}^{-1}}. \tag{5.10}$$

5.2.2 Convergence, shear and shear orientation

As well as magnification, the lens produces source deformation in the form of isotropic and anisotropic components. The isotropic deformation generates a uniform increase in size by a factor of $(1-\kappa)^{-1}$, where κ is defined as the *convergence*. The higher the density, the larger the convergence and thus the greater the size of the image. The anisotropic deformation causes an elongation of the image: for a circular source this leads to an increased ellipticity of the image, with the minor axis making an angle β with the horizontal. The amount of stretching/contracting of the source is controlled by a factor of $(1 - \kappa \mp |\gamma|)^{-1}$, where γ is defined as the *shear* and can be denoted as a complex number, $\gamma = \gamma_1 + i\gamma_2$ (Schneider et al., 1992). The effects of convergence and shear on a circular source are depicted in Figure 5.2.

The amplification matrix in equation 5.9 is conventionally written in terms of κ and γ. Since the Hessian of the gravitational potential is symmetric, the amplification matrix can be written in

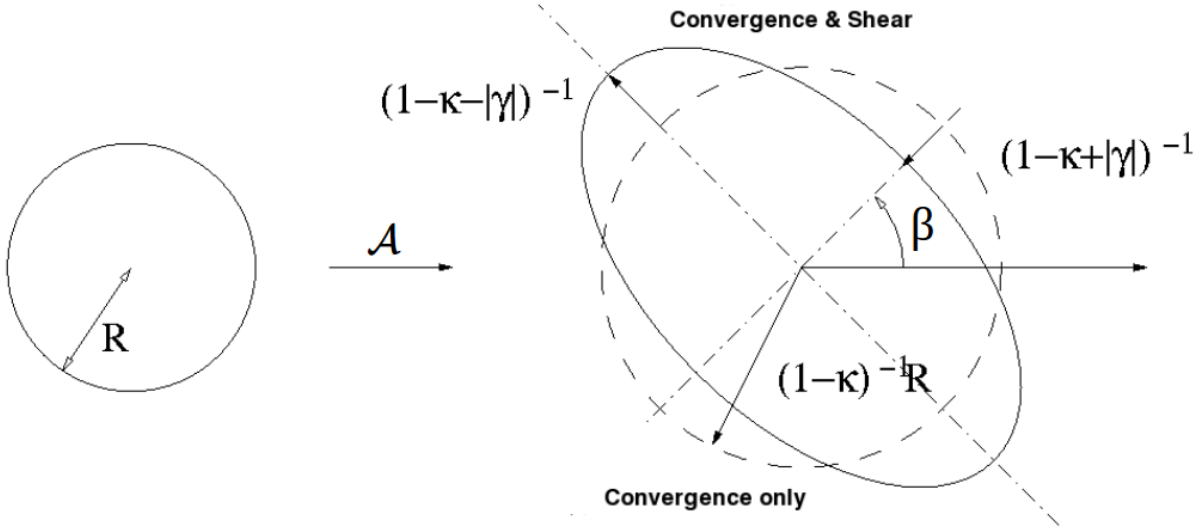

Figure 5.2: Lensing deformations on a circular source by the amplification matrix $\mathcal{A}$. The convergence, κ, enlarges the source isotropically, by a factor of $(1-\kappa)^{-1}$. The shear, γ, will distort the source along the amplification axis which forms an angle β with the horizontal. Source: adapted from M. Jauzac, PhD Thesis.

an arbitrary reference frame as

$$\mathcal{A}^{-1} = \begin{pmatrix} 1-\kappa-\gamma_1 & -\gamma_2 \\ -\gamma_2 & 1-\kappa+\gamma_1 \end{pmatrix} \tag{5.11}$$

The convergence can be expressed as a function of the lensing potential:

$$\kappa = \frac{\Delta\varphi}{2} = \frac{\Sigma}{\Sigma_{\text{crit}}}, \tag{5.12}$$

where Σ and Σ_{crit} are the surface density and critical lensing surface density respectively, with the latter defined as

$$\Sigma_{\text{crit}} = \frac{c^2}{4\pi G}\frac{D_{\text{OS}}}{D_{\text{OL}}D_{\text{LS}}}. \tag{5.13}$$

Therefore, the convergence, κ, can be physically defined as the line-of-sight surface mass density of the lens, and is another way to quantify the strength of the lens, i.e. whether the lens is sufficiently dense to fracture the wave front of source light in order to produce multiple images (strong lensing regime), or not (weak lensing regime). If the surface density of the lens is critical

or higher, i.e. $\Sigma \geqslant \Sigma_{\rm crit}$, then the lens is considered to be *strong* and sources viewed through this lens are likely to be multiply imaged. A *weak lens* is one for which $\Sigma \ll \Sigma_{\rm crit}$, and thus lensed sources used to trace the lensing mass are singly imaged with small magnification factors. This weak effect also pertains to the outer regions of strong lenses, where background sources are not affected by the high density in the cluster core.

The shear can also be expressed in terms of the lensing potential in the following way:

$$\gamma_1 = \frac{\partial_{yy}\varphi - \partial_{xx}\varphi}{2} \qquad \gamma_2 = \partial_{xy}\varphi = \partial_{yx}\varphi. \tag{5.14}$$

with the shear norm given by

$$\gamma = \frac{\sqrt{(\partial_{yy}\varphi - \partial_{xx}\varphi)^2 + (2\partial_{xy}\varphi)^2}}{2}, \tag{5.15}$$

and the shear direction given by the ratio of the components of the lensing potential,

$$\tan 2\theta_\gamma = \frac{2\partial_{xy}\varphi}{\partial_{yy}\varphi - \partial_{xx}\varphi}. \tag{5.16}$$

Thus the shear direction θ_γ is independent of the distance ratio ε and therefore of the source redshift z_S. The source redshift will only impact the shear magnitude (equation 5.15).

From equation 5.11 it is readily apparent that the amplification matrix is both real and symmetric and can therefore be diagonalized and written in terms of its principal axes:

$$\mathcal{A}^{-1} = \begin{pmatrix} 1-\kappa+\gamma & 0 \\ 0 & 1-\kappa-\gamma \end{pmatrix} = (1-\kappa)\left(\mathcal{I} + \frac{\gamma}{1-\kappa}\mathcal{S}\right). \tag{5.17}$$

where $\mathcal{I}$ is the identity matrix $\mathcal{I} = \begin{pmatrix} 1 & 0 \\ 0 & 1 \end{pmatrix}$ and $\mathcal{S}$ is the reflexion or shear matrix, $\mathcal{S} = \begin{pmatrix} 1 & 0 \\ 0 & -1 \end{pmatrix}$. The above form of the amplification matrix is perhaps a more intuitive indication of how the isotropic and anisotropic deformations relate to the convergence and shear. Equation 5.17 can be rewritten as

$$\mathcal{A}^{-1} = (1-\kappa)\left(\mathcal{I} + g\mathcal{S}\right) \tag{5.18}$$

where $g = \dfrac{\gamma}{1-\kappa}$ is the *reduced shear*, which completely describes the shape deformation. The reduced shear is observable in the strong lensing regime, since $\kappa \sim 1$. In the weak lensing regime, where $\kappa \ll 1$, it can be approximated by the complex shear alone.

5.2.3 Critical and caustic lines

The magnification μ in equation 5.10 can be rewritten in terms of the convergence, κ, and the shear, γ, using equation 5.17:

$$\mu^{-1} = \det\mathcal{A}^{-1} = (1-\kappa)^2 - \gamma^2 = (1-\kappa)^2(1-g^2). \tag{5.19}$$

If either of the principal values of the amplification matrix is zero, the magnification is infinite. The lines of infinite magnification are called *critical lines* and define the locus in the image plane at which images disappear. $\mu = \infty$ implies $g = \pm 1$ and as these solutions cannot exist simultaneously at the same location, the critical lines do not intersect. The corresponding regions in the source plane are called *caustic lines*, which can intersect each other, unlike their image plane counterparts. The caustic lines define the limiting area within which a source will be multiply imaged. In 1D they are called *caustic points*. In general, two critical lines can be identified for a simple mass distribution: an internal critical line where the deformations are radial ($g = +1$), and an external critical line where the distortions are tangential ($g = -1$) (see e.g. Kneib et al., 1993). Figure 5.3 shows different examples of critical and caustic lines for other simple mass distributions. These simple geometries generally break down when more complex mass distributions are considered.

In the most simplistic case of a circularly symmetric mass distribution, the amplification matrix in polar coordinates is

$$\mathcal{A}^{-1} = \begin{pmatrix} 1 - \partial_{rr}\varphi & 0 \\ 0 & 1 - \frac{1}{r}\partial_r\varphi \end{pmatrix}, \tag{5.20}$$

and thus both the critical and caustic lines are circles. In this case the tangential caustic line reduces to a single point when the corresponding critical line solution $r = \partial_r\varphi$ is fed into the lens equation. In the case of a circularly symmetric mass distribution, the projected mass enclosed within a radius r can be written as

$$M(r) = \frac{c^2}{4G}\frac{D_{\rm OS}D_{\rm OL}}{D_{\rm LS}} r\partial_r\varphi(r) = \pi\Sigma_{\rm crit} r\partial_r\varphi(r). \tag{5.21}$$

The tangential critical radius, also referred to as the Einstein radius $\theta_{\rm E}$ defined in §5.1, lies at $r_{\rm ctt} = \partial_r \varphi(r_{\rm ctt})$ and thus the mass within the Einstein radius is

$$M(\theta_{\rm E}) = \pi \Sigma_{\rm crit,E} \theta_{\rm E}^2. \tag{5.22}$$

Here $\Sigma_{\rm crit,E}$ is the mean surface density of the lens within the Einstein radius. §5.1 showed that the Einstein radius is an indicator of the lens power of the deflector. It also depends on the redshift of the source (z_S), the redshift of the lens (z_L), and the underlying cosmology. By varying $\Sigma_{\rm crit,E}$ for a given pair of (z_S, z_L), it can be shown that the most effective lens for a given mass distribution is placed approximately less than half the source redshift. The radial critical line in polar coordinates is defined to be

$$1 = \partial_{rr} \varphi(r) = \partial_r \left(\frac{M(r)}{\pi r \Sigma_{\rm crit}} \right). \tag{5.23}$$

The locus of the radial critical curve thus depends on the gradient of the mass distribution.

From equations 5.22 and 5.23 it can be inferred that (i) given the position of the tangential critical line, and assuming the source and lens redshifts are known precisely, the total mass within a circular aperture can be measured, and (ii) the slope of the mass profile near the centre of the cluster can be constrained by the location of the radial critical curve. Using the above process of linking the mass within a critical line to the area enclosed is a sound approximation considering the mass distribution involved is fairly similar to a circularly symmetric case (Kassiola and Kovner, 1993).

Therefore, when observing galaxies lensed by a galaxy cluster, identifying the particular sizes of the radial and tangential critical lines is a crucial first step towards measuring the cluster mass and its density within the inner regions. For the more general case without circular symmetry, solving for the critical lines cannot be achieved analytically except in a few cases of simple elliptical mass profiles (e.g. Kneib et al., 1993). In the case of a complex lens mass model, critical curve determination requires numerical methods for which there are several techniques (e.g. Jullo et al., 2007; Jullo and Kneib, 2009; Bradač et al., 2009; Oguri, 2010; Merten et al., 2011; Jauzac et al., 2012; Mohammed et al., 2014; Diego et al., 2015a).

5.3 Multiple images

A background galaxy will be multiply imaged if it lies within the caustic curves, and if the lens through which it is observed is dense enough to break the wave front coming from the galaxy into several pieces. The number of multiple images produced is the number of solutions to the lens equation (eqn. 5.6). This can be estimated via catastrophe theory (Zeeman, 1977; Erdl and Schneider, 1993), which stipulates that two additional images are produced per caustic line crossing, and predicts that there will always be an odd number of images for a non-singular mass distribution (Burke, 1981). However not all of these images are readily observable: some may be demagnified or obscured by the presence of a cluster galaxy.

5.3.1 Examples of multiple image configurations

The predicted geometry of multiple images is well prescribed and although critical lines are virtual and thus cannot be directly mapped, the multiple images which straddle them are usually readily identifiable in high resolution images. Simple patterns of images that are easily recognisable are tangential pairs or radial pairs (e.g. Miralda-Escude and Fort, 1993). The radially distorted images are found near radial critical lines, and similarly for images that are tangentially distorted.

In the case of tangentially distorted multiple images, there are two main configurations: *fold* and *cusp*, with the difference based on where the source lies in relation to the tangential caustic line. A fold configuration occurs when, in the source plane, the galaxy lies close to and inside the tangential caustic along one of the edges. This leads to two images placed symmetrically across the tangential critical line, with a third image, demagnified on the opposite side of the critical line. A cusp configuration is similar to that of the fold, however the source now lies close to an asteroid spike of the tangential caustic line. Three images are clustered towards the end of the semi-major axis of the tangential critical curve, sometimes appearing as an almost continuous arc. An example of fold and cusp configurations are shown in panels 10 and 6 of Figure 5.3, respectively.

For sources close to the radial caustic line, the image deformation is radial resulting in *radial*

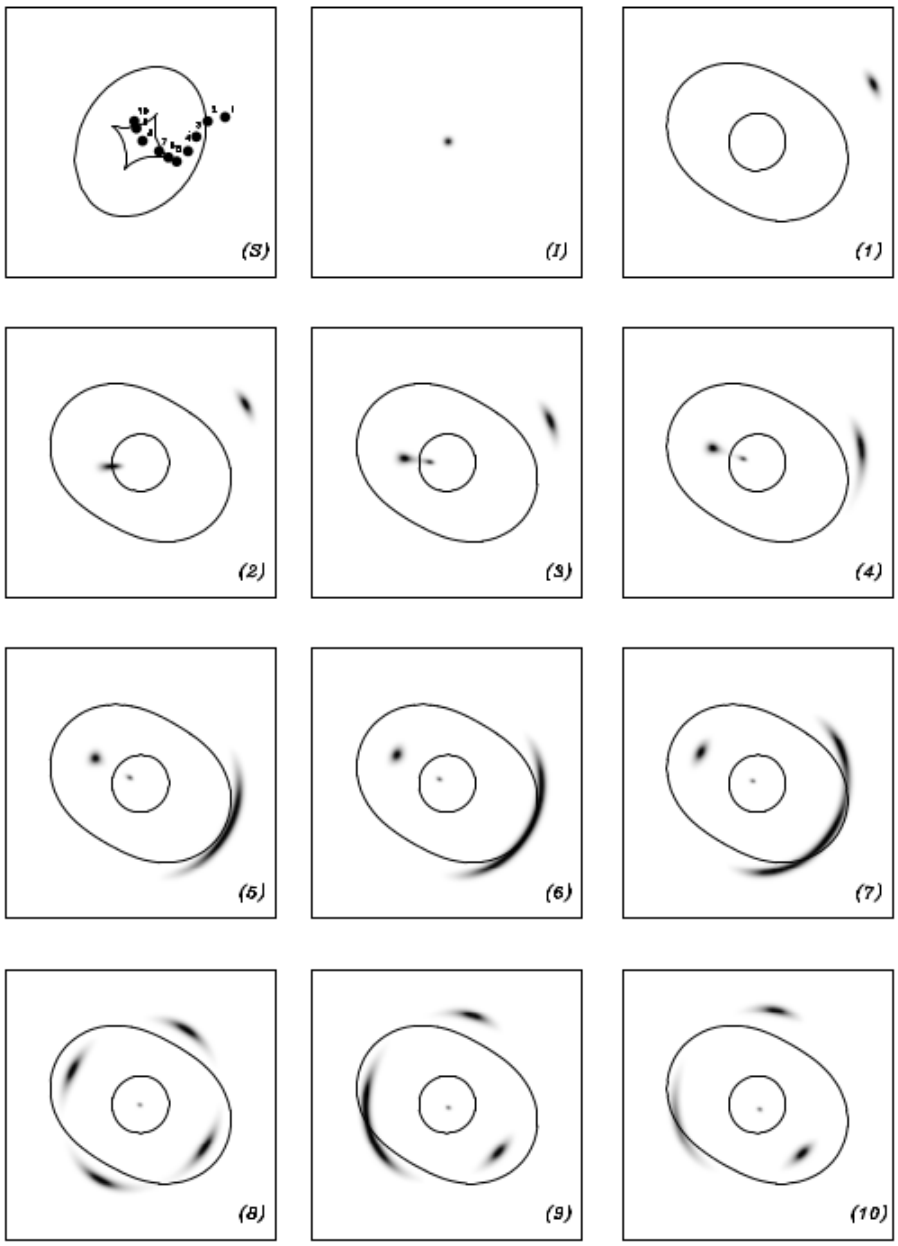

Figure 5.3: Multiple image configurations produced by a simple elliptical mass profile. Panel (S) shows the caustic lines in the source plane and the source image positions 1 to 10 relative to the caustic. Panel (I) shows the image of the source without lensing. Panels (1) to (10) show the resulting lensed images for the various source positions given in (S). Some of these configurations are well-known and are named as follows: (3) radial arc, (6) cusp arc, (8) Einstein cross, (10) fold arc. Source: Kneib and Natarajan (2011).

arcs when two images straddle the radial critical line and almost merge, with the third counter image appearing on the opposite side of the critical line. The configuration of radial multiple images is heavily dependent on the shape of the mass profile at the centre of the lens – the more peaked the profile, the closer the radial image will be to the centre. Thus for singular mass profiles the counter radial image could be demagnified to such an extent it disappears entirely. In this case, the radial configuration is identifiable only as an image pair. An example of a radial arc configuration is shown in panel 3 of Figure 5.3.

The above patterns of fold arcs, cusp arcs and radial arcs should be visible for clusters with one dominant mass clump (e.g. Fort et al., 1992; Mellier et al., 1993; Natarajan et al., 1998; Smith et al., 2001, 2003). Besides the configurations mentioned above, Figure 5.3 shows a range of multiple-image configurations produced by a single elliptical mass distribution. Furthermore, bimodal mass distributions can produce straight arcs (e.g. Pello et al., 1991; Kneib et al., 1994) and triplets (e.g. Kneib et al., 1993; Bézecourt et al., 1999; Limousin et al., 2012). Multiple image systems with higher multiplicities are created when the mass distribution exhibits a very complex structure with several massive core halos (Richard et al., 2014; Johnson et al., 2014; Lam et al., 2014; Jauzac et al., 2014, 2015b; Coe et al., 2015; Diego et al., 2015d). Each additional deforming mass clump typically adds two images to a simple configuration, provided the mass clump is well positioned relative to the central core. The set of seven multiple images of the E/S0 galaxy in Abell 2218 is an impressive example of such a system (Kneib et al., 1996). Other exotic configurations are also possible (see e.g. Cabanac et al., 2007; Bolton et al., 2008; Limousin et al., 2008; Shin and Evans, 2008; Orban de Xivry and Marshall, 2009; Collett and Bacon, 2015).

5.3.2 Multiple image identification

When galaxy clusters act as gravitational lenses, an analysis of the detailed configuration of the multiply-imaged sources can constrain the inner core of the cluster mass distribution. The correct identification of the multiple images represents a mandatory step in order to obtain reliable information on the mass distribution of the cluster. In order to do this, one needs to be able to

identify these multiple images. This can be done via their several distinct properties.

The giant arcs as seen in the cases of Abell 370 (Soucail, 1987) and CL2244-02 (Lynds and Petrosian, 1986) are the traditionally identified sets of multiple images, however an observed arc is not necessarily a result of multiple images from a single source. Some giant arcs are only a single image which has been distorted, and multiple-image arcs may have more than one background source contributing to the arc components (Ellis et al., 1991; Coe et al., 2010). One of the ways to identify the latter case is by the image colours and morphologies. Since lensing affects all wavelengths in the same geometric way, multiple images of the same source can be identified by the similarity of their colours, or by their shared brightness at a specific wavelength. Another useful property of multiple images is symmetry, in particular *mirror symmetry* where a counter image appears as the flipped version of a galaxy image with extremely similar morphology. This is best visible in high-resolution images in which the individual structure of the background galaxies can be resolved. The symmetries of multiple images are related to the parities of the eigenvalues of the amplification matrix. Every time a critical line is crossed, the parity of the image changes, resulting in the image appearing to be a "vertically" or "horizontally" flipped version of the counter image, depending on which side of the parity pair changes (Blandford and Narayan, 1986; Schneider et al., 1992).

The above methods for visually identifying multiply imaged systems are often used to identify multiple image candidates, some of which may be spurious identifications. The potential multiple images can be confirmed or rejected by detailed modelling of the cluster lens. Well calibrated lens models, usually based on a few unambiguous visual system detections, can be used to predict the position of a counter image as well as estimate the redshift of the source being multiply lensed (Kneib et al., 1993, 1996; Jauzac et al., 2014). The larger the number of multiply-imaged systems identified, the more constrained the lens model becomes in the region of those systems.

5.4 Weak lensing

The previous section dealt with the observable results from *strong lensing* visible in the central regions of massive galaxy clusters where the surface mass density is greater than the critical surface mass density of the lens. In the strong lensing regime, the convergence κ is approximately 1. However, outside of this region, background sources still experience a lensing distortion, only to a far lesser extent. In these regions, the lensing potential is not as strong as in the inner core, and thus leads to convergence values $\kappa \ll 1$. Thus the source images are minimally amplified and experience only small shear deformations. These effects are often dominated by the intrinsic ellipticity of the galaxy. This is the *weak lensing* regime as the effect on individual galaxies is so small, a weak lensing signal has to be extracted statistically.

5.4.1 Galaxy shape measurement

In the weak lensing regime one measures the mean ellipticity of faint galaxies in the frame in order to determine the surface mass density of the cluster. There are two main challenges which need to be overcome in order to relate these quantities. The first problem relates to the measurement of the galaxy shapes and is primarily due to instrumental effects. The shape of background galaxies are strongly affected by the point spread function (PSF) of the instrument used. Indeed the PSF size is comparable to the size of this faint and small background population. Moreover the PSF is not circular, nor stable in time and across the field of view. This is due to camera distortions and focus across the image, as well as other factors impacting the telescope itself (in the case of the Hubble Space Telescope, we face the 'breathing' of the telescope due to its orbit around the Earth, and the temperature gradients induced by the presence of the Sun). A second observational hurdle to accurate weak lensing estimates is the effect of crowding whereby the presence of cluster members obscures faint background galaxies. This, coupled with the intrinsic spatial fluctuations in galaxy distributions, will create a bias in the estimation of the variation in number density of faint background galaxies in the frame (Schneider et al., 1992; Sheldon et al., 2004; Leauthaud et al., 2007; Miller et al., 2007; Rhodes et al., 2010; Kneib and Natarajan, 2011; Becker and Kravtsov, 2011; Kacprzak et al., 2012; Refregier et al., 2012;

Hoekstra et al., 2013).

Several algorithms exist to correct for the above effects. Some correct for instrument dependent effects such as the charge transfer efficiency effect observed in Advanced Camera for Survey images from the Hubble Space Telescope (Massey et al., 2010), and other techniques correct for the observational impact of the PSF (e.g. Kaiser et al., 1995; Luppino and Kaiser, 1997; Rhodes et al., 2000; Hoekstra et al., 2000).

The other main challenge in relating the mean ellipticity of the weakly lensed galaxies to the mean surface mass density of the lens is theoretically based and relates to finding an optimal method of reconstructing the mass distribution using a combination of the shear γ or reduced shear g and/or the magnification μ. There are *direct* or *inverse* methods to do this. The former are based on the convolution of γ, the integration of the gradient of g, or parametrically fitting observables directly (Fahlman et al., 1994; Fischer and Tyson, 1997; Clowe et al., 1998; Clowe and Schneider, 2002; Kneib et al., 2003; Hetterscheidt et al., 2005; Hoekstra, 2007; Okabe et al., 2010). The inverse approaches involve the derivation of both the convergence κ and the lensing potential φ, using either maximum likelihood or maximum entropy methods. Examples of these inverse techniques can be found in Kuijken (1999); Bridle et al. (2002); Kitching et al. (2008); and Refregier and Bacon (2003).

5.4.2 Shape deformations to first order: shear

The previous section dealt with problems relating to accurately measuring the shape of background galaxies experiencing weak lensing. Here we consider how to measure this shape to first order, assuming that the contaminating factors have been corrected for. There are higher order effects that can be measured, e.g. flexion (Bacon et al., 2005; Leonard et al., 2006; Okura et al., 2007; Goldberg and Leonard, 2007; Leonard et al., 2007; Leonard and King, 2010; Leonard et al., 2011; Munshi et al., 2011; Cain et al., 2011; Fedeli et al., 2012; Er and Bartelmann, 2013), but these are not discussed here.

To first order, the light distribution of a background galaxy can be approximated as a source with elliptical isophotes. In this manner the shape and size of a galaxy is defined in terms of the

ellipse axis ratio and the area enclosed by a defined boundary. However, since the true shape of a galaxy is often irregular and not well approximated by an ellipse, the moments of the pixelised galaxy surface brightness can be used to define the shape instead.

Assume a weakly lensed image whose surface brightness distribution is described by $I(\theta)$ where $\theta = (\theta_i, \theta_j)$. The centre of the image $\theta^C = (\theta_i^C, \theta_j^C)$ is defined as the first order moment of $I(\theta)$:

$$\theta^C = \frac{\int W(I(\theta))\theta d\theta}{\int W(I(\theta))d\theta}, \tag{5.24}$$

where the window function $W(I)$ serves the purpose of ensuring the integrals are finite in the case of noisy data. Common choices for the weighting function are (i) the Heavyside step function $W(I) = H(I - I_{\rm iso}) = \begin{cases} 1, & I(\theta) > I_{\rm iso} \\ 0, & \text{otherwise} \end{cases}$, where $I_{\rm iso}$ is the minimum isophote of the galaxy detection, and (ii) $W(I) = I \times H(I - I_{\rm iso})$ where the integral is weighted by the light distribution within the detection isophote.

The second order moment matrix, centred on θ^C, is given by

$$M_{ij} = \frac{\int\int W(I(\theta))(\theta_i - \theta_i^C)(\theta_j - \theta_j^C)d\theta_i d\theta_j}{\int\int W(I(\theta))d\theta_i d\theta_j}. \tag{5.25}$$

That M_{ij} encapsulates the information about the galaxy size, axis ratio and orientation is readily apparent when written in terms of its principal axes:

$$M_{ij} = \mathcal{R}_\theta \begin{pmatrix} a^2 & 0 \\ 0 & b^2 \end{pmatrix} \mathcal{R}_{-\theta}. \tag{5.26}$$

Here $\mathcal{R}_\theta$ is the rotation matrix of the position angle θ, and a and b are the major and minor axes respectively. It is possible to define a complex ellipticity $\epsilon = |\epsilon| \mathrm{e}^{2i\theta}$ which encodes both the shape and orientation information. Over the course of lensing studies there have been several different forms for the norm of the complex ellipticity, however the current standard choice is

$$|\epsilon| = \frac{a - b}{a + b} \tag{5.27}$$

as it is a direct estimator of the measurable quantity, that being the reduced shear g. This is easily

shown using the shape deformations shown in Figure 5.2, where the major axis of the lensed source becomes $a = 1/(1 - \kappa - |\gamma|)$, and minor axis becomes $b = 1/(1 - \kappa + |\gamma|)$.

In the weak regime, the amplification matrix doesn't vary significantly across the image (Kochanek, 1990; Miralda-Escude, 1991), a simplification which doesn't hold for strong lensing. Combining this with Etherington's (1933) discovery that gravitational lensing conserves surface brightness, i.e. $I(\theta_I) = I(\theta_S)$, the above definitions can be used to mathematically express the shape deformation of a background galaxy due to lensing.

The lens mapping between the shapes of the source and the image is described by

$$\mathcal{M}^S = \mathcal{A}^{-1}\mathcal{M}^I \left(\mathcal{A}^{-1}\right)^T \tag{5.28}$$

for a singular amplification matrix, or

$$\mathcal{M}^I = \mathcal{A}\mathcal{M}^S\mathcal{A}^T \tag{5.29}$$

for a non-singular amplification matrix $\mathcal{A}^{-1}$. In the above relations, $\mathcal{M}^S$ and $\mathcal{M}^I$ are the moment matrices for the source and the image respectively, and X^T denotes the transpose of matrix X. Thus, for a measured image size of σ_I, the size of the source σ_S is given by

$$\sigma_S^2 = \det\mathcal{M}^S = \det\mathcal{M}^I \left(\det\mathcal{A}^{-1}\right)^2 = \sigma_I^2\mu^{-2}. \tag{5.30}$$

The image size is therefore a factor of the magnification μ larger than that of the source. Similarly, in the region outside of the critical lines, the complex ellipticity maps as

$$\epsilon_S = \frac{\epsilon_I - g}{1 - g\epsilon_I}, \qquad \text{for } |g| < 1 \tag{5.31}$$

between the source and image planes. For the region inside the critical lines, where $|g| > 1$, the source ellipticity is

$$\epsilon_S = \frac{1 - g^*\epsilon_I^*}{\epsilon_I^* - g^*}, \tag{5.32}$$

where * denotes the complex conjugate. In the weak lensing region, i.e. where $|g| \ll 1$, equation 5.31 simplifies to

$$\epsilon_I = \epsilon_S + g. \tag{5.33}$$

Thus in the weak lensing limit the shape of the image is a linear sum of the source shape and the lensing distortion. If the intrinsic shapes of the background galaxies were known before hand, they would be an excellent tracer of the deformations caused by gravitational lensing. However, galaxies exhibit a copious amount of individual shapes and a measurement of the lensing deformation is only obtainable via averaging over a large number of sources. Under the assumption that intrinsic source shapes are randomly oriented, their ensemble average $\langle \epsilon_S \rangle$ is zero, and the weak lensing mapping in equation 5.33 reduces to

$$\langle \epsilon_I \rangle = \langle g \rangle \,. \tag{5.34}$$

Therefore for the above form of the complex ellipticity (eqn. 5.27), when averaged over many sources, the image ellipticities are a direct measurement of the shear γ, as $\kappa \ll 1$. Note that this depends on the complicating factors mentioned in the previous section having been dealt with prior to making image shape measurements.

5.5 Mass modelling technique: LENSTOOL

Constraining the mass of the lens is one of the main applications of gravitational lensing. With regards to galaxy clusters, this requires an accurate model of the mass distribution within the cluster region using observational constraints such as multiple image positions (§5.3) and weak shear measurements (§5.4.2). The more observational constraints there are, the more precise the model will be. In order to obtain a sensible best fit mass model, the number of model parameters must be balanced by the number of available observational constraints.

There are several numerical methods for modelling clusters. These are separated into two main types: parametric and non-parametric. *Parametric* models are the traditional method of investigating strong lensing in clusters as they use a small number of model parameters, necessary when few constraints are available (e.g. Kneib et al., 1996; Natarajan and Kneib, 1997). Here the cluster is modelled by a finite number of mass halos (including both cluster and galaxy scales). Each of them are defined by a finite number of parameters, set by the density profile

chosen to parametrize the density profile of the halos[1]. With the availability of deep imaging, *non-parametric* models have been developed to readily make use of the larger numbers of identifiable constraints (e.g. Saha and Williams, 1997; Diego et al., 2005; Coe et al., 2010; Jullo and Kneib, 2009; Jauzac et al., 2012; Bradač et al., 2006). These methods reconstruct the mass distribution as a regular grid of smaller mass elements and few (or no) external priors are needed to describe the lens profile.

In this section we focus on the parametric version of LENSTOOL, using strong-lensing as observational constraints Jullo et al. (2007)[2]. The LENSTOOL software is the basis for the strong lensing analyses discussed in chapter §6. LENSTOOL has since been extended to include a non-parametric approach using strong-lensing at first (Jullo and Kneib, 2009), and then weak-lensing constraints (Jauzac et al., 2012). The combined strong and weak lensing study of MACSJ0416 in §6.1.2 uses the ehybrid-LENSTOOL, i.e. a combination of a parametric approach in the core to obtain a high-resolution mass distribution and a non-parametric approach in the outskirts to allow for more flexibility. However, the discussion of the non-parametric approach is not within the scope of this thesis.

5.5.1 LENSTOOL model computation: Bayesian MCMC method

Given a lens model and observational data to constrain it, there are various numerical methods to compute the best-fit to the data. LENSTOOL uses a Bayesian Markov Chain Monte Carlo (MCMC) method to optimise the lens model, based on prior knowledge of the probability density function (PDF) (Jullo et al., 2007, J07 hereafter). A Bayesian approach is aptly designed for use in strong lensing modelling, as there are generally few constraints available to improve the model. This method incorporates two levels of inference: parameter space exploration, and model comparison. Here we focus on the former.

§5.5.2 discusses how the model M can be built up into a multi-component and hence multi-

[1] Some of the more common choices are the circular Single Isothermal Sphere (SIS; Binney and Tremaine, 1987), Pseudo Isothermal Elliptical Mass Distribution (PIEMD; Kassiola and Kovner, 1993), and the NFW (Navarro et al., 1997) profiles.

[2] LENSTOOL is publicly available at `https://projets.lam.fr/projects/lenstool/wiki/`.

scale model for the mass distribution, with a set of priors $\vec{\theta}$ for its parameters. In §5.5.3 we introduce observational constraints that are used to optimise the model, referred to as the data, D. The relationship between these two factors is given by Bayes' Theorem, written in terms of PDFs:

$$\mathrm{P}(\vec{\theta}|D,M) = \frac{\mathrm{P}(D|\vec{\theta},M)\mathrm{P}(\vec{\theta}|M)}{\mathrm{P}(D|M)}. \tag{5.35}$$

The *prior*, $\mathrm{P}(\vec{\theta}|M)$, is the probability of the parameters $\vec{\theta}$ given the model, M. $\mathrm{P}(D|\vec{\theta},M)$ is the *likelihood* of the observed data given the input model and its parameters. The *posterior*, $\mathrm{P}(\vec{\theta}|D,M)$, gives the probability of the model parameters, given the data and the model. This will be highest for parameters $\vec{\theta}$ giving the best fit model while simultaneously consistent with the prior PDF, irrespective of the complexity of the model. Finally, the *evidence*, $\mathrm{P}(D|M)$, is the probability that the model would result in the observed data. This incorporates the complexity of M and penalises overly complex models when a simpler one would also fit the data.

MCMC methods use random walks to sample the parameter space, starting with the prior PDF, and converging on a set of best-fit parameters, i.e. the posterior. If the "distance" in parameter space between the prior and the posterior is large, the convergence from prior to posterior is very slow and the program becomes severely computationally expensive. This is usually the case for strong lensing analyses as the data has, by necessity, a high signal-to-noise ratio which leads to a small allowed posterior volume, compared to the full parameter space given by the priors. To address this issue, LENSTOOL uses annealed Markov Chains to progressively converge from prior to posterior PDFs. In this method, the convergence speed is controlled by a new RATE parameter, effectively controlling the size of the random walk steps in the parameter space. A high RATE value makes the model converge much faster, but runs the risk of missing the optimal region of parameter space. A value close to zero slows down the rate of convergence but allows more of the parameter space to be covered, greatly reducing the risk of missing the optimal values. More details on this adjusted method can be found in J07 and references therein.

5.5.2 Model definitions

The lens modelling method of J07 requires a first attempt at a model for the mass distribution of the lens. The model for the lensing potential given in equation 5.7 is initially defined using two sets of components: cluster-scale halos, which trace the overall mass distribution, and galaxy scale halos which trace the mass distribution on a these smaller scales and thus allow the model to take into account galaxy-galaxy lensing effects. N-body simulations have shown that the distribution of subhalo masses inside a cluster halo follows the Schechter function (Shaw et al., 2006) and thus the 2D cluster gravitational potential can be separated as follows (Natarajan and Kneib, 1997):

$$\phi_{\rm tot} = \sum_i \phi_{{\rm cluster},i} + \sum_j \phi_{{\rm subhalo},j}. \tag{5.36}$$

Here the smooth and large cluster-scale halos are given by $\phi_{{\rm cluster},i}$ and the additional subhalos which create minor but non-negligible perturbations are given by $\phi_{{\rm subhalo},j}$. These latter halos are defined as a potential hosting a galaxy. Each set of halos is modelled differently, as discussed below.

5.5.2.1 Cluster-scale halos

The main component of the lens mass model is made up of at least one cluster-scale mass halo to trace the overall/total mass distribution of the cluster. The simplest case is to start from a single cluster-scale halo, and increase the number of halos if the model requires it, i.e. we then look at the different parameter values produced by the model such as the χ^2 (see §5.5.3.2), the evidence (the normalisation of the posterior), and the rms difference between predicted and observed positions of multiple images.

Each halo is parameterized by its sky position (x_c, y_c), projected ellipticity ε_Σ, position angle β, and a set of additional parameters specific to the type of mass profile chosen. The parameters for a Singular Isothermal Sphere (SIS), a Sérsic profile, and a NFW profile are given in J07. Here I will focus on the PIEMD (Pseudo Isothermal Elliptical Mass Distribution) profile, which has

three additional parameters: the halo ellipticity, ε_φ, given by

$$\varepsilon_\varphi = \frac{1 - \sqrt{1 - \varepsilon_\Sigma^2}}{\varepsilon_\Sigma}; \tag{5.37}$$

the halo density distribution of the form

$$\rho(R) = \frac{\rho_0}{(1 + R^2/r_{\rm core}^2)\,(1 + R^2/r_{\rm cut}^2)}, \tag{5.38}$$

where ρ_0 is the central density which depends on the central velocity dispersion σ_0:

$$\rho_0 = \frac{\sigma_0^2}{2\pi G r_{\rm core}^2}; \tag{5.39}$$

Here $r_{\rm core}$ and $r_{\rm cut}$ are the core radius and cut-off radius respectively. The two-dimensional surface density distribution for the PIEMD profile (Limousin et al., 2005) is given by

$$\Sigma(R) = \frac{\sigma_0^2 r_{\rm cut}}{2G(r_{\rm cut} - r_{\rm core})} \left(\frac{1}{\sqrt{r_{\rm core}^2 + R^2}} - \frac{1}{\sqrt{r_{\rm cut}^2 + R^2}} \right). \tag{5.40}$$

Note that the brightest cluster galaxy, called the cD galaxy, can be modelled either as part of a cluster-halo, or as its own subhalo. We usually model it independently of the cluster-scale halos as the centre of mass of a cluster-scale halo is not necessarily the same as the centre of the cD galaxy (Smith et al., 2005).

5.5.2.2 Galaxy-scale halos

In addition to the effect caused by the main cluster-scale halos, smaller lensing perturbations are introduced by cluster galaxies themselves (galaxy-galaxy lensing effect). These small-scale perturbers are thus modelled using galaxy-scale halos, and are essential to reproduce the observed patterns of multiple images (Kneib et al., 1996). However, so as not to over-complicate a lensing model, the optimal number of subhalos needs to be quantified. J07 use the following criteria for inclusion of a subhalo:

- First, the strong lensing deviation angle α (as per equation 5.5) is measured and compared to the spatial resolution δ of the observation (for the HST, $\delta \sim 0.1''$). If the deflection angle is significantly increased at the position of the subhalo galaxy, that subhalo is included.

- For a cluster member, a subhalo is included if its Einstein radius, defined in equation 5.4, satisfies $\theta_{\rm E} > \delta/\mu$, where μ is the magnification at the position of the member; otherwise the lensing contribution of the cluster galaxy is regarded as negligible and ignored.

- Non-cluster members are treated differently according to their position in projection relative to the strong lensing (SL) region:

  outside SL region: a subhalo is included at the cluster redshift if $\theta_{\rm E} > \delta/\mu$, by rescaling its mass so its global lensing effect is preserved.

  inside SL region: if its lensing effect is detectable, then the subhalo is included using a multi-plane lensing technique which takes into account gravitational field variations between the lens and the source, and the lens and observer (not covered here, but see e.g. Schneider, 2014, and references therein).

Once the set of subhalos to include in the model has been identified, certain assumptions need to be made in order to ensure the number of subhalo parameters is comparable with the number of available constraints. First, the subhalo position, ellipticity, and orientation are matched to their luminous counterparts. This assumption is based on the strong correlation between the light and mass profiles of elliptical galaxies in the field, observed by Koopmans et al. (2006). Secondly, the number of subhalo parameters can be reduced by enforcing exact scaling relations between the luminosity of the associated galaxy and the subhalo mass. For PIEMD potentials, the subhalo properties are related to those of the galaxy at the cluster redshift (denoted by *) by the following:

$$\sigma_0 = \sigma_0^* \left(\frac{L}{L^*}\right)^{1/4} \quad ; \quad r_{\rm core} = r_{\rm core}^* \left(\frac{L}{L^*}\right)^{1/2} \quad ; \quad r_{\rm cut} = r_{\rm cut}^* \left(\frac{L}{L^*}\right)^{\eta}. \tag{5.41}$$

The total mass of the subhalo can thus be defined in terms of the properties of the associated galaxy:

$$M = \frac{\pi}{G}\sigma_0^{*2} r_{\rm cut}^* \frac{L}{L^*}^{1/2+\eta}. \tag{5.42}$$

The scaling of the velocity dispersion with total luminosity agrees with the Tully-Fisher relation for spiral galaxies, and the Faber-Jackson relation for ellipticals. The scaling for $r_{\rm cut}$ is less

constrained. For example, with $\eta = 0.5$, $r_{\rm cut}$ has a constant mass-to-light ratio, making it independent of the galaxy luminosity. However with $\eta = 0.8$, the mass-to-light ratio scales as $L^{0.3}$, which is similar to the scaling of the fundamental plane (Jørgensen et al., 1996; Natarajan and Kneib, 1997; Halkola et al., 2006).

5.5.3 Model constraints

With the model now defined by a combination of cluster- and galaxy-scale halos, it can be constrained with a variety of observational measurements. In addition to priors on the location of critical lines and the weak shear signal (Jullo et al., 2007), the most powerful set of constraints on a lensing model is the identification of multiply-imaged systems, the correct identification of which is an *iterative* process and strongly interdependent on the mass profile determination.

5.5.3.1 Multiple images

Multiple images are a consequence of the wave front of light from a background source being fractured into several parts as it passes through a high density region (the lens), in our case a massive galaxy cluster. The size and shape of the lens, and the redshift of the background source, will determine the observable properties of the multiple images. These are position, ellipticity, and orientation, and are discussed in §5.3. A precise measurement of the multiple image positions and source redshift imposes strong constraints on the lens model.

In addition to the positions of multiple images, tighter constraints can be included if several bright components can be identified in one image and their counterparts identified in the other images of the system.

The process of multiple image identification and model making is codependent and several iterations are needed before a precise lens model is achieved. The initial mass model is constrained by using the most obvious and unambiguous multiple images such as fold, cusp, or radial arcs (see §5.3.1 and Figure 5.3 for these and other example configurations). Perturbations caused by galaxy-scale subhalos can then be considered and added to the model. Although these subhalos rarely create their own multiple images, they will affect the observed positions of multiple im-

ages created by the core lens. In extreme cases galaxy-scale halos can also increase the number of multiple images of a source, although this is very rare.

With an updated model, other multiple image candidates can be confirmed or rejected. The confirmed systems can in turn further constrain the lens model. This process is repeated until the model converges, or no new multiply-imaged systems are identified. Note that the model is also used to predict multiple images before they are observationally confirmed.

The viability of multiple image candidates can be constrained by their colours, fluxes and redshifts (if known). However the application of these properties is not always straightforward. For example, the colour of an image can be contaminated by a nearby galaxy, making it redder than its counter images, or an incorrect redshift prior could bias the model by forcing the Bayesian posterior into an incorrectly refined parameter space. Spectroscopic redshifts are the best inputs, but such measurements are rare, and also usually known for only one or two of the multiples within the same system. Photometric redshifts can be adequate, provided they are accurate enough. If computational time is not a concern, the source redshift can be set as a free parameter, giving the model more freedom. Coupled with the other observational constraints, this may lead to a more accurate redshift estimate for the multiple image system, and an independent way to check measured redshifts.

5.5.3.2 Multiple image likelihood

The constraints from the multiple images are input to the optimisation of the lens model as part of the likelihood. The multiple images' likelihood is the probability of the observed positions, D or $x_{\rm obs}$, given the positions predicted by the model, $x(\theta)$. The general definition of the likelihood function can be applied under the assumption that the uncertainties on the measured image positions are Gaussian and uncorrelated between images. The likelihood is therefore

$$\mathcal{L} = \mathrm{P}(D|x(\theta)) = \prod_{i=1}^{N} \left[\exp^{-\chi_i^2/2} / \prod_j \sigma_{ij}\sqrt{2\pi} \right]. \tag{5.43}$$

with the contribution to the overall χ^2 from multiply-imaged system i given by

$$\chi_i^2 = \sum_{j=1}^{n_i} \frac{\left(x_{\rm obs}^j - x^j(\theta)\right)^2}{\sigma_{ij}}. \tag{5.44}$$

Here N is the total number of sources for which multiple images are detected, n_i is the number of multiple images of the i-th source, and σ_{ij} is the uncertainty of the measured position of image j of source i. In this method, many models have to be tested and rejected before the Bayesian sampler (see above) focuses on the region of best-fit parameters.

An important aspect of the χ^2 calculation is how to match the predicted and observed images one at a time. LENSTOOL uses a simplex method algorithm (Press et al., 1986) of image transport (Schneider et al., 1992) that evades the matching problems experienced by techniques for finding the roots of the lens equation. In this method the observed image and predicted image is coupled throughout the iterative improvement of the predicted position and the χ^2 is simple to calculate. However, this method fails when a model produces opposing multiple image configurations (e.g. a tangential instead of radial system), and that model is rejected. This situation often occurs when the model is relatively unconstrained and the rejections significantly retard the speed of the model convergence.

This issue can be circumvented by computing the χ^2 in the source plane rather than the image plane. This equates to finding the difference between the source position of an observed image, $x_S(\theta)$, and the barycentre position of all the n_i source positions, $\langle x_S(\theta)\rangle$. The χ^2 in the source plane is therefore given by

$$\chi^2_{S_i} = \sum_{j=1}^{n_i} \frac{\left(x^j_S(\theta) - \left\langle x^j_S(\theta)\right\rangle\right)^2}{\mu_j^{-2}\sigma^2_{ij}}, \tag{5.45}$$

where μ_j is the magnification for image j. In this form, it is unnecessary to solve the lens equation, speeding up the computation of χ^2.

The Bayesian MCMC method implemented in LENSTOOL (see §5.5.1) incorporates both the image plane and source plane optimization to calculate χ^2. To achieve the best balance between computation time and accurate refinement of the model, the best-fit region is narrowed using the source plane method, and then the image plane method is invoked to refine the models.

CHAPTER 6

GRAVITATIONAL LENSING WITH THE HUBBLE FRONTIER FIELDS PROGRAM

Gravitational lensing is an exceptionally effective tool for probing the dark matter distribution within massive clusters. On the cluster scale, it is a probe of the deep universe as massive clusters act as "cosmic telescopes", magnifying undetectable high-redshift galaxies into the observable frame.

Successful strong lensing cluster studies rely on high quality imaging in which several multiple images can be located. The superior resolution and multi-colour images from the Hubble Space Telescope (HST) make it an ideal telescope for strong lensing analysis. In 2013, the Space Telescope Science Institute (STScI) started the Hubble Frontier Fields[1] (HFF) program, the aim of which is to exploit the gravitational magnification by massive clusters to study the distant universe to unparalleled depth. Six massive galaxy clusters were selected for the program, each observed for 140 orbits spread over 7 passbands, covering the optical up to the near-infrared, the latter wavelength coverage being mandatory to identify high-redshift objects. All six targets have

[1] http://www.stsci.edu/hst/campaigns/frontier-fields/

mass models derived from pre-HFF data which are publicly available[2]. This pre-HFF mass mapping initiative allows the high-redshift community, which includes non-lensing experts, access to lensing mass models to study the high redshift universe.

In this section we present the results obtained by strong lensing analysis of two HFF clusters as part of the CATS collaboration, carried out with the LENSTOOL software. Both clusters were discovered in the MAssive Cluster Survey (MACS; Ebeling et al., 2010). The work detailed below has led to three peer-reviewed papers (Jauzac et al., 2014, 2015a,c) and a press release by the European Space Agency[3]. My contribution to these papers was the identification and verification of multiple image systems for the strong lensing analysis.

6.1 MACSJ0416.1-2403

MACSJ0416.1-2403 (z=0.397, hereafter MACSJ0416) was first observed by HST with WFPC2 in 2007 as part of a SNAPshot program (ObsID: GO-11103, PI: Ebeling). These observations showed MACSJ0416 to have a large Einstein radius and was hence selected as one of the "high magnification" clusters for the Cluster Lensing And Supernova survey with Hubble (CLASH; Postman et al., 2012). The CLASH data consisted of one orbit per band over 16 passbands covering the UV to the near infrared. The first strong lensing mass model of this cluster was published by Zitrin et al. (2013). The pre-HFF mass mapping initiative led to the revision of this model by the 6 lensing teams involved in the program, some of them combining both strong and weak lensing constraints (Richard et al., 2014; Johnson et al., 2014; Coe et al., 2015).

As part of the HFF program, MACSJ0416 was observed with the *Advanced Camera for Survey* (ACS) between 5th of January and the 9th of February 2014 in three passbands, namely F435W, F606W, F814W with observing times of 20, 12, and 48 orbits in these bands, respectively. HFF observations with the *Wide Field Camera 3* (WFC3) over the remaining four HFF passbands (observed from July to September 2014) were not yet taken at the time of this work. Basic data reduction steps were followed using HSTCAL using the most recent HST calibration

[2] https://archive.stsci.edu/prepds/frontier/lensmodels/

[3] http://www.spacetelescope.org/news/heic1416/

files. For each passband, all orbit images were combined, resulting in a single image for each band. The pixel scale of these images is 0.03″. In the following we discuss the HFF lensing analysis of MACSJ0416 (Jauzac et al., 2014, 2015a), focusing on the multiple image identification and strong lensing (SL) mass modelling.

6.1.1 Strong lensing analysis

6.1.1.1 The pre-HFF mass model

The mass model consists of large-scale dark matter halos, the individual masses of which are greater than the mass of a typical galaxy group ($\sim 10^{14} M_{\odot}$ within 50″), and smaller galaxy scale dark matter halos which account for extra distortions due to individual cluster members. A similar approach to that outlined in §5.5 was followed whereby all mass components are modelled by dual Pseudo Isothermal Elliptical Mass Distributions (dPIEMDs; Limousin et al., 2007; Elíasdóttir et al., 2007) which are parameterized by a velocity distribution σ_0, a core radius $r_{\rm core}$, and a cut-off or scale radius $r_{\rm cut}$.

The parameters for the galaxy-scale halos are set to those of their associated light distribution (Kneib et al., 1996; Limousin et al., 2007; Richard et al., 2010). The dynamical dPIEMD parameters σ and $r_{\rm cut}$ are then related to the observed luminosity of the galaxy by imposing (without scatter) the scaling relations given in equation 5.41. In order to account for the effect of tidal stripping of galactic dark matter halos, priors on the dynamical parameters are set at $100\ \mathrm{km\ s^{-1}} < \sigma_0 < 250\ \mathrm{km\ s^{-1}}$, and $r_{\rm cut} < 70$ kpc (Limousin et al., 2007; Natarajan et al., 2009; Wetzel and White, 2010).

The first strong lensing analysis of MACSJ0416 (Zitrin et al., 2013) discovered 23 lensed sources in the redshift range $0.7 < z < 6$, resulting in 70 multiply lensed images. However only 13 of the most securely identified systems (34 multiple images) were chosen to optimise the pre-HFF mass models. This number was extended to 47 multiple images from 17 sources by evolving the model over several iterations (Richard et al., 2014; Johnson et al., 2014; Coe et al., 2015). Nine of these sources had spectroscopic confirmations. The above model was calibrated with the Richard et al. (2014) set of multiple images to provide pre-HFF mass models

of MACSJ0416, to be delivered to the community prior to the start of the HFF observations in October 2013.

6.1.1.2 Multiple images

As the HFF infrared bands had yet to be observed at the time of this analysis, the search for multiply-imaged galaxies was carried out using only the three-band optical data. These images had a magnitude limit of mag_{AB} = 29, which revealed a large number of faint galaxies in the field. Before beginning the search for multiple images, the gravitational deflection field from the image to source planes due to the cluster lens is computed on a grid with a spacing of $0.2''$ per pixel. This source to image transformation scales with redshift via the distance ratio $\frac{D_{\rm LS}}{D_{\rm OS}}$ and thus only needs to be calculated once. Since the lowest frequency band for which data was available at the time of this work was the ACS F814W filter, we had less sensitivity to high-redshift systems which are brightest in the infrared filters. We therefore restricted the area within which to search for lensed galaxies to the area enclosed by the $z = 7$ critical line.

A thorough inspection of all faint galaxies in this region was carried out, as well as a search for sensible potential counter images. Starting from the pre-HFF set of 47 multiple images, likely multiple image systems were added and tested against the predictions with LENSTOOL. Once a new set of secure identifications was obtained, the model was updated and used to predict the positions of more counter-images for multiple image candidates. After several iterations of this process, a **total of 194 multiple images stemming from 68 background sources** were identified, making it the largest number of multiple images found for a single cluster lens. Figure 6.1 shows a 3-colour image of the core of MACSJ0416 with the multiple image detections superimposed. Systems securely classified as multiple images are denoted by cyan circles, with the less certain multiple image candidates shown in magenta (45 images). The positions of all multiple image systems are provided in Table C.1. The image identification is in the form {source no.}.{component}, i.e. the third image belonging to the second system has the ID 2.3. Fourteen systems consist of an obvious pair, with the third counter image being less certain often due to minor differences in colour or brightness between counter images (see §5.3.2), or a difference

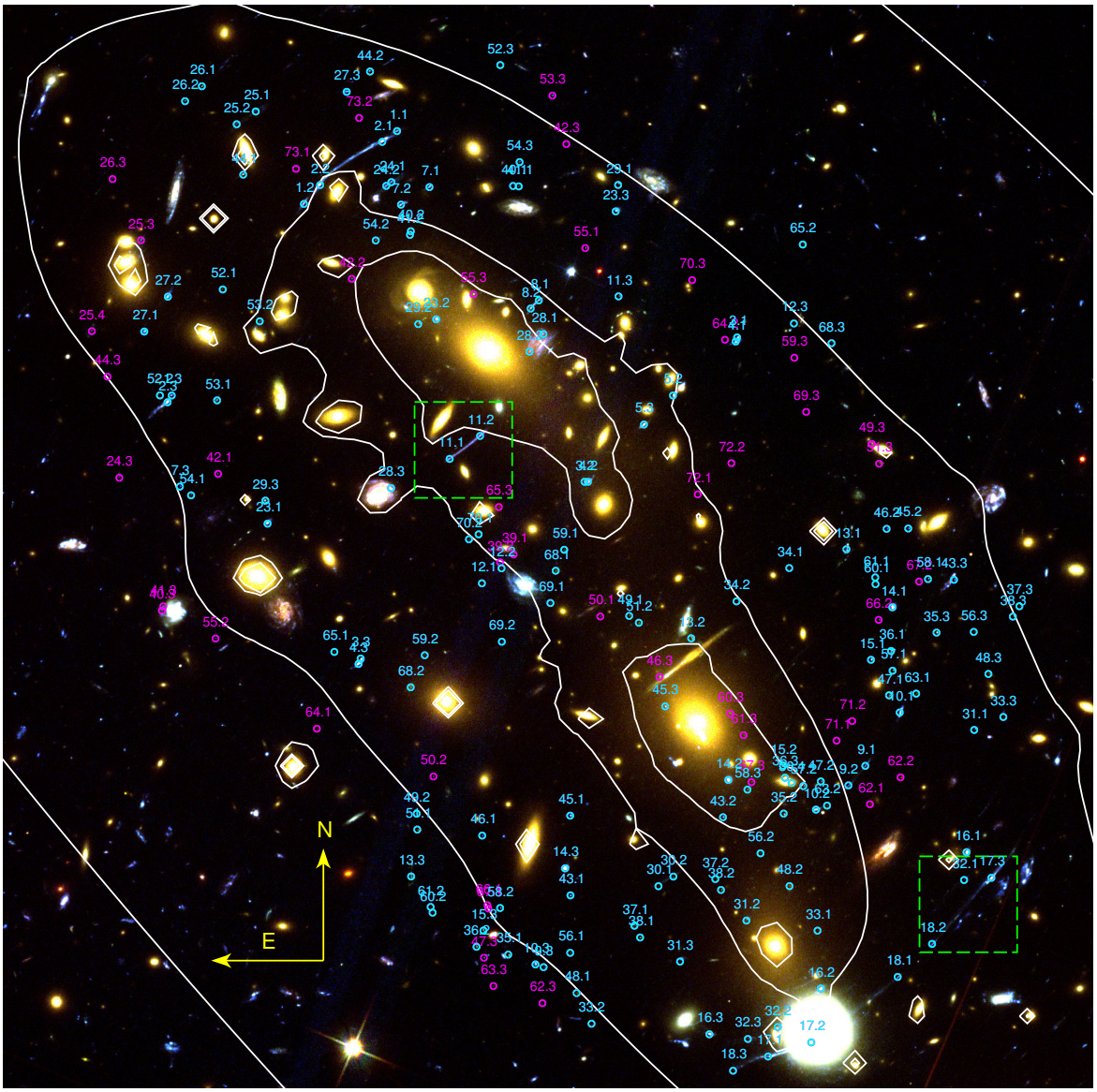

Figure 6.1: Composite F435W, F606W, and F814W HST/ACS image of the core of MACSJ0416 showing all multiple images. Secure identifications which were used to optimise the HFF mass model are shown by cyan circles (149 images). Magenta squares indicate the multiple image candidates (45 images). The best-fit mass model mass contours are superimposed in white. The green dashed boxes indicate the regions shown in Figure 6.2. Source: Adapted from Jauzac et al. (2014).

between observed and predicted position.

MACSJ0416 is host to several lensing arcs and arc-like features. One of the challenges hindering the correct identification of multiple image systems is the blending of several images

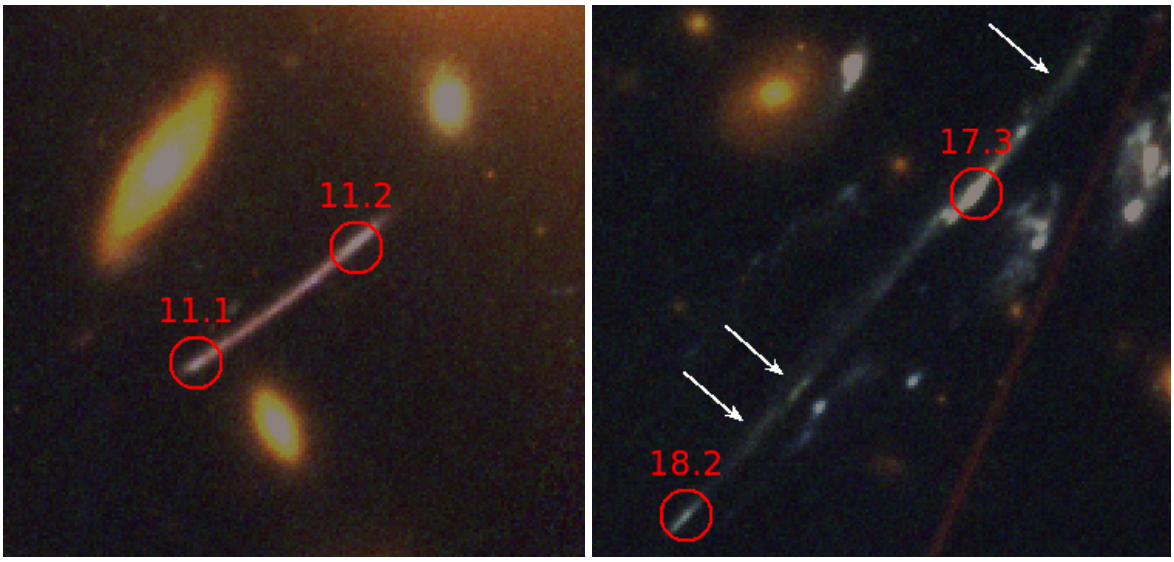

Figure 6.2: Composite (F435W, F606W, F814W) HST image zoomed in on arc-like features in MACSJ0416. *Left:* Typical lensing arc created by the blending of two multiple images of the same source, in this case system 11. The similar colours of images 1 and 2 are a good indication that they belong to the same source. *Right:* This arc-like feature is in fact made up of images from two securely identified systems: 17 (third image) and 18 (second image). Further visual inspection of the arc shows that it is also comprised of several other unidentified images indicated by the white arrows. Colour differences between different sections of an arc can assist in separating the features into images from different systems.

into the same arc. In some cases the arc is the result of lensing a single system, an example of which is shown in the left panel of Figure 6.2. The first and second images of multiply-lensed system 11 are almost blended together into one continuous arc. In this case the galaxy being lensed is close to the caustic at its redshift, and the critical line at the source redshift will lie between the two images, equidistant from each. The position of the critical line is one way to estimate the redshift of the source, in this case $z_{11} \approx 1.1$. Other cases exist where the observed arc is actually composed of several images from different systems and it is merely coincidental that they form an arc-like feature in the image plane. With the right compromise between brightness and contrast of all the filters, the arc can be visually broken up into several parts by variations in brightness, colour, or a combination of the two. An example of this is shown in the right panel of Figure 6.2. The brightest image belongs to system 17 and the blue image at the end of the arc belongs to system 18. If the filters are not adjusted correctly, these

two images may appear very similar. A well-calibrated model should be able to reject the case when these two positions are assumed to be part of the same system. Looking closer at this arc, note that it is made up of at least three other images indicated by the white arrows. These have not as yet been identified as multiple images.

6.1.1.3 Lens modelling

Although 194 images were identified at the time of this analysis, corresponding to 68 background galaxies, some of these identifications are less certain and, in terms of constraining the HFF mass model, are considered multiple image candidates and candidate systems. Thus only fully secure identifications are used in the lens mass modelling, amounting to 57 systems lensed over 149 images, still the largest number achieved in lensing studies to date. A system is considered secure if: (i) there is no observable colour difference between the counter images, (ii) in the case of resolved images, the counter images have morphological similarities, and (iii) the set of images are in a sensible geometric configuration (see §5.3.1). Although there has been a three-fold increase in the number of multiple images compared to the pre-HFF set from Richard et al. (2014), the new images are not in a significantly different region of the cluster and therefore the improved mass model discussed below doesn't radially extend far past the pre-HFF model. However, the vast increase in numbers does significantly improve the precision of the lens model of the cluster inner core.

Initial HST images showed a bimodality in the cluster core, which may indicate a merging state. X-ray observations of MACSJ0416 confirmed this to be a merging cluster, with a bimodal X-ray surface brightness profile (Mann and Ebeling, 2012). The light distribution exhibits similar characteristics: it is elongated along the NE/SW direction and hosts two cD-type galaxies. It is therefore sensible to initialise the mass model with two cluster-scale dark matter halos, each centred on one of the cD galaxies. The centres of the halos are allowed to vary within $20''$ of the corresponding galaxy light peak (see §5.5.2.1). Priors on the other PIEMD parameters are set as follows:

- halo ellipticity: $\epsilon = \dfrac{a^2 - b^2}{a^2 + b^2} < 0.7$,

- core radius: $1'' < r_{\rm core} < 30''$,
- velocity dispersion: 600 km/s $< \sigma <$ 3000 km/s, and
- cut-off radius (strong lensing analysis): $r_{\rm cut}$ = 1000 kpc.

We fix the cut-off radius to 1 Mpc for the strong lensing analysis, as strong lensing alone doesn't probe the mass distribution outside the multiple image region. Added to these large scale halos are 98 galaxy-scale halos to incorporate the lensing perturbations by cluster members. As per the recipe presented in §5.5.2.2, the parameters of these subhalos are set to those of the associated galaxy. Using the secure multiple images, the free model parameters are optimised using LENSTOOL.

Although the large number of multiple images is an impressive achievement showing the power of deep HST imaging, it also presents a technical challenge for the model optimisation in the image plane. In §5.5.1, the RATE parameter was introduced for an annealed MCMC method which controlled the speed at which the MCMC process converged. The usual choice in LENSTOOL is RATE = 0.1. However, the vast increase in multiple images, and therefore model constraints, causes a large increase in computational time required for convergence, even with the annealed method. A value of 0.4 was chosen to combat this issue, although this meant that less of the multi-dimensional parameter space was sampled, increasing the risk of missing the best-fit region.

The final best-fit model in the image plane is extremely successful in predicting image positions (see §5.5.1), with a positional RMS, the difference between observed and predicted positions of the images, of 0.68″. Putting this level of precision into perspective, Abell 1689 had the previous best positional RMS errors of 3.2″ (Broadhurst et al., 2005), 2.7″ (Halkola et al., 2006), and 2.87″ (Limousin et al., 2007). Although the pre-HFF results for MACSJ0416 have lower RMS values than those for A1689, they're still at least a factor of two higher than our HFF results (1.37″ to 1.89″; Zitrin et al., 2013). The best-fit parameters for the HFF mass model are provided in Table 6.1.

To check the results of the best-fit image plane mass model, a source plane optimisation is run with the usual RATE parameter of 0.1. This checks the robustness of the model when more of the

Table 6.1: Best-fit PIEMD parameters for the two cluster-scale dark matter halos in the MACSJ0416 HFF mass model. All errors are the 1σ uncertainties. Parameters in brackets are not optimised. The reference magnitude for scaling relations is $mag_{\rm F814W}$ = 19.8. Masses are quoted within an aperture of 20″ (∼100 kpc). [a] With respect to $\alpha = 64.0381013, \delta = -24.0674860$.

	Clump 1	Clump 2	L* elliptical galaxy
ΔRA (arcsec)[a]	-4.5$^{+0.7}_{-0.6}$	24.5$^{+0.5}_{-0.4}$	–
ΔDEC (arcsec)[a]	1.5$^{+0.5}_{-0.6}$	-44.5$^{+0.6}_{-0.8}$	–
ε	0.7 ± 0.02	0.70 ± 0.02	–
θ (degrees)	58.0$^{+0.7}_{-1.2}$	37.4 ± 0.4	–
$r_{\rm core}$ (kpc)	77.8$^{+4.1}_{-4.6}$	103.3 ± 4.7	[0.15]
$r_{\rm cut}$ (kpc)	[1000]	[1000]	29.5$^{+7.4}_{-4.3}$
σ (km s^{-1})	779$^{+22}_{-20}$	955$^{+17}_{-22}$	147.9 ± 6.2
$M(10^{13}M_{\odot})$	6.02 ± 0.09	6.12 ± 0.09	–

parameter space is explored, as well as enabling a redshift estimation for all 68 multiply-lensed systems/candidates. The source plane results are fully consistent with those of the image plane. The redshift estimates for each system (other than those that are spectroscopically confirmed) are listed in Table C.1. The 68 sources lie in an estimated redshift range of 1.0 to 5.9. The lack of near-infrared passbands at the time of the analysis did not allow us to investigate higher redshift lensed objects, as they will only be visible in ACS/F814W and the WFC3 bands (see Atek et al., 2014, 2015b,a) following the drop-out technique.

The assumption of bimodality that was the starting point of the mass model structure is tested by adding a large-scale halo for the third brightest cluster member and re-running the mass model. The resultant best-fit model gives a positional RMS difference of 0.86″, 20% higher than in the original best-fit model. The increase is interpreted as a third large-scale mode being unnecessary and in fact unsupported by the current observational constraints.

Finally, to determine a strong lensing mass for MACSJ0416, the mass map produced by the best-fit model is integrated in annuli centred on some chosen coordinates. In this case the centre was chosen to be $\alpha = 64.0364, \delta = -24.0718$, such that all multiple images are encompassed by a 60″-radius circle centred on this point. The 2D projected mass within this aperture is $M(<$

$320h^{-1}\mathrm{kpc}) = (3.26 \pm 0.03) \times 10^{14} M_{\odot}$ and the mass within a 200 kpc radius is $M(< 200\mathrm{kpc}) = (1.60 \pm 0.01) \times 10^{14} M_{\odot}$. These results show that the deep HFF images are indeed producing high-precision mass estimates of cluster lenses.

6.1.2 Combined multi-wavelength results

The bulk of the work done on MACSJ0416 for this thesis is on the strong lensing analysis of the cluster core, and in particular the identification of multiple images. A combined weak- and strong-lensing analysis has been conducted, using the results from the previous section, and combined with optical and X-ray data to constrain the geometry and history of the merger occurring in this cluster (Jauzac et al., 2015a). For clarity and completeness the results of this analysis are summarised below.

6.1.2.1 Combined weak- and strong-lensing analysis

The weak lensing constraints are based on shape measurements in the HFF ACS/F814W band image. We use a similar method for identifying cluster members and foreground objects as Jauzac et al. (2012). These unlensed sources contaminate the observed shear measurement and thus reduce the significance of all parameters derived from it. By using CLASH photometry from HST images in 16 passbands, as well as colour-colour diagrams from the three HFF ACS images, we remove 88% of the contaminating sources. The shape measurements are carried out using an adaptation of the RRG method of Rhodes et al. (2000), which measures the size and ellipticity of all galaxies in the field after interfering sources are removed. The final weak-lensing catalogue comprises 714 background galaxies, corresponding to a density of $\sim$ 100 galaxies per square arcminute. This is almost double the weakly-lensed galaxy density of the pre-HFF analysis (Richard et al., 2014). The increase is not as large as for the strong lensing multiple images (factor of 4) since the deeper HFF images reveal more contaminants, for example more blue dwarf cluster members, to the weak lensing signal.

To incorporate the weak lensing constraints into the lens model discussed in §6.1.1.3, we add a grid-based model using Radial Basis Functions (RBFs) to trace the mass distribution outside

the inner core of the cluster. The updated model therefore combines a parametric approach in the cluster core to provide high resolution, with a non-parametric approach in the cluster outskirts to allow for more flexibility in this region. The model is composed of two cluster-scale halos (C1 and C2) and 146 galaxy-scale halos, covering the entire ACS field-of-view. Each RBF's radial profile is modelled with a PIEMD potential (Elíasdóttir et al., 2009), with only the amplitudes allowed to vary. Following Jullo and Kneib (2009), core and cut radii are set to the distance between a RBF and its closest neighbour, and triple the core radius, respectively. Further constraints on the best-fit model are provided by the CLASH photometry which provided a photometric redshift for 236 of the galaxies in the weak lensing catalogue.

The reconstructed mass distribution for MACSJ0416 using both strong- and weak-lensing constraints is shown by white contours in Figure 6.3. The surface mass distribution is bimodal and elongated in the NE-SW direction, with little substructure away from the major axis. The updated mass distribution is more elliptical than that obtained in the strong lensing-only analysis, which implies that the strong lensing model under-predicted the mass density as well as the shear in the outer regions of the cluster. The global cluster centre is defined to be the same as in the strong lensing analysis: $\alpha = 64.0364$ deg, $\delta = -24.0718$ deg, marked by a yellow cross in Figure 6.3. The combined weak- and strong- lensing analysis enables a mass measurement out to 950 kpc, $M(R < 950 \text{ kpc}) = (1.15 \pm 0.07) \times 10^{15} h_{70}^{-1} M_{\odot}$. When comparing against the strong lensing-only mass of $M_{SL}(R < 320 \text{ kpc}) = (3.26 \pm 0.03) \times 10^{14} h_{70}^{-1} M_{\odot}$, the combined lensing analysis agrees with the values but achieves a lower precision: $M_{WL+SL}(R < 320 \text{ kpc}) = (3.15 \pm 0.13) \times 10^{14} h_{70}^{-1} M_{\odot}$. The joint analysis value is less precise as weak lensing constraints are already relevant at this distance from the cluster centre.

The joint weak- and strong-lensing mass reconstruction reveals two new substructures in the outskirts of the cluster, labelled S1 and S2 in orange in Figure 6.3. These structures are detected at high significance (7.5σ and 7.3σ, respectively), with one of them seemingly linked to the cluster itself. Their projected masses (estimated within $\sim$ 100 kpc) are typical of galaxy groups: $M_{S1} = (4.22 \pm 0.56) \times 10^{13} h_{70}^{-1} M_{\odot}$ and $M_{S2} = (1.50 \pm 0.20) \times 10^{13} h_{70}^{-1} M_{\odot}$, respectively. Although there is no obvious indication that S2 is a galaxy group, S1 coincides with an overdensity in the cluster light distribution, shown as yellow contours in the figure.

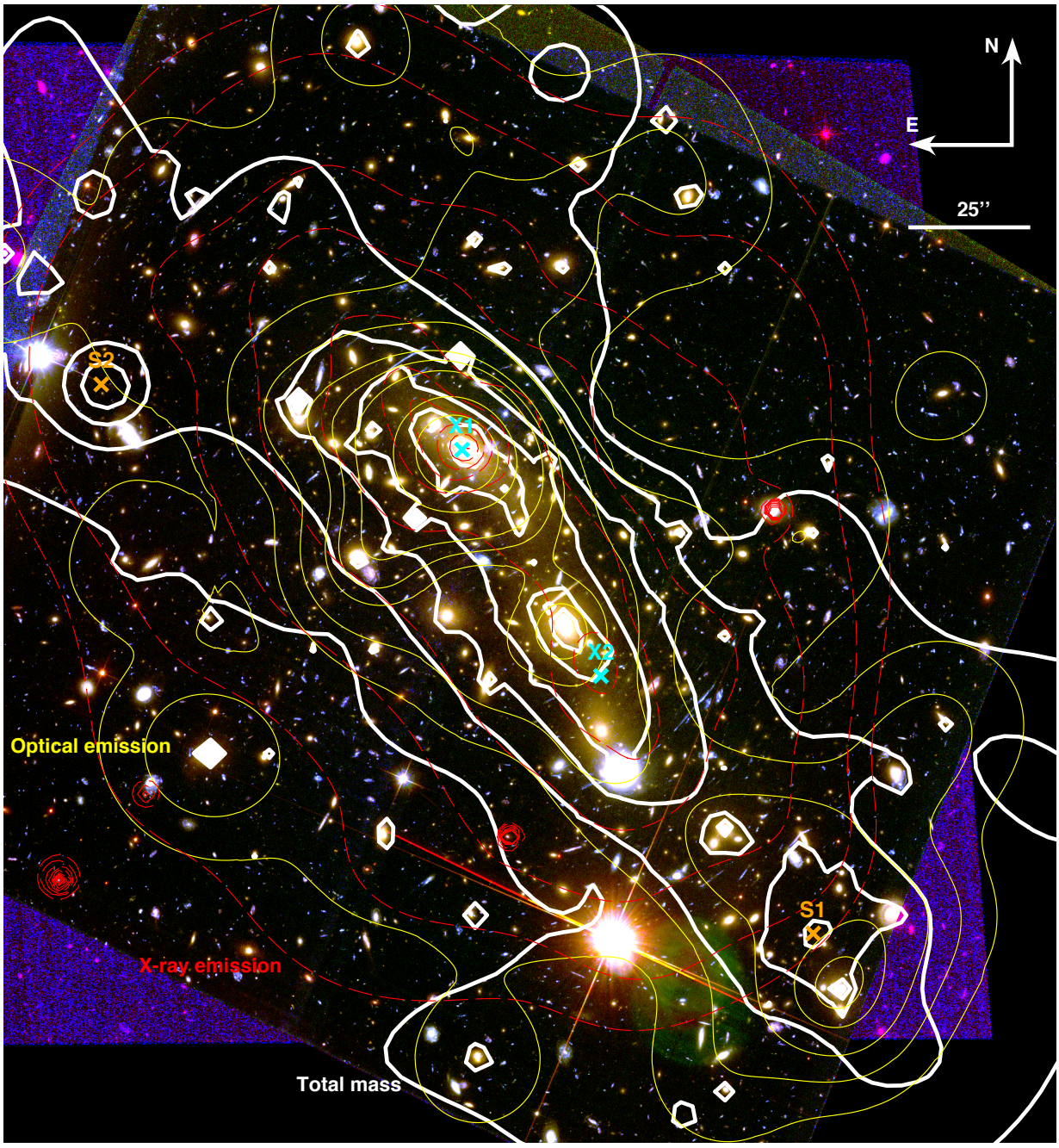

Figure 6.3: Three-colour (F814W, F606W, F435W) HST image of MACSJ0416. Mass contours from the combined strong- and weak-lensing analysis are shown in bold white, adaptively smoothed X-ray contours in the 0.77 keV band from *Chandra* are shown in dashed red, and yellow contours indicate the light distribution. Substructures S1 and S2 are marked with orange crosses while the two X-ray peaks, labelled X1 and X2, are marked by cyan crosses. Source: Jauzac et al. (2015a).

6.1.2.2 Optical and X-ray cluster analysis

Following Jauzac et al. (2012), we measure the stellar mass distribution, M_*, across the field of view using the F814W band image. K-band galaxy luminosities $L_{\rm K}$ are estimated from the F814W magnitudes using empirical relations. These are then used with the Arnouts et al. (2007) relation for inactive (red) galaxies, $\log M_*/L_{\rm K} = az + b$, to determine an average mass-to-light ratio of $M_*/L_{\rm K} = 0.99 \pm 0.03 M_\odot/L_\odot$ over the image. This process assumes a Salpeter initial mass function and relation parameters $a = -0.18 \pm 0.03$ and $b = -0.05 \pm 0.03$. The total stellar mass is computed to be $M_* = (3.10 \pm 0.01) \times 10^{13} h_{70}^{-1} M_\odot$.

Using shallow *Chandra* data (53 ks), we obtain an exposure-corrected, adaptively smoothed, 0.7-7 keV band X-ray image of MACSJ0416. The X-ray contours are shown as red dashed contours in Figure 6.3. The overall X-ray morphology is elongated in the same direction as the mass distribution and reveals two peaks (X1 and X2), the former coinciding with the C1 mass concentration identified in the lensing analysis. The X-ray peak X2 is offset from the second mass concentration, C2, by $\sim 15''$to the SW, indicating a pronounced offset between the dark matter and the gas. There is no X-ray counterpart for the newly identified substructure S1 which may indicate that this structure is non-virialised and possibly part of a large-scale filament almost aligned with the line of sight. From the X-ray data, we determine an average ICM temperature of $kT = 11.0^{+1.4}_{-1.3}$ keV, an Fe abundance of $0.20^{+0.09}_{-0.08} Z_\odot$, and a gas mass of $M_{gas}(R < 1 \text{ Mpc}) = (8.6 \pm 0.7) \times 10^{13} h_{70}^{-1} M_\odot$.

The fraction profiles of stars, gas, and baryons (stars + gas) in MACSJ0416 are shown in the left panel of 6.4. From the stellar and gas fractions, a baryon fraction of $f_b(R < 1 \text{ Mpc}) = 0.099 \pm 0.008$ is calculated. This value is 5σ below the cosmological value measured by the Planck collaboration (Planck Collaboration et al., 2014c), and is also inconsistent with that measured by Mantz et al. (2014), who used galaxy clusters as cosmological probes.

Finally, using spectroscopic redshifts from Ebeling et al. (2014) and from a VLT programme (ObsID: 186_A-0798; Balestra et al., 2015), we investigate the redshift distributions of sources in the regions of the two main mass concentrations, C1 and C2, as well as the substructures S1 and S2. The redshift distributions for the various components are shown in the right panel

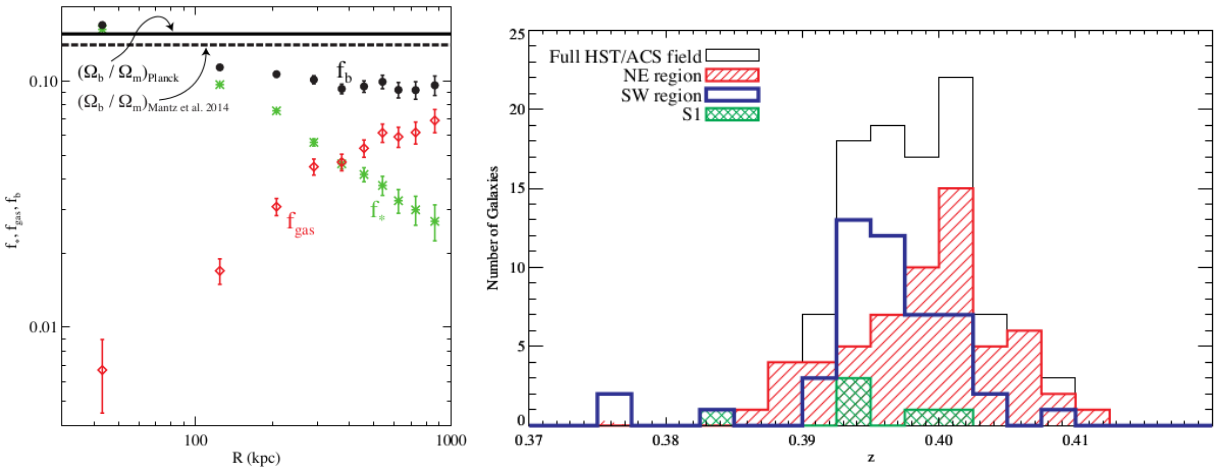

Figure 6.4: *Left:* Fraction of baryons f_b (black circles), stars f_* (green asterisks), and gas f_{gas} (red diamonds) within MACSJ0416. Over-plotted are the baryon fractions measured by Planck ($f_b = \Omega_b/\Omega_m = 0.1551 \pm 0.0055$, solid line) and by Mantz et al. (2014) ($f_b = \Omega_b/\Omega_m = 0.14 \pm 0.02$, dashed line). *Right:* Spectroscopic redshift distribution of galaxies in the HST/ACS field of view of MACSJ0416. The red (blue) histogram shows the redshift distribution in the NE (SW) section of the field. The redshift distribution for substructure S1 is shown by the green histogram. Source: Jauzac et al. (2015a).

of Figure 6.4. The cluster as a whole has an average redshift of $z = 0.3980$ and a velocity dispersion of 740 km s^{-1}, based on 106 spectroscopic redshifts. C1 and C2 are found to be separated along the line of sight, with average redshifts of 0.3990 and 0.3966 respectively. With no redshift information for galaxies within 15″ of the centre of S2, we are unable to estimate a redshift for this substructure. However, using six spectroscopic redshifts within 13″ of its centre, we determine an average redshift of $z = 0.3944$ for substructure S1.

6.1.2.3 Merger geometry and history

In order to probe the merger history and geometry of MACSJ0416, we combine the above multi-wavelength measurements to constrain the interactions between the separate components. There are two possible scenarios for the observed merger which differ primarily in terms of whether the system is observed in a pre- or post-merger state. These are schematically represented in Figure 6.5. Both scenarios take the NE mass component (C1) to be the most massive structure.

In the first scenario, the cluster is observed close to first core passage, with the second mass

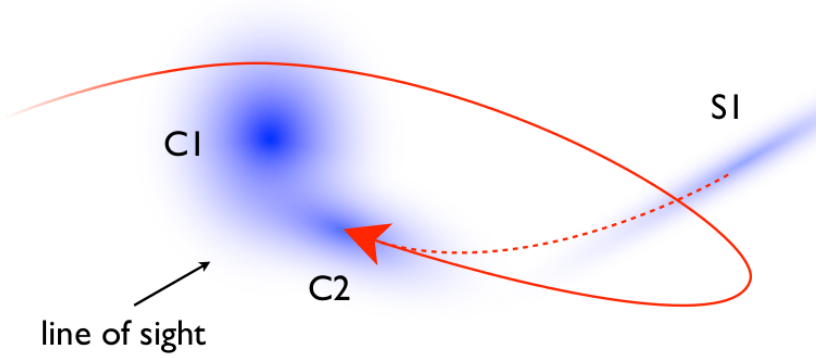

Figure 6.5: Schematic of the two hypothesised merger scenarios in a face-on view of the plane of the collision. The dotted red line marks the trajectory of C2 in the first scenario. The solid red line represents the second (preferred) scenario. Source: Jauzac et al. (2015a).

component, C2, approaching C1 at a significant impact parameter from the large-scale filamentary structure associated with S1 (dotted red line in Figure 6.5). In this case, the projected spatial differences between the dark matter, X-ray gas, and cluster galaxies of C2 are due, in part, to the fact that lensing mass reconstructions show the projected mass along the line of sight, regardless of the dynamical state of the structures. With C1 not yet disturbed, the offset between X-ray and lensing mass contours of C2 can be explained by ram pressure stripping.

In the second scenario, the cluster has already undergone an initial merger, with C2 approaching C1 for the second time (solid red line in Figure 6.5). Here, C2 originated from the NE, passed C1 with a low impact parameter, before being pulled back towards the main component for a second time. In this case the core of C1 would be significantly disrupted by the first core crossing, but due to the viewing angle, any resulting X-ray tracers would be projected onto the core. The filamentary structure S1 may be behind the cluster along the line of sight (as depicted in Figure 6.5), or well in front of it, outside of the virial radius.

We favour the second scenario on the basis of multi-phase gas being evident in the ICM

coinciding with the core of C1. The two hypotheses predict different X-ray structures around C1 and the intervening region between C2. As such, deep X-ray observations, which allow the detection of merger signatures such as shock fronts, cold cores, and sloshing gas, will be able to test and distinguish between the scenarios. Recent deep *Chandra* data favours the first scenario as the new X-ray data reveals X-ray cavities in the non-cool core NE component (Ogrean et al., 2015).

6.2 MACSJ1149.6+2223

The first strong lensing analyses of MACSJ1149.6+2223 (z=0.544; hereafter MACSJ1149) were based on shallow HST imaging with ACS (Smith et al., 2009; Zitrin and Broadhurst, 2009; Zitrin et al., 2011) and revealed a cluster with a very complex core which is host to a spectacular triply lensed face-on spiral at $z = 1.491$ (Smith et al., 2009). This massive cluster was also selected as a CLASH target, and thus got HST data spanning from the UV up to the near-infrared. This data led to an updated strong lensing analysis (Rau et al., 2014) and the discovery of a high-redshift, $z = 9.6$, singly lensed galaxy close to the cluster core (Zheng et al., 2012). MACSJ1149 was also observed with WFC3 in November 2014 as part of the Grism Lens-Amplified Survey from Space (GLASS) programme, leading to one of the most beautiful and interesting discoveries made with the HFF project, *SN Refsdal*. Kelly et al. (2015) discovered a lensed supernova (named *SN Refsdal*) in one of the face-on spiral images, making it the first observational confirmation of an event that's been predicted since the sixties (e.g. Refsdal, 1964; Kovner and Paczynski, 1988). Previously only candidates for lensed supernova had been reported (Goobar et al., 2009; Quimby et al., 2014; Patel et al., 2014).

The most recent data on this cluster was obtained as part of the HFF campaign and is comprised of observations over all seven HFF passbands using both the WFC3 and ACS instruments. The self-calibrated data (version v1.0) from STScI is used in the following HFF analysis, which combines all HST data available for MACSJ1149. This combined data amounts to 18, 10, and 42 orbits with ACS for the F435W, F606W, and F814W filters respectively, and 25, 20.5, 20, and 34.5 orbits with WFC3 for the F105W, F125W, F140W, and F160W filters respectively.

The limiting magnitude of this data is $mag_{\rm AB} = 29$ for all seven filters, typical of ultra-deep field observations. The final images have a pixel size of $0.03''$. In the following I will discuss the strong lensing HFF analysis of MACSJ1149 (Jauzac et al., 2015c), focusing on the multiple image identification and mass modelling.

6.2.1 The pre-HFF mass model

There are several pre-HFF lensing studies of MACSJ1149 (Smith et al., 2009; Zitrin and Broadhurst, 2009; Zitrin et al., 2011; Rau et al., 2014; Richard et al., 2014; Johnson et al., 2014; Coe et al., 2014; Sharon and Johnson, 2015; Oguri, 2015; Diego et al., 2015b)[4], each of which provide a mass model to initialise the HFF analysis of this cluster. The following analysis uses the pre-HFF model produced by Richard et al. (2014), following a similar approach as that discussed in §6.1.1.1 for MACSJ0416.

In Richard et al. (2014), small-scale dark matter clumps are associated with each of the spectroscopically confirmed cluster members (for MACSJ1149, taken from Ebeling et al., 2014) and large-scale dark matter clumps are associated with prominent concentrations of cluster galaxies. Each dark matter clump is described by a dPIEMD potential (Richard et al., 2009; Limousin et al., 2012). There are two models, optimised by strong lensing only, or combined strong- and weak-lensing constraints, respectively. Here we use only strong lensing constraints to optimise the pre-HFF MACSJ1149 mass model from Richard et al. (2014), which consists of four cluster-scale dark matter potentials. These constraints are the multiple images from Smith et al. (2009), three of which have spectroscopic redshifts, combined with six new images identified by Zitrin et al. (2011), and extended to 35 multiple images, produced by 12 background galaxies in the redshift range $1.31 < z < 2.61$, by further model optimisations by Richard et al. (2014).

6.2.2 Multiple images

Following the procedure used for MACSJ0416, before searching for new multiple images, the gravitational deflection field for MACSJ1149 was computed once, using a grid spacing of $0.2''$

[4]Diego et al. (2015b) also used a third of the HFF data.

per pixel, and the region in which to search for multiple images was restricted to that enclosed by the critical line at $z = 7$.

After several meticulous searches of the cluster region, and many iterations of testing predictions and updating the mass model, 30 new multiple images were identified, **increasing the number of multiple images to 65, produced by 22 background galaxies**. Figure 6.6 shows a 3-colour (F814W, F606W, and F435W) image of MACSJ1149 with multiple image detections superimposed. Although this almost doubles the pre-HFF count, the final number of multiple images is disappointing when compared to the results of the HFF analyses on the first two HFF clusters: 51 systems in MACSJ0416 (Jauzac et al., 2014, 2015a, ; §6.1) and 34 systems in A2744 (Jauzac et al., 2015b). Jauzac et al. (2015c) investigated the evolution with source redshift of the image plane surface area within which multiple images are expected for all HFF clusters. The overall shape of the curves shown in Figure 6.7 is very similar for two thirds of the HFF clusters. However, the curves for MACSJ1149 and MACSJ0717, the two highest-redshift clusters, exhibit a different evolution. Their curves start at much lower surface areas at $z_S = 1$, but the surface area increases rapidly, leading to much steeper curves than those of the other four HFF clusters. Jauzac et al. (2015c) argue that the differing trend for these two clusters is linked to their complex and extended morphology, which causes disjoint critical lines at low redshift and thus creating a disadvantage for lensing low redshift background galaxies. At higher redshifts, when the critical lines join, complex clusters gain on simpler ones in terms of multiple image surface area, however these higher redshift systems are more difficult to identify, even in deep HST images, due to their intrinsically faint nature (Atek et al., 2014, 2015b,a; McLeod et al., 2015; Ishigaki et al., 2015; Wilkins et al., 2016). Of all the HFF clusters, MACSJ1149 has the smallest area for multiply imaging background galaxies at redshifts $z_S < 3$, and this may account for the relatively low number of HFF multiple images identified.

In addition to the 65 multiple images, the face-on spiral hosting the lensed supernova *SN Refsdal* (source 1, discussed in §6.2.4) is decomposed into 24 separately identifiable features (Rau et al., 2014), those being the brightest components of the spiral. The supernova *SN Refsdal* has 6 multiple images: one in image 1.3, which appeared years ago and is no longer visible; one in image 1.1 that has been quadruply-imaged by a cluster member; and one to appear in image 1.2

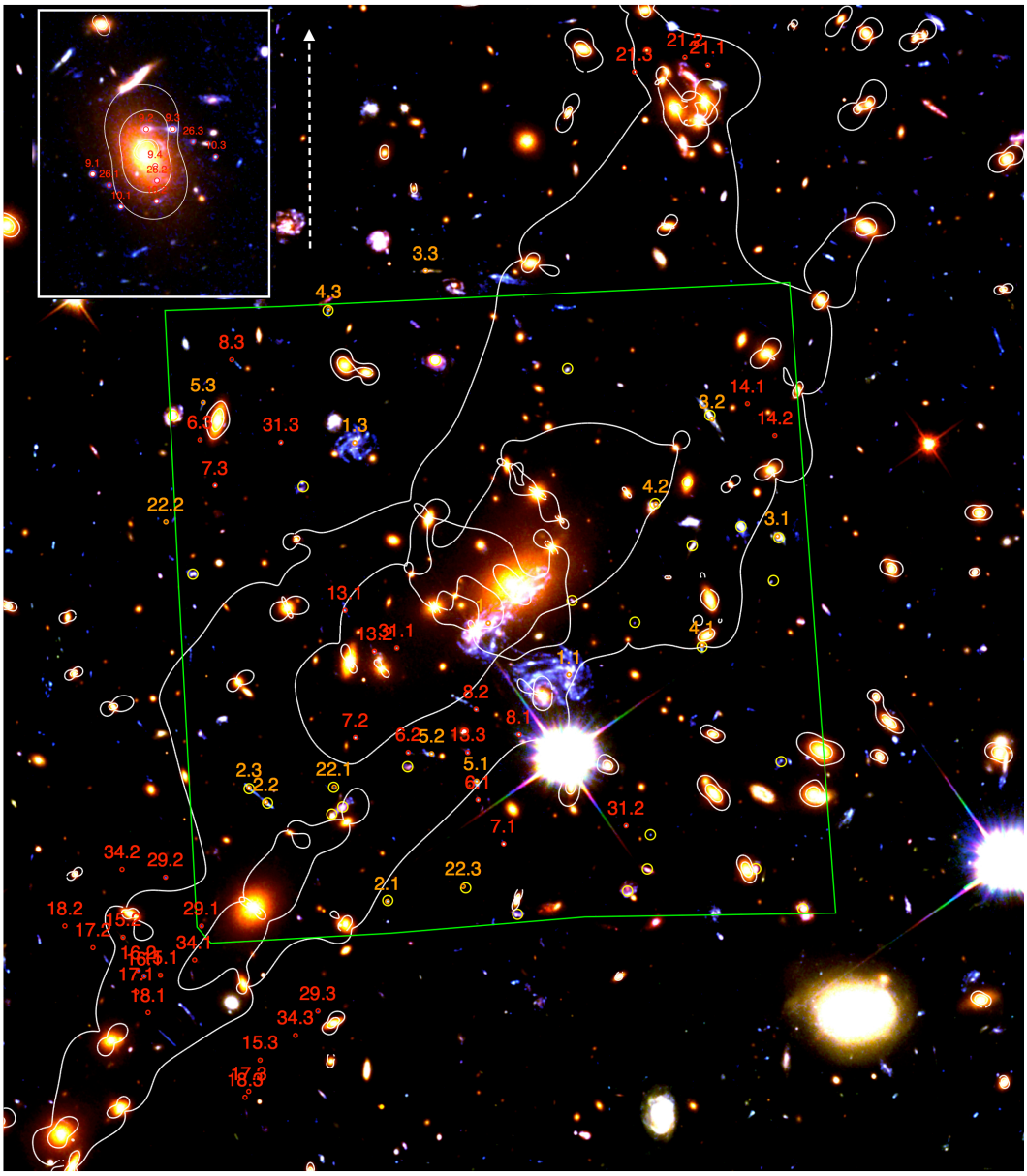

Figure 6.6: 3-colour HST/ACS (F814W, F606W, F435W) image of MACSJ1149 showing all multiple image identifications used to optimise the lens model (65 images, red and orange circles). The orange circles indicate images with a spectroscopic redshift from either GMOS or MUSE. Background sources with a MUSE redshift are indicated by yellow circles. System #1 is split into 24 individual sources at the same redshift, not labelled on the figure for clarity (see Table C.2 for their coordinates). Critical lines at z = 1.49, and z = 7.0 are shown in white. The green rectangle highlights the VLT/MUSE field of view. The top left inset shows a close-up view of the Northern component of the cluster (Clump #4 in Table 6.2). North is up and East is left. Source: Jauzac et al. (2015c).

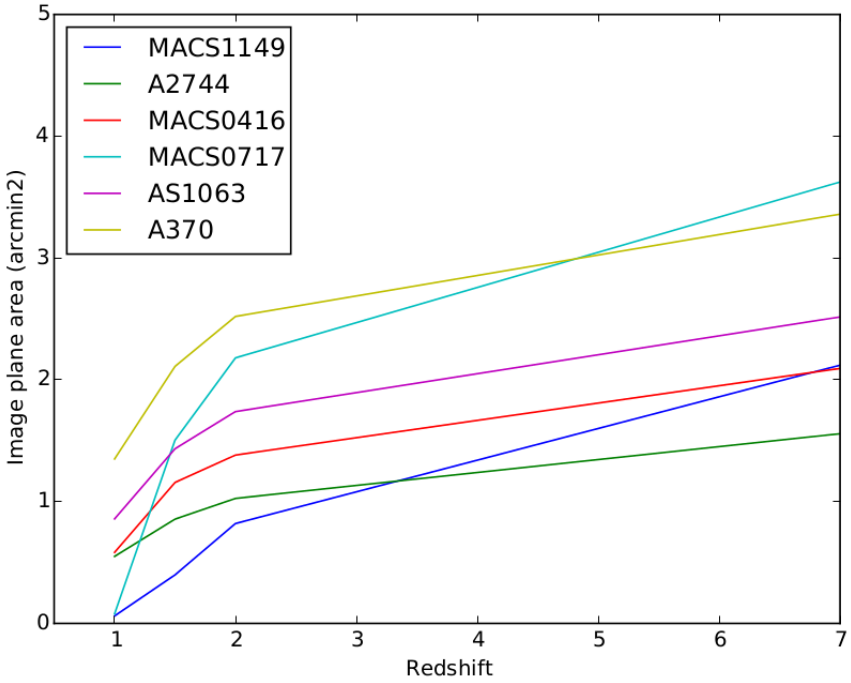

Figure 6.7: Evolution of the surface area in the image plane within which multiple images are observed, as a function of the source redshift. Source: Jauzac et al. (2015c).

at some future time. The four visible supernova images are labelled S1, S2, S3, and S4, following the same notation as Kelly et al. (2015), Sharon and Johnson (2015), and Oguri (2015). Figure 6.9 in §6.2.4 shows the three images of the lensed spiral galaxy, with bright features identified by orange circles, and supernova images (both visible and predicted) indicated by red circles.

The separate spiral galaxy features, along with the four visible images of *SN Refsdal*, are added to the list of images used to optimise the lens model. The full list of identified multiple images and other constraints used to optimise the lens model is provided in Appendix C, Table C.2.

To test the reliability of the multiple image identifications, a flux-χ^2 statistic was used to quantify the probability of two images originating from the same source (Mahler et al., 2015) by testing how similar the photometry of a pair of images (A and B) within a given system is:

$$\chi^2_{photo} = \frac{1}{N-1}\min_\alpha \left(\sum_{i=1}^{N} \frac{(f_i^A - \alpha f_i^B)^2}{(\sigma_i^A)^2 + (\alpha\sigma_i^B)^2} \right) \tag{6.1}$$

where N is the total number of filters, f_i and σ_i are the fluxes and errors in the i-th filter, and α is the minimisation factor rescaling both SEDs. Acceptable values ($\chi^2_{photo} \sim 1$–3) were found for most of the images. Slightly higher values were found for sources whose photometry was contaminated by bright nearby sources. The one exception is image 3.3 which was identified in the pre-HFF images. Based on predictions of its position and morphology from a lensing model constrained by 3.1 and 3.2 only, 3.3 appears to be the most plausible counter image for this system, however this image has a significant χ^2_{photo} value of 51. Figure 6.8 shows the comparison between the observed multiple images of system 3 in composite HST ACS/WFC3 3-colour, and the corresponding predicted image morphologies (based on a source matching 3.1) in monochrome. The predicted locations and morphologies of systems 3.2 and 3.3 are a close match with the identified counterparts, however the colour of 3.3 is reddened compared to the other images. If the magnitude difference due to lensing amplification is ignored, the flux difference between images 3.1 and 3.3 in all filters follows a reddening curve that's readily modelled by a Milky Way (MW; Allen, 1976) or Small Magellanic Cloud (SMC; Bouchet et al., 1985; Prevot et al., 1984) extinction curve. Dust extinction has been reported in the outskirts of clusters (e.g. Chelouche et al., 2007) but in the case of system 3.3, dust extinction by an intervening galaxy in front of or behind the cluster cannot be ruled out. Although the significant colour difference between 3.3 and the other two images would usually lead to treating this image as only a candidate, it is included in the optimisation of the lens model due to the strength of the above predictions.

The multiple image identifications have also been improved with more extensive redshift constraints. Only three pre-HFF systems were spectroscopically confirmed: $z_1 = 1.491$, $z_2 = 1.894$, and $z_3 = 2.497$ (Smith et al., 2009). We used spectroscopic data from GMOS on Gemini North to fix the redshifts for known multiple images, as well as measure new redshifts for those sources. This allowed us to have fewer free parameters in the model, as well as to constrain the parameter space that would be explored by LENSTOOL which lessened the computational time in optimising the model. The new spectroscopic data led to updated redshifts for systems 1 and 3 ($z_1 = 1.4888$ and $z_3 = 3.128$), as well as new spectroscopic redshifts for systems 4, 5, 9, and 22: $z_4 = 2.95, z_5 = 2.79, z_9 = 0.981$ and $z_{22} = 3.216$.

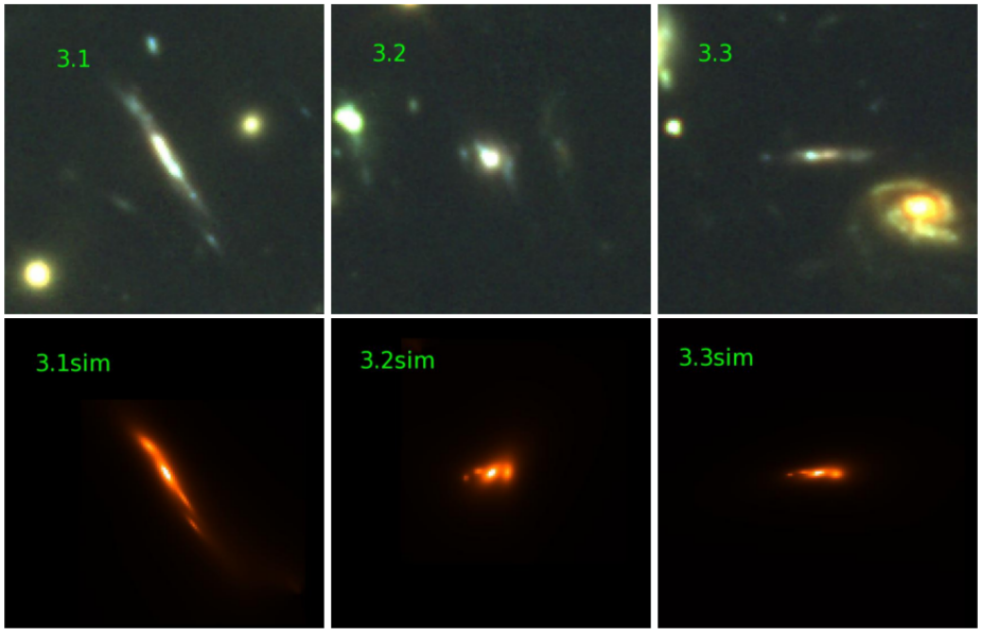

Figure 6.8: Comparison of predicted vs observed images for system 3 in MACSJ1149. *Top panels:* HST ACS/WFC3 composite colour images of the multiple images of system 3 (F814W, F105W, and F160W filters as RGB). *Bottom panels:* Monochrome simulated images showing the predicted morphology of multiple images from a source matching image 3.1. Source: Jauzac et al. (2015c).

In addition, we used data from MUSE on the Very large Telescope (VLT) to provide redshifts for multiple images, as well as many of the singly-imaged sources in the field. This new spectroscopy confirmed the lens model predictions of the singly imaged background sources, as at their redshifts they couldn't be multiply lensed. It also provided an extra level of rejection criteria for potential new multiple images during the iterative search mentioned above.

6.2.3 Lens modelling

The HFF mass model of MACSJ1149 is set up in a similar way to that of MACSJ0416, namely using a parametric model where dark matter potentials are described by dPIEMDs and are defined as either cluster-scale, to model large-scale mass distributions, or galaxy-scale, to incorporate small-scale lensing perturbations. For galaxy-scale halos, the dPIEMD parameters of $r_{\rm core}$, r_{cut}, and σ are fixed to the light distribution of the corresponding cluster member and empirical scaling

relations are assumed in order to relate the dynamical dPIEMD parameters to the observed galaxy luminosity (see §5.5.2.2). For an L* galaxy, priors on the dynamical parameters are set to be 100km/s $< \sigma^* <$ 250 km/s and $r^*_{\rm cut} <$ 70 kpc.

The pre-HFF mass model discussed in §6.2.1 is the starting point for this new lens model, however an extra cluster-scale halo south-east of the cluster BCG is added, bringing the total number of cluster-scale halos to five. This additional halo is confirmed as necessary by a lower RMS value and improved χ^2 compared to the pre-HFF model. The positions of these cluster-scale halos are allowed to vary within 20″ of the associated light peak and the ellipticities, described by $\varepsilon = \dfrac{a^2 - b^2}{a^2 + b^2}$ are limited to $\varepsilon < 0.7$. As in the MACSJ0416 model, the cut-off radius is fixed at $r_{\rm cut} = 1000$ kpc as only strong lensing is being incorporated. Finally, the core radius and velocity dispersion for each cluster-scale halo is restricted to the following values: $1'' < r_{\rm core} < 35''$, and 100km/s $< \sigma <$ 2000 km/s.

The model is completed by adding galaxy-scale halos of 216 likely cluster members (Richard et al., 2014) as well as an additional two galaxy-scale halos to model the perturbations due to the cluster BCG (clump #6 in Table 6.2), and the cluster member responsible for quadruply-lensing *SN Refsdal* in image 1.1 (clump #7 in Table 6.2).

This model is optimised with LENSTOOL using the list of multiple images and redshift constraints given in Table C.2. The final best-fit parameters for the five cluster-scale halos and the two additional galaxy-scale halos are provided in Table 6.2. The best-fit model has a positional RMS error of 0.91″ which is a little higher than the one obtained by the Richard et al. (2014) model. One of the contributing factors to this is the high individual χ^2 of image 3.3, however, as stated above it is still considered a robust identification and included in the optimisation.

In order to determine a lensing mass, a centre position of $\alpha = 177.3987300, \delta = 22.35290$ is chosen for the annuli to integrate over. A 2D cylindrical mass of $M_{\rm HFF}(R < 500{\rm kpc}) = (6.29 \pm 0.03) \times 10^{14} M_\odot$ is measured within 80″. This is somewhat lower than the value of $M(R < 500$ kpc$) = (6.7 \pm 0.4) \times 10^{14} M_\odot$ determined by Smith et al. (2009), but is nevertheless within their error bars and has a much higher precision. The mass within 30″ was calculated by Zitrin et al. (2011) to be $M(R < 200{\rm kpc}) = (1.71 \pm 0.20) \times 10^{14} M_\odot$ which is in good agreement with the HFF value determined here: $M_{\rm HFF}(R < 200$ kpc$) = (1.840 \pm 0.006) \times 10^{14} M_\odot$. Again,

Table 6.2: Best-fit PIEMD parameters for the five cluster-scale dark matter halos in the MACSJ1149 HFF mass model. Clumps #6 and #7 are galaxy-scale halos that were modelled separately from the scaling relations to model the BCG of the cluster and the cluster member responsible for lensing *SN Refsdal*, respectively. L* refers to the L* elliptical galaxy. Coordinates are given with respect to $\alpha = 177.3987300, \delta = 22.3985290$. All errors are the 1σ uncertainties. Parameters in brackets are not optimised. The reference magnitude for scaling relations is $mag_{\rm F814W}$ = 20.65.

Clump	$\Delta\alpha$ (arcsec)	$\Delta\delta$ (arcsec)	ε	θ (degrees)	$r_{\rm core}$ (kpc)	$r_{\rm cut}$ (kpc)	σ (km s^{-1})
#1	$-1.95^{+0.10}_{-0.19}$	$0.17^{+0.15}_{-0.22}$	0.58 ± 0.01	$30.58^{+0.35}_{-0.51}$	$112.9^{+3.6}_{-2.1}$	[1000]	1015^{+7}_{-6}
#2	$-28.02^{+0.26}_{-0.17}$	$-36.02^{+0.27}_{-0.21}$	0.70 ± 0.02	$39.02^{+2.23}_{-1.9}$	$16.5^{+2.7}_{-3.9}$	[1000]	331^{+13}_{-9}
#3	$-48.65^{+0.13}_{-0.49}$	$-51.35^{+0.30}_{-0.22}$	0.35 ± 0.02	$126.48^{+7.11}_{-4.42}$	$64.2^{+6.8}_{-9.6}$	[1000]	286^{+24}_{-16}
#4	$17.62^{+0.28}_{-0.18}$	$46.90^{+0.36}_{-0.28}$	0.15 ± 0.02	$54.66^{+3.51}_{-4.83}$	$110.5^{+1.2}_{-2.1}$	[1000]	688^{+9}_{-17}
#5	$-17.22^{+0.17}_{-0.18}$	$101.85^{+0.08}_{-0.07}$	0.44 ± 0.05	$62.29^{+5.14}_{-4.61}$	$2.1^{+0.5}_{-0.1}$	[1000]	263^{+8}_{-7}
#6	[0.0]	[0.0]	[0.2]	[34.0]	$3.95^{+0.57}_{-0.89}$	$92.08^{+6.50}_{-7.91}$	284^{+8}_{-8}
#7	[3.16]	[-11.10]	0.22 ± 0.02	$103.56^{+7.09}_{-7.95}$	[0.15]	$43.17^{+1.34}_{-1.02}$	152^{+2}_{-1}
L*	–	–	–	–	[0.15]	$52.48^{+2.17}_{-0.89}$	148^{+2}_{-3}

a much higher precision is achieved with the HFF data compared to pre-HFF results.

6.2.4 Time delays and future predictions for SN Refsdal

MACSJ1149 is host to a triply-lensed face-on spiral, system 1 in the list of multiple images. One of the spiral images (1.1) is host to a supernova (SN), named *SN Refsdal* by the group who first identified it, which is lensed into an Einstein cross by a nearby cluster member (Kelly et al., 2015). The discovery of this supernova led to several pre-HFF strong-lensing analyses of MACSJ1149 in the attempt to determine the order of appearance of the SN images, as well as the time delays between them, and when the SN event will appear in the other spiral image (Sharon and Johnson, 2015; Oguri, 2015; Diego et al., 2015b). The models all predict six multiple images of *SN Refsdal*: one in each of the spiral images (SX in 1.2 and SY in 1.3), with that in image 1.1 being quadruply lensed into an Einstein cross formation comprised of images S1, S2, S3, and S4

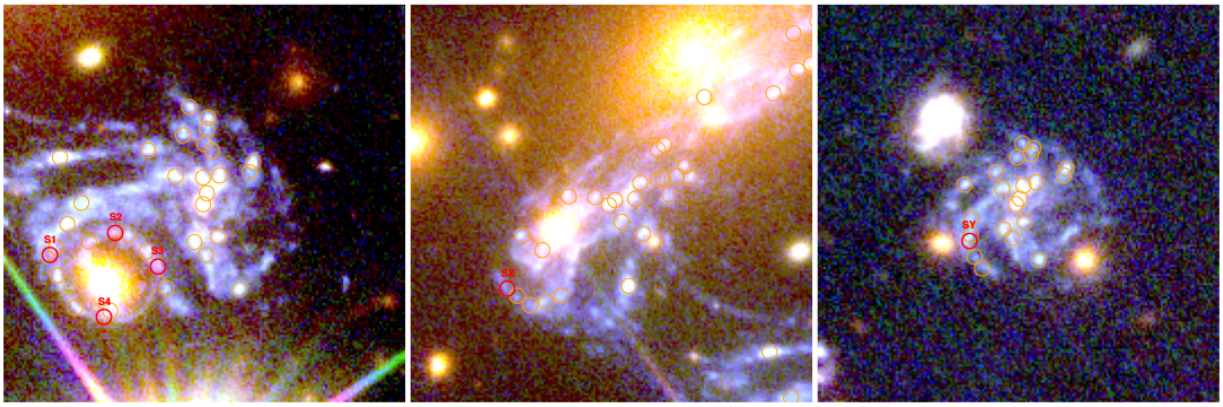

Figure 6.9: HST ACS 3-colour images of the multiple images of system 1. Orange circles highlight the 24 bright features of the spiral used in the mass model. Red circles show the positions (real or predicted) of the supernova *SN Refsdal*. *Left:* Image 1.1 which hosts the supernova *SN Refsdal* lensed into an Einstein cross. The component images are labelled as S1, S2, S3, and S4. *Middle:* Image 1.2 with SX being the predicted location of *SN Refsdal* predicted to appear in January 2016. *Right:* Image 1.3 with SY being the predicted position of *SN Refsdal* that is predicted to have appeared 11.5 years ago. Source: Jauzac et al. (2015c).

(see the left panel in Figure 6.9). The results of these pre-HFF analyses all differ in both the order of appearance of the multiple images S1 to S4, as well as the time delays between them. The time delays depend on the slope of the mass profile at the location of the cluster member responsible for the Einstein cross. This slope can only be truly constrained by the unlikely identification of the 5th demagnified image of the Einstein cross configuration. The uncertainty on the mass profile slope is a major contributing factor to the current uncertainties between team results.

The mass model described in the previous section, which is the only current model based on the full HFF data, can also be used to determine time delays and predictions for the six images of *SN Refsdal*. Figure 6.9 shows the observed positions of images making up the Einstein cross in 1.1, as well as the positions of SX and SY in the other spiral images predicted by this model. Although this model doesn't include any time delay constraints, the optimisation does include the positions of the multiply lensed SN (S1, S2, S3, S4) as well as a dPIEMD potential for the cluster member (clump #7). Note that the 5th SN multiple image of the Einstein cross is not detected in this analysis either, and so the best-fit parameters for clump #7 are not as constrained as they theoretically could be. The results from the three previous analyses are compared with

Table 6.3: Time delays obtained for each image of *SN Refsdal*, with S1 as the reference image, from this model and the three pre-HFF analyses. Subscripts on the time delays refer to the following analyses: CATS: This model, Jauzac et al. (2015c); SJ15: Sharon and Johnson (2015); O15: Oguri (2015); D15: Diego et al. (2015b). Time delays are given in days. The positional information for each image is from the predictions of this model.

Image	R.A.	Dec.	Δt_{CATS}	Δt_{SJ15}	Δt_{O15}	Δt_{D15}
S1	177.39823	22.395628	0.0	0.0	0.0	–
S2	177.39771	22.395628	90 ± 17	2.0	9.2	–
S3	177.39737	22.395542	30 ± 35	-5.0	5.2	–
S4	177.39780	22.395172	-60 ± 41	7.0	22.5	–
SX	177.40024	22.396811	449 ± 45	237^{+37}_{-50}	357.1	376 ± 25
SY	177.40380	22.402149	-4654 ± 358	-4251^{+369}_{-373}	-6193.5	-3325 ± 763

the results from this model in Table 6.3.

The best-fit model with parameters given in Table 6.2 predict the order of appearance of the SN images to be S4-S1-S3-S2, which is again different to any of the pre-HFF predictions. Using S1 as a reference, the time delays predicted by this model are $\Delta t_{S2-S1} = 90 \pm 17$ days, $\Delta t_{S3-S1} = 30 \pm 35$ days, and $\Delta t_{S2-S1} = -60 \pm 41$ days, leading to a total delay from appearance of the first to the last image of $\sim$5 months.This is significantly longer than that predicted in the pre-HFF models where the total delay is approximately 1.5 months. This difference is particularly interesting in the case of Sharon and Johnson (2015) as they also used LENSTOOL for their analysis. One of the main differences between the analyses is the fact that Sharon and Johnson (2015) used pre-HFF data which means they had fewer multiple images as constraints and they used the redshift for system 3 from Smith et al. (2009), $z_3 = 2.497$, which has been updated in this analysis to $z_3 = 3.128$ using the new MUSE data. Running the optimisation of the pre-HFF mass model of Richard et al. (2014) with both the old and new redshift, the time delays using the old redshift are indeed shorter than those determined using the updated value. Thus the erroneous pre-HFF value is expected to have an impact on the difference in time delays between this model and the pre-HFF analyses.

All four models predict that SY was the first to appear, with this analysis predicting it appeared $\sim$13 years before S1, which is in rough agreement with the results from Sharon and Johnson (2015) and Diego et al. (2015b). SX is predicted to appear in image 1.2 approximately 1.3 years after S1. Assuming S2 appeared in November 2014 (Kelly et al., 2015), SX is therefore expected to appear some time between November 2015 and January 2016, which is readily observable with a reasonable investment of time and resources.

Note, however, that only photometric follow-up observations of *SN Refsdal* will constrain the true time delays between the six predicted images. Once secure time delays are obtained, they can be included in the optimisation of the lens model and thus enable the characterisation of the lensing galaxy (clump #7) to unprecedented precision. This in turn will allow for the study of the stellar and dark matter distribution within the galaxy, which would significantly augment the effort to determine the nature of dark matter (Massey et al., 2015).

CHAPTER 7

CONCLUSION

Galaxy clusters are unique laboratories in which to study astrophysical processes as well as the evolution of the Universe. There are several observational probes of clusters. Low-frequency radio observations may reveal diffuse cluster emission which can be used to study the magnetic fields and cosmic ray processes in the intracluster medium. At higher frequencies, gravitational lensing analyses of deep optical images can constrain the dark matter content and distribution within the cluster lenses to high precision.

In chapter two we provided a background to diffuse radio emission in galaxy clusters and discussed the observational properties of the three main classifications of this diffuse emission, namely radio halos, radio relics, and mini-halos. In addition we introduced the current competing theories for the formation of radio halos and highlighted the observational link between dynamically disturbed clusters and diffuse radio emission.

In chapter three we introduced our observing sample of eight clusters taken from the equatorial Atacama Cosmology Telescope (ACT) cluster catalogue and discussed our new radio observations aimed at detecting radio halos in these clusters. We presented our data reduction procedure which used ionospheric modelling to correct direction-dependent phase errors. We detected a giant radio halo in only one of our targets, with no evidence of diffuse emission in

the remaining clusters. We determined radio halo power upper limits for the latter systems by injecting simulated halos into the calibrated data. For our high redshift clusters we measured radio power upper limits that lie slightly below to slightly above the radio power-mass correlation. Finally, we noted two radio galaxies which are visible in the two of our cluster fields which are interesting systems to follow up. The low radio halo detection rate in our sample is likely due to the dynamical state of the clusters, most of which appear to be relaxed systems based on recent optical substructure measurements. Low frequency radio observations of a large ($\sim$100) complete SZ-selected cluster sample would provide a statistical test of the effect of SZ-selection on the detection rate of diffuse emission. Such a study could be undertaken with the large sample of new clusters detected by the new polarization-sensitive instrument on ACT, ACTPol.

In chapter four we presented a multi-wavelength study on the single cluster in our sample which hosts diffuse cluster emission, ACT-CL J0256.5+0006. We presented radio observational results at two frequencies and detected a giant radio halo in this system, making it one of the lowest-mass clusters found to host such emission. Furthermore, the detected halo was found to agree well with correlations from the literature. We investigated the presence of cluster dynamical substructure using archival X-ray imaging, and optical spectroscopic redshift measurements, concluding that ACT-CL J0256.5+0006 is composed of two subcluster components with a 7:4 mass ratio. Using the observed projected separation and line-of-sight velocity difference between components, we constructed a simple merger model to constrain the merger geometry, for which we found two possible cases. The merger model allowed us to estimate a time-scale for the cluster merger. We compared our results to magnetohydrodynamical simulations and concluded that ACT-CL J0256.5+0006 is observed close to, but before, first core crossing when we would expect the radio halo to be "switching on". Future multi-wavelength merger analyses of the complete sample of clusters hosting radio halos would be extremely beneficial in terms of understanding the dynamical environment producing the radio emission. Moreover, new and upcoming high-sensitivity instruments such as LOFAR and the SKA will enable detections of fainter diffuse emission in lower mass or higher redshift clusters which will improve our understanding of the physical processes driving the emission.

In chapter five we provided the background and basic theory related to cluster gravitational

lensing in both the strong- and weak-lensing regimes. In addition, we discussed mass modelling techniques used to obtain cluster lensing mass measurements from strong lensing observational constraints. We focused on the parametric technique implemented in the LENSTOOL software.

In the final chapter we presented the gravitational lensing analysis of two clusters observed as part of the Hubble Frontier Fields (HFF) program. The deep HFF images resulted in lensing mass measurements with percent-level precision for the first time. For MACSJ0416.1−2403, we discussed the identification of ∼200 multiple images in the HFF data and the resulting lens model which they constrained. We then summarised the combined strong- and weak-lensing results for this cluster and discussed the merger history and geometry constrained by joint optical and X-ray analyses. Two possible scenarios were presented. Deep X-ray observations are required in order to test and distinguish between them. For MACSJ1149.6+2223, we discussed the HFF strong lensing multiple image identification and mass modelling. In addition, we investigated the time delays and future predictions for the lensed supernova observed in one of the multiply imaged galaxies. We predicted the next supernova image to appear between November 2015 and January 2016. With additional HFF data on this cluster now available, the strong lensing constraints on the mass model can potentially be extended to include fainter multiple images, in addition to being combined with a weak lensing analysis in order to expand the mass model out to larger radii.

7.1 Future Work

Radio and optical gravitational lensing observations are both powerful tools to investigate the galaxy cluster environment, providing complementary information about the dynamics and physical processes occurring in clusters. When combined with other wavelength data such as X-ray, SZ, and optical spectroscopy, the dynamical state of the cluster can be determined and, in the case of a merging system, the dynamics and geometry of the merger can be investigated.

An extension to this work would be to collect and analyse multiwavelength data for the entire ACT cluster sample. This would allow us to investigate the statistics of an SZ-selected cluster sample in terms of cluster dynamical state, as well as to improve our understanding of

the mechanisms involved in merger events and whether there is any evolution in their properties over large ranges in redshift or mass.

A first step towards this goal would be to observe a complete sample of SZ-selected clusters from ACTPol with the ultra-sensitive instrument MeerKAT over the next few years. ACTPol surveys a larger area than previous ACT programmes and is providing scores of new cluster detections over a large range of redshifts and mass. MeerKAT should allow us to observe diffuse emission in clusters out to redshifts of $z \sim 1$ within a reasonable integration time, and will be sensitive enough to determine whether diffuse emission exists in low mass merger systems as well. With high-resolution SZ imaging of ACTPol clusters with MUSTANG 2.0, we would be able to determine the dynamical state of the clusters without X-ray imaging. Although blind surveys, as we carried out in this thesis, are important for determining statistical information about a cluster population, having dynamical information about the clusters prior to the radio observations would increase the probability of detecting radio halos and relics. Multiwavelength follow-up with X-rays, optical spectroscopy, and lensing of those clusters hosting diffuse emission or with merger signatures in the SZ would be necessary to produce a complete analysis of the merging clusters and the processes occurring within them.

APPENDIX A

PRIMARY BEAM-CORRECTED, FULL-RESOLUTION RADIO IMAGES

We present here the full-resolution radio images for each of the clusters in our sample. The images are fluxscale, astrometry and primary beam corrected.

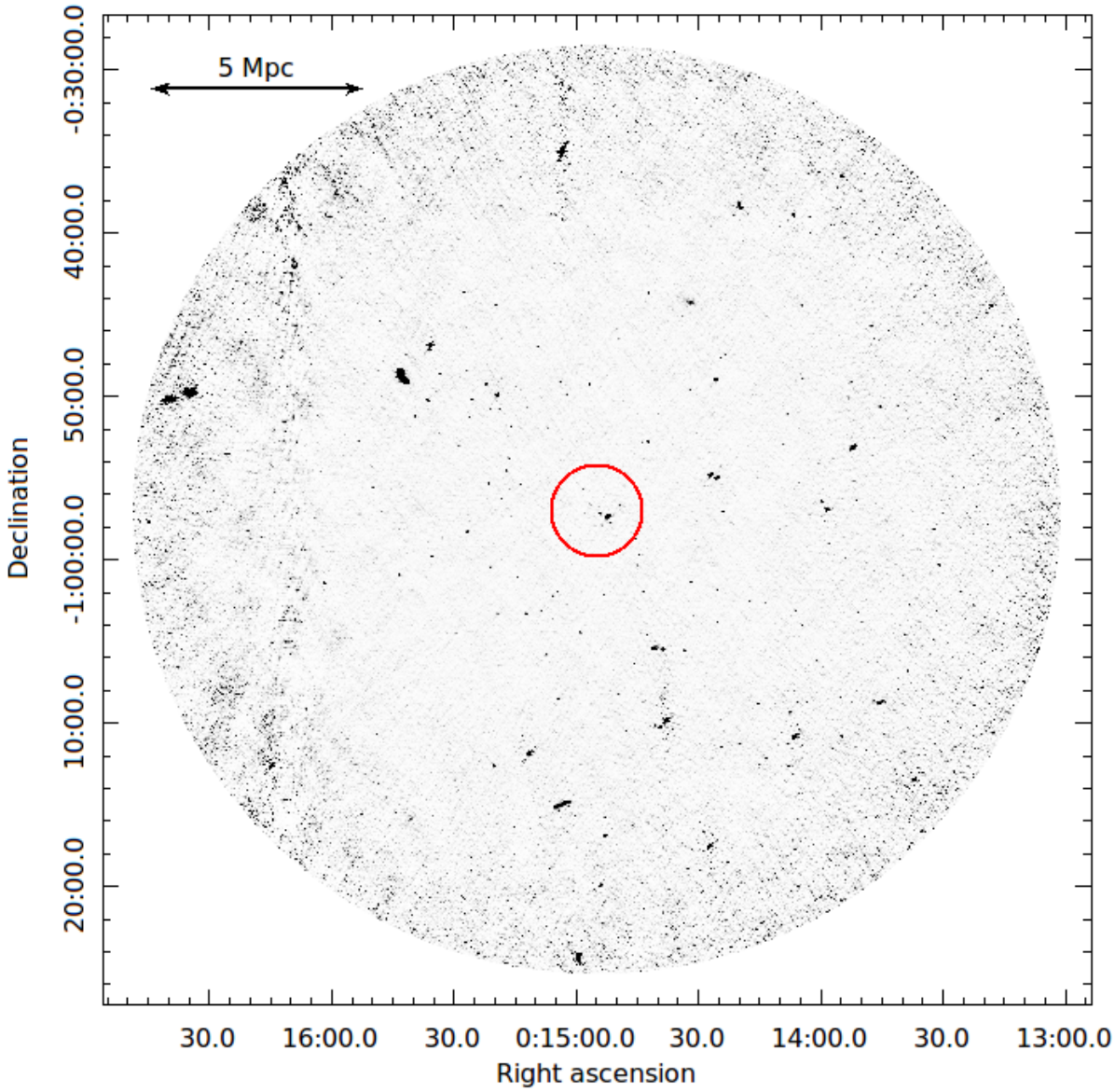

Figure A.1: Full-resolution, primary beam corrected image of ACT-CL J0014.9−0056. The physical scale at the cluster redshift of $z = 0.535$ is shown in the top left corner. The red circle denotes the SZ cluster scale, $\theta_{500} = 2.8'$, centred on the SZ peak. The central rms map noise is 34.9 μJy beam^{-1}.

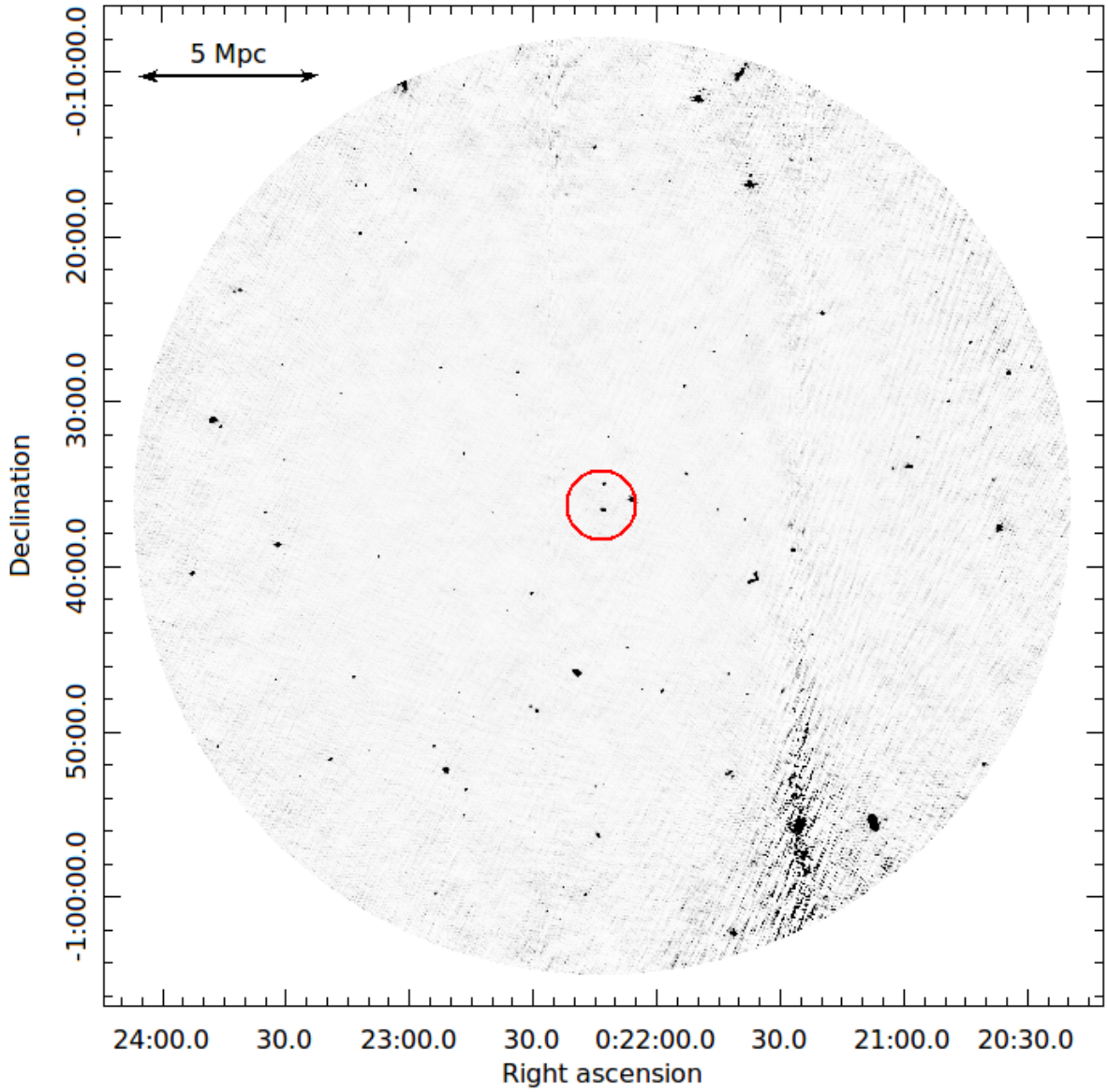

Figure A.2: Full-resolution, primary beam corrected image of ACT-CL J0022.2−0036. The physical scale at the cluster redshift of $z = 0.805$ is shown in the top left corner. The red circle denotes the SZ cluster scale, $\theta_{500} = 2.1'$, centred on the SZ peak. The central rms map noise is 57.9 μJy beam^{-1}.

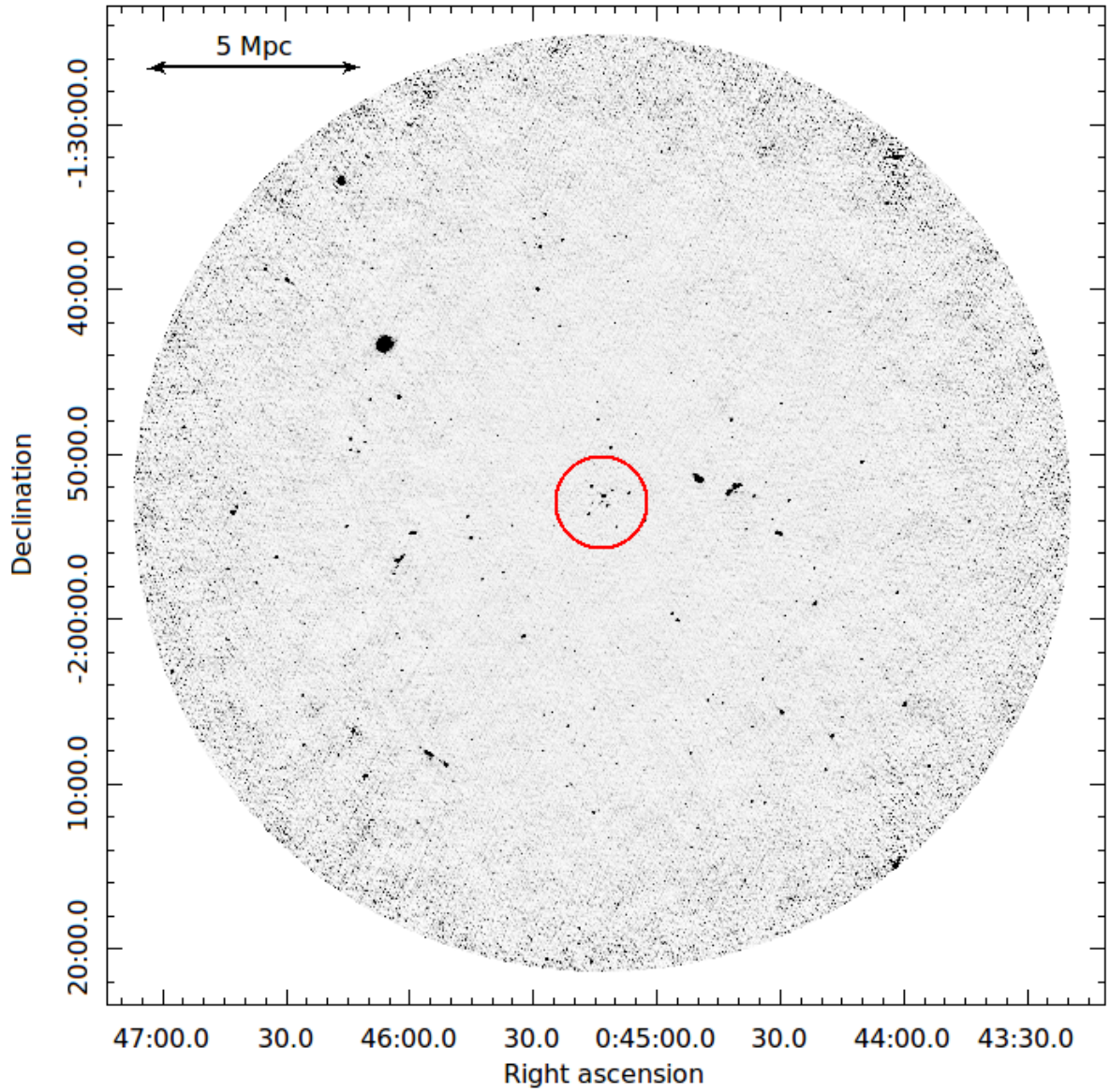

Figure A.3: Full-resolution, primary beam corrected image of ACT-CL J0045.2−0.152. The physical scale at the cluster redshift of $z = 0.545$ is shown in the top left corner. The red circle denotes the SZ cluster scale, $\theta_{500} = 2.8'$, centred on the SZ peak. The central rms map noise is 40.8 μJy beam^{-1}. The bright source North-East of the cluster region is NGC 0245 ($z = 0.013604$, see section 3.3.1.2).

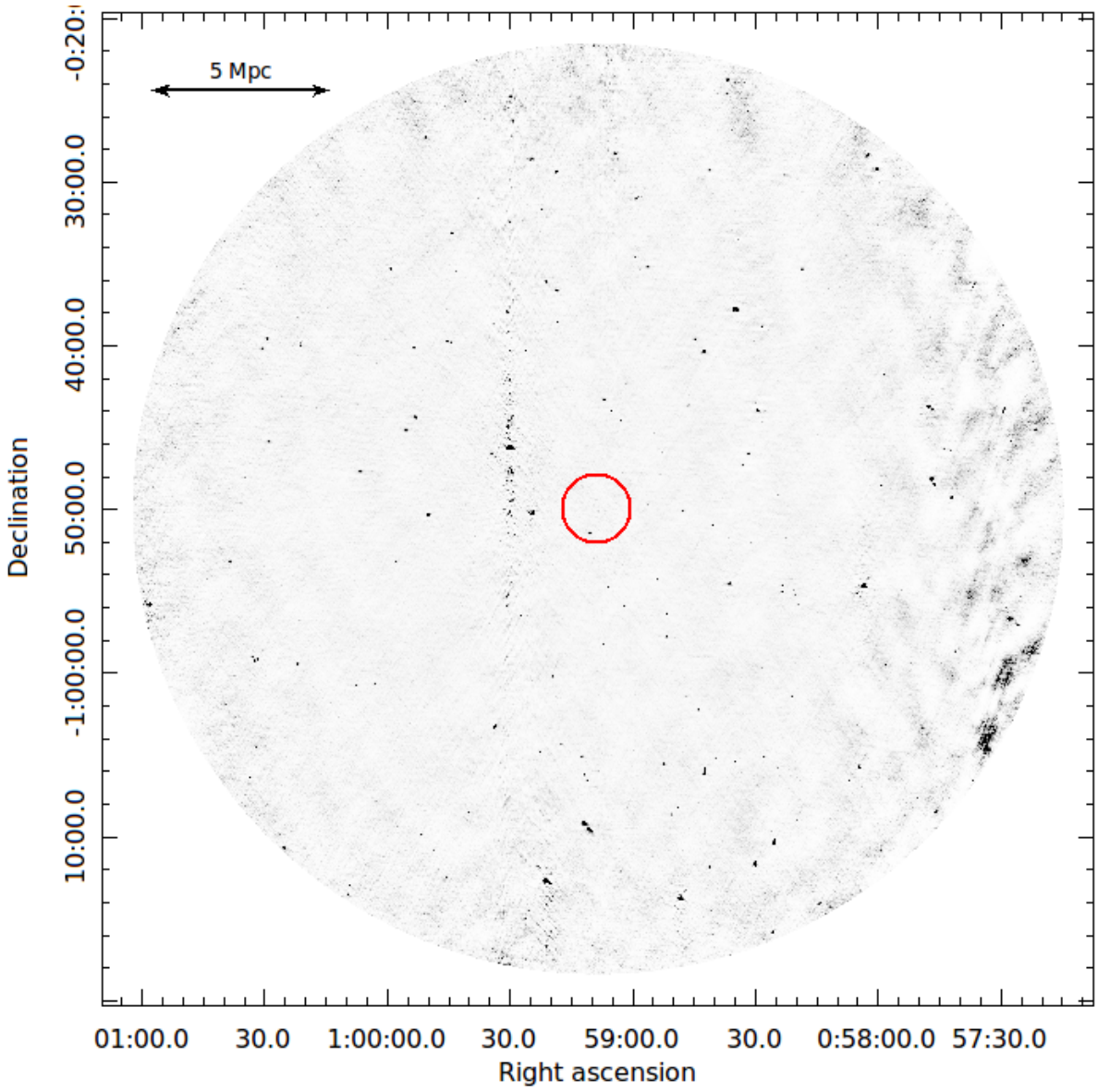

Figure A.4: Full-resolution, primary beam corrected image of ACT-CL J0059.1−0049. The physical scale at the cluster redshift of $z = 0.786$ is shown in the top left corner. The red circle denotes the SZ cluster scale, $\theta_{500} = 2.1'$, centred on the SZ peak. The central rms map noise is 49.7 μJy beam^{-1}.

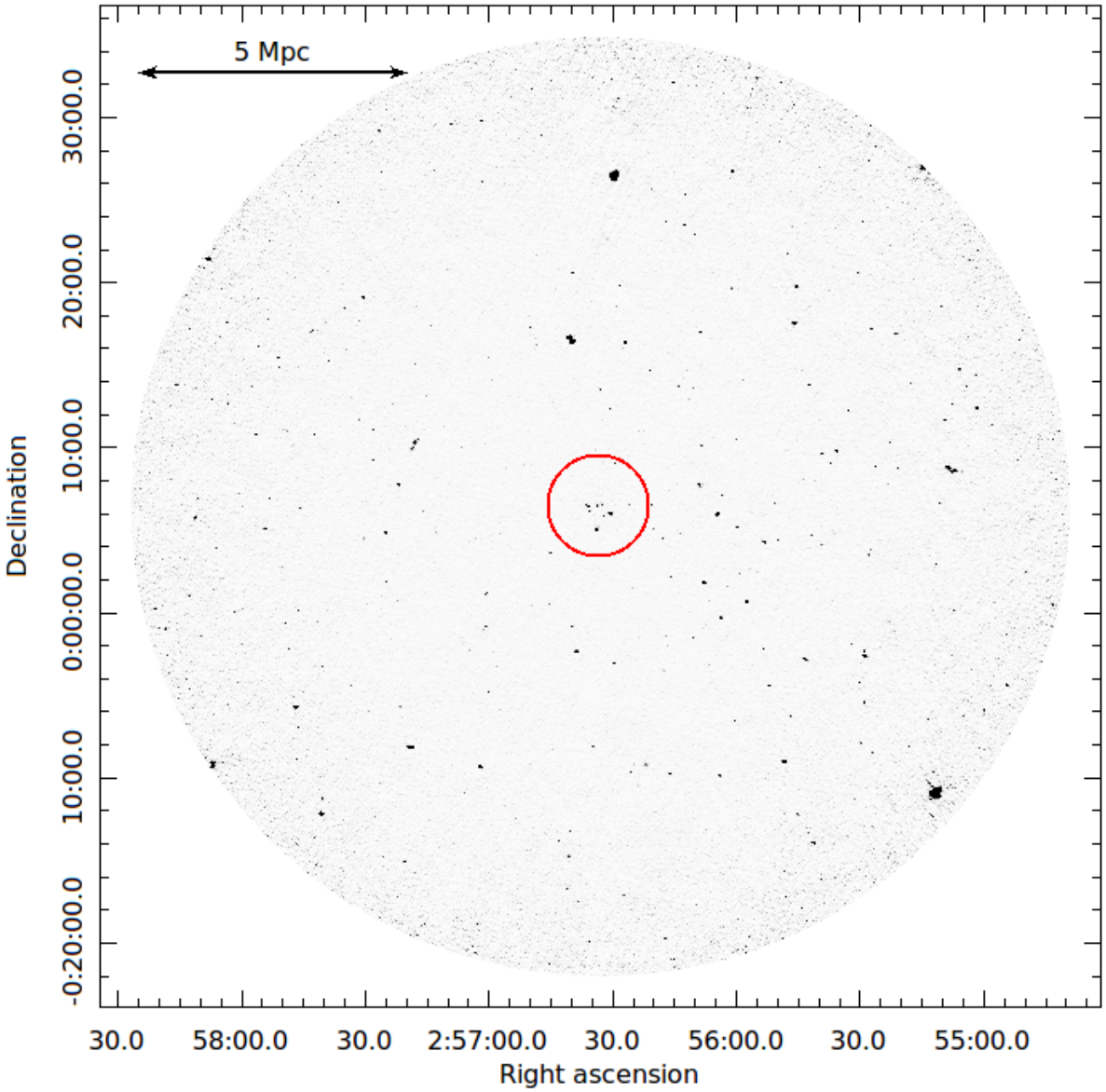

Figure A.5: Full-resolution, primary beam corrected image of ACT-CL J0256.5+0006. The physical scale at the cluster redshift of $z = 0.363$ is shown in the top left corner. The red circle denotes the SZ cluster scale, $\theta_{500} = 3.1'$, centred on the SZ peak. The central rms map noise is 28.1 μJy beam^{-1}.

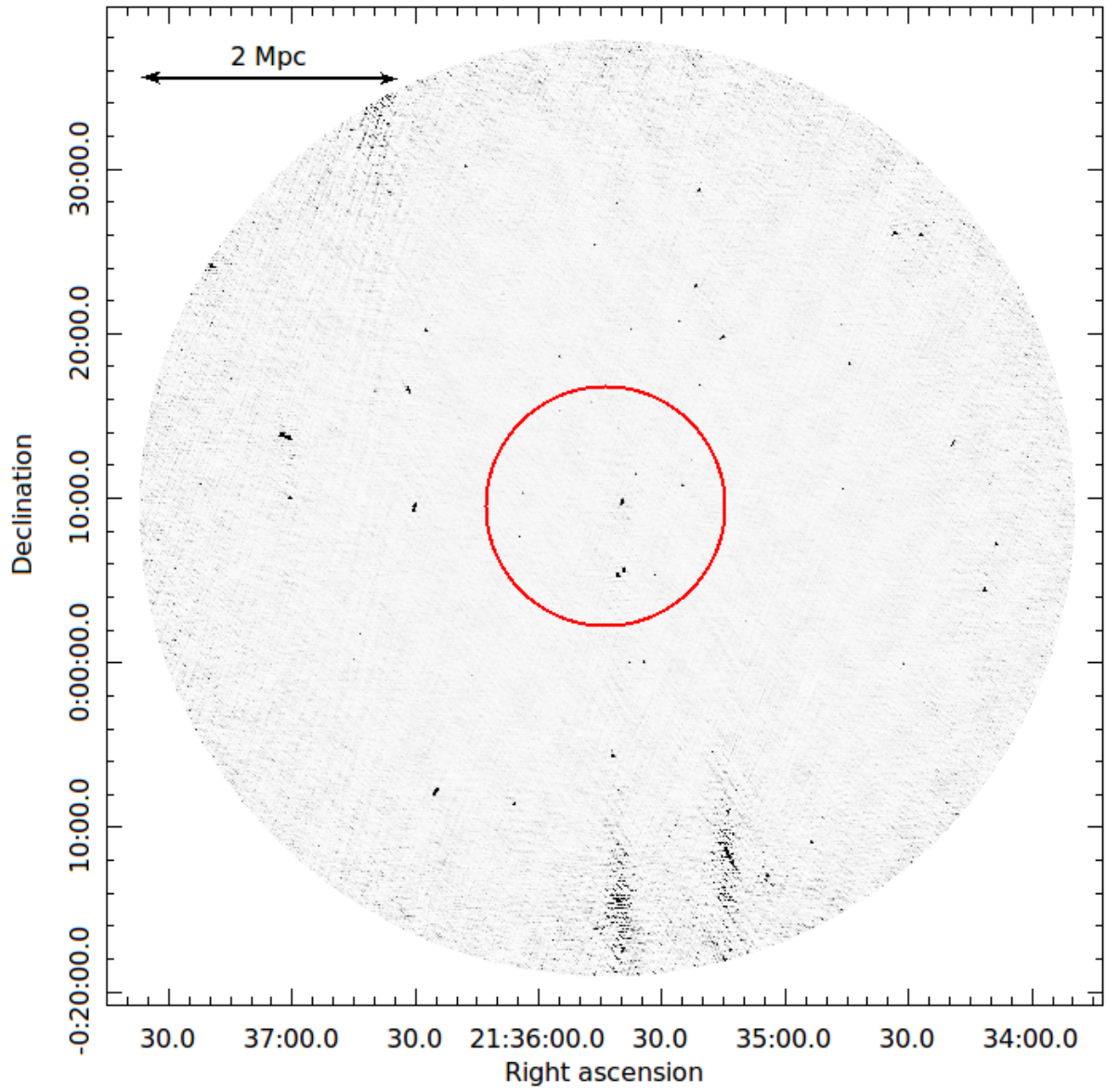

Figure A.6: Full-resolution, primary beam corrected image of ACT-CL J2135.7+0009. The physical scale at the cluster redshift of $z = 0.117$ is shown in the top left corner. The red circle denotes the SZ cluster scale, $\theta_{500} = 7.3'$, centred on the SZ peak. The central rms map noise is 98.7 μJy beam^{-1}.

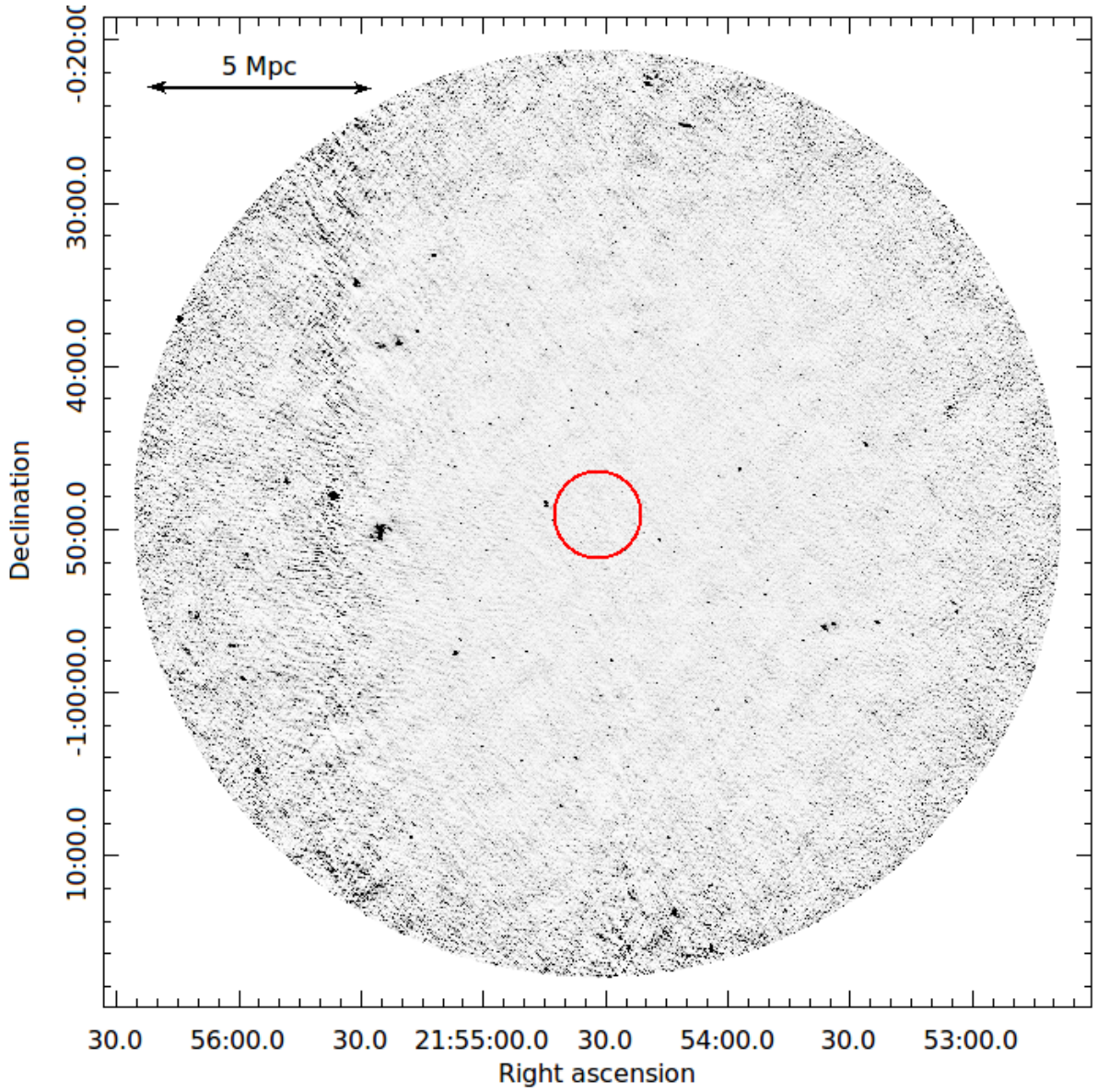

Figure A.7: Full-resolution, primary beam corrected image of ACT-CL J2154.5−0049. The physical scale at the cluster redshift of $z = 0.488$ is shown in the top left corner. The red circle denotes the SZ cluster scale, $\theta_{500} = 2.7'$, centred on the SZ peak. The central rms map noise is 45.8 μJy beam^{-1}.

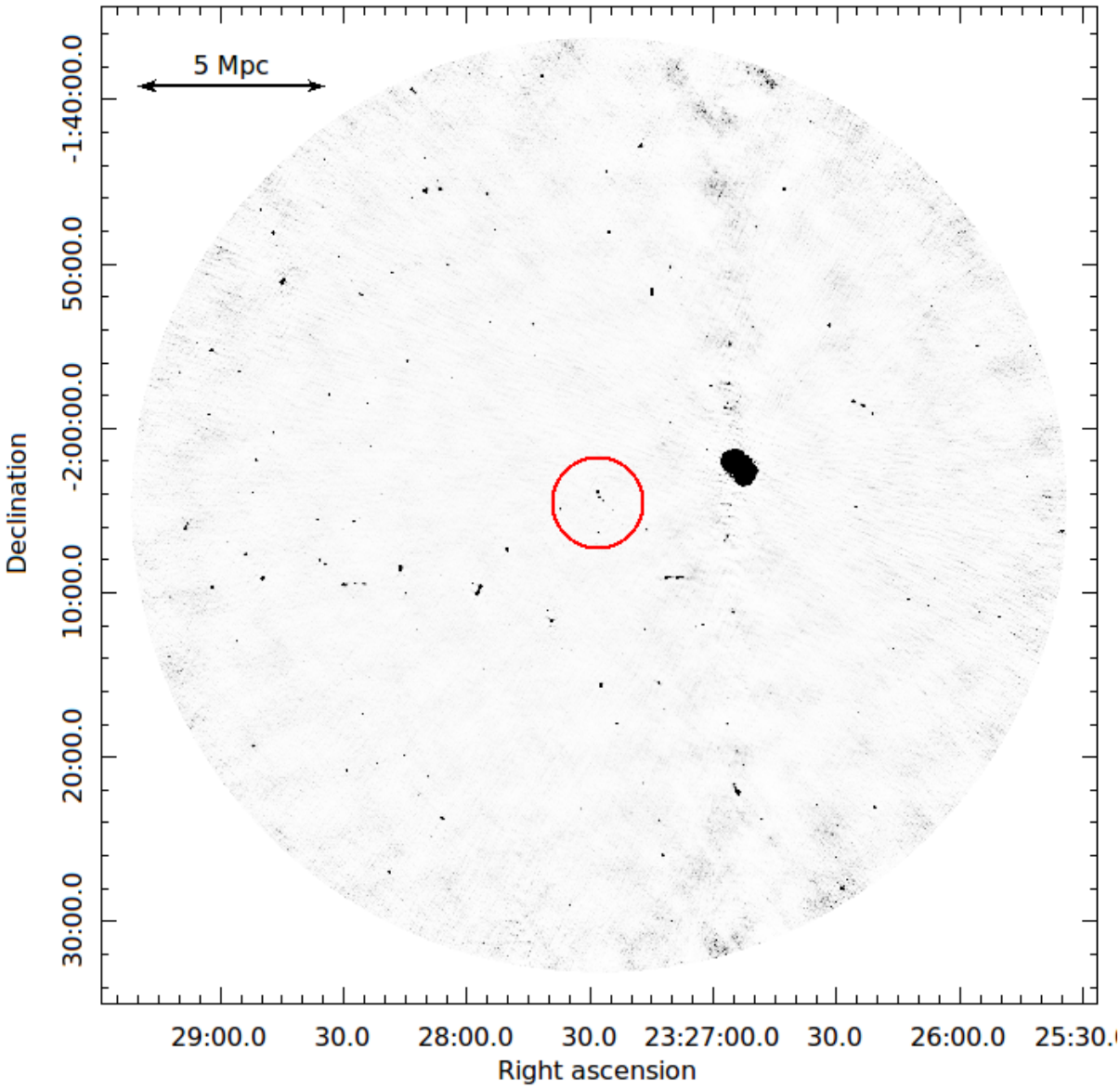

Figure A.8: Full-resolution, primary beam corrected image of ACT-CL J2327.4−0204. The physical scale at the cluster redshift of $z = 0.705$ is shown in the top left corner. The red circle denotes the SZ cluster scale, $\theta_{500} = 2.8'$, centred on the SZ peak. The central rms map noise is 57.2 μJy beam^{-1}. The bright extended source to the West of the cluster region is the nearby radio galaxy PKS 2324-02 ($z = 0.188$, see section 3.3.1.2).

APPENDIX B

MERGER MODEL FOR ACT-CL J0256.5+0006

In Chapter 4 we set up a simple merger model for the the merging components of ACT-CL J0256.5+0006 under the simplifying assumptions of a purely gravitational two-body interaction, i.e. pressure free and no external effects such as dynamical friction, and that the subcluster can be approximated by a point mass. The model is set up in the rest frame of the main component, whose mass distribution is defined by a NFW mass profile (Navarro et al., 1997):

$$M(r) = M_0 \left[\ln(1 + c_r) - \frac{c_r}{1 + c_r} \right] \tag{B.1}$$

where $M_0 = 4\pi\rho_0 \left(\frac{r}{c_r} \right)^3$ and c_r is the mass concentration at a given radius. The model thus depends on the infall velocity v of the subcluster and the physical separation d between the two components. Here we show the derivation of the physical expression for v(d) used in §4.6.

The gravitational law of a two-body interaction in which one component has a point mass gives:

$$\frac{d\mathbf{v}}{dt} = -\frac{GM(r)}{d^2}\hat{\mathbf{i}} \tag{B.2}$$

where the unit vector $\hat{\mathbf{i}}$ points in the direction of increasing d and is oriented along the merger axis. Assuming the two cluster components were an almost infinite distance apart well before the merger, and taking r_{200} to be sufficiently similar to the virialised cluster radius, there are two possible scenarios:

- $d > r_{200}$: the merger has yet to begin and the main cluster component can be approximated by a point mass located at its centre. The subcluster velocity in this case id $v = \sqrt{\frac{2GM_{200}}{d}}$.
- $d < r_{200}$: here the mass distribution of the main component given in equation B.1 is significant and needs to be taken into account.

For the second scenario, the law of gravitation can then be written as

$$\frac{vdv}{dr} = -GM_0 \frac{dr}{r^2} \left[\ln(1 + c_r) - \frac{c_r}{1 + c_r} \right] \tag{B.3}$$

Let $c_r = \frac{r}{r_s}$, with $r_s = \frac{r_{200}}{c_{200}}$ being a specific scale radius. Integrating equation B.3 inwards from r_{200} to d gives:

$$\begin{aligned}
\int_{v_{200}}^{v} v'dv' &= -GM_0 \int_{r_{200}}^{d} \frac{dr}{r^2} \left[\ln(1 + \frac{r}{r_s}) - \frac{r/r_s}{1 + r/r_s} \right] \qquad \text{(B.4)} \\
\frac{1}{2}\left(v^2 - v_{200}^2\right) &= -GM_0 \left[-\frac{1}{r} \ln(1 + \frac{r}{r_s}) \right]_{r_{200}}^{d} \\
&= \frac{GM_0}{r_s} \left[\left(\frac{d}{r_s}\right)^{-1} \ln(1 + \frac{d}{r_s}) - \left(\frac{r_{200}}{r_s}\right)^{-1} \ln(1 + \frac{r_{200}}{r_s}) \right] \\
v^2 &= v_{200}^2 + \frac{2GM_0}{r_s} \left[\left(\frac{d}{r_s}\right)^{-1} \ln(1 + \frac{d}{r_s}) - c_{200} \ln(1 + c_{200}) \right]
\end{aligned}$$

Writing v_{200} in terms of the known properties of the main component, we have an analytical expression for the subcluster infall velocity given a physical component separation:

$$v^2(d) = \frac{2GM_{200}}{r_{200}} + \frac{2GM_0}{r_s} \left[\frac{\ln(1 + d/r_s)}{d/r_s} - \frac{\ln(1 + c_{200})}{c_{200}} \right] \tag{B.5}$$

with $M_0 = 4\pi\rho_0 r_s^3$. For small d, when the subcluster is close to the core of the main component, the binomial theorem applies:

$$\frac{\ln(1+d/r_s)}{d/r_s} = \frac{x - x^2 + ...}{x} \approx 1 \qquad \left(x = \frac{d}{r_s} \ll 1\right) \tag{B.6}$$

which implies

$$v^2(d=0) = v_{200}^2 + \frac{2GM_0}{r_s}\left[1 - \frac{\ln(1+c_{200})}{c_{200}}\right]. \tag{B.7}$$

Here the expression in square brackets is positive for all values of c_{200}. The expression in equation B.5 can be numerically integrated to obtain timescales associated with different physical separations between the cluster components (see §4.7).

APPENDIX C

LISTS OF MULTIPLE IMAGES IDENTIFIED IN THE HUBBLE FRONTIER FIELDS IMAGES

We present here the lists of multiple images identified in the Hubble Frontier Fields data for clusters MACSJ0416.1-2403 and MACSJ1149.6+2223.

Table C.1: Multiply imaged systems identified in the HFF data for MACSJ0416. Asterisks indicate the image identifications which are less confident. + Even though we have not confirmed system 4 spectroscopically, we assume that systems 3 and 4 correspond to different sub-structures of the same background source. Some of the magnitudes are not quoted because we were facing deblending issues that did not allow us to get reliable measurements. The flux magnification factors come from the best-fit mass model (see section 6.1.1.3), with errors derived from MCMC sampling.

ID	R.A.	Dec	$z_{\rm spec}$	$z_{\rm model}$	F814W	μ
1.1	64.04075	-24.061592	1.896	–	25.2	5.1 ± 0.2
1.2	64.043479	-24.063542	1.896	–	24.2	18.9 ± 5.1
1.3	64.047354	-24.068669	1.896	–	26.0	3.1 ± 0.1

Continued on next page

Table C.1 – *Continued from previous page*

ID	R.A.	Dec	$z_{\rm spec}$	$z_{\rm model}$	F814W	μ
2.1	64.041183	-24.061881	1.8925	–	23.6	6.0 ± 0.3
2.2	64.043004	-24.063036	1.8925	–	25.2	6.4 ± 0.5
2.3	64.047475	-24.06885	1.8925	–	24.1	3.0 ± 0.1
3.1	64.030783	-24.067117	1.9885	–	25.5	3.3 ± 0.1
3.2	64.035254	-24.070981	1.9885	–	26.6	2.2 ± 0.1
3.3	64.041817	-24.075711	1.9885	–	25.2	3.2 ± 0.1
+4.1	64.030825	-24.067225	–	1.9	24.3	3.4 ± 0.1
+4.2	64.035154	-24.070981	–	1.9	22.9	2.1 ± 0.1
+4.3	64.041879	-24.075856	–	1.9	24.3	3.0 ± 0.1
5.2	64.032663	-24.068669	–	1.6	24.6	14.6 ± 1.6
5.3	64.033513	-24.069447	–	1.6	23.5	> 30
7.1	64.0398	-24.063092	2.0854	–	25.0	10.8 ± 1.0
7.2	64.040633	-24.063561	2.0854	–	25.1	23.3 ± 5.4
7.3	64.047117	-24.071108	2.0854	–	28.0	2.6 ± 0.1
8.1	64.036596	-24.066125	–	2.2	25.8	25.9 ± 4.6
8.2	64.036833	-24.066342	–	2.2	24.0	> 30
9.1	64.027025	-24.078583	–	2.25	25.6	23.0 ± 3.0
9.2	64.027521	-24.079106	–	2.25	25.5	> 30
9.3	64.036453	-24.083973	–	2.25	28.0	2.5 ± 0.1
10.1	64.026017	-24.077156	2.2982	–	24.7	6.5 ± 0.3
10.2	64.028471	-24.079756	2.2982	–	24.9	5.2 ± 0.2
10.3	64.036692	-24.083901	2.2982	–	25.6	2.4 ± 0.1
11.1	64.039208	-24.070367	–	1.1	24.3	21.1 ± 5.1
11.2	64.038317	-24.069753	–	1.1	24.0	> 30
11.3	64.034259	-24.066018	–	1.1	27.0	3.3 ± 0.1
12.1	64.038263	-24.073696	–	1.8	25.0	> 30
12.2	64.037686	-24.073294	–	1.8	25.8	> 30
12.3	64.029117	-24.066742	–	1.7	–	2.4 ± 0.1
13.1	64.027579	-24.072786	3.2226	–	25.2	7.5 ± 0.5
13.2	64.032129	-24.075169	3.2226	–	23.8	3.1 ± 0.1
13.3	64.040338	-24.081544	3.2226	–	25.5	2.2 ± 0.1
14.1	64.026233	-24.074339	2.0531	–	23.4	4.1 ± 0.1
14.2	64.031042	-24.078961	2.0531	–	23.6	2.4 ± 0.1
14.3	64.035825	-24.081328	2.0531	–	23.2	4.1 ± 0.1
15.1	64.02686	-24.075745	–	2.8	26.2	7.3 ± 0.4
15.2	64.029438	-24.078583	–	2.8	25.3	3.8 ± 0.1
15.3	64.038217	-24.082993	–	2.8	25.9	2.4 ± 0.1
16.1	64.024058	-24.080894	1.9644	–	23.9	6.2 ± 0.2
16.2	64.028329	-24.084542	1.9644	–	22.4	8.7 ± 0.7
16.3	64.031596	-24.085769	–	1.9	24.2	3.8 ± 0.1

Continued on next page

Table C.1 – *Continued from previous page*

ID	R.A.	Dec	$z_{\rm spec}$	$z_{\rm model}$	F814W	μ
17.1	64.029875	-24.086364	2.2181	–	23.4	10.2 ± 0.8
17.2	64.028608	-24.085986	2.2181	–	–	6.7 ± 0.3
17.3	64.023329	-24.081581	2.2181	–	24.0	5.8 ± 0.2
18.1	64.026075	-24.084233	–	2.1	25.6	28.6 ± 6.1
18.2	64.025067	-24.08335	–	2.1	25.4	26.0 ± 3.9
18.3	64.0309	-24.086744	–	2.1	27.1	3.8 ± 0.1
23.1	64.044546	-24.0721	–	2.1	24.8	3.6 ± 0.1
23.2	64.039604	-24.066631	–	2.1	25.2	1.4 ± 0.1
23.3	64.034342	-24.063742	–	2.1	25.1	3.1 ± 0.1
24.1	64.040915	-24.062959	–	2.2	26.9	> 30
24.2	64.041066	-24.063057	–	2.2	26.0	> 30
24.3	64.048893	-24.070871	–	2.2	26.6	2.3 ± 0.1
25.1	64.044891	-24.061068	–	2.9	25.4	14.4 ± 2.5
25.2	64.045448	-24.061409	–	2.9	25.5	6.8 ± 0.6
25.3	64.048254	-24.064513	–	2.9	24.9	> 30
*25.4	64.049697	-24.066948	–	2.9	25.8	3.3 ± 0.1
26.1	64.04647	-24.060393	–	5.9	26.2	> 30
26.2	64.046963	-24.060793	–	5.9	27.3	> 30
*26.3	64.049089	-24.062876	–	5.9	27.6	> 30
27.1	64.048159	-24.066959	–	2.2	24.3	5.0 ± 0.3
27.2	64.047465	-24.066026	–	2.2	23.3	18.0 ± 4.9
27.3	64.042226	-24.060543	–	2.2	25.6	4.6 ± 0.2
28.1	64.036457	-24.067026	–	1.0	23.9	15.4 ± 2.5
28.2	64.03687	-24.067498	–	1.0	24.1	12.6 ± 1.8
28.3	64.040923	-24.071151	–	1.0	26.4	6.8 ± 0.3
29.1	64.034272	-24.063032	–	2.4	25.4	2.8 ± 0.1
29.2	64.040131	-24.066757	–	2.4	24.7	4.0 ± 0.2
29.3	64.04461	-24.071482	–	2.4	25.8	3.7 ± 0.1
30.1	64.033088	-24.081806	–	4.5	26.9	> 30
30.2	64.032649	-24.081546	–	4.5	27.3	17.5 ± 2.7
31.1	64.023833	-24.077621	–	1.9	26.4	3.7 ± 0.1
31.2	64.030507	-24.082725	–	1.9	26.5	4.7 ± 0.2
31.3	64.032456	-24.083821	–	1.9	25.6	5.3 ± 0.2
32.1	64.02413	-24.08164	–	1.9	26.3	7.2 ± 0.3
32.2	64.029591	-24.085572	–	1.9	–	9.4 ± 0.6
32.3	64.030468	-24.085895	–	1.9	28.2	5.1 ± 0.2
33.1	64.028427	-24.082995	–	5.9	24.8	6.5 ± 0.3
33.2	64.035052	-24.085486	–	5.9	28.1	2.9 ± 0.1
33.3	64.02298	-24.077275	–	5.9	26.5	4.6 ± 0.2
34.1	64.029254	-24.073289	–	3.2	26.5	11.7 ± 1.0

Continued on next page

Table C.1 – *Continued from previous page*

ID	R.A.	Dec	$z_{\rm spec}$	$z_{\rm model}$	F814W	μ
34.2	64.030798	-24.07418	–	3.2	26.8	18.9 ± 2.5
35.1	64.037492	-24.083636	–	4.0	26.5	2.6 ± 0.1
35.2	64.029418	-24.079861	–	4.0	28.2	2.8 ± 0.1
35.3	64.024937	-24.075016	–	4.0	26.5	4.3 ± 0.2
36.1	64.02627	-24.075507	–	3.4	25.8	6.4 ± 0.3
36.2	64.03842	-24.083428	–	3.4	26.7	2.3 ± 0.1
36.3	64.02938	-24.0789	–	3.4	–	2.4 ± 0.1
36.4	64.029184	-24.079041	–	3.4	–	2.0 ± 0.03
37.1	64.033791	-24.082863	–	3.7	26.4	6.4 ± 0.4
37.2	64.031419	-24.081613	–	3.7	25.5	4.9 ± 0.2
37.3	64.022507	-24.07431	–	3.7	26.8	2.9 ± 0.1
38.1	64.033625	-24.083178	–	3.2	27.3	5.7 ± 0.3
38.2	64.031255	-24.081905	–	3.2	25.5	5.1 ± 0.3
38.3	64.022701	-24.074589	–	3.2	28.0	2.9 ± 0.1
39.1	64.037335	-24.072924	–	1.2	22.1	26.8 ± 11.8
39.2	64.037731	-24.073135	–	1.2	25.2	14.1 ± 2.2
40.1	64.037349	-24.063062	–	3.4	28.8	5.5 ± 0.2
40.2	64.040346	-24.064271	–	3.4	28.3	4.4 ± 0.2
40.3	64.047642	-24.07443	–	3.4	28.4	2.3 ± 0.1
41.1	64.037183	-24.063073	–	3.4	28.4	5.2 ± 0.2
41.2	64.040369	-24.064369	–	3.4	27.2	3.9 ± 0.1
41.3	64.047605	-24.074313	–	3.4	28.2	2.3 ± 0.1
42.1	64.045994	-24.070768	–	2.6	27.1	3.3 ± 0.1
42.2	64.042073	-24.065547	–	2.6	25.3	2.8 ± 0.1
42.3	64.035786	-24.061938	–	2.6	26.7	2.9 ± 0.1
43.1	64.035667	-24.08205	–	2.5	27.0	3.8 ± 0.1
43.2	64.031195	-24.079959	–	2.5	25.2	3.3 ± 0.1
43.3	64.024425	-24.073603	–	2.5	27.1	3.1 ± 0.1
44.1	64.045259	-24.062757	–	3.7	25.1	12.3 ± 1.9
44.2	64.041543	-24.059997	–	3.7	25.6	7.2 ± 0.4
44.3	64.049237	-24.068168	–	3.7	27.4	3.1 ± 0.1
45.1	64.035673	-24.079918	–	1.9	26.4	5.4 ± 0.2
45.2	64.025766	-24.072231	–	1.9	25.0	4.1 ± 0.1
45.3	64.032893	-24.076993	–	1.9	–	1.7 ± 0.03
46.1	64.038256	-24.080451	–	2.2	28.3	2.9 ± 0.1
46.2	64.026402	-24.072239	–	2.2	27.6	3.9 ± 0.1
46.3	64.033057	-24.076204	–	2.2	–	3.9 ± 0.1
47.1	64.026328	-24.076694	–	3.5	25.3	12.3 ± 1.1
47.2	64.028329	-24.078999	–	3.5	27.2	6.7 ± 0.3
47.3	64.038206	-24.083719	–	3.5	27.8	2.3 ± 0.1

Continued on next page

Table C.1 – *Continued from previous page*

ID	R.A.	Dec	$z_{\rm spec}$	$z_{\rm model}$	F814W	μ
48.1	64.035489	-24.084668	–	4.0	26.1	2.8 ± 0.1
48.2	64.029244	-24.081802	–	4.0	24.0	3.8 ± 0.1
48.3	64.023416	-24.076122	–	4.0	25.3	3.8 ± 0.1
49.1	64.033944	-24.074569	–	4.0	29.3	2.4 ± 0.1
49.2	64.040175	-24.079864	–	4.0	27.0	2.7 ± 0.1
49.3	64.026833	-24.069967	–	4.0	24.9	6.6 ± 0.3
50.1	64.03479	-24.074585	–	3.3	28.5	3.3 ± 0.1
50.2	64.039683	-24.078869	–	3.3	28.4	3.2 ± 0.1
51.1	64.04016	-24.08029	–	4.0	26.3	2.5 ± 0.1
51.2	64.033663	-24.074752	–	4.0	26.3	2.4 ± 0.1
51.3	64.02662	-24.070494	–	4.0	24.9	4.3 ± 0.1
52.1	64.045857	-24.06583	–	4.5	25.9	10.5 ± 1.7
52.2	64.047698	-24.068668	–	4.5	27.1	3.9 ± 0.2
52.3	64.037724	-24.059826	–	4.5	26.6	2.9 ± 0.1
53.1	64.046023	-24.0688	–	3.0	25.9	5.1 ± 0.3
53.2	64.044776	-24.066682	–	3.0	24.4	> 30
53.3	64.036197	-24.060643	–	3.0	26.5	2.6 ± 0.1
54.1	64.046789	-24.071342	–	2.4	27.0	2.8 ± 0.1
54.2	64.041376	-24.064519	–	2.4	26.1	3.3 ± 0.1
54.3	64.037157	-24.062423	–	2.4	26.9	3.7 ± 0.1
55.1	64.035233	-24.064726	–	2.6	28.1	4.9 ± 0.2
55.2	64.04607	-24.075174	–	2.6	28.3	2.3 ± 0.04
55.3	64.038514	-24.065965	–	2.6	25.5	5.2 ± 0.2
56.1	64.035676	-24.083589	–	3.3	28.2	3.1 ± 0.1
56.2	64.030097	-24.080924	–	3.3	28.3	3.1 ± 0.1
56.3	64.023847	-24.074998	–	3.3	28.3	3.5 ± 0.1
57.1	64.026224	-24.076036	–	3.0	26.4	6.2 ± 0.3
57.2	64.028843	-24.079126	–	3.0	26.7	3.5 ± 0.1
58.1	64.025187	-24.073582	–	3.2	27.6	3.7 ± 0.1
58.2	64.03773	-24.08239	–	3.2	27.4	3.0 ± 0.1
58.3	64.030481	-24.07922	–	3.2	25.3	2.2 ± 0.1
59.1	64.035851	-24.072799	–	2.0	27.8	8.2 ± 0.7
59.2	64.039936	-24.075622	–	2.0	27.9	6.0 ± 0.3
59.3	64.029105	-24.067658	–	2.0	28.2	2.9 ± 0.1
60.1	64.026724	-24.07372	–	4.1	27.7	5.6 ± 0.3
60.2	64.039708	-24.082514	–	4.1	28.3	2.2 ± 0.1
60.3	64.030984	-24.077181	–	4.1	–	20.7 ± 0.9
61.1	64.026732	-24.07354	–	4.1	27.7	5.6 ± 0.3
61.2	64.039768	-24.08236	–	4.1	28.0	2.2 ± 0.1
61.3	64.030593	-24.07776	–	4.1	28.8	3.7 ± 0.1

Continued on next page

Table C.1 – *Continued from previous page*

ID	R.A.	Dec	$z_{\rm spec}$	$z_{\rm model}$	F814W	μ
62.1	64.026889	-24.07961	–	3.3	25.5	24.1 ± 3.6
62.2	64.025993	-24.078892	–	3.3	26.4	16.5 ± 1.7
62.3	64.036488	-24.084935	–	3.3	28.2	2.4 ± 0.1
63.1	64.025535	-24.07665	–	3.9	26.5	6.7 ± 0.4
63.2	64.028147	-24.079648	–	3.9	27.2	5.1 ± 0.2
63.3	64.037925	-24.084479	–	3.9	27.8	2.3 ± 0.1
64.1	64.0431	-24.07759	–	2.8	27.1	2.4 ± 0.1
64.2	64.031139	-24.067177	–	2.8	28.0	4.1 ± 0.1
65.1	64.042589	-24.075532	–	5.0	26.8	3.6 ± 0.1
65.2	64.028858	-24.064627	–	5.0	26.9	2.3 ± 0.1
65.3	64.037768	-24.071656	–	5.0	28.0	7.3 ± 0.4
66.1	64.038101	-24.082315	–	2.4	28.8	2.6 ± 0.1
66.2	64.026635	-24.074675	–	2.4	27.6	5.0 ± 0.2
67.1	64.038075	-24.082404	–	3.2	28.7	2.7 ± 0.1
67.2	64.025451	-24.073651	–	3.2	27.7	3.9 ± 0.1
67.3	64.030363	-24.079019	–	3.2	26.5	2.0 ± 0.1
68.1	64.036098	-24.073362	–	2.8	26.3	5.5 ± 0.4
68.2	64.040352	-24.076481	–	2.8	23.7	6.4 ± 0.3
68.3	64.028017	-24.06727	–	2.8	26.8	2.6 ± 0.1
69.1	64.036256	-24.074225	–	1.6	26.9	16.1 ± 3.1
69.2	64.037681	-24.07526	–	1.6	28.2	10.6 ± 1.0
69.3	64.028759	-24.069109	–	1.6	28.1	3.1 ± 0.1
70.1	64.03836	-24.072385	–	1.5	25.6	> 30
70.2	64.03864	-24.07252	–	1.5	27.2	19.4 ± 3.5
70.3	64.0321	-24.06558	–	1.5	27.9	3.0 ± 0.1
71.1	64.027865	-24.077908	–	4.6	28.5	> 30
71.2	64.02741	-24.077382	–	4.6	27.7	28.6 ± 4.5
72.1	64.031937	-24.071316	–	2.6	28.2	12.7 ± 1.4
72.2	64.030952	-24.07048	–	2.6	28.1	14.4 ± 1.9
73.1	64.043712	-24.062603	–	2.4	27.4	18.4 ± 4.5
73.2	64.041861	-24.061243	–	2.4	29.3	6.2 ± 0.4

Table C.2: Multiply imaged systems identified in the HFF data for MACSJ1149. Thanks to the VLT/MUSE data, we were able to revise spectroscopic redshift of system #1, from z = 1.491 as in Smith et al. (2009) to z = 1.4888. indicate the different components of system #1 we have used for our model, following the decomposition presented in Rau et al. (2014). We include the predicted magnification given by our model. Some of the magnitudes are not quoted because we were facing deblending issues that did not allow us to get reliable measurements. The flux magnification factors come from our best-fit mass model (see section 6.2.3), with errors derived from MCMC sampling.

ID	R.A.	Dec	z	mag_{F814W}	μ
+1.1	177.39700	22.396007	1.4888	22.46 ± 0.01	3.7 ± 0.1
+1.2	177.39941	22.397438	1.4888	23.39 ± 0.01	4.1 ± 0.1
+1.3	177.40341	22.402426	1.4888	22.73 ± 0.01	9.7 ± 0.3
2.1	177.40243	22.389739	1.894	26.46 ± 0.02	4.6 ± 0.1
2.2	177.40607	22.392484	1.894	24.4 ± 0.01	> 20
2.3	177.40657	22.392881	1.894	24.49 ± 0.01	18.5 ± 1.6
3.1	177.39076	22.399840	3.128	23.36 ± 0.0	10.5 ± 0.4
3.2	177.39272	22.403074	3.128	22.77 ± 0.0	10.3 ± 0.4
3.3	177.40129	22.407182	3.128	24.01 ± 0.01	4.3 ± 0.1
4.1	177.39301	22.396826	2.95	25.41 ± 0.01	–
4.2	177.39440	22.400729	2.95	–	7.4 ± 0.2
4.3	177.40419	22.406120	2.95	25.96 ± 0.03	3.4 ± 0.1
5.1	177.39976	22.393062	2.79	25.15 ± 0.01	15.5 ± 0.7
5.2	177.40111	22.393824	2.79	25.01 ± 0.01	12.0 ± 0.5
5.3	177.40794	22.403538	2.79	26.12 ± 0.02	4.3 ± 0.1
6.1	177.39972	22.392545	2.66 ± 0.02	26.37 ± 0.03	9.0 ± 0.3
6.2	177.40181	22.393858	–	26.4 ± 0.02	8.1 ± 0.3
6.3	177.40804	22.402505	–	27.41 ± 0.06	4.7 ± 0.1
7.1	177.39895	22.391332	2.79 ± 0.02	25.87 ± 0.02	4.5 ± 0.1
7.2	177.40339	22.394269	–	26.16 ± 0.02	4.6 ± 0.1
7.3	177.40759	22.401243	–	26.3 ± 0.03	4.2 ± 0.1
8.1	177.39849	22.394351	2.81 ± 0.02	26.12 ± 0.02	> 20
8.2	177.39978	22.395055	–	24.7 ± 0.04	15.1 ± 0.6
8.3	177.40709	22.404720	–	26.03 ± 0.02	3.2 ± 0.1
9.1	177.40515	22.426221	0.981	24.81 ± 0.01	1.7 ± 0.1
9.2	177.40387	22.427217	0.981	24.57 ± 0.01	4.9 ± 1.3
9.3	177.40323	22.427221	0.981	24.14 ± 0.0	2.9 ± 0.3
9.4	177.40365	22.426408	0.981	25.11 ± 0.01	3.4 ± 0.3
10.1	177.40447	22.425508	1.34 ± 0.01	25.99 ± 0.01	3.0 ± 0.2
10.2	177.40362	22.425629	–	26.09 ± 0.01	2.2 ± 0.1
10.3	177.40220	22.426611	–	26.5 ± 0.02	1.8 ± 0.1

Continued on next page

Table C.2 – *Continued from previous page*

ID	R.A.	Dec	z	mag_{F814W}	μ
13.1	177.40370	22.397787	1.28 ± 0.01	25.87 ± 0.03	> 20
13.2	177.40282	22.396656	–	26.14 ± 0.02	11.9 ± 0.6
13.3	177.40003	22.393857	–	25.78 ± 0.02	5.3 ± 0.1
14.1	177.39166	22.403504	3.50 ± 0.06	27.06 ± 0.03	13.4 ± 0.7
14.2	177.39084	22.402624	–	27.13 ± 0.03	> 20
15.1	177.40922	22.387695	3.58 ± 0.08	26.57 ± 0.03	7.5 ± 0.9
15.2	177.41034	22.388745	–	25.86 ± 0.02	> 20
15.3	177.40624	22.385349	–	27.19 ± 0.04	3.8 ± 0.1
16.1	177.40971	22.387662	2.65 ± 1.45	27.19 ± 0.04	> 20
16.2	177.40989	22.387828	–	27.34 ± 0.04	> 20
17.1	177.40994	22.387232	6.28 ± 0.17	28.02 ± 0.06	5.5 ± 0.4
17.2	177.41124	22.388457	–	28.14 ± 0.07	15.2 ± 1.1
17.3	177.40658	22.384483	–	28.46 ± 0.08	3.6 ± 0.1
18.1	177.40959	22.386660	7.76 ± 0.16	28.51 ± 0.23	3.4 ± 0.2
18.2	177.41208	22.389057	–	–	8.3 ± 0.3
18.3	177.40669	22.384319	–	–	3.6 ± 0.1
21.1	177.39284	22.412870	2.48 ± 0.04	26.38 ± 0.02	> 20
21.2	177.39353	22.413083	–	22.52 ± 0.06	> 20
21.3	177.39504	22.412686	–	27.5 ± 0.04	14.6 ± 1.1
22.1	177.40402	22.392900	3.216	27.86 ± 0.05	5.0 ± 0.2
22.2	177.40906	22.400233	3.216	27.85 ± 0.05	3.9 ± 0.1
22.3	177.40016	22.390150	3.216	27.57 ± 0.05	4.1 ± 0.1
26.1	177.40475	22.425978	1.49 ± 0.03	26.87 ± 0.03	3.5 ± 0.4
26.2	177.40361	22.426078	–	26.44 ± 0.03	4.0 ± 0.5
26.3	177.40274	22.426936	–	26.7 ± 0.02	2.5 ± 0.1
29.1	177.40799	22.389056	2.76 ± 0.05	27.99 ± 0.07	10.7 ± 2.0
29.2	177.40907	22.390406	–	27.55 ± 0.04	9.2 ± 0.4
29.3	177.40451	22.386702	–	28.56 ± 0.08	4.0 ± 0.1
31.1	177.40215	22.396747	2.78 ± 0.03	26.86 ± 0.03	2.3 ± 0.1
31.2	177.39529	22.391833	–	26.2 ± 0.02	3.2 ± 0.1
31.3	177.40562	22.402439	–	26.1 ± 0.02	4.2 ± 0.1
34.1	177.40820	22.388116	3.42 ± 0.08	27.28 ± 0.04	4.3 ± 0.5
34.2	177.41037	22.390621	–	27.35 ± 0.05	6.7 ± 0.2
34.3	177.40518	22.386031	–	27.66 ± 0.06	4.0 ± 0.1

BIBLIOGRAPHY

Abell, G. O. (1958). The Distribution of Rich Clusters of Galaxies. *Astrophys. J. Supp.*, 3:211.

Abell, G. O., Corwin, Jr., H. G., and Olowin, R. P. (1989). A catalog of rich clusters of galaxies. *Astrophys. J. Supp.*, 70:1–138.

Ackermann, M., Ajello, M., Baldini, L., Ballet, J., Barbiellini, G., Baring, M. G., Bastieri, D., Bechtol, K., Bellazzini, R., Berenji, B., Bhat, P. N., Bissaldi, E., Blandford, R. D., Bonamente, E., Borgland, A. W., Bouvier, A., Bregeon, J., Brez, A., Briggs, M. S., Brigida, M., Bruel, P., Buehler, R., Buson, S., Caliandro, G. A., Cameron, R. A., Caraveo, P. A., Carrigan, S., Casandjian, J. M., Cecchi, C., Çelik, Ö., Charles, E., Chekhtman, A., Chiang, J., Ciprini, S., Claus, R., Cohen-Tanugi, J., Connaughton, V., Conrad, J., Cutini, S., Dermer, C. D., de Angelis, A., de Palma, F., Digel, S. W., Silva, E. d. C. e., Drell, P. S., Dubois, R., Favuzzi, C., Fegan, S. J., Ferrara, E. C., Frailis, M., Fukazawa, Y., Fusco, P., Gargano, F., Gasparrini, D., Gehrels, N., Germani, S., Giglietto, N., Giommi, P., Giordano, F., Giroletti, M., Glanzman, T., Godfrey, G., Granot, J., Grenier, I. A., Grove, J. E., Guillemot, L., Guiriec, S., Hadasch, D., Hays, E., Horan, D., Hughes, R. E., Jóhannesson, G., Johnson, A. S., Johnson, W. N., Kamae, T., Katagiri, H., Kippen, R. M., Knödlseder, J., Kocevski, D., Kuss, M., Lande, J., Latronico, L., Lee, S.-H., Llena Garde, M., Longo, F., Loparco, F., Lovellette, M. N., Lubrano, P., Makeev, A., Mazziotta, M. N., McBreen, S., McEnery, J. E., McGlynn, S., Meegan, C.,

Mehault, J., Mészáros, P., Michelson, P. F., Mizuno, T., Moiseev, A. A., Monte, C., Monzani, M. E., Moretti, E., Morselli, A., Moskalenko, I. V., Murgia, S., Nakajima, H., Nakamori, T., Naumann-Godo, M., Nolan, P. L., Norris, J. P., Nuss, E., Ohno, M., Ohsugi, T., Okumura, A., Omodei, N., Orlando, E., Ormes, J. F., Ozaki, M., Paciesas, W. S., Paneque, D., Panetta, J. H., Parent, D., Pelassa, V., Pepe, M., Pesce-Rollins, M., Petrosian, V., Piron, F., Porter, T. A., Preece, R., Racusin, J. L., Rainò, S., Rando, R., Rau, A., Razzano, M., Razzaque, S., Reimer, A., Reimer, O., Ripken, J., Roth, M., Ryde, F., Sadrozinski, H. F.-W., Sander, A., Scargle, J. D., Schalk, T. L., Sgrò, C., Siskind, E. J., Smith, P. D., Spandre, G., Spinelli, P., Stamatikos, M., Strickman, M. S., Suson, D. J., Tajima, H., Takahashi, H., Tanaka, T., Thayer, J. B., Thayer, J. G., Tibaldo, L., Torres, D. F., Tosti, G., Tramacere, A., Uehara, T., Usher, T. L., Vandenbroucke, J., van der Horst, A. J., Vasileiou, V., Vilchez, N., Vitale, V., von Kienlin, A., Waite, A. P., Wang, P., Wilson-Hodge, C., Winer, B. L., Wood, K. S., Wu, X. F., Yamazaki, R., Yang, Z., Ylinen, T., Ziegler, M., Fermi LAT Collaboration, and Fermi GBM Collaboration (2010). Fermi Observations of High-energy Gamma-ray Emission from GRB 090217A. *Astrophys. J. Lett.*, 717:L127–L132.

Adam, R., Comis, B., Bartalucci, I., Adane, A., Ade, P., André, P., Arnaud, M., Beelen, A., Belier, B., Benoît, A., Bideaud, A., Billot, N., Bourrion, O., Calvo, M., Catalano, A., Coiffard, G., D'Addabbo, A., Désert, F.-X., Doyle, S., Goupy, J., Hasnoun, B., Hermelo, I., Kramer, C., Lagache, G., Leclercq, S., Macías-Pérez, J.-F., Martino, J., Mauskopf, P., Mayet, F., Monfardini, A., Pajot, F., Pascale, E., Perotto, L., Pointecouteau, E., Ponthieu, N., Pratt, G. W., Revéret, V., Ritacco, A., Rodriguez, L., Savini, G., Schuster, K., Sievers, A., Triqueneaux, S., Tucker, C., and Zylka, R. (2015). High angular resolution Sunyaev-Zel'dovich observations of MACS J1423.8+2404 with NIKA: multi-wavelength analysis. *ArXiv e-prints*.

Akamatsu, H., Takizawa, M., Nakazawa, K., Fukazawa, Y., Ishisaki, Y., and Ohashi, T. (2012). X-Ray View of the Shock Front in the Merging Cluster Abell 3376 with Suzaku. *Pub. Astron. Soc. Japan*, 64:67.

Alam, S., Albareti, F. D., Allende Prieto, C., Anders, F., Anderson, S. F., Anderton, T., Andrews,

B. H., Armengaud, E., Aubourg, É., Bailey, S., and et al. (2015). The Eleventh and Twelfth Data Releases of the Sloan Digital Sky Survey: Final Data from SDSS-III. *Astrophys. J. Supp.*, 219:12.

Allen, D. A. (1976). An attempt to determine the circumstellar reddening law. *Mon. Not. R. Astron. Soc.*, 174:29P–33P.

Amendola, L., Campos, G. C., and Rosenfeld, R. (2007). Consequences of dark matter-dark energy interaction on cosmological parameters derived from typeIa supernova data. *Physical Review D.*, 75(8):083506.

Anderson, L., Aubourg, E., Bailey, S., Bizyaev, D., Blanton, M., Bolton, A. S., Brinkmann, J., Brownstein, J. R., Burden, A., Cuesta, A. J., da Costa, L. A. N., Dawson, K. S., de Putter, R., Eisenstein, D. J., Gunn, J. E., Guo, H., Hamilton, J.-C., Harding, P., Ho, S., Honscheid, K., Kazin, E., Kirkby, D., Kneib, J.-P., Labatie, A., Loomis, C., Lupton, R. H., Malanushenko, E., Malanushenko, V., Mandelbaum, R., Manera, M., Maraston, C., McBride, C. K., Mehta, K. T., Mena, O., Montesano, F., Muna, D., Nichol, R. C., Nuza, S. E., Olmstead, M. D., Oravetz, D., Padmanabhan, N., Palanque-Delabrouille, N., Pan, K., Parejko, J., Pâris, I., Percival, W. J., Petitjean, P., Prada, F., Reid, B., Roe, N. A., Ross, A. J., Ross, N. P., Samushia, L., Sánchez, A. G., Schlegel, D. J., Schneider, D. P., Scóccola, C. G., Seo, H.-J., Sheldon, E. S., Simmons, A., Skibba, R. A., Strauss, M. A., Swanson, M. E. C., Thomas, D., Tinker, J. L., Tojeiro, R., Magaña, M. V., Verde, L., Wagner, C., Wake, D. A., Weaver, B. A., Weinberg, D. H., White, M., Xu, X., Yèche, C., Zehavi, I., and Zhao, G.-B. (2012). The clustering of galaxies in the SDSS-III Baryon Oscillation Spectroscopic Survey: baryon acoustic oscillations in the Data Release 9 spectroscopic galaxy sample. *Mon. Not. R. Astron. Soc.*, 427:3435–3467.

Arnaud, M. and Evrard, A. E. (1999). The L_X-T relation and intracluster gas fractions of X-ray clusters. *Mon. Not. R. Astron. Soc.*, 305:631–640.

Arnaud, M., Pratt, G. W., Piffaretti, R., Böhringer, H., Croston, J. H., and Pointecouteau, E. (2010). The universal galaxy cluster pressure profile from a representative sample of nearby systems (REXCESS) and the Y_{SZ} - M_{500} relation. *Astron. Astrophys.*, 517:A92.

Arnouts, S., Walcher, C. J., Le Fèvre, O., Zamorani, G., Ilbert, O., Le Brun, V., Pozzetti, L., Bardelli, S., Tresse, L., Zucca, E., Charlot, S., Lamareille, F., McCracken, H. J., Bolzonella, M., Iovino, A., Lonsdale, C., Polletta, M., Surace, J., Bottini, D., Garilli, B., Maccagni, D., Picat, J. P., Scaramella, R., Scodeggio, M., Vettolani, G., Zanichelli, A., Adami, C., Cappi, A., Ciliegi, P., Contini, T., de la Torre, S., Foucaud, S., Franzetti, P., Gavignaud, I., Guzzo, L., Marano, B., Marinoni, C., Mazure, A., Meneux, B., Merighi, R., Paltani, S., Pellò, R., Pollo, A., Radovich, M., Temporin, S., and Vergani, D. (2007). The SWIRE-VVDS-CFHTLS surveys: stellar mass assembly over the last 10 Gyr. Evidence for a major build up of the red sequence between z = 2 and z = 1. *Astron. Astrophys.*, 476:137–150.

Astier, P., Guy, J., Regnault, N., Pain, R., Aubourg, E., Balam, D., Basa, S., Carlberg, R. G., Fabbro, S., Fouchez, D., Hook, I. M., Howell, D. A., Lafoux, H., Neill, J. D., Palanque-Delabrouille, N., Perrett, K., Pritchet, C. J., Rich, J., Sullivan, M., Taillet, R., Aldering, G., Antilogus, P., Arsenijevic, V., Balland, C., Baumont, S., Bronder, J., Courtois, H., Ellis, R. S., Filiol, M., Gonçalves, A. C., Goobar, A., Guide, D., Hardin, D., Lusset, V., Lidman, C., McMahon, R., Mouchet, M., Mourao, A., Perlmutter, S., Ripoche, P., Tao, C., and Walton, N. (2006). The Supernova Legacy Survey: measurement of Ω_M, Ω_Λ and w from the first year data set. *Astron. Astrophys.*, 447:31–48.

Atek, H., Richard, J., Jauzac, M., Kneib, J.-P., Natarajan, P., Limousin, M., Schaerer, D., Jullo, E., Ebeling, H., Egami, E., and Clement, B. (2015a). Are Ultra-faint Galaxies at z = 6 - 8 Responsible for Cosmic Reionization? Combined Constraints from the Hubble Frontier Fields Clusters and Parallels. *Astrophys. J.*, 814:69.

Atek, H., Richard, J., Kneib, J.-P., Clement, B., Egami, E., Ebeling, H., Jauzac, M., Jullo, E., Laporte, N., Limousin, M., and Natarajan, P. (2014). Probing the z $>$ 6 Universe with the First Hubble Frontier Fields Cluster A2744. *Astrophys. J.*, 786:60.

Atek, H., Richard, J., Kneib, J.-P., Jauzac, M., Schaerer, D., Clement, B., Limousin, M., Jullo, E., Natarajan, P., Egami, E., and Ebeling, H. (2015b). New Constraints on the Faint End of

the UV Luminosity Function at z ˜ 7-8 Using the Gravitational Lensing of the Hubble Frontier Fields Cluster A2744. *Astrophys. J.*, 800:18.

Atwood, W. B., Abdo, A. A., Ackermann, M., Althouse, W., Anderson, B., Axelsson, M., Baldini, L., Ballet, J., Band, D. L., Barbiellini, G., and et al. (2009). The Large Area Telescope on the Fermi Gamma-Ray Space Telescope Mission. *Astrophys. J.*, 697:1071–1102.

Bacchi, M., Feretti, L., Giovannini, G., and Govoni, F. (2003). Deep images of cluster radio halos. *Astron. Astrophys.*, 400:465–476.

Bacon, D. J., Taylor, A. N., Brown, M. L., Gray, M. E., Wolf, C., Meisenheimer, K., Dye, S., Wisotzki, L., Borch, A., and Kleinheinrich, M. (2005). Evolution of the dark matter distribution with three-dimensional weak lensing. *Mon. Not. R. Astron. Soc.*, 363:723–733.

Bagchi, J., Durret, F., Neto, G. B. L., and Paul, S. (2006). Giant Ringlike Radio Structures Around Galaxy Cluster Abell 3376. *Science*, 314:791–794.

Bahcall, N. A. and Soneira, R. M. (1983). The spatial correlation function of rich clusters of galaxies. *Astrophys. J.*, 270:20–38.

Balestra, I., Mercurio, A., Sartoris, B., Girardi, M., Grillo, C., Nonino, M., Rosati, P., Biviano, A., Ettori, S., Forman, W., Jones, C., Koekemoer, A., Medezinski, E., Ogrean, G. A., Tozzi, P., Umetsu, K., Vanzella, E., van Weeren, R. J., Zitrin, A., Annunziatella, M., Caminha, G. B., Broadhurst, T., Coe, D., Donahue, M., Fritz, A., Frye, B., Kelson, D., Lombardi, M., Maier, C., Meneghetti, M., Monna, A., Postman, M., Scodeggio, M., Seitz, S., and Ziegler, B. (2015). CLASH-VLT: Dissecting the Frontier Fields Galaxy Cluster MACS J0416.1-2403 with ~ 800 Spectra of Member Galaxies. *ArXiv e-prints*.

Ballarati, B., Feretti, L., Ficarra, A., Giovannini, G., Nanni, M., Olori, M. C., and Gavazzi, G. (1981). 408 MHz observations of clusters of galaxies. I - Halo sources in the Coma-A 1367 supercluster. *Astron. Astrophys.*, 100:323–325.

Bartelmann, M. and Schneider, P. (2001). Weak gravitational lensing. *Phys. Rep.*, 340:291–472.

Basu, K. (2012). A Sunyaev-Zel'dovich take on cluster radio haloes - I. Global scaling and bi-modality using Planck data. *Mon. Not. R. Astron. Soc.*, 421:L112–L116.

Battaglia, N., Leauthaud, A., Miyatake, H., Hasselfield, M., Gralla, M. B., Allison, R., Bond, J. R., Calabrese, E., Crichton, D., Devlin, M. J., Dunkley, J., Dünner, R., Erben, T., Ferrara, S., Halpern, M., Hilton, M., Hill, J. C., Hincks, A. D., Hložek, R., Huffenberger, K. M., Hughes, J. P., Kneib, J. P., Kosowsky, A., Makler, M., Marriage, T. A., Menanteau, F., Miller, L., Moodley, K., Moraes, B., Niemack, M. D., Page, L., Shan, H., Sehgal, N., Sherwin, B. D., Sievers, J. L., Sifón, C., Spergel, D. N., Staggs, S. T., Taylor, J., Thornton, R., van Waerbeke, L., and Wollack, E. J. (2015). Weak-Lensing Mass Calibration of the Atacama Cosmology Telescope Equatorial Sunyaev-Zeldovich Cluster Sample with the Canada-France-Hawaii Telescope Stripe 82 Survey. *ArXiv e-prints*.

Baumgardt, H. and Mieske, S. (2008). High mass-to-light ratios of ultra-compact dwarf galaxies - evidence for dark matter? *Mon. Not. R. Astron. Soc.*, 391:942–948.

Becker, M. R. and Kravtsov, A. V. (2011). On the Accuracy of Weak-lensing Cluster Mass Reconstructions. *Astrophys. J.*, 740:25.

Becker, R. H., White, R. L., and Helfand, D. J. (1995). The FIRST Survey: Faint Images of the Radio Sky at Twenty Centimeters. *Astrophys. J.*, 450:559.

Bell, A. R. (1978). The acceleration of cosmic rays in shock fronts. I. *Mon. Not. R. Astron. Soc.*, 182:147–156.

Benjamin, J., Heymans, C., Semboloni, E., van Waerbeke, L., Hoekstra, H., Erben, T., Gladders, M. D., Hetterscheidt, M., Mellier, Y., and Yee, H. K. C. (2007). Cosmological constraints from the 100-deg^2 weak-lensing survey. *Mon. Not. R. Astron. Soc.*, 381:702–712.

Bennett, C. L., Halpern, M., Hinshaw, G., Jarosik, N., Kogut, A., Limon, M., Meyer, S. S., Page, L., Spergel, D. N., Tucker, G. S., Wollack, E., Wright, E. L., Barnes, C., Greason, M. R., Hill, R. S., Komatsu, E., Nolta, M. R., Odegard, N., Peiris, H. V., Verde, L., and Weiland, J. L.

(2003). First-Year Wilkinson Microwave Anisotropy Probe (WMAP) Observations: Preliminary Maps and Basic Results. *Astrophys. J. Supp.*, 148:1–27.

Bennett, C. L., Larson, D., Weiland, J. L., Jarosik, N., Hinshaw, G., Odegard, N., Smith, K. M., Hill, R. S., Gold, B., Halpern, M., Komatsu, E., Nolta, M. R., Page, L., Spergel, D. N., Wollack, E., Dunkley, J., Kogut, A., Limon, M., Meyer, S. S., Tucker, G. S., and Wright, E. L. (2013). Nine-year Wilkinson Microwave Anisotropy Probe (WMAP) Observations: Final Maps and Results. *Astrophys. J. Supp.*, 208:20.

Beresnyak, A., Xu, H., Li, H., and Schlickeiser, R. (2013). Magnetohydrodynamic Turbulence and Cosmic-Ray Reacceleration in Galaxy Clusters. *Astrophys. J.*, 771:131.

Best, P. N., von der Linden, A., Kauffmann, G., Heckman, T. M., and Kaiser, C. R. (2007). On the prevalence of radio-loud active galactic nuclei in brightest cluster galaxies: implications for AGN heating of cooling flows. *Mon. Not. R. Astron. Soc.*, 379:894–908.

Bézecourt, J., Kneib, J. P., Soucail, G., and Ebbels, T. M. D. (1999). Lensed galaxies in Abell 370. I. Modeling the number counts and redshift distribution of background sources. *Astron. Astrophys.*, 347:21–29.

Binney, J. and Tremaine, S. (1987). *Galactic dynamics*.

Blake, C., Glazebrook, K., Davis, T. M., Brough, S., Colless, M., Contreras, C., Couch, W., Croom, S., Drinkwater, M. J., Forster, K., Gilbank, D., Gladders, M., Jelliffe, B., Jurek, R. J., Li, I.-H., Madore, B., Martin, D. C., Pimbblet, K., Poole, G. B., Pracy, M., Sharp, R., Wisnioski, E., Woods, D., Wyder, T. K., and Yee, H. K. C. (2011). The WiggleZ Dark Energy Survey: measuring the cosmic expansion history using the Alcock-Paczynski test and distant supernovae. *Mon. Not. R. Astron. Soc.*, 418:1725–1735.

Blandford, R. and Eichler, D. (1987). Particle acceleration at astrophysical shocks: A theory of cosmic ray origin. *Phys. Rep.*, 154:1–75.

Blandford, R. and Narayan, R. (1986). Fermat's principle, caustics, and the classification of gravitational lens images. *Astrophys. J.*, 310:568–582.

Blanton, E. L., Randall, S. W., Clarke, T. E., Sarazin, C. L., McNamara, B. R., Douglass, E. M., and McDonald, M. (2011). A Very Deep Chandra Observation of A2052: Bubbles, Shocks, and Sloshing. *Astrophys. J.*, 737:99.

Blasi, P. and Colafrancesco, S. (1999). Cosmic rays, radio halos and nonthermal X-ray emission in clusters of galaxies. *Astroparticle Physics*, 12:169–183.

Blasi, P., Gabici, S., and Brunetti, G. (2007). Gamma Rays from Clusters of Galaxies. *International Journal of Modern Physics A*, 22:681–706.

Bliton, M., Rizza, E., Burns, J. O., Owen, F. N., and Ledlow, M. J. (1998). Cluster-subcluster mergers and the formation of narrow-angle tailed radio sources. *Mon. Not. R. Astron. Soc.*, 301:609–625.

Bode, P., Ostriker, J. P., Cen, R., and Trac, H. (2012). Calibration of Nonthermal Pressure in Global Dark Matter Simulations of Clusters of Galaxies. *ArXiv e-prints*.

Boggess, N. W., Mather, J. C., Weiss, R., Bennett, C. L., Cheng, E. S., Dwek, E., Gulkis, S., Hauser, M. G., Janssen, M. A., Kelsall, T., Meyer, S. S., Moseley, S. H., Murdock, T. L., Shafer, R. A., Silverberg, R. F., Smoot, G. F., Wilkinson, D. T., and Wright, E. L. (1992). The COBE mission - Its design and performance two years after launch. *Astrophys. J.*, 397:420–429.

Böhringer, H., Pratt, G. W., Arnaud, M., Borgani, S., Croston, J. H., Ponman, T. J., Ameglio, S., Temple, R. F., and Dolag, K. (2010). Substructure of the galaxy clusters in the REXCESS sample: observed statistics and comparison to numerical simulations. *Astron. Astrophys.*, 514:A32.

Böhringer, H. and Schuecker, P. (2002). Observational signatures and statistics of galaxy Cluster Mergers: Results from X-ray observations with ROSAT, ASCA, and XMM-Newton. In Feretti, L., Gioia, I. M., and Giovannini, G., editors, *Merging Processes in Galaxy Clusters*, volume 272 of *Astrophysics and Space Science Library*, pages 133–162.

Böhringer, H., Schuecker, P., Guzzo, L., Collins, C. A., Voges, W., Cruddace, R. G., Ortiz-Gil, A., Chincarini, G., De Grandi, S., Edge, A. C., MacGillivray, H. T., Neumann, D. M., Schindler, S., and Shaver, P. (2004). The ROSAT-ESO Flux Limited X-ray (REFLEX) Galaxy cluster survey. V. The cluster catalogue. *Astron. Astrophys.*, 425:367–383.

Bolton, A. S., Burles, S., Koopmans, L. V. E., Treu, T., Gavazzi, R., Moustakas, L. A., Wayth, R., and Schlegel, D. J. (2008). The Sloan Lens ACS Survey. V. The Full ACS Strong-Lens Sample. *Astrophys. J.*, 682:964–984.

Bonafede, A., Brüggen, M., van Weeren, R., Vazza, F., Giovannini, G., Ebeling, H., Edge, A. C., Hoeft, M., and Klein, U. (2012). Discovery of radio haloes and double relics in distant MACS galaxy clusters: clues to the efficiency of particle acceleration. *Mon. Not. R. Astron. Soc.*, 426:40–56.

Bonafede, A., Feretti, L., Giovannini, G., Govoni, F., Murgia, M., Taylor, G. B., Ebeling, H., Allen, S., Gentile, G., and Pihlström, Y. (2009). Revealing the magnetic field in a distant galaxy cluster: discovery of the complex radio emission from MACS J0717.5 +3745. *Astron. Astrophys.*, 503:707–720.

Bonafede, A., Feretti, L., Murgia, M., Govoni, F., Giovannini, G., Dallacasa, D., Dolag, K., and Taylor, G. B. (2010). The Coma cluster magnetic field from Faraday rotation measures. *Astron. Astrophys.*, 513:A30.

Bonafede, A., Intema, H. T., Brüggen, M., Girardi, M., Nonino, M., Kantharia, N., van Weeren, R. J., and Röttgering, H. J. A. (2014a). Evidence for Particle Re-acceleration in the Radio Relic in the Galaxy Cluster PLCKG287.0+32.9. *Astrophys. J.*, 785:1.

Bonafede, A., Intema, H. T., Brüggen, M., Russell, H. R., Ogrean, G., Basu, K., Sommer, M., van Weeren, R. J., Cassano, R., Fabian, A. C., and Röttgering, H. J. A. (2014b). A giant radio halo in the cool core cluster CL1821+643. *Mon. Not. R. Astron. Soc.*, 444:L44–L48.

Booth, R. S. and Jonas, J. L. (2012). An Overview of the MeerKAT Project. *African Skies*, 16:101.

Boschin, W., Girardi, M., Barrena, R., Biviano, A., Feretti, L., and Ramella, M. (2004). Internal dynamics of the radio-halo cluster A2219: A multi-wavelength analysis. *Astron. Astrophys.*, 416:839–851.

Boschin, W., Girardi, M., Spolaor, M., and Barrena, R. (2006). Internal dynamics of the radio halo cluster Abell 2744. *Astron. Astrophys.*, 449:461–474.

Bouchet, F. R. (2009). The Planck Satellite: Status & Perspectives. *ArXiv e-prints*.

Bouchet, P., Lequeux, J., Maurice, E., Prevot, L., and Prevot-Burnichon, M. L. (1985). The visible and infrared extinction law and the gas-to-dust ratio in the Small Magellanic Cloud. *Astron. Astrophys.*, 149:330–336.

Bradač, M., Allen, S. W., Treu, T., Ebeling, H., Massey, R., Morris, R. G., von der Linden, A., and Applegate, D. (2008). Revealing the Properties of Dark Matter in the Merging Cluster MACS J0025.4-1222. *Astrophys. J.*, 687:959–967.

Bradač, M., Clowe, D., Gonzalez, A. H., Marshall, P., Forman, W., Jones, C., Markevitch, M., Randall, S., Schrabback, T., and Zaritsky, D. (2006). Strong and Weak Lensing United. III. Measuring the Mass Distribution of the Merging Galaxy Cluster 1ES 0657-558. *Astrophys. J.*, 652:937–947.

Bradač, M., Treu, T., Applegate, D., Gonzalez, A. H., Clowe, D., Forman, W., Jones, C., Marshall, P., Schneider, P., and Zaritsky, D. (2009). Focusing Cosmic Telescopes: Exploring Redshift z $\sim$ 5-6 Galaxies with the Bullet Cluster 1E0657 - 56. *Astrophys. J.*, 706:1201–1212.

Bradford, J. D., Geha, M., Muñoz, R. R., Santana, F. A., Simon, J. D., Côté, P., Stetson, P. B., Kirby, E., and Djorgovski, S. G. (2011). Structure and Dynamics of the Globular Cluster Palomar 13. *Astrophys. J.*, 743:167.

Bridges, T., Gebhardt, K., Sharples, R., Faifer, F. R., Forte, J. C., Beasley, M. A., Zepf, S. E., Forbes, D. A., Hanes, D. A., and Pierce, M. (2006). The globular cluster kinematics and galaxy dark matter content of NGC 4649 (M60). *Mon. Not. R. Astron. Soc.*, 373:157–166.

Bridle, S. L., Kneib, J.-P., Bardeau, S., and Gull, S. F. (2002). Bayesian Galaxy Shape Estimation. In Natarajan, P., editor, *The Shapes of Galaxies and their Dark Halos*, pages 38–46.

Briggs, D. S. (1995). High Fidelity Interferometric Imaging: Robust Weighting and NNLS Deconvolution. In *American Astronomical Society Meeting Abstracts*, volume 27 of *Bulletin of the American Astronomical Society*, page #112.02.

Broadhurst, T., Benítez, N., Coe, D., Sharon, K., Zekser, K., White, R., Ford, H., Bouwens, R., Blakeslee, J., Clampin, M., Cross, N., Franx, M., Frye, B., Hartig, G., Illingworth, G., Infante, L., Menanteau, F., Meurer, G., Postman, M., Ardila, D. R., Bartko, F., Brown, R. A., Burrows, C. J., Cheng, E. S., Feldman, P. D., Golimowski, D. A., Goto, T., Gronwall, C., Herranz, D., Holden, B., Homeier, N., Krist, J. E., Lesser, M. P., Martel, A. R., Miley, G. K., Rosati, P., Sirianni, M., Sparks, W. B., Steindling, S., Tran, H. D., Tsvetanov, Z. I., and Zheng, W. (2005). Strong-Lensing Analysis of A1689 from Deep Advanced Camera Images. *Astrophys. J.*, 621:53–88.

Brook, C. B. and Shankar, F. (2016). A matter of measurement: rotation velocities and the velocity function of dwarf galaxies. *Mon. Not. R. Astron. Soc.*, 455:3841–3847.

Brown, S., Duesterhoeft, J., and Rudnick, L. (2011a). Multiple Shock Structures in a Radio-selected Cluster of Galaxies. *Astrophys. J. Lett.*, 727:L25.

Brown, S., Emerick, A., Rudnick, L., and Brunetti, G. (2011b). Probing the Off-state of Cluster Giant Radio Halos. *Astrophys. J. Lett.*, 740:L28.

Brown, S. and Rudnick, L. (2011). Diffuse radio emission in/around the Coma cluster: beyond simple accretion. *Mon. Not. R. Astron. Soc.*, 412:2–12.

Brüggen, M., Bykov, A., Ryu, D., and Röttgering, H. (2012). Magnetic Fields, Relativistic Particles, and Shock Waves in Cluster Outskirts. *Space Sci. Rev.*, 166:187–213.

Brunetti, G. (2004). Particle Acceleration and Non-Thermal Emission from Galaxy Clusters. *Journal of Korean Astronomical Society*, 37:493–500.

Brunetti, G. and Blasi, P. (2005). Alfvénic reacceleration of relativistic particles in galaxy clusters in the presence of secondary electrons and positrons. *Mon. Not. R. Astron. Soc.*, 363:1173–1187.

Brunetti, G., Blasi, P., Cassano, R., and Gabici, S. (2004). Alfvénic reacceleration of relativistic particles in galaxy clusters: MHD waves, leptons and hadrons. *Mon. Not. R. Astron. Soc.*, 350:1174–1194.

Brunetti, G., Blasi, P., Cassano, R., and Gabici, S. (2008). Gamma ray emission and stochastic particle acceleration in galaxy clusters. In Aharonian, F. A., Hofmann, W., and Rieger, F., editors, *American Institute of Physics Conference Series*, volume 1085 of *AIPC*, pages 628–631.

Brunetti, G., Cassano, R., Dolag, K., and Setti, G. (2009). On the evolution of giant radio halos and their connection with cluster mergers. *Astron. Astrophys.*, 507:661–669.

Brunetti, G. and Jones, T. W. (2014). Cosmic Rays in Galaxy Clusters and Their Nonthermal Emission. *International Journal of Modern Physics D*, 23:30007.

Brunetti, G. and Lazarian, A. (2011). Acceleration of primary and secondary particles in galaxy clusters by compressible MHD turbulence: from radio haloes to gamma-rays. *Mon. Not. R. Astron. Soc.*, 410:127–142.

Brunetti, G., Setti, G., Feretti, L., and Giovannini, G. (2001). Particle reacceleration in the Coma cluster: radio properties and hard X-ray emission. *Mon. Not. R. Astron. Soc.*, 320:365–378.

Brunetti, G., Venturi, T., Dallacasa, D., Cassano, R., Dolag, K., Giacintucci, S., and Setti, G. (2007). Cosmic Rays and Radio Halos in Galaxy Clusters: New Constraints from Radio Observations. *Astrophys. J. Lett.*, 670:L5–L8.

Buote, D. A. (2001). On the Origin of Radio Halos in Galaxy Clusters. *Astrophys. J. Lett.*, 553:L15–L18.

Buote, D. A. and Tsai, J. C. (1995). Quantifying the Morphologies and Dynamical Evolution of Galaxy Clusters. I. The Method. *Astrophys. J.*, 452:522.

Burenin, R. A., Vikhlinin, A., Hornstrup, A., Ebeling, H., Quintana, H., and Mescheryakov, A. (2007). The 400 Square Degree ROSAT PSPC Galaxy Cluster Survey: Catalog and Statistical Calibration. *Astrophys. J. Supp.*, 172:561–582.

Burke, D. J., Collins, C. A., Sharples, R. M., Romer, A. K., Holden, B. P., and Nichol, R. C. (1997). The Southern SHARC Survey: the Z = 0.3–0.7 Cluster X-Ray Luminosity Function 1. *Astrophys. J. Lett.*, 488:L83–L86.

Burke, W. L. (1981). Multiple Gravitational Imaging by Distributed Masses. *Astrophys. J. Lett.*, 244:L1.

Burns, J. O. (1990). The radio properties of cD galaxies in Abell clusters. I - an X-ray selected sample. *Astron. J.*, 99:14–30.

Burns, J. O., Sulkanen, M. E., Gisler, G. R., and Perley, R. A. (1992). Where have all the cluster halos gone? *Astrophys. J. Lett.*, 388:L49–L52.

Cabanac, R. A., Alard, C., Dantel-Fort, M., Fort, B., Gavazzi, R., Gomez, P., Kneib, J. P., Le Fèvre, O., Mellier, Y., Pello, R., Soucail, G., Sygnet, J. F., and Valls-Gabaud, D. (2007). The CFHTLS strong lensing legacy survey. I. Survey overview and T0002 release sample. *Astron. Astrophys.*, 461:813–821.

Cain, B., Schechter, P. L., and Bautz, M. W. (2011). Measuring Gravitational Lensing Flexion in A1689 Using an Analytic Image Model. *Astrophys. J.*, 736:43.

Campbell, H., D'Andrea, C. B., Nichol, R. C., Sako, M., Smith, M., Lampeitl, H., Olmstead, M. D., Bassett, B., Biswas, R., Brown, P., Cinabro, D., Dawson, K. S., Dilday, B., Foley, R. J., Frieman, J. A., Garnavich, P., Hlozek, R., Jha, S. W., Kuhlmann, S., Kunz, M., Marriner, J., Miquel, R., Richmond, M., Riess, A., Schneider, D. P., Sollerman, J., Taylor, M., and Zhao, G.-B. (2013). Cosmology with Photometrically Classified Type Ia Supernovae from the SDSS-II Supernova Survey. *Astrophys. J.*, 763:88.

Cao, S., Biesiada, M., Gavazzi, R., Piórkowska, A., and Zhu, Z.-H. (2015). Cosmology with Strong-lensing Systems. *Astrophys. J.*, 806:185.

Carilli, C. L. and Taylor, G. B. (2002). Cluster Magnetic Fields. *Annu. Rev. Astron. Astrophys.*, 40:319–348.

Carlstrom, J. E., Holder, G. P., and Reese, E. D. (2002). Cosmology with the Sunyaev-Zel'dovich Effect. *Annu. Rev. Astron. Astrophys.*, 40:643–680.

Carter, D. and Metcalfe, N. (1980). The morphology of clusters of galaxies. *Mon. Not. R. Astron. Soc.*, 191:325–337.

Cassano, R. (2010). The radio-X-ray luminosity correlation of radio halos at low radio frequency. Application of the turbulent re-acceleration model. *Astron. Astrophys.*, 517:A10.

Cassano, R. and Brunetti, G. (2005). Cluster mergers and non-thermal phenomena: a statistical magneto-turbulent model. *Mon. Not. R. Astron. Soc.*, 357:1313–1329.

Cassano, R., Brunetti, G., and Setti, G. (2006a). Constraining B in galaxy clusters from statistics of giant radio halos. *Astronomische Nachrichten*, 327:557.

Cassano, R., Brunetti, G., and Setti, G. (2006b). Statistics of giant radio haloes from electron reacceleration models. *Mon. Not. R. Astron. Soc.*, 369:1577–1595.

Cassano, R., Brunetti, G., Setti, G., Govoni, F., and Dolag, K. (2007). New scaling relations in cluster radio haloes and the re-acceleration model. *Mon. Not. R. Astron. Soc.*, 378:1565–1574.

Cassano, R., Brunetti, G., and Venturi, T. (2011). The Connection between Radio Halos and Cluster Mergers and the Statistical Properties of the Radio Halo Population. *Journal of Astrophysics and Astronomy*, 32:519–527.

Cassano, R., Brunetti, G., Venturi, T., Setti, G., Dallacasa, D., Giacintucci, S., and Bardelli, S. (2008). Revised statistics of radio halos and the reacceleration model. *Astron. Astrophys.*, 480:687–697.

Cassano, R., Ettori, S., Brunetti, G., Giacintucci, S., Pratt, G. W., Venturi, T., Kale, R., Dolag, K., and Markevitch, M. (2013). Revisiting Scaling Relations for Giant Radio Halos in Galaxy Clusters. *Astrophys. J.*, 777:141.

Cassano, R., Ettori, S., Giacintucci, S., Brunetti, G., Markevitch, M., Venturi, T., and Gitti, M. (2010). On the Connection Between Giant Radio Halos and Cluster Mergers. *Astrophys. J. Lett.*, 721:L82–L85.

Chandra, P., Ray, A., and Bhatnagar, S. (2004). The Late-Time Radio Emission from SN 1993J at Meter Wavelengths. *Astrophys. J.*, 612:974–987.

Chandrasekhar, S. (1939). *An introduction to the study of stellar structure*.

Chelouche, D., Koester, B. P., and Bowen, D. V. (2007). The Dust Content of Galaxy Clusters. *Astrophys. J. Lett.*, 671:L97–L100.

Clarke, T. E. and Ensslin, T. A. (2006). Deep 1.4 GHz Very Large Array Observations of the Radio Halo and Relic in Abell 2256. *Astron. J.*, 131:2900–2912.

Clarke, T. E., Kronberg, P. P., and Böhringer, H. (2001). A New Radio-X-Ray Probe of Galaxy Cluster Magnetic Fields. *Astrophys. J. Lett.*, 547:L111–L114.

Clowe, D., Luppino, G. A., Kaiser, N., Henry, J. P., and Gioia, I. M. (1998). Weak Lensing by Two Z approximately 0.8 Clusters of Galaxies. *Astrophys. J. Lett.*, 497:L61–L64.

Clowe, D. and Schneider, P. (2002). Wide field weak lensing observations of A1835 and A2204. *Astron. Astrophys.*, 395:385–397.

Coe, D., Benítez, N., Broadhurst, T., and Moustakas, L. A. (2010). A High-resolution Mass Map of Galaxy Cluster Substructure: LensPerfect Analysis of A1689. *Astrophys. J.*, 723:1678–1702.

Coe, D., Bradley, L., and Zitrin, A. (2015). Frontier Fields: High-redshift Predictions and Early Results. *Astrophys. J.*, 800:84.

Coe, D. and Moustakas, L. A. (2009). Cosmological Constraints from Gravitational Lens Time Delays. *Astrophys. J.*, 706:45–59.

Coe, D. A., Lotz, J., Natarajan, P., Richard, J., Zitrin, A., Kneib, J., Ebeling, H., Sharon, K., Johnson, T., Limousin, M., Bradac, M., Hoag, A., Cain, B., Merten, J., Williams, L. L., Sebesta, K., Meneghetti, M., Koekemoer, A. M., and Barker, E. A. (2014). The HST Frontier Fields: Gravitational Lensing Models Release. In *American Astronomical Society Meeting Abstracts #223*, volume 223 of *American Astronomical Society Meeting Abstracts*, page #254.04.

Cohen, A. S. and Clarke, T. E. (2011). An Ultra-steep-spectrum Radio Relic in the Galaxy Cluster A2443. *Astron. J.*, 141:149.

Cohen, A. S., Lane, W. M., Cotton, W. D., Kassim, N. E., Lazio, T. J. W., Perley, R. A., Condon, J. J., and Erickson, W. C. (2007). The VLA Low-Frequency Sky Survey. *Astron. J.*, 134:1245–1262.

Colafrancesco, S. and Mele, B. (2001). Neutralinos and the Origin of Radio Halos in Clusters of Galaxies. *Astrophys. J.*, 562:24–41.

Collett, T. E. and Bacon, D. J. (2015). Compound lensing: Einstein Zig-Zags and high multiplicity lensed images. *ArXiv e-prints*.

Condon, J. J., Cotton, W. D., Greisen, E. W., Yin, Q. F., Perley, R. A., Taylor, G. B., and Broderick, J. J. (1998). The NRAO VLA Sky Survey. *Astron. J.*, 115:1693–1716.

Conley, A., Guy, J., Sullivan, M., Regnault, N., Astier, P., Balland, C., Basa, S., Carlberg, R. G., Fouchez, D., Hardin, D., Hook, I. M., Howell, D. A., Pain, R., Palanque-Delabrouille, N., Perrett, K. M., Pritchet, C. J., Rich, J., Ruhlmann-Kleider, V., Balam, D., Baumont, S., Ellis, R. S., Fabbro, S., Fakhouri, H. K., Fourmanoit, N., González-Gaitán, S., Graham, M. L., Hudson, M. J., Hsiao, E., Kronborg, T., Lidman, C., Mourao, A. M., Neill, J. D., Perlmutter, S., Ripoche, P., Suzuki, N., and Walker, E. S. (2011). Supernova Constraints and Systematic Uncertainties from the First Three Years of the Supernova Legacy Survey. *Astrophys. J. Supp.*, 192:1.

Cordey, R. A. (1985). The radio halo and active galaxies in the Coma cluster. *Mon. Not. R. Astron. Soc.*, 215:437–451.

Cotton, W. D. (2008). Obit: A Development Environment for Astronomical Algorithms. *Pub. Astron. Soc. Pacific*, 120:439–448.

Cotton, W. D., Condon, J. J., Perley, R. A., Kassim, N., Lazio, J., Cohen, A., Lane, W., and Erickson, W. C. (2004). Beyond the isoplanatic patch in the VLA Low-frequency Sky Survey. In Oschmann, Jr., J. M., editor, *Ground-based Telescopes*, volume 5489 of *Society of Photo-Optical Instrumentation Engineers (SPIE) Conference Series*, pages 180–189.

Dallacasa, D., Brunetti, G., Giacintucci, S., Cassano, R., Venturi, T., Macario, G., Kassim, N. E., Lane, W., and Setti, G. (2009). Deep 1.4 GHz Follow-up of the Steep Spectrum Radio Halo in A521. *Astrophys. J.*, 699:1288–1292.

Das, S., Louis, T., Nolta, M. R., Addison, G. E., Battistelli, E. S., Bond, J. R., Calabrese, E., Crichton, D., Devlin, M. J., Dicker, S., Dunkley, J., Dünner, R., Fowler, J. W., Gralla, M., Hajian, A., Halpern, M., Hasselfield, M., Hilton, M., Hincks, A. D., Hlozek, R., Huffenberger, K. M., Hughes, J. P., Irwin, K. D., Kosowsky, A., Lupton, R. H., Marriage, T. A., Marsden, D., Menanteau, F., Moodley, K., Niemack, M. D., Page, L. A., Partridge, B., Reese, E. D., Schmitt, B. L., Sehgal, N., Sherwin, B. D., Sievers, J. L., Spergel, D. N., Staggs, S. T., Swetz, D. S., Switzer, E. R., Thornton, R., Trac, H., and Wollack, E. (2014). The Atacama Cosmology Telescope: temperature and gravitational lensing power spectrum measurements from three seasons of data. *Journal of Cosmology and Astroparticle Physics.*, 4:14.

Das, S., Marriage, T. A., Ade, P. A. R., Aguirre, P., Amiri, M., Appel, J. W., Barrientos, L. F., Battistelli, E. S., Bond, J. R., Brown, B., Burger, B., Chervenak, J., Devlin, M. J., Dicker, S. R., Bertrand Doriese, W., Dunkley, J., Dünner, R., Essinger-Hileman, T., Fisher, R. P., Fowler, J. W., Hajian, A., Halpern, M., Hasselfield, M., Hernández-Monteagudo, C., Hilton, G. C., Hilton, M., Hincks, A. D., Hlozek, R., Huffenberger, K. M., Hughes, D. H., Hughes, J. P., Infante, L., Irwin, K. D., Baptiste Juin, J., Kaul, M., Klein, J., Kosowsky, A., Lau, J. M.,

Limon, M., Lin, Y.-T., Lupton, R. H., Marsden, D., Martocci, K., Mauskopf, P., Menanteau, F., Moodley, K., Moseley, H., Netterfield, C. B., Niemack, M. D., Nolta, M. R., Page, L. A., Parker, L., Partridge, B., Reid, B., Sehgal, N., Sherwin, B. D., Sievers, J., Spergel, D. N., Staggs, S. T., Swetz, D. S., Switzer, E. R., Thornton, R., Trac, H., Tucker, C., Warne, R., Wollack, E., and Zhao, Y. (2011). The Atacama Cosmology Telescope: A Measurement of the Cosmic Microwave Background Power Spectrum at 148 and 218 GHz from the 2008 Southern Survey. *Astrophys. J.*, 729:62.

Davis, M., Efstathiou, G., Frenk, C. S., and White, S. D. M. (1985). The evolution of large-scale structure in a universe dominated by cold dark matter. *Astrophys. J.*, 292:371–394.

de Gasperin, F., Intema, H. T., van Weeren, R. J., Dawson, W. A., Golovich, N., Wittman, D., Bonafede, A., and Brüggen, M. (2015). A powerful double radio relic system discovered in PSZ1 G108.18-11.53: evidence for a shock with non-uniform Mach number? *Mon. Not. R. Astron. Soc.*, 453:3483–3498.

DeBoer, D. R., Gough, R. G., Bunton, J. D., Cornwell, T. J., Beresford, R. J., Johnston, S., Feain, I. J., Schinckel, A. E., Jackson, C. A., Kesteven, M. J., Chippendale, A., Hampson, G. A., O'Sullivan, J. D., Hay, S. G., Jacka, C. E., Sweetnam, T. W., Storey, M. C., Ball, L., and Boyle, B. J. (2009). Australian SKA Pathfinder: A High-Dynamic Range Wide-Field of View Survey Telescope. *IEEE Proceedings*, 97:1507–1521.

Deiss, B. M., Reich, W., Lesch, H., and Wielebinski, R. (1997). The large-scale structure of the diffuse radio halo of the Coma cluster at 1.4GHz. *Astron. Astrophys.*, 321:55–63.

Dennison, B. (1980). Formation of radio halos in clusters of galaxies from cosmic-ray protons. *Astrophys. J. Lett.*, 239:L93–L96.

Dicke, R. H. and Peebles, P. J. E. (1979). The big bang cosmology - enigmas and nostrums. In Hawking, S. W. and Israel, W., editors, *General Relativity: An Einstein centenary survey*, pages 504–517.

Diego, J. M., Broadhurst, T., Benitez, N., Umetsu, K., Coe, D., Sendra, I., Sereno, M., Izzo, L., and Covone, G. (2015a). A free-form lensing grid solution for A1689 with new multiple images. *Mon. Not. R. Astron. Soc.*, 446:683–704.

Diego, J. M., Broadhurst, T., Chen, C., Lim, J., Zitrin, A., Chan, B., Coe, D., Ford, H. C., Lam, D., and Zheng, W. (2015b). A Free-Form Prediction for the Reappearance of Supernova Refsdal in the Hubble Frontier Fields Cluster MACSJ1149.5+2223. *ArXiv e-prints*.

Diego, J. M., Broadhurst, T., Molnar, S. M., Lam, D., and Lim, J. (2015c). Free-form lensing implications for the collision of dark matter and gas in the frontier fields cluster MACS J0416.1-2403. *Mon. Not. R. Astron. Soc.*, 447:3130–3149.

Diego, J. M., Broadhurst, T., Zitrin, A., Lam, D., Lim, J., Ford, H. C., and Zheng, W. (2015d). Hubble Frontier Field free-form mass mapping of the massive multiple-merging cluster MACSJ0717.5+3745. *Mon. Not. R. Astron. Soc.*, 451:3920–3932.

Diego, J. M., Protopapas, P., Sandvik, H. B., and Tegmark, M. (2005). Non-parametric inversion of strong lensing systems. *Mon. Not. R. Astron. Soc.*, 360:477–491.

Dogiel, V. A., Colafrancesco, S., Ko, C. M., Kuo, P. H., Hwang, C. Y., Ip, W. H., Birkinshaw, M., and Prokhorov, D. A. (2007). In-situ acceleration of subrelativistic electrons in the Coma halo and the halo's influence on the Sunyaev-Zeldovich effect. *Astron. Astrophys.*, 461:433–443.

Dolag, K., Bartelmann, M., and Lesch, H. (1999). SPH simulations of magnetic fields in galaxy clusters. *Astron. Astrophys.*, 348:351–363.

Dolag, K., Bartelmann, M., and Lesch, H. (2002). Evolution and structure of magnetic fields in simulated galaxy clusters. *Astron. Astrophys.*, 387:383–395.

Dolag, K. and Enßlin, T. A. (2000). Radio halos of galaxy clusters from hadronic secondary electron injection in realistic magnetic field configurations. *Astron. Astrophys.*, 362:151–157.

Dolag, K., Grasso, D., Springel, V., and Tkachev, I. (2005a). Constrained simulations of the magnetic field in the local Universe and the propagation of ultrahigh energy cosmic rays. *Journal of Cosmology and Astroparticle Physics.*, 1:9.

Dolag, K., Vazza, F., Brunetti, G., and Tormen, G. (2005b). Turbulent gas motions in galaxy cluster simulations: the role of smoothed particle hydrodynamics viscosity. *Mon. Not. R. Astron. Soc.*, 364:753–772.

Donnert, J., Dolag, K., Brunetti, G., and Cassano, R. (2013). Rise and fall of radio haloes in simulated merging galaxy clusters. *Mon. Not. R. Astron. Soc.*, 429:3564–3569.

Dressler, A. and Shectman, S. A. (1988). Evidence for substructure in rich clusters of galaxies from radial-velocity measurements. *Astron. J.*, 95:985–995.

Drury, L. O. (1983). An introduction to the theory of diffusive shock acceleration of energetic particles in tenuous plasmas. *Reports on Progress in Physics*, 46:973–1027.

Duffy, A. R., Schaye, J., Kay, S. T., and Dalla Vecchia, C. (2008). Dark matter halo concentrations in the Wilkinson Microwave Anisotropy Probe year 5 cosmology. *Mon. Not. R. Astron. Soc.*, 390:L64–L68.

Ebeling, H., Edge, A. C., and Henry, J. P. (2001). MACS: A Quest for the Most Massive Galaxy Clusters in the Universe. *Astrophys. J.*, 553:668–676.

Ebeling, H., Edge, A. C., Mantz, A., Barrett, E., Henry, J. P., Ma, C. J., and van Speybroeck, L. (2010). The X-ray brightest clusters of galaxies from the Massive Cluster Survey. *Mon. Not. R. Astron. Soc.*, 407:83–93.

Ebeling, H., Ma, C.-J., and Barrett, E. (2014). Spectroscopic Redshifts of Galaxies within the Frontier Fields. *Astrophys. J. Supp.*, 211:21.

Eddington, A. S. (1919). The Deflection of Light during a Solar Eclipse. *Nature.*, 104:372.

Eisenstein, D. J., Zehavi, I., Hogg, D. W., Scoccimarro, R., Blanton, M. R., Nichol, R. C., Scranton, R., Seo, H.-J., Tegmark, M., Zheng, Z., Anderson, S. F., Annis, J., Bahcall, N., Brinkmann, J., Burles, S., Castander, F. J., Connolly, A., Csabai, I., Doi, M., Fukugita, M., Frieman, J. A., Glazebrook, K., Gunn, J. E., Hendry, J. S., Hennessy, G., Ivezić, Z., Kent, S., Knapp, G. R., Lin, H., Loh, Y.-S., Lupton, R. H., Margon, B., McKay, T. A., Meiksin, A., Munn, J. A., Pope, A., Richmond, M. W., Schlegel, D., Schneider, D. P., Shimasaku, K., Stoughton, C., Strauss, M. A., SubbaRao, M., Szalay, A. S., Szapudi, I., Tucker, D. L., Yanny, B., and York, D. G. (2005). Detection of the Baryon Acoustic Peak in the Large-Scale Correlation Function of SDSS Luminous Red Galaxies. *Astrophys. J.*, 633:560–574.

Elíasdóttir, Á., Fynbo, J. P. U., Hjorth, J., Ledoux, C., Watson, D. J., Andersen, A. C., Malesani, D., Vreeswijk, P. M., Prochaska, J. X., Sollerman, J., and Jaunsen, A. O. (2009). Dust Extinction in High-z Galaxies with Gamma-Ray Burst Afterglow Spectroscopy: The 2175 Å Feature at z = 2.45. *Astrophys. J.*, 697:1725–1740.

Elíasdóttir, Á., Limousin, M., Richard, J., Hjorth, J., Kneib, J.-P., Natarajan, P., Pedersen, K., Jullo, E., and Paraficz, D. (2007). Where is the matter in the Merging Cluster Abell 2218? *ArXiv e-prints*.

Ellis, R., Allington-Smith, J., and Smail, I. (1991). Spectroscopy of arcs in the rich cluster Abell 963. *Mon. Not. R. Astron. Soc.*, 249:184–190.

Enßlin, T., Pfrommer, C., Miniati, F., and Subramanian, K. (2011). Cosmic ray transport in galaxy clusters: implications for radio halos, gamma-ray signatures, and cool core heating. *Astron. Astrophys.*, 527:A99.

Ensslin, T. A., Biermann, P. L., Klein, U., and Kohle, S. (1998). Cluster radio relics as a tracer of shock waves of the large-scale structure formation. *Astron. Astrophys.*, 332:395–409.

Enßlin, T. A. and Brüggen, M. (2002). On the formation of cluster radio relics. *Mon. Not. R. Astron. Soc.*, 331:1011–1019.

Enßlin, T. A. and Gopal-Krishna (2001). Reviving fossil radio plasma in clusters of galaxies by adiabatic compression in environmental shock waves. *Astron. Astrophys.*, 366:26–34.

Er, X. and Bartelmann, M. (2013). Estimation of halo ellipticity using spin-3 flexion. *Mon. Not. R. Astron. Soc.*, 428:103–108.

Erdl, H. and Schneider, P. (1993). Classification of the multiple deflection two point-mass gravitational lens models and application of catastrophe theory in lensing. *Astron. Astrophys.*, 268:453–471.

Etherington, I. M. H. (1933). On the Definition of Distance in General Relativity. *Philosophical Magazine*, 15:761.

Fahlman, G., Kaiser, N., Squires, G., and Woods, D. (1994). Dark matter in MS 1224 from distortion of background galaxies. *Astrophys. J.*, 437:56–62.

Fedeli, C., Bartelmann, M., and Moscardini, L. (2012). Constraining primordial non-Gaussianity with cosmological weak lensing: shear and flexion. *Journal of Cosmology and Astroparticle Physics.*, 10:18.

Feretti, L. (1999). Observational Results on Cluster Diffuse Emission. In Boehringer, H., Feretti, L., and Schuecker, P., editors, *Diffuse Thermal and Relativistic Plasma in Galaxy Clusters*, page 3.

Feretti, L. (2002). Observational Properties of Diffuse Halos in Clusters. In Pramesh Rao, A., Swarup, G., and Gopal-Krishna, editors, *The Universe at Low Radio Frequencies*, volume 199 of *IAU Symposium*, page 133.

Feretti, L., Bacchi, M., Slee, O. B., Giovannini, G., Govoni, F., Andernach, H., and Tsarevsky, G. (2006). Diffuse radio sources in the cluster of galaxies Abell 548b. *Mon. Not. R. Astron. Soc.*, 368:544–552.

Feretti, L., Boehringer, H., Giovannini, G., and Neumann, D. (1997). The radio and X-ray properties of Abell 2255. *Astron. Astrophys.*, 317:432–440.

Feretti, L., Brunetti, G., Giovannini, G., Kassim, N., Orrú, E., and Setti, G. (2004a). Properties and Spectral Behaviour of Cluster Radio Halos. *Journal of Korean Astronomical Society*, 37:315–322.

Feretti, L., Fusco-Femiano, R., Giovannini, G., and Govoni, F. (2001). The giant radio halo in Abell 2163. *Astron. Astrophys.*, 373:106–112.

Feretti, L. and Giovannini, G. (2008). Clusters of Galaxies in the Radio: Relativistic Plasma and ICM/Radio Galaxy Interaction Processes. In Plionis, M., López-Cruz, O., and Hughes, D., editors, *A Pan-Chromatic View of Clusters of Galaxies and the Large-Scale Structure*, volume 740 of *Lecture Notes in Physics, Berlin Springer Verlag*, page 143.

Feretti, L., Giovannini, G., Govoni, F., and Murgia, M. (2012). Clusters of galaxies: observational properties of the diffuse radio emission. *Astron. Astrophys. Rev.*, 20:54.

Feretti, L., Orrù, E., Brunetti, G., Giovannini, G., Kassim, N., and Setti, G. (2004b). Spectral index maps of the radio halos in Abell 665 and Abell 2163. *Astron. Astrophys.*, 423:111–119.

Fermi, E. (1949). On the Origin of the Cosmic Radiation. *Physical Review*, 75:1169–1174.

Ferrari, C., Govoni, F., Schindler, S., Bykov, A. M., and Rephaeli, Y. (2008). Observations of Extended Radio Emission in Clusters. *Space Sci. Rev.*, 134:93–118.

Ferrari, C., Intema, H. T., Orrù, E., Govoni, F., Murgia, M., Mason, B., Bourdin, H., Asad, K. M., Mazzotta, P., Wise, M. W., Mroczkowski, T., and Croston, J. H. (2011). Discovery of the correspondence between intra-cluster radio emission and a high pressure region detected through the Sunyaev-Zel'dovich effect. *Astron. Astrophys.*, 534:L12.

Ferrari, C., Maurogordato, S., Cappi, A., and Benoist, C. (2003). Multiple merging events in Abell 521. *Astron. Astrophys.*, 399:813–828.

Finoguenov, A., Sarazin, C. L., Nakazawa, K., Wik, D. R., and Clarke, T. E. (2010). XMM-Newton Observation of the Northwest Radio Relic Region in A3667. *Astrophys. J.*, 715:1143–1151.

Fischer, P. and Tyson, J. A. (1997). The Mass Distribution of the Most Luminous X-Ray Cluster RXJ 1347.5-1145 From Gravitational Lensing. *Astron. J.*, 114:14–24.

Fort, B., Le Fevre, O., Hammer, F., and Cailloux, M. (1992). An arc system with a radial gravitational image in the cluster MS 2137-23. *Astrophys. J. Lett.*, 399:L125–L127.

Friedman, A. S., Wood-Vasey, W. M., Marion, G. H., Challis, P., Mandel, K. S., Bloom, J. S., Modjaz, M., Narayan, G., Hicken, M., Foley, R. J., Klein, C. R., Starr, D. L., Morgan, A., Rest, A., Blake, C. H., Miller, A. A., Falco, E. E., Wyatt, W. F., Mink, J., Skrutskie, M. F., and Kirshner, R. P. (2015). CfAIR2: Near-infrared Light Curves of 94 Type Ia Supernovae. *Astrophys. J. Supp.*, 220:9.

Frieman, J. A., Turner, M. S., and Huterer, D. (2008). Dark Energy and the Accelerating Universe. *Annu. Rev. Astron. Astrophys.*, 46:385–432.

Fujita, Y., Takizawa, M., and Sarazin, C. L. (2003). Nonthermal Emissions from Particles Accelerated by Turbulence in Clusters of Galaxies. *Astrophys. J.*, 584:190–202.

Gal, R. R., de Carvalho, R. R., Lopes, P. A. A., Djorgovski, S. G., Brunner, R. J., Mahabal, A., and Odewahn, S. C. (2003). The Northern Sky Optical Cluster Survey. II. An Objective Cluster Catalog for 5800 Square Degrees. *Astron. J.*, 125:2064–2084.

Gal, R. R., de Carvalho, R. R., Odewahn, S. C., Djorgovski, S. G., and Margoniner, V. E. (2000). The Northern Sky Optical Cluster Survey. I. Detection of Galaxy Clusters in DPOSS. *Astron. J.*, 119:12–20.

Gal, R. R., Lopes, P. A. A., de Carvalho, R. R., Kohl-Moreira, J. L., Capelato, H. V., and Djorgovski, S. G. (2009). The Northern Sky Optical Cluster Survey. III. A Cluster Catalog Covering PI Steradians. *Astron. J.*, 137:2981–2999.

Geller, M. J. and Beers, T. C. (1982). Substructure within clusters of galaxies. *Pub. Astron. Soc. Pacific*, 94:421–439.

Giacconi, R., Murray, S., Gursky, H., Kellogg, E., Schreier, E., and Tananbaum, H. (1972). The Uhuru catalog of X-ray sources. *Astrophys. J.*, 178:281–308.

Giacintucci, S. (2011). Diffuse radio sources in colliding galaxy clusters . Low frequency follow up of the GMRT Radio Halo Survey. *Mem. Societa Astronomica Italiana*, 82:541.

Giacintucci, S., Dallacasa, D., Venturi, T., Brunetti, G., Cassano, R., Markevitch, M., and Athreya, R. M. (2011). An unlikely radio halo in the low X-ray luminosity galaxy cluster RXC J1514.9-1523. *Astron. Astrophys.*, 534:A57.

Giacintucci, S., Kale, R., Wik, D. R., Venturi, T., and Markevitch, M. (2013). Discovery of a Giant Radio Halo in a New Planck Galaxy Cluster PLCKG171.9-40.7. *Astrophys. J.*, 766:18.

Giacintucci, S., Venturi, T., Brunetti, G., Bardelli, S., Dallacasa, D., Ettori, S., Finoguenov, A., Rao, A. P., and Zucca, E. (2005). Spectral properties and origin of the radio halo in A3562. *Astron. Astrophys.*, 440:867–879.

Giacintucci, S., Venturi, T., Cassano, R., Dallacasa, D., and Brunetti, G. (2009). A Giant Radio Halo in the Massive and Merging Cluster Abell 1351. *Astrophys. J. Lett.*, 704:L54–L57.

Giacintucci, S., Venturi, T., Macario, G., Dallacasa, D., Brunetti, G., Markevitch, M., Cassano, R., Bardelli, S., and Athreya, R. (2008). Shock acceleration as origin of the radio relic in A 521? *Astron. Astrophys.*, 486:347–358.

Giovannini, G., Bonafede, A., Feretti, L., Govoni, F., Murgia, M., Ferrari, F., and Monti, G. (2009). Radio halos in nearby ($z < 0.4$) clusters of galaxies. *Astron. Astrophys.*, 507:1257–1270.

Giovannini, G. and Feretti, L. (2000). Halo and relic sources in clusters of galaxies. *New Astron.*, 5:335–347.

Giovannini, G. and Feretti, L. (2002). Diffuse Radio Sources and Cluster Mergers: Radio Halos and Relics. In Feretti, L., Gioia, I. M., and Giovannini, G., editors, *Merging Processes in Galaxy Clusters*, volume 272 of *Astrophysics and Space Science Library*, pages 197–227.

Giovannini, G., Feretti, L., and Stanghellini, C. (1991). The Coma cluster radio source 1253 + 275, revisited. *Astron. Astrophys.*, 252:528–537.

Giovannini, G., Feretti, L., Venturi, T., Kim, K.-T., and Kronberg, P. P. (1993). The halo radio source Coma C and the origin of halo sources. *Astrophys. J.*, 406:399–406.

Girardi, M. and Biviano, A. (2002). Optical Analysis of Cluster Mergers. In Feretti, L., Gioia, I. M., and Giovannini, G., editors, *Merging Processes in Galaxy Clusters*, volume 272 of *Astrophysics and Space Science Library*, pages 39–77.

Gitti, M., Brunetti, G., Feretti, L., and Setti, G. (2004). Particle acceleration in cooling flow clusters of galaxies: The case of Abell 2626. *Astron. Astrophys.*, 417:1–11.

Gitti, M., Brunetti, G., and Setti, G. (2002). Modeling the interaction between ICM and relativistic plasma in cooling flows: The case of the Perseus cluster. *Astron. Astrophys.*, 386:456–463.

Gladders, M. D. and Yee, H. K. C. (2005). The Red-Sequence Cluster Survey. I. The Survey and Cluster Catalogs for Patches RCS 0926+37 and RCS 1327+29. *Astrophys. J. Supp.*, 157:1–29.

Goldberg, D. M. and Leonard, A. (2007). Measuring Flexion. *Astrophys. J.*, 660:1003–1015.

Goobar, A., Paech, K., Stanishev, V., Amanullah, R., Dahlén, T., Jönsson, J., Kneib, J. P., Lidman, C., Limousin, M., Mörtsell, E., Nobili, S., Richard, J., Riehm, T., and von Strauss, M. (2009). Near-IR search for lensed supernovae behind galaxy clusters. II. First detection and future prospects. *Astron. Astrophys.*, 507:71–83.

Govoni, F., Enßlin, T. A., Feretti, L., and Giovannini, G. (2001a). A comparison of radio and X-ray morphologies of four clusters of galaxies containing radio halos. *Astron. Astrophys.*, 369:441–449.

Govoni, F., Feretti, L., Giovannini, G., Böhringer, H., Reiprich, T. H., and Murgia, M. (2001b). Radio and X-ray diffuse emission in six clusters of galaxies. *Astron. Astrophys.*, 376:803–819.

Govoni, F., Markevitch, M., Vikhlinin, A., van Speybroeck, L., Feretti, L., and Giovannini, G. (2004). Chandra Temperature Maps for Galaxy Clusters with Radio Halos. *Astrophys. J.*, 605:695–708.

Govoni, F., Murgia, M., Feretti, L., Giovannini, G., Dallacasa, D., and Taylor, G. B. (2005). A2255: The first detection of filamentary polarized emission in a radio halo. *Astron. Astrophys.*, 430:L5–L8.

Govoni, F., Murgia, M., Giovannini, G., Vacca, V., and Bonafede, A. (2011). The large-scale diffuse radio emission in A781. *Astron. Astrophys.*, 529:A69.

Govoni, F., Murgia, M., Markevitch, M., Feretti, L., Giovannini, G., Taylor, G. B., and Carretti, E. (2009). A search for diffuse radio emission in the relaxed, cool-core galaxy clusters A1068, A1413, A1650, A1835, A2029, and Ophiuchus. *Astron. Astrophys.*, 499:371–383.

Gursky, H., Kellogg, E., Murray, S., Leong, C., Tananbaum, H., and Giacconi, R. (1971). A Strong X-Ray Source in the Coma Cluster Observed by UHURU. *Astrophys. J. Lett.*, 167:L81.

Guth, A. H. (1981). Inflationary universe: A possible solution to the horizon and flatness problems. *Physical Review D.*, 23:347–356.

Haiman, Z., Mohr, J. J., and Holder, G. P. (2001). Constraints on Cosmological Parameters from Future Galaxy Cluster Surveys. *Astrophys. J.*, 553:545–561.

Halkola, A., Seitz, S., and Pannella, M. (2006). Parametric strong gravitational lensing analysis of Abell 1689. *Mon. Not. R. Astron. Soc.*, 372:1425–1462.

Hallman, E. J. and Jeltema, T. E. (2011). Structure and turbulence in simulated galaxy clusters and the implications for the formation of radio haloes. *Mon. Not. R. Astron. Soc.*, 418:2467–2480.

Hamana, T., Miyazaki, S., Shimasaku, K., Furusawa, H., Doi, M., Hamabe, M., Imi, K., Kimura, M., Komiyama, Y., Nakata, F., Okada, N., Okamura, S., Ouchi, M., Sekiguchi, M., Yagi, M.,

and Yasuda, N. (2003). Cosmic Shear Statistics in the Suprime-Cam 2.1 Square Degree Field: Constraints on Ω_m and σ_8. *Astrophys. J.*, 597:98–110.

Hanisch, R. J. (1980). Diffuse radio emission in the Coma cluster and Abell 1367 - Observations at 430 and 1400 MHz. *Astron. J.*, 85:1565–1576.

Hanisch, R. J. and Erickson, W. C. (1980). Low frequency radio observations of five rich clusters of galaxies. *Astron. J.*, 85:183–190.

Hao, C.-N., Kennicutt, R. C., Johnson, B. D., Calzetti, D., Dale, D. A., and Moustakas, J. (2011). Dust-corrected Star Formation Rates of Galaxies. II. Combinations of Ultraviolet and Infrared Tracers. *Astrophys. J.*, 741:124.

Haslam, C. G. T., Salter, C. J., and Stoffel, H. (1981). The All-Sky 408-MHZ Survey. In Setti, G., Spada, G., and Wolfendale, A. W., editors, *Origin of Cosmic Rays*, volume 94 of *IAU Symposium*, page 217.

Hasselfield, M., Hilton, M., Marriage, T. A., Addison, G. E., Barrientos, L. F., Battaglia, N., Battistelli, E. S., Bond, J. R., Crichton, D., Das, S., Devlin, M. J., Dicker, S. R., Dunkley, J., Dünner, R., Fowler, J. W., Gralla, M. B., Hajian, A., Halpern, M., Hincks, A. D., Hlozek, R., Hughes, J. P., Infante, L., Irwin, K. D., Kosowsky, A., Marsden, D., Menanteau, F., Moodley, K., Niemack, M. D., Nolta, M. R., Page, L. A., Partridge, B., Reese, E. D., Schmitt, B. L., Sehgal, N., Sherwin, B. D., Sievers, J., Sifón, C., Spergel, D. N., Staggs, S. T., Swetz, D. S., Switzer, E. R., Thornton, R., Trac, H., and Wollack, E. J. (2013). The Atacama Cosmology Telescope: Sunyaev-Zel'dovich selected galaxy clusters at 148 GHz from three seasons of data. *Journal of Cosmology and Astroparticle Physics.*, 7:8.

Henning, P. A. (1989). 30.9 MHz observations of the radio halo in the coma cluster of galaxies. *Astron. J.*, 97:1561–1565.

Henriksen, M. J. and Mushotzky, R. F. (1986). The X-ray spectrm of the Coma Cluster of galaxies. *Astrophys. J.*, 302:287–295.

Hernandez-Jimenez, J. A., Pastoriza, M. G., Rodrigues, I., Krabbe, A. C., Winge, C., and Bonatto, C. (2013). Photometry and dynamics of the minor merger AM 1219-430 with Gemini GMOS-S. *Mon. Not. R. Astron. Soc.*, 435:3342–3352.

Hetterscheidt, M., Erben, T., Schneider, P., Maoli, R., van Waerbeke, L., and Mellier, Y. (2005). Searching for galaxy clusters using the aperture mass statistics in 50 VLT fields. *Astron. Astrophys.*, 442:43–61.

Hicken, M., Wood-Vasey, W. M., Blondin, S., Challis, P., Jha, S., Kelly, P. L., Rest, A., and Kirshner, R. P. (2009). Improved Dark Energy Constraints from ˜100 New CfA Supernova Type Ia Light Curves. *Astrophys. J.*, 700:1097–1140.

Hinshaw, G., Nolta, M. R., Bennett, C. L., Bean, R., Doré, O., Greason, M. R., Halpern, M., Hill, R. S., Jarosik, N., Kogut, A., Komatsu, E., Limon, M., Odegard, N., Meyer, S. S., Page, L., Peiris, H. V., Spergel, D. N., Tucker, G. S., Verde, L., Weiland, J. L., Wollack, E., and Wright, E. L. (2007). Three-Year Wilkinson Microwave Anisotropy Probe (WMAP) Observations: Temperature Analysis. *Astrophys. J. Supp.*, 170:288–334.

Hinshaw, G., Weiland, J. L., Hill, R. S., Odegard, N., Larson, D., Bennett, C. L., Dunkley, J., Gold, B., Greason, M. R., Jarosik, N., Komatsu, E., Nolta, M. R., Page, L., Spergel, D. N., Wollack, E., Halpern, M., Kogut, A., Limon, M., Meyer, S. S., Tucker, G. S., and Wright, E. L. (2009). Five-Year Wilkinson Microwave Anisotropy Probe Observations: Data Processing, Sky Maps, and Basic Results. *Astrophys. J. Supp.*, 180:225–245.

Hoeft, M. and Brüggen, M. (2007). Radio signature of cosmological structure formation shocks. *Mon. Not. R. Astron. Soc.*, 375:77–91.

Hoeft, M., Brüggen, M., and Yepes, G. (2004). Radio relics in a cosmological cluster merger simulation. *Mon. Not. R. Astron. Soc.*, 347:389–393.

Hoeft, M., Brüggen, M., Yepes, G., Gottlöber, S., and Schwope, A. (2008). Diffuse radio emission from clusters in the MareNostrum Universe simulation. *Mon. Not. R. Astron. Soc.*, 391:1511–1526.

Hoekstra, H. (2007). A comparison of weak-lensing masses and X-ray properties of galaxy clusters. *Mon. Not. R. Astron. Soc.*, 379:317–330.

Hoekstra, H., Bartelmann, M., Dahle, H., Israel, H., Limousin, M., and Meneghetti, M. (2013). Masses of Galaxy Clusters from Gravitational Lensing. *Space Sci. Rev.*, 177:75–118.

Hoekstra, H., Franx, M., and Kuijken, K. (2000). Hubble Space Telescope Weak-Lensing Study of the z=0.83 Cluster MS 1054-03. *Astrophys. J.*, 532:88–108.

Holder, G., Haiman, Z., and Mohr, J. J. (2001). Constraints on Ω_m, Ω, and σ_8 from Galaxy Cluster Redshift Distributions. *Astrophys. J. Lett.*, 560:L111–L114.

Hong, S. E., Kang, H., and Ryu, D. (2015). Radio and X-Ray Shocks in Clusters of Galaxies. *Astrophys. J.*, 812:49.

Iapichino, L. and Niemeyer, J. C. (2008). Hydrodynamical adaptive mesh refinement simulations of turbulent flows - II. Cosmological simulations of galaxy clusters. *Mon. Not. R. Astron. Soc.*, 388:1089–1100.

Iapichino, L., Schmidt, W., Niemeyer, J. C., and Merklein, J. (2011). Turbulence production and turbulent pressure support in the intergalactic medium. *Mon. Not. R. Astron. Soc.*, 414:2297–2308.

Intema, H. T. (2014). SPAM: A data reduction recipe for high-resolution, low-frequency radio-interferometric observations. *ArXiv e-prints*.

Intema, H. T., van der Tol, S., Cotton, W. D., Cohen, A. S., van Bemmel, I. M., and Röttgering, H. J. A. (2009). Ionospheric calibration of low frequency radio interferometric observations using the peeling scheme. I. Method description and first results. *Astron. Astrophys.*, 501:1185–1205.

Ishigaki, M., Kawamata, R., Ouchi, M., Oguri, M., Shimasaku, K., and Ono, Y. (2015). Hubble Frontier Fields First Complete Cluster Data: Faint Galaxies at z ˜ 5-10 for UV Luminosity Functions and Cosmic Reionization. *Astrophys. J.*, 799:12.

Jacobson, A. R. and Erickson, W. C. (1992). Wavenumber-resolved observations of ionospheric waves using the Very Large Array radiotelescope. *PLANSS*, 40:447–455.

Jaffe, W. J. (1977). Origin and transport of electrons in the halo radio source in the Coma cluster. *Astrophys. J.*, 212:1–7.

Jaffe, W. J., Valentijn, E. A., and Perola, G. C. (1976). A Westerbork survey of rich clusters of galaxies. III - Observations of the Coma Cluster at 610 MHz. *Astron. Astrophys.*, 49:179–192.

Jansen, F., Lumb, D., Altieri, B., Clavel, J., Ehle, M., Erd, C., Gabriel, C., Guainazzi, M., Gondoin, P., Much, R., Munoz, R., Santos, M., Schartel, N., Texier, D., and Vacanti, G. (2001). XMM-Newton observatory. I. The spacecraft and operations. *Astron. Astrophys.*, 365:L1–L6.

Jauzac, M., Clément, B., Limousin, M., Richard, J., Jullo, E., Ebeling, H., Atek, H., Kneib, J.-P., Knowles, K., Natarajan, P., Eckert, D., Egami, E., Massey, R., and Rexroth, M. (2014). Hubble Frontier Fields: a high-precision strong-lensing analysis of galaxy cluster MACSJ0416.1-2403 using $\sim$200 multiple images. *Mon. Not. R. Astron. Soc.*, 443:1549–1554.

Jauzac, M., Jullo, E., Eckert, D., Ebeling, H., Richard, J., Limousin, M., Atek, H., Kneib, J.-P., Clément, B., Egami, E., Harvey, D., Knowles, K., Massey, R., Natarajan, P., Neichel, B., and Rexroth, M. (2015a). Hubble Frontier Fields: the geometry and dynamics of the massive galaxy cluster merger MACSJ0416.1-2403. *Mon. Not. R. Astron. Soc.*, 446:4132–4147.

Jauzac, M., Jullo, E., Kneib, J.-P., Ebeling, H., Leauthaud, A., Ma, C.-J., Limousin, M., Massey, R., and Richard, J. (2012). A weak lensing mass reconstruction of the large-scale filament feeding the massive galaxy cluster MACS J0717.5+3745. *Mon. Not. R. Astron. Soc.*, 426:3369–3384.

Jauzac, M., Richard, J., Jullo, E., Clément, B., Limousin, M., Kneib, J.-P., Ebeling, H., Natarajan, P., Rodney, S., Atek, H., Massey, R., Eckert, D., Egami, E., and Rexroth, M. (2015b). Hubble Frontier Fields: a high-precision strong-lensing analysis of the massive galaxy cluster Abell 2744 using $\sim$180 multiple images. *Mon. Not. R. Astron. Soc.*, 452:1437–1446.

Jauzac, M., Richard, J., Limousin, M., Knowles, K., Mahler, G., Smith, G. P., Kneib, J.-P., Jullo, E., Natarajan, P., Ebeling, H., Atek, H., Clément, B., Eckert, D., Egami, E., Massey, R., and Rexroth, M. (2015c). Hubble Frontier Fields: Predictions for the Return of SN Refsdal with the MUSE and GMOS Spectrographs. *ArXiv e-prints*.

Jeltema, T. E., Canizares, C. R., Bautz, M. W., and Buote, D. A. (2005). The Evolution of Structure in X-Ray Clusters of Galaxies. *Astrophys. J.*, 624:606–629.

Jeltema, T. E. and Profumo, S. (2011). Implications of Fermi Observations For Hadronic Models of Radio Halos in Clusters of Galaxies. *Astrophys. J.*, 728:53.

Johnson, T. L., Sharon, K., Bayliss, M. B., Gladders, M. D., Coe, D., and Ebeling, H. (2014). Lens Models and Magnification Maps of the Six Hubble Frontier Fields Clusters. *Astrophys. J.*, 797:48.

Johnston-Hollitt, M. (2003). *Detection of magnetic fields and diffuse radio emission in Abell 3667 and other rich southern clusters of galaxies*. PhD thesis, University of Adelaide.

Johnston-Hollitt, M., Ekers, R. D., Hunstead, R. W., Clay, R. W., and Wieringa, M. H. (2002). Cluster merger in A3667? New radio observations shed more light. *Highlights of Astronomy*, 12:535–536.

Jones, F. C. and Ellison, D. C. (1991). The plasma physics of shock acceleration. *Space Sci. Rev.*, 58:259–346.

Jones, T. W. (2011). Particle Acceleration at Shocks: Insights from Supernova Remnant Shocks. *Journal of Astrophysics and Astronomy*, 32:427–435.

Jørgensen, I., Franx, M., and Kjaergaard, P. (1996). The Fundamental Plane for cluster E and S0 galaxies. *Mon. Not. R. Astron. Soc.*, 280:167–185.

Jullo, E. and Kneib, J.-P. (2009). Multiscale cluster lens mass mapping - I. Strong lensing modelling. *Mon. Not. R. Astron. Soc.*, 395:1319–1332.

Jullo, E., Kneib, J.-P., Limousin, M., Elíasdóttir, Á., Marshall, P. J., and Verdugo, T. (2007). A Bayesian approach to strong lensing modelling of galaxy clusters. *New Journal of Physics*, 9:447.

Jullo, E., Natarajan, P., Kneib, J.-P., D'Aloisio, A., Limousin, M., Richard, J., and Schimd, C. (2010). Cosmological Constraints from Strong Gravitational Lensing in Clusters of Galaxies. *Science*, 329:924–927.

Kacprzak, T., Zuntz, J., Rowe, B., Bridle, S., Refregier, A., Amara, A., Voigt, L., and Hirsch, M. (2012). Measurement and calibration of noise bias in weak lensing galaxy shape estimation. *Mon. Not. R. Astron. Soc.*, 427:2711–2722.

Kaiser, N., Squires, G., and Broadhurst, T. (1995). A Method for Weak Lensing Observations. *Astrophys. J.*, 449:460.

Kale, R. and Dwarakanath, K. S. (2010). Spectral Index Studies of the Diffuse Radio Emission in Abell 2256: Implications for Merger Activity. *Astrophys. J.*, 718:939–946.

Kale, R. and Dwarakanath, K. S. (2012). Multi-frequency Studies of Radio Relics in the Galaxy Clusters A4038, A1664, and A786. *Astrophys. J.*, 744:46.

Kale, R., Dwarakanath, K. S., Bagchi, J., and Paul, S. (2012). Spectral and polarization study of the double relics in Abell 3376 using the Giant Metrewave Radio Telescope and the Very Large Array. *Mon. Not. R. Astron. Soc.*, 426:1204–1211.

Kale, R., Venturi, T., Giacintucci, S., Dallacasa, D., Cassano, R., Brunetti, G., Macario, G., and Athreya, R. (2013). The Extended GMRT Radio Halo Survey. I. New upper limits on radio halos and mini-halos. *Astron. Astrophys.*, 557:A99.

Kang, H. and Jones, T. W. (2005). Efficiency of Nonlinear Particle Acceleration at Cosmic Structure Shocks. *Astrophys. J.*, 620:44–58.

Kang, H. and Ryu, D. (2011). Re-acceleration of Non-thermal Particles at Weak Cosmological Shock Waves. *Astrophys. J.*, 734:18.

Kang, H., Ryu, D., Cen, R., and Ostriker, J. P. (2007). Cosmological Shock Waves in the Large-Scale Structure of the Universe: Nongravitational Effects. *Astrophys. J.*, 669:729–740.

Kang, H., Ryu, D., and Jones, T. W. (2012). Diffusive Shock Acceleration Simulations of Radio Relics. *Astrophys. J.*, 756:97.

Kassiola, A. and Kovner, I. (1993). Elliptic Mass Distributions versus Elliptic Potentials in Gravitational Lenses. *Astrophys. J.*, 417:450.

Katgert, P., Mazure, A., Perea, J., den Hartog, R., Moles, M., Le Fevre, O., Dubath, P., Focardi, P., Rhee, G., Jones, B., Escalera, E., Biviano, A., Gerbal, D., and Giuricin, G. (1996). The ESO Nearby Abell Cluster Survey. I. Description of the dataset and definition of physical systems. *Astron. Astrophys.*, 310:8–30.

Kazemi, S., Yatawatta, S., and Zaroubi, S. (2013). Clustered calibration: an improvement to radio interferometric direction-dependent self-calibration. *Mon. Not. R. Astron. Soc.*, 430:1457–1472.

Kelly, P. L., Rodney, S. A., Treu, T., Foley, R. J., Brammer, G., Schmidt, K. B., Zitrin, A., Sonnenfeld, A., Strolger, L.-G., Graur, O., Filippenko, A. V., Jha, S. W., Riess, A. G., Bradac, M., Weiner, B. J., Scolnic, D., Malkan, M. A., von der Linden, A., Trenti, M., Hjorth, J., Gavazzi, R., Fontana, A., Merten, J. C., McCully, C., Jones, T., Postman, M., Dressler, A., Patel, B., Cenko, S. B., Graham, M. L., and Tucker, B. E. (2015). Multiple images of a highly magnified supernova formed by an early-type cluster galaxy lens. *Science*, 347:1123–1126.

Keshet, U. and Loeb, A. (2010). Using Radio Halos and Minihalos to Measure the Distributions of Magnetic Fields and Cosmic Rays in Galaxy Clusters. *Astrophys. J.*, 722:737–749.

Keshet, U., Markevitch, M., Birnboim, Y., and Loeb, A. (2010). Dynamics and Magnetization in Galaxy Cluster Cores Traced by X-ray Cold Fronts. *Astrophys. J. Lett.*, 719:L74–L78.

Keshet, U., Waxman, E., and Loeb, A. (2004). Imprint of Intergalactic Shocks on the Radio Sky. *Astrophys. J.*, 617:281–302.

Kettenis, M., van Langevelde, H. J., Reynolds, C., and Cotton, B. (2006). ParselTongue: AIPS Talking Python. In Gabriel, C., Arviset, C., Ponz, D., and Enrique, S., editors, *Astronomical Data Analysis Software and Systems XV*, volume 351 of *Astronomical Society of the Pacific Conference Series*, page 497.

Kilbinger, M., Fu, L., Heymans, C., Simpson, F., Benjamin, J., Erben, T., Harnois-Déraps, J., Hoekstra, H., Hildebrandt, H., Kitching, T. D., Mellier, Y., Miller, L., Van Waerbeke, L., Benabed, K., Bonnett, C., Coupon, J., Hudson, M. J., Kuijken, K., Rowe, B., Schrabback, T., Semboloni, E., Vafaei, S., and Velander, M. (2013). CFHTLenS: combined probe cosmological model comparison using 2D weak gravitational lensing. *Mon. Not. R. Astron. Soc.*, 430:2200–2220.

Kim, K.-T., Kronberg, P. P., Dewdney, P. E., and Landecker, T. L. (1990). The halo and magnetic field of the Coma cluster of galaxies. *Astrophys. J.*, 355:29–37.

Kitching, T. D., Miller, L., Heymans, C. E., van Waerbeke, L., and Heavens, A. F. (2008). Bayesian galaxy shape measurement for weak lensing surveys - II. Application to simulations. *Mon. Not. R. Astron. Soc.*, 390:149–167.

Kneib, J.-P., Ellis, R. S., Smail, I., Couch, W. J., and Sharples, R. M. (1996). Hubble Space Telescope Observations of the Lensing Cluster Abell 2218. *Astrophys. J.*, 471:643.

Kneib, J.-P., Hudelot, P., Ellis, R. S., Treu, T., Smith, G. P., Marshall, P., Czoske, O., Smail, I., and Natarajan, P. (2003). A Wide-Field Hubble Space Telescope Study of the Cluster Cl 0024+1654 at z=0.4. II. The Cluster Mass Distribution. *Astrophys. J.*, 598:804–817.

Kneib, J. P., Mellier, Y., Fort, B., and Mathez, G. (1993). The Distribution of Dark Matter in Distant Cluster Lenses - Modelling A:370. *Astron. Astrophys.*, 273:367.

Kneib, J. P., Melnick, J., and Gopal-Krishna (1994). The Cl2236-04 lens cluster. Looking for a third gravitational image? *Astron. Astrophys.*, 290:L25–L28.

Kneib, J.-P. and Natarajan, P. (2011). Cluster lenses. *Astron. Astrophys. Rev.*, 19:47.

Kochanek, C. S. (1990). Inverting Cluster Gravitational Lenses. *Mon. Not. R. Astron. Soc.*, 247:135.

Koester, B. P., McKay, T. A., Annis, J., Wechsler, R. H., Evrard, A., Bleem, L., Becker, M., Johnston, D., Sheldon, E., Nichol, R., Miller, C., Scranton, R., Bahcall, N., Barentine, J., Brewington, H., Brinkmann, J., Harvanek, M., Kleinman, S., Krzesinski, J., Long, D., Nitta, A., Schneider, D. P., Sneddin, S., Voges, W., and York, D. (2007). A MaxBCG Catalog of 13,823 Galaxy Clusters from the Sloan Digital Sky Survey. *Astrophys. J.*, 660:239–255.

Komatsu, E., Smith, K. M., Dunkley, J., Bennett, C. L., Gold, B., Hinshaw, G., Jarosik, N., Larson, D., Nolta, M. R., Page, L., Spergel, D. N., Halpern, M., Hill, R. S., Kogut, A., Limon, M., Meyer, S. S., Odegard, N., Tucker, G. S., Weiland, J. L., Wollack, E., and Wright, E. L. (2011). Seven-year Wilkinson Microwave Anisotropy Probe (WMAP) Observations: Cosmological Interpretation. *Astrophys. J. Supp.*, 192:18.

Koopmans, L. V. E., Treu, T., Bolton, A. S., Burles, S., and Moustakas, L. A. (2006). The Sloan Lens ACS Survey. III. The Structure and Formation of Early-Type Galaxies and Their Evolution since z ˜ 1. *Astrophys. J.*, 649:599–615.

Kosowsky, A. (2006). The Atacama Cosmology Telescope project: A progress report. *New Astron. Rev.*, 50:969–976.

Kovner, I. and Paczynski, B. (1988). Supernovae in luminous arcs. *Astrophys. J. Lett.*, 335:L9–L13.

Kowalski, M., Rubin, D., Aldering, G., Agostinho, R. J., Amadon, A., Amanullah, R., Balland, C., Barbary, K., Blanc, G., Challis, P. J., Conley, A., Connolly, N. V., Covarrubias, R., Dawson, K. S., Deustua, S. E., Ellis, R., Fabbro, S., Fadeyev, V., Fan, X., Farris, B., Folatelli, G., Frye, B. L., Garavini, G., Gates, E. L., Germany, L., Goldhaber, G., Goldman, B., Goobar, A., Groom, D. E., Haissinski, J., Hardin, D., Hook, I., Kent, S., Kim, A. G., Knop, R. A., Lidman, C., Linder, E. V., Mendez, J., Meyers, J., Miller, G. J., Moniez, M., Mourão, A. M., Newberg, H., Nobili, S., Nugent, P. E., Pain, R., Perdereau, O., Perlmutter, S., Phillips, M. M., Prasad,

V., Quimby, R., Regnault, N., Rich, J., Rubenstein, E. P., Ruiz-Lapuente, P., Santos, F. D., Schaefer, B. E., Schommer, R. A., Smith, R. C., Soderberg, A. M., Spadafora, A. L., Strolger, L.-G., Strovink, M., Suntzeff, N. B., Suzuki, N., Thomas, R. C., Walton, N. A., Wang, L., Wood-Vasey, W. M., Yun, J. L., and Supernova Cosmology Project (2008). Improved Cosmological Constraints from New, Old, and Combined Supernova Data Sets. *Astrophys. J.*, 686:749–778.

Kronberg, P. P., Kothes, R., Salter, C. J., and Perillat, P. (2007). Discovery of New Faint Radio Emission on 8° to 3′ Scales in the Coma Field, and Some Galactic and Extragalactic Implications. *Astrophys. J.*, 659:267–274.

Kuijken, K. (1999). Weak weak lensing: correcting weak shear measurements accurately for PSF anisotropy. *Astron. Astrophys.*, 352:355–362.

Kuo, P.-H., Hwang, C.-Y., and Ip, W.-H. (2004). The Evolution of Diffuse Radio Sources in Galaxy Clusters. *Astrophys. J.*, 604:108–115.

Lam, D., Broadhurst, T., Diego, J. M., Lim, J., Coe, D., Ford, H. C., and Zheng, W. (2014). A Rigorous Free-form Lens Model of A2744 to Meet the Hubble Frontier Fields Challenge. *Astrophys. J.*, 797:98.

Laporte, N., Streblyanska, A., Clement, B., Pérez-Fournon, I., Schaerer, D., Atek, H., Boone, F., Kneib, J.-P., Egami, E., Martínez-Navajas, P., Marques-Chaves, R., Pelló, R., and Richard, J. (2014). The first Frontier Fields cluster: 4.5 μm excess in a z ˜ 8 galaxy candidate in Abell 2744. *Astron. Astrophys.*, 562:L8.

Laporte, N., Streblyanska, A., Kim, S., Pelló, R., Bauer, F. E., Bina, D., Brammer, G., De Leo, M. A., Infante, L., and Pérez-Fournon, I. (2015). Frontier Fields: Combining HST, VLT, and Spitzer data to explore the z ˜ 8 Universe behind the lensing cluster MACSJ0416.1-2403. *Astron. Astrophys.*, 575:A92.

Large, M. I., Mathewson, D. S., and Haslam, C. G. T. (1959). A High-Resolution Survey of the Coma Cluster of Galaxies at 408 Mc./s. *Nature.*, 183:1663–1664.

Lavalley, M., Isobe, T., and Feigelson, E. (1992). ASURV: Astronomy Survival Analysis Package. In Worrall, D. M., Biemesderfer, C., and Barnes, J., editors, *Astronomical Data Analysis Software and Systems I*, volume 25 of *Astronomical Society of the Pacific Conference Series*, page 245.

Leauthaud, A., Massey, R., Kneib, J.-P., Rhodes, J., Johnston, D. E., Capak, P., Heymans, C., Ellis, R. S., Koekemoer, A. M., Le Fèvre, O., Mellier, Y., Réfrégier, A., Robin, A. C., Scoville, N., Tasca, L., Taylor, J. E., and Van Waerbeke, L. (2007). Weak Gravitational Lensing with COSMOS: Galaxy Selection and Shape Measurements. *Astrophys. J. Supp.*, 172:219–238.

Ledlow, M. J., Voges, W., Owen, F. N., and Burns, J. O. (2003). The X-Ray Properties of Nearby Abell Clusters from the ROSAT All-Sky Survey: The Sample and Correlations with Optical Properties. *Astron. J.*, 126:2740–2751.

Leonard, A., Deb, S., and Goldberg, D. M. (2006). Gravitational Flexion by Galaxy Clusters. In *American Astronomical Society Meeting Abstracts #207*, volume 207 of *American Astronomical Society Meeting Abstracts*, page #206.09.

Leonard, A., Goldberg, D. M., Haaga, J. L., and Massey, R. (2007). Gravitational Shear, Flexion, and Strong Lensing in Abell 1689. *Astrophys. J.*, 666:51–63.

Leonard, A. and King, L. J. (2010). A new tool to determine masses and mass profiles using gravitational flexion. *Mon. Not. R. Astron. Soc.*, 405:1854–1866.

Leonard, A., King, L. J., and Goldberg, D. M. (2011). New constraints on the complex mass substructure in Abell 1689 from gravitational flexion. *Mon. Not. R. Astron. Soc.*, 413:789–804.

Liang, H., Hunstead, R. W., Birkinshaw, M., and Andreani, P. (2000). A Powerful Radio Halo in the Hottest Known Cluster of Galaxies 1E 0657-56. *Astrophys. J.*, 544:686–701.

Limousin, M., Ebeling, H., Richard, J., Swinbank, A. M., Smith, G. P., Jauzac, M., Rodionov, S., Ma, C.-J., Smail, I., Edge, A. C., Jullo, E., and Kneib, J.-P. (2012). Strong lensing by a

node of the cosmic web. The core of MACS J0717.5+3745 at z = 0.55. *Astron. Astrophys.*, 544:A71.

Limousin, M., Kneib, J.-P., and Natarajan, P. (2005). Constraining the mass distribution of galaxies using galaxy-galaxy lensing in clusters and in the field. *Mon. Not. R. Astron. Soc.*, 356:309–322.

Limousin, M., Richard, J., Jullo, E., Kneib, J.-P., Fort, B., Soucail, G., Elíasdóttir, Á., Natarajan, P., Ellis, R. S., Smail, I., Czoske, O., Smith, G. P., Hudelot, P., Bardeau, S., Ebeling, H., Egami, E., and Knudsen, K. K. (2007). Combining Strong and Weak Gravitational Lensing in Abell 1689. *Astrophys. J.*, 668:643–666.

Limousin, M., Richard, J., Kneib, J.-P., Brink, H., Pelló, R., Jullo, E., Tu, H., Sommer-Larsen, J., Egami, E., Michałowski, M. J., Cabanac, R., and Stark, D. P. (2008). Strong lensing in Abell 1703: constraints on the slope of the inner dark matter distribution. *Astron. Astrophys.*, 489:23–35.

Linder, E. V. (2011). Lensing time delays and cosmological complementarity. *Physical Review D.*, 84(12):123529.

Lindner, R. R., Baker, A. J., Hughes, J. P., Battaglia, N., Gupta, N., Knowles, K., Marriage, T. A., Menanteau, F., Moodley, K., Reese, E. D., and Srianand, R. (2014). The Radio Relics and Halo of El Gordo, a Massive z = 0.870 Cluster Merger. *Astrophys. J.*, 786:49.

Liu, J., Petri, A., Haiman, Z., Hui, L., Kratochvil, J. M., and May, M. (2015). Cosmology constraints from the weak lensing peak counts and the power spectrum in CFHTLenS data. *Physical Review D.*, 91(6):063507.

Lloyd-Davies, E. J., Romer, A. K., Mehrtens, N., Hosmer, M., Davidson, M., Sabirli, K., Mann, R. G., Hilton, M., Liddle, A. R., Viana, P. T. P., Campbell, H. C., Collins, C. A., Dubois, E. N., Freeman, P., Harrison, C. D., Hoyle, B., Kay, S. T., Kuwertz, E., Miller, C. J., Nichol, R. C., Sahlén, M., Stanford, S. A., and Stott, J. P. (2011). The XMM Cluster Survey: X-ray analysis methodology. *Mon. Not. R. Astron. Soc.*, 418:14–53.

Lochner, M., Natarajan, I., Zwart, J. T. L., Smirnov, O., Bassett, B. A., Oozeer, N., and Kunz, M. (2015). Bayesian inference for radio observations. *Mon. Not. R. Astron. Soc.*, 450:1308–1319.

Loewenstein, M. and Mathews, W. G. (1987). Evolution of hot galactic flows. *Astrophys. J.*, 319:614–631.

Loewenstein, M. and Mushotzky, R. F. (1996). Measurement of the Elemental Abundances in Four Rich Clusters of Galaxies. II. The Initial Mass Function and Mass Loss in Elliptical Galaxies, Enrichment, and Energetics in the ICM. *Astrophys. J.*, 466:695.

Longair, M. S. (2011). *High Energy Astrophysics*.

Lonsdale, C. J. (2005). Configuration Considerations for Low Frequency Arrays. In Kassim, N., Perez, M., Junor, W., and Henning, P., editors, *From Clark Lake to the Long Wavelength Array: Bill Erickson's Radio Science*, volume 345 of *Astronomical Society of the Pacific Conference Series*, page 399.

Lucey, J. R. (1983). An assessment of the completeness and correctness of the Abell catalogue. *Mon. Not. R. Astron. Soc.*, 204:33–43.

Luppino, G. A. and Kaiser, N. (1997). Detection of Weak Lensing by a Cluster of Galaxies at z = 0.83. *Astrophys. J.*, 475:20–28.

Lynds, R. and Petrosian, V. (1986). Giant Luminous Arcs in Galaxy Clusters. In *Bulletin of the American Astronomical Society*, volume 18 of *Bulletin of the American Astronomical Society*, page 1014.

Macario, G., Markevitch, M., Giacintucci, S., Brunetti, G., Venturi, T., and Murray, S. S. (2011). A Shock Front in the Merging Galaxy Cluster A754: X-ray and Radio Observations. *Astrophys. J.*, 728:82.

Mahler, G., Richard, J., Patricio, V., Clément, B., and Lagattuta, D. (2015). Automatic Selection of Multiple Images in the Frontier Field Clusters. *IAU General Assembly*, 22:57080.

Majerowicz, S., Neumann, D. M., Romer, A. K., Nichol, R. C., Burke, D. J., and Collins, C. A. (2004). RX J0256.5+0006: A merging cluster of galaxies at z = 0.36 observed with XMM-NEWTON. *Astron. Astrophys.*, 425:15–32.

Mann, A. W. and Ebeling, H. (2012). X-ray-optical classification of cluster mergers and the evolution of the cluster merger fraction. *Mon. Not. R. Astron. Soc.*, 420:2120–2138.

Mantz, A. B., Allen, S. W., Morris, R. G., Rapetti, D. A., Applegate, D. E., Kelly, P. L., von der Linden, A., and Schmidt, R. W. (2014). Cosmology and astrophysics from relaxed galaxy clusters - II. Cosmological constraints. *Mon. Not. R. Astron. Soc.*, 440:2077–2098.

Marian, L. and Bernstein, G. M. (2006). Dark energy constraints from lensing-detected galaxy clusters. *Physical Review D.*, 73(12):123525.

Markevitch, M. (2010). Intergalactic shock fronts. *ArXiv e-prints*.

Markevitch, M., Govoni, F., Brunetti, G., and Jerius, D. (2005). Bow Shock and Radio Halo in the Merging Cluster A520. *Astrophys. J.*, 627:733–738.

Markevitch, M. and Vikhlinin, A. (2007). Shocks and cold fronts in galaxy clusters. *Phys. Rep.*, 443:1–53.

Marriage, T. A., Acquaviva, V., Ade, P. A. R., Aguirre, P., Amiri, M., Appel, J. W., Barrientos, L. F., Battistelli, E. S., Bond, J. R., Brown, B., Burger, B., Chervenak, J., Das, S., Devlin, M. J., Dicker, S. R., Bertrand Doriese, W., Dunkley, J., Dünner, R., Essinger-Hileman, T., Fisher, R. P., Fowler, J. W., Hajian, A., Halpern, M., Hasselfield, M., Hernández-Monteagudo, C., Hilton, G. C., Hilton, M., Hincks, A. D., Hlozek, R., Huffenberger, K. M., Handel Hughes, D., Hughes, J. P., Infante, L., Irwin, K. D., Baptiste Juin, J., Kaul, M., Klein, J., Kosowsky, A., Lau, J. M., Limon, M., Lin, Y.-T., Lupton, R. H., Marsden, D., Martocci, K., Mauskopf, P., Menanteau, F., Moodley, K., Moseley, H., Netterfield, C. B., Niemack, M. D., Nolta, M. R., Page, L. A., Parker, L., Partridge, B., Quintana, H., Reese, E. D., Reid, B., Sehgal, N., Sherwin, B. D., Sievers, J., Spergel, D. N., Staggs, S. T., Swetz, D. S., Switzer, E. R., Thornton, R., Trac, H., Tucker, C., Warne, R., Wilson, G., Wollack, E., and Zhao, Y. (2011).

The Atacama Cosmology Telescope: Sunyaev-Zel'dovich-Selected Galaxy Clusters at 148 GHz in the 2008 Survey. *Astrophys. J.*, 737:61.

Massey, R., Stoughton, C., Leauthaud, A., Rhodes, J., Koekemoer, A., Ellis, R., and Shaghoulian, E. (2010). Pixel-based correction for Charge Transfer Inefficiency in the Hubble Space Telescope Advanced Camera for Surveys. *Mon. Not. R. Astron. Soc.*, 401:371–384.

Massey, R., Williams, L., Smit, R., Swinbank, M., Kitching, T. D., Harvey, D., Jauzac, M., Israel, H., Clowe, D., Edge, A., Hilton, M., Jullo, E., Leonard, A., Liesenborgs, J., Merten, J., Mohammed, I., Nagai, D., Richard, J., Robertson, A., Saha, P., Santana, R., Stott, J., and Tittley, E. (2015). The behaviour of dark matter associated with four bright cluster galaxies in the 10 kpc core of Abell 3827. *Mon. Not. R. Astron. Soc.*, 449:3393–3406.

Mathews, W. G. and Brighenti, F. (2008). Creation of the X-Ray Cavity Jet and Its Radio Lobe in M87/Virgo with Cosmic Rays: Relevance to Relic Radio Sources. *Astrophys. J.*, 676:880–888.

Maughan, B. J., Jones, C., Forman, W., and Van Speybroeck, L. (2008). Images, Structural Properties, and Metal Abundances of Galaxy Clusters Observed with Chandra ACIS-I at $0.1<z<1.3$. *Astrophys. J. Supp.*, 174:117–135.

Mazzotta, P. and Giacintucci, S. (2008). Do Radio Core-Halos and Cold Fronts in Non-Major-Merging Clusters Originate from the Same Gas Sloshing? *Astrophys. J. Lett.*, 675:L9–L12.

McLeod, D. J., McLure, R. J., Dunlop, J. S., Robertson, B. E., Ellis, R. S., and Targett, T. A. (2015). New redshift $z \simeq 9$ galaxies in the Hubble Frontier Fields: implications for early evolution of the UV luminosity density. *Mon. Not. R. Astron. Soc.*, 450:3032–3044.

McMullin, J. P., Waters, B., Schiebel, D., Young, W., and Golap, K. (2007). CASA Architecture and Applications. In Shaw, R. A., Hill, F., and Bell, D. J., editors, *Astronomical Data Analysis Software and Systems XVI*, volume 376 of *Astronomical Society of the Pacific Conference Series*, page 127.

Meekins, J. F., Fritz, G., Chubb, T. A., and Friedman, H. (1971). Physical Sciences: X-rays from the Coma Cluster of Galaxies. *Nature.*, 231:107–108.

Meiksin, A. (1990). The evolution of cooling flows in clusters of galaxies. *Astrophys. J.*, 352:466–494.

Mellier, Y. (1999). Probing the Universe with Weak Lensing. *Annu. Rev. Astron. Astrophys.*, 37:127–189.

Mellier, Y., Fort, B., and Kneib, J.-P. (1993). The dark matter distribution in MS 2137-23 from the modeling of the multiple arc systems. *Astrophys. J.*, 407:33–45.

Menanteau, F., Hughes, J. P., Sifón, C., Hilton, M., González, J., Infante, L., Barrientos, L. F., Baker, A. J., Bond, J. R., Das, S., Devlin, M. J., Dunkley, J., Hajian, A., Hincks, A. D., Kosowsky, A., Marsden, D., Marriage, T. A., Moodley, K., Niemack, M. D., Nolta, M. R., Page, L. A., Reese, E. D., Sehgal, N., Sievers, J., Spergel, D. N., Staggs, S. T., and Wollack, E. (2012). The Atacama Cosmology Telescope: ACT-CL J0102-4915 "El Gordo," a Massive Merging Cluster at Redshift 0.87. *Astrophys. J.*, 748:7.

Menanteau, F., Sifón, C., Barrientos, L. F., Battaglia, N., Bond, J. R., Crichton, D., Das, S., Devlin, M. J., Dicker, S., Dünner, R., Gralla, M., Hajian, A., Hasselfield, M., Hilton, M., Hincks, A. D., Hughes, J. P., Infante, L., Kosowsky, A., Marriage, T. A., Marsden, D., Moodley, K., Niemack, M. D., Nolta, M. R., Page, L. A., Partridge, B., Reese, E. D., Schmitt, B. L., Sievers, J., Spergel, D. N., Staggs, S. T., Switzer, E., and Wollack, E. J. (2013). The Atacama Cosmology Telescope: Physical Properties of Sunyaev-Zel'dovich Effect Clusters on the Celestial Equator. *Astrophys. J.*, 765:67.

Meng, X.-L., Treu, T., Agnello, A., Auger, M. W., Liao, K., and Marshall, P. J. (2015). Precision cosmology with time delay lenses: high resolution imaging requirements. *Journal of Cosmology and Astroparticle Physics.*, 9:59.

Merten, J., Coe, D., Dupke, R., Massey, R., Zitrin, A., Cypriano, E. S., Okabe, N., Frye, B., Braglia, F. G., Jiménez-Teja, Y., Benítez, N., Broadhurst, T., Rhodes, J., Meneghetti, M., Moustakas, L. A., Sodré, Jr., L., Krick, J., and Bregman, J. N. (2011). Creation of cos-

mic structure in the complex galaxy cluster merger Abell 2744. *Mon. Not. R. Astron. Soc.*, 417:333–347.

Meszaros, P. (1974). The behaviour of point masses in an expanding cosmological substratum. *Astron. Astrophys.*, 37:225–228.

Miley, G. K. and Perola, G. C. (1975). The Large Scale Radio Structure of NGC 1275. *Astron. Astrophys.*, 45:223.

Miller, L., Kitching, T. D., Heymans, C., Heavens, A. F., and van Waerbeke, L. (2007). Bayesian galaxy shape measurement for weak lensing surveys - I. Methodology and a fast-fitting algorithm. *Mon. Not. R. Astron. Soc.*, 382:315–324.

Miniati, F. (2014). The Matryoshka Run: A Eulerian Refinement Strategy to Study the Statistics of Turbulence in Virialized Cosmic Structures. *Astrophys. J.*, 782:21.

Miniati, F., Jones, T. W., Kang, H., and Ryu, D. (2001a). Cosmic-Ray Electrons in Groups and Clusters of Galaxies: Primary and Secondary Populations from a Numerical Cosmological Simulation. *Astrophys. J.*, 562:233–253.

Miniati, F., Ryu, D., Kang, H., and Jones, T. W. (2001b). Cosmic-Ray Protons Accelerated at Cosmological Shocks and Their Impact on Groups and Clusters of Galaxies. *Astrophys. J.*, 559:59–69.

Miniati, F., Ryu, D., Kang, H., Jones, T. W., Cen, R., and Ostriker, J. P. (2000). Properties of Cosmic Shock Waves in Large-Scale Structure Formation. *Astrophys. J.*, 542:608–621.

Miralda-Escude, J. (1991). Gravitational lensing by clusters of galaxies - Constraining the mass distribution. *Astrophys. J.*, 370:1–14.

Miralda-Escude, J. and Fort, B. (1993). Gravitational Lensing Pairs in Clusters of Galaxies: A New Probe to the High-Redshift Universe. *Astrophys. J. Lett.*, 417:L5.

Misner, C. W., Thorne, K. S., and Wheeler, J. A. (1973). *Gravitation*.

Mitchell, J. L., Keeton, C. R., Frieman, J. A., and Sheth, R. K. (2005). Improved Cosmological Constraints from Gravitational Lens Statistics. *Astrophys. J.*, 622:81–98.

Mittal, R., Hudson, D. S., Reiprich, T. H., and Clarke, T. (2009). AGN heating and ICM cooling in the HIFLUGCS sample of galaxy clusters. *Astron. Astrophys.*, 501:835–850.

Moffet, A. T. and Birkinshaw, M. (1989). A VLA survey of the three clusters of galaxies 0016 + 16, Abell 665, and Abell 2218. *Astron. J.*, 98:1148–1174.

Mohammed, I., Liesenborgs, J., Saha, P., and Williams, L. L. R. (2014). Mass-galaxy offsets in Abell 3827, 2218 and 1689: intrinsic properties or line-of-sight substructures? *Mon. Not. R. Astron. Soc.*, 439:2651–2661.

Mohan, N. and Rafferty, D. (2015). PyBDSM: Python Blob Detection and Source Measurement. Astrophysics Source Code Library.

Mohr, J. J., Fabricant, D. G., and Geller, M. J. (1993). An X-ray method for detecting substructure in galaxy clusters - Application to Perseus, A2256, Centaurus, Coma, and Sersic 40/6. *Astrophys. J.*, 413:492–505.

Molina, M., Bassani, L., Malizia, A., Bird, A. J., Bazzano, A., Ubertini, P., and Venturi, T. (2014). IGR J17488-2338: a newly discovered giant radio galaxy. *Astron. Astrophys.*, 565:A2.

Morlino, G. and Caprioli, D. (2012). Strong evidence for hadron acceleration in Tycho's supernova remnant. *Astron. Astrophys.*, 538:A81.

Moshir, M., Kopan, G., Conrow, T., McCallon, H., Hacking, P., Gregorich, D., Rohrbach, G., Melnyk, M., Rice, W., Fullmer, L., White, J., and Chester, T. (1990). The IRAS Faint Source Catalog, Version 2. In *Bulletin of the American Astronomical Society*, volume 22 of *Bulletin of the American Astronomical Society*, page 1325.

Moustakas, J. and Kennicutt, Jr., R. C. (2006). An Integrated Spectrophotometric Survey of Nearby Star-forming Galaxies. *Astrophys. J. Supp.*, 164:81–98.

Munari, E., Biviano, A., Borgani, S., Murante, G., and Fabjan, D. (2013). The relation between velocity dispersion and mass in simulated clusters of galaxies: dependence on the tracer and the baryonic physics. *Mon. Not. R. Astron. Soc.*, 430:2638–2649.

Munshi, D., Smidt, J., Heavens, A., Coles, P., and Cooray, A. (2011). Higher order statistics of weak lensing shear and flexion. *Mon. Not. R. Astron. Soc.*, 411:2241–2258.

Muratov, A. L. and Gnedin, O. Y. (2010). Modeling the Metallicity Distribution of Globular Clusters. *Astrophys. J.*, 718:1266–1288.

Murgia, M., Eckert, D., Govoni, F., Ferrari, C., Pandey-Pommier, M., Nevalainen, J., and Paltani, S. (2010a). GMRT observations of the Ophiuchus galaxy cluster. *Astron. Astrophys.*, 514:A76.

Murgia, M., Govoni, F., Feretti, L., and Giovannini, G. (2010b). A double radio halo in the close pair of galaxy clusters Abell 399 and Abell 401. *Astron. Astrophys.*, 509:A86.

Murgia, M., Govoni, F., Markevitch, M., Feretti, L., Giovannini, G., Taylor, G. B., and Carretti, E. (2009). Comparative analysis of the diffuse radio emission in the galaxy clusters A1835, A2029, and Ophiuchus. *Astron. Astrophys.*, 499:679–695.

Nagai, D., Lau, E. T., Avestruz, C., Nelson, K., and Rudd, D. H. (2013). Predicting Merger-induced Gas Motions in ΛCDM Galaxy Clusters. *Astrophys. J.*, 777:137.

Natarajan, P. and Kneib, J.-P. (1997). Lensing by galaxy haloes in clusters of galaxies. *Mon. Not. R. Astron. Soc.*, 287:833–847.

Natarajan, P., Kneib, J.-P., Smail, I., and Ellis, R. S. (1998). The Mass-to-Light Ratio of Early-Type Galaxies: Constraints from Gravitational Lensing in the Rich Cluster AC 114. *Astrophys. J.*, 499:600–607.

Natarajan, P., Kneib, J.-P., Smail, I., Treu, T., Ellis, R., Moran, S., Limousin, M., and Czoske, O. (2009). The Survival of Dark Matter Halos in the Cluster Cl 0024+16. *Astrophys. J.*, 693:970–983.

Navarro, J. F., Frenk, C. S., and White, S. D. M. (1997). A Universal Density Profile from Hierarchical Clustering. *Astrophys. J.*, 490:493–508.

Noordam, J. E. (2004). LOFAR calibration challenges. In Oschmann, Jr., J. M., editor, *Ground-based Telescopes*, volume 5489 of *Society of Photo-Optical Instrumentation Engineers (SPIE) Conference Series*, pages 817–825.

Noordam, J. E. and de Bruyn, A. G. (1982). High dynamic range mapping of strong radio sources, with application to 3C84. *Nature.*, 299:597.

Núñez, D., González-Morales, A. X., Cervantes-Cota, J. L., and Matos, T. (2010). Testing dark matter halos using rotation curves and lensing: A warning on the determination of the halo mass. *Physical Review D.*, 82(2):024025.

O'Dea, C. P. (1985). Constraints on bent beams in narrow angle tail radio sources. *Astrophys. J.*, 295:80–88.

Ogrean, G. A., Brüggen, M., Röttgering, H., Simionescu, A., Croston, J. H., van Weeren, R., and Hoeft, M. (2013a). XMM-Newton observations of the merging galaxy cluster CIZA J2242.8+5301. *Mon. Not. R. Astron. Soc.*, 429:2617–2633.

Ogrean, G. A., Brüggen, M., van Weeren, R. J., Röttgering, H., Croston, J. H., and Hoeft, M. (2013b). Challenges to our understanding of radio relics: X-ray observations of the Toothbrush cluster. *Mon. Not. R. Astron. Soc.*, 433:812–824.

Ogrean, G. A., van Weeren, R. J., Jones, C., Clarke, T. E., Sayers, J., Mroczkowski, T., Nulsen, P. E. J., Forman, W., Murray, S. S., Pandey-Pommier, M., Randall, S., Churazov, E., Bonafede, A., Kraft, R., David, L., Andrade-Santos, F., Merten, J., Zitrin, A., Umetsu, K., Goulding, A., Roediger, E., Bagchi, J., Bulbul, E., Donahue, M., Ebeling, H., Johnston-Hollitt, M., Mason, B., Rosati, P., and Vikhlinin, A. (2015). Frontier Fields Clusters: Chandra and JVLA View of the Pre-merging Cluster MACS J0416.1-2403. *Astrophys. J.*, 812:153.

Oguri, M. (2010). The Mass Distribution of SDSS J1004+4112 Revisited. *Pub. Astron. Soc. Japan*, 62:1017–.

Oguri, M. (2015). Predicted properties of multiple images of the strongly lensed supernova SN Refsdal. *Mon. Not. R. Astron. Soc.*, 449:L86–L89.

O'Hara, T. B., Mohr, J. J., Bialek, J. J., and Evrard, A. E. (2006). Effects of Mergers and Core Structure on the Bulk Properties of Nearby Galaxy Clusters. *Astrophys. J.*, 639:64–80.

Okabe, N., Zhang, Y.-Y., Finoguenov, A., Takada, M., Smith, G. P., Umetsu, K., and Futamase, T. (2010). LoCuSS: Calibrating Mass-observable Scaling Relations for Cluster Cosmology with Subaru Weak-lensing Observations. *Astrophys. J.*, 721:875–885.

Okura, Y., Umetsu, K., and Futamase, T. (2007). A New Measure for Weak-Lensing Flexion. *Astrophys. J.*, 660:995–1002.

Orban de Xivry, G. and Marshall, P. (2009). An atlas of predicted exotic gravitational lenses. *Mon. Not. R. Astron. Soc.*, 399:2–20.

Orrú, E., Murgia, M., Feretti, L., Govoni, F., Brunetti, G., Giovannini, G., Girardi, M., and Setti, G. (2007). Low-frequency study of two clusters of galaxies: A2744 and A2219. *Astron. Astrophys.*, 467:943–954.

Owers, M. S., Nulsen, P. E. J., Couch, W. J., Ma, C.-J., David, L. P., Forman, W. R., Hopkins, A. M., Jones, C., and van Weeren, R. J. (2014). A Merger Shock in A2034. *Astrophys. J.*, 780:163.

Paczynski, B. (1987). Giant luminous arcs discovered in two clusters of galaxies. *Nature.*, 325:572–573.

Patel, B., McCully, C., Jha, S. W., Rodney, S. A., Jones, D. O., Graur, O., Merten, J., Zitrin, A., Riess, A. G., Matheson, T., Sako, M., Holoien, T. W.-S., Postman, M., Coe, D., Bartelmann, M., Balestra, I., Benítez, N., Bouwens, R., Bradley, L., Broadhurst, T., Cenko, S. B., Donahue, M., Filippenko, A. V., Ford, H., Garnavich, P., Grillo, C., Infante, L., Jouvel, S., Kelson, D., Koekemoer, A., Lahav, O., Lemze, D., Maoz, D., Medezinski, E., Melchior, P., Meneghetti, M., Molino, A., Moustakas, J., Moustakas, L. A., Nonino, M., Rosati, P., Seitz, S., Strolger,

L. G., Umetsu, K., and Zheng, W. (2014). Three Gravitationally Lensed Supernovae behind CLASH Galaxy Clusters. *Astrophys. J.*, 786:9.

Paul, S., Iapichino, L., Miniati, F., Bagchi, J., and Mannheim, K. (2011). Evolution of Shocks and Turbulence in Major Cluster Mergers. *Astrophys. J.*, 726:17.

Peacock, J. A., Cole, S., Norberg, P., Baugh, C. M., Bland-Hawthorn, J., Bridges, T., Cannon, R. D., Colless, M., Collins, C., Couch, W., Dalton, G., Deeley, K., De Propris, R., Driver, S. P., Efstathiou, G., Ellis, R. S., Frenk, C. S., Glazebrook, K., Jackson, C., Lahav, O., Lewis, I., Lumsden, S., Maddox, S., Percival, W. J., Peterson, B. A., Price, I., Sutherland, W., and Taylor, K. (2001). A measurement of the cosmological mass density from clustering in the 2dF Galaxy Redshift Survey. *Nature.*, 410:169–173.

Pearson, T. J. and Readhead, A. C. S. (1984). Image Formation by Self-Calibration in Radio Astronomy. *Annu. Rev. Astron. Astrophys.*, 22:97–130.

Pello, R., Sanahuja, B., Le Borgne, J.-F., Soucail, G., and Mellier, Y. (1991). A straight gravitational image in Abell 2390 - A striking case of lensing by a cluster of galaxies. *Astrophys. J.*, 366:405–411.

Penzias, A. A. and Wilson, R. W. (1965). A Measurement of Excess Antenna Temperature at 4080 Mc/s. *Astrophys. J.*, 142:419–421.

Percival, W. J., Baugh, C. M., Bland-Hawthorn, J., Bridges, T., Cannon, R., Cole, S., Colless, M., Collins, C., Couch, W., Dalton, G., De Propris, R., Driver, S. P., Efstathiou, G., Ellis, R. S., Frenk, C. S., Glazebrook, K., Jackson, C., Lahav, O., Lewis, I., Lumsden, S., Maddox, S., Moody, S., Norberg, P., Peacock, J. A., Peterson, B. A., Sutherland, W., and Taylor, K. (2001). The 2dF Galaxy Redshift Survey: the power spectrum and the matter content of the Universe. *Mon. Not. R. Astron. Soc.*, 327:1297–1306.

Pérez-González, P. G., Gil de Paz, A., Zamorano, J., Gallego, J., Alonso-Herrero, A., and Aragón-Salamanca, A. (2003). Stellar populations in local star-forming galaxies - II. Recent star formation properties and stellar masses. *Mon. Not. R. Astron. Soc.*, 338:525–543.

Perlmutter, S., Aldering, G., Goldhaber, G., Knop, R. A., Nugent, P., Castro, P. G., Deustua, S., Fabbro, S., Goobar, A., Groom, D. E., Hook, I. M., Kim, A. G., Kim, M. Y., Lee, J. C., Nunes, N. J., Pain, R., Pennypacker, C. R., Quimby, R., Lidman, C., Ellis, R. S., Irwin, M., McMahon, R. G., Ruiz-Lapuente, P., Walton, N., Schaefer, B., Boyle, B. J., Filippenko, A. V., Matheson, T., Fruchter, A. S., Panagia, N., Newberg, H. J. M., Couch, W. J., and Project, T. S. C. (1999). Measurements of Ω and Λ from 42 High-Redshift Supernovae. *Astrophys. J.*, 517:565–586.

Petrosian, V. (2001). On the Nonthermal Emission and Acceleration of Electrons in Coma and Other Clusters of Galaxies. *Astrophys. J.*, 557:560–572.

Pfrommer, C. and Enßlin, T. A. (2004). Constraining the population of cosmic ray protons in cooling flow clusters with γ-ray and radio observations: Are radio mini-halos of hadronic origin? *Astron. Astrophys.*, 413:17–36.

Pfrommer, C., Enßlin, T. A., Springel, V., Jubelgas, M., and Dolag, K. (2007). Simulating cosmic rays in clusters of galaxies - I. Effects on the Sunyaev-Zel'dovich effect and the X-ray emission. *Mon. Not. R. Astron. Soc.*, 378:385–408.

Pfrommer, C., Springel, V., Enßlin, T. A., and Jubelgas, M. (2006). Detecting shock waves in cosmological smoothed particle hydrodynamics simulations. *Mon. Not. R. Astron. Soc.*, 367:113–131.

Pierpaoli, E., Borgani, S., Scott, D., and White, M. (2003). On determining the cluster abundance normalization. *Mon. Not. R. Astron. Soc.*, 342:163–175.

Pinzke, A., Oh, S. P., and Pfrommer, C. (2013). Giant radio relics in galaxy clusters: reacceleration of fossil relativistic electrons? *Mon. Not. R. Astron. Soc.*, 435:1061–1082.

Pizzo, R. F. and de Bruyn, A. G. (2009). Radio spectral study of the cluster of galaxies Abell 2255. *Astron. Astrophys.*, 507:639–659.

Planck Collaboration, Ade, P. A. R., Aghanim, N., Alves, M. I. R., Armitage-Caplan, C., Arnaud, M., Ashdown, M., Atrio-Barandela, F., Aumont, J., Aussel, H., and et al. (2014a). Planck 2013 results. I. Overview of products and scientific results. *Astron. Astrophys.*, 571:A1.

Planck Collaboration, Ade, P. A. R., Aghanim, N., Armitage-Caplan, C., Arnaud, M., Ashdown, M., Atrio-Barandela, F., Aumont, J., Aussel, H., Baccigalupi, C., and et al. (2014b). Planck 2013 results. XXIX. The Planck catalogue of Sunyaev-Zeldovich sources. *Astron. Astrophys.*, 571:A29.

Planck Collaboration, Ade, P. A. R., Aghanim, N., Armitage-Caplan, C., Arnaud, M., Ashdown, M., Atrio-Barandela, F., Aumont, J., Baccigalupi, C., Banday, A. J., and et al. (2014c). Planck 2013 results. XVI. Cosmological parameters. *Astron. Astrophys.*, 571:A16.

Planck Collaboration, Ade, P. A. R., Aghanim, N., Armitage-Caplan, C., Arnaud, M., Ashdown, M., Atrio-Barandela, F., Aumont, J., Baccigalupi, C., Banday, A. J., and et al. (2014d). Planck 2013 results. XX. Cosmology from Sunyaev-Zeldovich cluster counts. *Astron. Astrophys.*, 571:A20.

Planck Collaboration, Ade, P. A. R., Aghanim, N., Arnaud, M., Ashdown, M., Aumont, J., Baccigalupi, C., Balbi, A., Banday, A. J., Barreiro, R. B., and et al. (2011). Planck early results. VIII. The all-sky early Sunyaev-Zeldovich cluster sample. *Astron. Astrophys.*, 536:A8.

Poole, G. B., Babul, A., McCarthy, I. G., Fardal, M. A., Bildfell, C. J., Quinn, T., and Mahdavi, A. (2007). The impact of mergers on relaxed X-ray clusters - II. Effects on global X-ray and Sunyaev-Zel'dovich properties and their scaling relations. *Mon. Not. R. Astron. Soc.*, 380:437–454.

Poole, G. B., Fardal, M. A., Babul, A., McCarthy, I. G., Quinn, T., and Wadsley, J. (2006). The impact of mergers on relaxed X-ray clusters - I. Dynamical evolution and emergent transient structures. *Mon. Not. R. Astron. Soc.*, 373:881–905.

Postman, M., Coe, D., Benítez, N., Bradley, L., Broadhurst, T., Donahue, M., Ford, H., Graur, O., Graves, G., Jouvel, S., Koekemoer, A., Lemze, D., Medezinski, E., Molino, A., Moustakas, L., Ogaz, S., Riess, A., Rodney, S., Rosati, P., Umetsu, K., Zheng, W., Zitrin, A., Bartelmann, M., Bouwens, R., Czakon, N., Golwala, S., Host, O., Infante, L., Jha, S., Jimenez-Teja, Y., Kelson, D., Lahav, O., Lazkoz, R., Maoz, D., McCully, C., Melchior, P., Meneghetti, M.,

Merten, J., Moustakas, J., Nonino, M., Patel, B., Regös, E., Sayers, J., Seitz, S., and Van der Wel, A. (2012). The Cluster Lensing and Supernova Survey with Hubble: An Overview. *Astrophys. J. Supp.*, 199:25.

Postman, M., Lubin, L. M., Gunn, J. E., Oke, J. B., Hoessel, J. G., Schneider, D. P., and Christensen, J. A. (1996). The Palomar Distant Clusters Survey. I. The Cluster Catalog. *Astron. J.*, 111:615.

Press, W. H., Flannery, B. P., and Teukolsky, S. A. (1986). *Numerical recipes. The art of scientific computing*.

Prevot, M. L., Lequeux, J., Prevot, L., Maurice, E., and Rocca-Volmerange, B. (1984). The typical interstellar extinction in the Small Magellanic Cloud. *Astron. Astrophys.*, 132:389–392.

Quillen, A. C. and Frogel, J. A. (1997). The Distribution of Dark Matter in a Ringed Galaxy. *Astrophys. J.*, 487:603–616.

Quimby, R. M., Oguri, M., More, A., More, S., Moriya, T. J., Werner, M. C., Tanaka, M., Folatelli, G., Bersten, M. C., Maeda, K., and Nomoto, K. (2014). Detection of the Gravitational Lens Magnifying a Type Ia Supernova. *Science*, 344:396–399.

Racine, R. (1981). The Canada-France-Hawaii Telescope - Gestation, infancy and future. *Journal of the Royal Astronomical Society of Canada*, 75:305–315.

Randall, S. W., Clarke, T. E., Nulsen, P. E. J., Owers, M. S., Sarazin, C. L., Forman, W. R., and Murray, S. S. (2010). Radio and Deep Chandra Observations of the Disturbed Cool Core Cluster Abell 133. *Astrophys. J.*, 722:825–846.

Randall, S. W., Sarazin, C. L., and Ricker, P. M. (2002). The Effect of Merger Boosts on the Luminosity, Temperature, and Inferred Mass Functions of Clusters of Galaxies. *Astrophys. J.*, 577:579–594.

Rau, S., Vegetti, S., and White, S. D. M. (2014). Lensing model of MACS J1149.5+2223 - I. Cluster mass reconstruction. *Mon. Not. R. Astron. Soc.*, 443:957–968.

Refregier, A. and Bacon, D. (2003). Shapelets - II. A method for weak lensing measurements. *Mon. Not. R. Astron. Soc.*, 338:48–56.

Refregier, A., Kacprzak, T., Amara, A., Bridle, S., and Rowe, B. (2012). Noise bias in weak lensing shape measurements. *Mon. Not. R. Astron. Soc.*, 425:1951–1957.

Refsdal, S. (1964). The gravitational lens effect. *Mon. Not. R. Astron. Soc.*, 128:295.

Rego, M., Cordero-Gracia, M., Zamorano, J., and Gallego, J. (1993). IRAS observations of H-alpha selected emission-line galaxies. *Astron. J.*, 105:427–436.

Reid, A. D., Hunstead, R. W., Lemonon, L., and Pierre, M. M. (1999). Radio study of X-ray clusters of galaxies – II. A1300: a post-merger cluster at z=0.31 containing a halo and a relic. *Mon. Not. R. Astron. Soc.*, 302:571–581.

Reid, B., Ho, S., Padmanabhan, N., Percival, W. J., Tinker, J., Tojeiro, R., White, M., Eisenstein, D. J., Maraston, C., Ross, A. J., Sánchez, A. G., Schlegel, D., Sheldon, E., Strauss, M. A., Thomas, D., Wake, D., Beutler, F., Bizyaev, D., Bolton, A. S., Brownstein, J. R., Chuang, C.-H., Dawson, K., Harding, P., Kitaura, F.-S., Leauthaud, A., Masters, K., McBride, C. K., More, S., Olmstead, M. D., Oravetz, D., Nuza, S. E., Pan, K., Parejko, J., Pforr, J., Prada, F., Rodríguez-Torres, S., Salazar-Albornoz, S., Samushia, L., Schneider, D. P., Scóccola, C. G., Simmons, A., and Vargas-Magana, M. (2016). SDSS-III Baryon Oscillation Spectroscopic Survey Data Release 12: galaxy target selection and large-scale structure catalogues. *Mon. Not. R. Astron. Soc.*, 455:1553–1573.

Reid, B. A. and Spergel, D. N. (2006). Sunyaev-Zel'dovich Effect Signals in Cluster Models. *Astrophys. J.*, 651:643–657.

Reimer, O., Pohl, M., Sreekumar, P., and Mattox, J. R. (2003). EGRET Upper Limits on the High-Energy Gamma-Ray Emission of Galaxy Clusters. *Astrophys. J.*, 588:155–164.

Rest, A., Scolnic, D., Foley, R. J., Huber, M. E., Chornock, R., Narayan, G., Tonry, J. L., Berger, E., Soderberg, A. M., Stubbs, C. W., Riess, A., Kirshner, R. P., Smartt, S. J., Schlafly, E., Rodney, S., Botticella, M. T., Brout, D., Challis, P., Czekala, I., Drout, M., Hudson, M. J., Kotak, R., Leibler, C., Lunnan, R., Marion, G. H., McCrum, M., Milisavljevic, D., Pastorello, A., Sanders, N. E., Smith, K., Stafford, E., Thilker, D., Valenti, S., Wood-Vasey, W. M., Zheng, Z., Burgett, W. S., Chambers, K. C., Denneau, L., Draper, P. W., Flewelling, H., Hodapp, K. W., Kaiser, N., Kudritzki, R.-P., Magnier, E. A., Metcalfe, N., Price, P. A., Sweeney, W., Wainscoat, R., and Waters, C. (2014). Cosmological Constraints from Measurements of Type Ia Supernovae Discovered during the First 1.5 yr of the Pan-STARRS1 Survey. *Astrophys. J.*, 795:44.

Rhee, G. F. R. N. and Katgert, P. (1987). A study of the elongation of Abell clusters. I - A sample of 37 clusters studied earlier by Binggeli and Struble and Peebles. *Astron. Astrophys.*, 183:217–227.

Rhee, G. F. R. N., van Haarlem, M. P., and Katgert, P. (1991). Substructure in Abell clusters. *Astron. Astrophys.*, 246:301–312.

Rhodes, J., Leauthaud, A., Stoughton, C., Massey, R., Dawson, K., Kolbe, W., and Roe, N. (2010). The Effects of Charge Transfer Inefficiency (CTI) on Galaxy Shape Measurements. *Pub. Astron. Soc. Pacific*, 122:439–450.

Rhodes, J., Refregier, A., and Groth, E. J. (2000). Weak Lensing Measurements: A Revisited Method and Application to Hubble Space Telescope Images. *Astrophys. J.*, 536:79–100.

Richard, J., Jauzac, M., Limousin, M., Jullo, E., Clément, B., Ebeling, H., Kneib, J.-P., Atek, H., Natarajan, P., Egami, E., Livermore, R., and Bower, R. (2014). Mass and magnification maps for the Hubble Space Telescope Frontier Fields clusters: implications for high-redshift studies. *Mon. Not. R. Astron. Soc.*, 444:268–289.

Richard, J., Kneib, J.-P., Limousin, M., Edge, A., and Jullo, E. (2010). Abell 370 revisited: refurbished Hubble imaging of the first strong lensing cluster. *Mon. Not. R. Astron. Soc.*, 402:L44–L48.

Richard, J., Pei, L., Limousin, M., Jullo, E., and Kneib, J. P. (2009). Keck spectroscopic survey of strongly lensed galaxies in Abell 1703: further evidence of a relaxed, unimodal cluster. *Astron. Astrophys.*, 498:37–47.

Ricker, P. M. and Sarazin, C. L. (2001). Off-Axis Cluster Mergers: Effects of a Strongly Peaked Dark Matter Profile. *Astrophys. J.*, 561:621–644.

Riess, A. G., Filippenko, A. V., Challis, P., Clocchiatti, A., Diercks, A., Garnavich, P. M., Gilliland, R. L., Hogan, C. J., Jha, S., Kirshner, R. P., Leibundgut, B., Phillips, M. M., Reiss, D., Schmidt, B. P., Schommer, R. A., Smith, R. C., Spyromilio, J., Stubbs, C., Suntzeff, N. B., and Tonry, J. (1998). Observational Evidence from Supernovae for an Accelerating Universe and a Cosmological Constant. *Astron. J.*, 116:1009–1038.

Riess, A. G., Strolger, L.-G., Casertano, S., Ferguson, H. C., Mobasher, B., Gold, B., Challis, P. J., Filippenko, A. V., Jha, S., Li, W., Tonry, J., Foley, R., Kirshner, R. P., Dickinson, M., MacDonald, E., Eisenstein, D., Livio, M., Younger, J., Xu, C., Dahlén, T., and Stern, D. (2007). New Hubble Space Telescope Discoveries of Type Ia Supernovae at z >= 1: Narrowing Constraints on the Early Behavior of Dark Energy. *Astrophys. J.*, 659:98–121.

Riess, A. G., Strolger, L.-G., Tonry, J., Casertano, S., Ferguson, H. C., Mobasher, B., Challis, P., Filippenko, A. V., Jha, S., Li, W., Chornock, R., Kirshner, R. P., Leibundgut, B., Dickinson, M., Livio, M., Giavalisco, M., Steidel, C. C., Benítez, T., and Tsvetanov, Z. (2004). Type Ia Supernova Discoveries at z $>$ 1 from the Hubble Space Telescope: Evidence for Past Deceleration and Constraints on Dark Energy Evolution. *Astrophys. J.*, 607:665–687.

Rigault, M., Aldering, G., Kowalski, M., Copin, Y., Antilogus, P., Aragon, C., Bailey, S., Baltay, C., Baugh, D., Bongard, S., Boone, K., Buton, C., Chen, J., Chotard, N., Fakhouri, H. K., Feindt, U., Fagrelius, P., Fleury, M., Fouchez, D., Gangler, E., Hayden, B., Kim, A. G., Leget,

P.-F., Lombardo, S., Nordin, J., Pain, R., Pecontal, E., Pereira, R., Perlmutter, S., Rabinowitz, D., Runge, K., Rubin, D., Saunders, C., Smadja, G., Sofiatti, C., Suzuki, N., Tao, C., and Weaver, B. A. (2015). Confirmation of a Star Formation Bias in Type Ia Supernova Distances and its Effect on the Measurement of the Hubble Constant. *Astrophys. J.*, 802:20.

Rindler, W. (1956). Visual horizons in world models. *Mon. Not. R. Astron. Soc.*, 116:662.

Roettiger, K., Stone, J. M., and Burns, J. O. (1999). Magnetic Field Evolution in Merging Clusters of Galaxies. *Astrophys. J.*, 518:594–602.

Rosati, P., Borgani, S., and Norman, C. (2002). The Evolution of X-ray Clusters of Galaxies. *Annu. Rev. Astron. Astrophys.*, 40:539–577.

Röttgering, H., Afonso, J., Barthel, P., Batejat, F., Best, P., Bonafede, A., Brüggen, M., Brunetti, G., Chyży, K., Conway, J., Gasperin, F. D., Ferrari, C., Haverkorn, M., Heald, G., Hoeft, M., Jackson, N., Jarvis, M., Ker, L., Lehnert, M., Macario, G., McKean, J., Miley, G., Morganti, R., Oosterloo, T., Orrù, E., Pizzo, R., Rafferty, D., Shulevski, A., Tasse, C., Bemmel, I. V., van der Tol, B., van Weeren, R., Verheijen, M., White, G., and Wise, M. (2011). LOFAR and APERTIF Surveys of the Radio Sky: Probing Shocks and Magnetic Fields in Galaxy Clusters. *Journal of Astrophysics and Astronomy*, 32:557–566.

Röttgering, H., van Weeren, R., Brüggen, M., Croston, J., Hoeft, M., Ogrean, G., Barthel, P., Best, P., Bonafede, A., Brunetti, G., Cassano, R., Chyży, K., Conway, J., De Gasperin, F., Ferrari, C., Heald, G., Jackson, N., Jarvis, M., Lehnert, M., Macario, G., Miley, G., Orrú, E., Pizzo, R., Rafferty, D., Stroe, A., Tasse, C., van der Tol, S., White, G., Wise, M., and LOFAR Collaboration (2013). The "Sausage" and "Toothbrush" clusters of galaxies and the prospects of LOFAR observations of clusters of galaxies. *Astronomische Nachrichten*, 334:333.

Rottgering, H. J. A., Wieringa, M. H., Hunstead, R. W., and Ekers, R. D. (1997). The extended radio emission in the luminous X-ray cluster A3667. *Mon. Not. R. Astron. Soc.*, 290:577–584.

Rubin, V. C., Ford, W. K. J., and . Thonnard, N. (1980). Rotational properties of 21 SC galaxies with a large range of luminosities and radii, from NGC 4605 /R = 4kpc/ to UGC 2885 /R = 122 kpc/. *Astrophys. J.*, 238:471–487.

Ruhl, J., Ade, P. A. R., Carlstrom, J. E., Cho, H.-M., Crawford, T., Dobbs, M., Greer, C. H., Halverson, N. w., Holzapfel, W. L., Lanting, T. M., Lee, A. T., Leitch, E. M., Leong, J., Lu, W., Lueker, M., Mehl, J., Meyer, S. S., Mohr, J. J., Padin, S., Plagge, T., Pryke, C., Runyan, M. C., Schwan, D., Sharp, M. K., Spieler, H., Staniszewski, Z., and Stark, A. A. (2004). The South Pole Telescope. In Bradford, C. M., Ade, P. A. R., Aguirre, J. E., Bock, J. J., Dragovan, M., Duband, L., Earle, L., Glenn, J., Matsuhara, H., Naylor, B. J., Nguyen, H. T., Yun, M., and Zmuidzinas, J., editors, *Z-Spec: a broadband millimeter-wave grating spectrometer: design, construction, and first cryogenic measurements*, volume 5498 of *Society of Photo-Optical Instrumentation Engineers (SPIE) Conference Series*, pages 11–29.

Russell, H. R., van Weeren, R. J., Edge, A. C., McNamara, B. R., Sanders, J. S., Fabian, A. C., Baum, S. A., Canning, R. E. A., Donahue, M., and O'Dea, C. P. (2011). A merger mystery: no extended radio emission in the merging cluster Abell 2146. *Mon. Not. R. Astron. Soc.*, 417:L1–L5.

Rybicki, G. B. and Lightman, A. P. (1986). *Radiative Processes in Astrophysics*.

Ryu, D., Kang, H., Cho, J., and Das, S. (2008). Turbulence and Magnetic Fields in the Large-Scale Structure of the Universe. *Science*, 320:909–.

Ryu, D., Kang, H., Hallman, E., and Jones, T. W. (2003). Cosmological Shock Waves and Their Role in the Large-Scale Structure of the Universe. *Astrophys. J.*, 593:599–610.

Saha, P. and Williams, L. L. R. (1997). Non-parametric reconstruction of the galaxy lens in PG 1115+080. *Mon. Not. R. Astron. Soc.*, 292:148.

Sahlén, M., Viana, P. T. P., Liddle, A. R., Romer, A. K., Davidson, M., Hosmer, M., Lloyd-Davies, E., Sabirli, K., Collins, C. A., Freeman, P. E., Hilton, M., Hoyle, B., Kay, S. T., Mann, R. G., Mehrtens, N., Miller, C. J., Nichol, R. C., Stanford, S. A., and West, M. J. (2009).

The XMM Cluster Survey: forecasting cosmological and cluster scaling-relation parameter constraints. *Mon. Not. R. Astron. Soc.*, 397:577–607.

Samurović, S. (2014). Investigation of dark matter and modified Newtonian dynamics in early-type galaxies through globular cluster systems. *Astron. Astrophys.*, 570:A132.

Sanders, J. S., Fabian, A. C., Churazov, E., Schekochihin, A. A., Simionescu, A., Walker, S. A., and Werner, N. (2013). Linear Structures in the Core of the Coma Cluster of Galaxies. *Science*, 341:1365–1368.

Santos, J. S., Rosati, P., Tozzi, P., Böhringer, H., Ettori, S., and Bignamini, A. (2008). Searching for cool core clusters at high redshift. *Astron. Astrophys.*, 483:35–47.

Sarazin, C. L. (1986). X-ray emission from clusters of galaxies. *Reviews of Modern Physics*, 58:1–115.

Sarazin, C. L. (1999). The Energy Spectrum of Primary Cosmic-Ray Electrons in Clusters of Galaxies and Inverse Compton Emission. *Astrophys. J.*, 520:529–547.

Sarazin, C. L. and Boller, T. (1989). Book-Review - X-Ray Emission from Clusters of Galaxies. *Astronomische Nachrichten*, 310:362.

Sastry, C. V. and Shevgaonkar, R. K. (1983). Diffuse radio emission from the Coma cluster of galaxies at decametre wavelengths. *Journal of Astrophysics and Astronomy*, 4:47–51.

Schlickeiser, R., Sievers, A., and Thiemann, H. (1987). The diffuse radio emission from the Coma cluster. *Astron. Astrophys.*, 182:21–35.

Schneider, P. (2014). Generalized multi-plane gravitational lensing: time delays, recursive lens equation, and the mass-sheet transformation. *ArXiv e-prints*.

Schneider, P., Ehlers, J., and Falco, E. E. (1992). *Gravitational Lenses*.

Schuecker, P., Böhringer, H., Reiprich, T. H., and Feretti, L. (2001). A systematic study of X-ray substructure of galaxy clusters detected in the ROSAT All-Sky Survey. *Astron. Astrophys.*, 378:408–427.

Schuecker, P., Finoguenov, A., Miniati, F., Böhringer, H., and Briel, U. G. (2004). Probing turbulence in the Coma galaxy cluster. *Astron. Astrophys.*, 426:387–397.

Schwab, F. R. (1984). Relaxing the isoplanatism assumption in self-calibration; applications to low-frequency radio interferometry. *Astron. J.*, 89:1076–1081.

Sharon, K. and Johnson, T. L. (2015). Revised Lens Model for the Multiply Imaged Lensed Supernova, S̈N Refsdalïn MACS J1149+2223. *Astrophys. J. Lett.*, 800:L26.

Shaw, L. D., Weller, J., Ostriker, J. P., and Bode, P. (2006). Statistics of Physical Properties of Dark Matter Clusters. *Astrophys. J.*, 646:815–833.

Sheldon, E. S., Johnston, D. E., Frieman, J. A., Scranton, R., McKay, T. A., Connolly, A. J., Budavári, T., Zehavi, I., Bahcall, N. A., Brinkmann, J., and Fukugita, M. (2004). The Galaxy-Mass Correlation Function Measured from Weak Lensing in the Sloan Digital Sky Survey. *Astron. J.*, 127:2544–2564.

Shin, E. M. and Evans, N. W. (2008). Lensing by binary galaxies modelled as isothermal spheres. *Mon. Not. R. Astron. Soc.*, 390:505–522.

Shirokoff, E., Reichardt, C. L., Shaw, L., Millea, M., Ade, P. A. R., Aird, K. A., Benson, B. A., Bleem, L. E., Carlstrom, J. E., Chang, C. L., Cho, H. M., Crawford, T. M., Crites, A. T., de Haan, T., Dobbs, M. A., Dudley, J., George, E. M., Halverson, N. W., Holder, G. P., Holzapfel, W. L., Hrubes, J. D., Joy, M., Keisler, R., Knox, L., Lee, A. T., Leitch, E. M., Lueker, M., Luong-Van, D., McMahon, J. J., Mehl, J., Meyer, S. S., Mohr, J. J., Montroy, T. E., Padin, S., Plagge, T., Pryke, C., Ruhl, J. E., Schaffer, K. K., Spieler, H. G., Staniszewski, Z., Stark, A. A., Story, K., Vanderlinde, K., Vieira, J. D., Williamson, R., and Zahn, O. (2011). Improved Constraints on Cosmic Microwave Background Secondary Anisotropies from the Complete 2008 South Pole Telescope Data. *Astrophys. J.*, 736:61.

Sifón, C., Battaglia, N., Menanteau, F., Hasselfield, M., Barrientos, L. F., Bond, J. R., Crichton, D., Devlin, M. J., Dünner, R., Hilton, M., Hincks, A. D., Hlozek, R., Huffenberger, K. M., Hughes, J. P., Infante, L., Kosowsky, A., Marsden, D., Marriage, T. A., Moodley, K., Niemack, M. D., Page, L. A., Spergel, D. N., Staggs, S. T., Trac, H., and Wollack, E. J. (2015). The Atacama Cosmology Telescope: Dynamical masses for 44 SZ-selected galaxy clusters over 755 square degrees. *ArXiv e-prints*.

Sifón, C., Menanteau, F., Hasselfield, M., Marriage, T. A., Hughes, J. P., Barrientos, L. F., González, J., Infante, L., Addison, G. E., Baker, A. J., Battaglia, N., Bond, J. R., Crichton, D., Das, S., Devlin, M. J., Dunkley, J., Dünner, R., Gralla, M. B., Hajian, A., Hilton, M., Hincks, A. D., Kosowsky, A. B., Marsden, D., Moodley, K., Niemack, M. D., Nolta, M. R., Page, L. A., Partridge, B., Reese, E. D., Sehgal, N., Sievers, J., Spergel, D. N., Staggs, S. T., Thornton, R. J., Trac, H., and Wollack, E. J. (2013). The Atacama Cosmology Telescope: Dynamical Masses and Scaling Relations for a Sample of Massive Sunyaev-Zel'dovich Effect Selected Galaxy Clusters. *Astrophys. J.*, 772:25.

Sijbring, L. G. (1993). *A radio continuum and HI line study of the perseus cluster*.

Skillman, S. W., Hallman, E. J., O'Shea, B. W., Burns, J. O., Smith, B. D., and Turk, M. J. (2011). Galaxy Cluster Radio Relics in Adaptive Mesh Refinement Cosmological Simulations: Relic Properties and Scaling Relationships. *Astrophys. J.*, 735:96.

Skillman, S. W., O'Shea, B. W., Hallman, E. J., Burns, J. O., and Norman, M. L. (2008). Cosmological Shocks in Adaptive Mesh Refinement Simulations and the Acceleration of Cosmic Rays. *Astrophys. J.*, 689:1063–1077.

Slee, O. B., Roy, A. L., Murgia, M., Andernach, H., and Ehle, M. (2001). Four Extreme Relic Radio Sources in Clusters of Galaxies. *Astron. J.*, 122:1172–1193.

Smirnov, O. M. (2011). Revisiting the radio interferometer measurement equation. I. A full-sky Jones formalism. *Astron. Astrophys.*, 527:A106.

Smith, G. P., Ebeling, H., Limousin, M., Kneib, J.-P., Swinbank, A. M., Ma, C.-J., Jauzac, M., Richard, J., Jullo, E., Sand, D. J., Edge, A. C., and Smail, I. (2009). Hubble Space Telescope Observations of a Spectacular New Strong-Lensing Galaxy Cluster: MACS J1149.5+2223 at z = 0.544. *Astrophys. J. Lett.*, 707:L163–L168.

Smith, G. P., Edge, A. C., Eke, V. R., Nichol, R. C., Smail, I., and Kneib, J.-P. (2003). Measuring σ_8 with Cluster Lensing: Biases from Unrelaxed Clusters. *Astrophys. J. Lett.*, 590:L79–L82.

Smith, G. P., Kneib, J.-P., Ebeling, H., Czoske, O., and Smail, I. (2001). A Hubble Space Telescope Lensing Survey of X-Ray Luminous Galaxy Clusters. I. A383. *Astrophys. J.*, 552:493–503.

Smith, G. P., Kneib, J.-P., Smail, I., Mazzotta, P., Ebeling, H., and Czoske, O. (2005). A Hubble Space Telescope lensing survey of X-ray luminous galaxy clusters - IV. Mass, structure and thermodynamics of cluster cores at z= 0.2. *Mon. Not. R. Astron. Soc.*, 359:417–446.

Solovyeva, L., Anokhin, S., Feretti, L., Sauvageot, J. L., Teyssier, R., Giovannini, G., Govoni, F., and Neumann, D. (2008). The dynamical state of A548 from XMM-Newton data: X-ray and radio connection. *Astron. Astrophys.*, 484:621–630.

Sommer, M. W. and Basu, K. (2014). A comparative study of radio halo occurrence in SZ and X-ray selected galaxy cluster samples. *Mon. Not. R. Astron. Soc.*, 437:2163–2179.

Soucail, G. (1987). Observations des arcs dans les amas de galaxies: mise en évidence d'un mirage gravitationnel dans Abell 370. *Journal des Astronomes Francais*, 31:31.

Soucail, G., Mellier, Y., Fort, B., Mathez, G., and Cailloux, M. (1988). The giant arc in A 370 - Spectroscopic evidence for gravitational lensing from a source at Z = 0.724. *Astron. Astrophys.*, 191:L19–L21.

Spergel, D. N., Bean, R., Doré, O., Nolta, M. R., Bennett, C. L., Dunkley, J., Hinshaw, G., Jarosik, N., Komatsu, E., Page, L., Peiris, H. V., Verde, L., Halpern, M., Hill, R. S., Kogut, A., Limon, M., Meyer, S. S., Odegard, N., Tucker, G. S., Weiland, J. L., Wollack, E., and Wright,

E. L. (2007). Three-Year Wilkinson Microwave Anisotropy Probe (WMAP) Observations: Implications for Cosmology. *Astrophys. J. Supp.*, 170:377–408.

Stanford, S. A., Elston, R., Eisenhardt, P. R., Spinrad, H., Stern, D., and Dey, A. (1997). An IR-Selected Galaxy Cluster at ζ=1.27. *Astron. J.*, 114:2232.

Stroe, A., Harwood, J. J., Hardcastle, M. J., and Röttgering, H. J. A. (2014a). Spectral age modelling of the 'Sausage' cluster radio relic. *Mon. Not. R. Astron. Soc.*, 445:1213–1222.

Stroe, A., Rumsey, C., Harwood, J. J., van Weeren, R. J., Röttgering, H. J. A., Saunders, R. D. E., Sobral, D., Perrott, Y. C., and Schammel, M. P. (2014b). The highest frequency detection of a radio relic: 16 GHz AMI observations of the 'Sausage' cluster. *Mon. Not. R. Astron. Soc.*, 441:L41–L45.

Stroe, A., Shimwell, T., Rumsey, C., van Weeren, R., Kierdorf, M., Donnert, J., Jones, T. W., Röttgering, H. J. A., Hoeft, M., Rodriguez-Gonzalvez, C., Harwood, J. J., and Saunders, R. D. E. (2015). The widest-frequency radio relic spectra: observations from 150 MHz to 30 GHz. *ArXiv e-prints*.

Stroe, A., Sobral, D., Röttgering, H. J. A., and van Weeren, R. J. (2014c). The role of cluster mergers and travelling shocks in shaping the Hα luminosity function at z $\sim$ 0.2: 'sausage' and 'toothbrush' clusters. *Mon. Not. R. Astron. Soc.*, 438:1377–1390.

Subrahmanya, C. R. (1991). Low frequency imaging and the non-isoplanatic atmosphere. In Cornwell, T. J. and Perley, R. A., editors, *IAU Colloq. 131: Radio Interferometry. Theory, Techniques, and Applications*, volume 19 of *Astronomical Society of the Pacific Conference Series*, pages 218–222.

Subramanian, K., Shukurov, A., and Haugen, N. E. L. (2006). Evolving turbulence and magnetic fields in galaxy clusters. *Mon. Not. R. Astron. Soc.*, 366:1437–1454.

Sunyaev, R. A., Norman, M. L., and Bryan, G. L. (2003). On the Detectability of Turbulence and Bulk Flows in X-ray Clusters. *Astronomy Letters*, 29:783–790.

Sunyaev, R. A. and Zel'dovich, Y. B. (1972). Formation of Clusters of Galaxies; Protocluster Fragmentation and Intergalactic Gas Heating. *Astron. Astrophys.*, 20:189.

Sutherland, W. (1988). The 3-D distribution of Abell clusters. *Mon. Not. R. Astron. Soc.*, 234:159–172.

Sweet, S. M., Drinkwater, M. J., Meurer, G., Kilborn, V., Audcent-Ross, F., Baumgardt, H., and Bekki, K. (2016). Kinematics of dwarf galaxies in gas-rich groups, and the survival and detectability of tidal dwarf galaxies. *Mon. Not. R. Astron. Soc.*, 455:2508–2528.

Swetz, D. S., Ade, P. A. R., Amiri, M., Appel, J. W., Battistelli, E. S., Burger, B., Chervenak, J., Devlin, M. J., Dicker, S. R., Doriese, W. B., Dünner, R., Essinger-Hileman, T., Fisher, R. P., Fowler, J. W., Halpern, M., Hasselfield, M., Hilton, G. C., Hincks, A. D., Irwin, K. D., Jarosik, N., Kaul, M., Klein, J., Lau, J. M., Limon, M., Marriage, T. A., Marsden, D., Martocci, K., Mauskopf, P., Moseley, H., Netterfield, C. B., Niemack, M. D., Nolta, M. R., Page, L. A., Parker, L., Staggs, S. T., Stryzak, O., Switzer, E. R., Thornton, R., Tucker, C., Wollack, E., and Zhao, Y. (2011). Overview of the Atacama Cosmology Telescope: Receiver, Instrumentation, and Telescope Systems. *Astrophys. J. Supp.*, 194:41.

Tago, E., Einasto, J., Saar, E., Einasto, M., Suhhonenko, I., Jõeveer, M., Vennik, J., Heinämäki, P., and Tucker, D. L. (2006). Clusters and groups of galaxies in the 2dF galaxy redshift survey: A new catalogue. *Astronomische Nachrichten*, 327:365.

Takahashi, T., Mitsuda, K., Kelley, R., Aharonian, F., Akimoto, F., Allen, S., Anabuki, N., Angelini, L., Arnaud, K., Awaki, H., Bamba, A., Bando, N., Bautz, M., Blandford, R., Boyce, K., Brown, G., Chernyakova, M., Coppi, P., Costantini, E., Cottam, J., Crow, J., de Plaa, J., de Vries, C., den Herder, J.-W., Dipirro, M., Done, C., Dotani, T., Ebisawa, K., Enoto, T., Ezoe, Y., Fabian, A., Fujimoto, R., Fukazawa, Y., Funk, S., Furuzawa, A., Galeazzi, M., Gandhi, P., Gendreau, K., Gilmore, K., Haba, Y., Hamaguchi, K., Hatsukade, I., Hayashida, K., Hiraga, J., Hirose, K., Hornschemeier, A., Hughes, J., Hwang, U., Iizuka, R., Ishibashi, K., Ishida, M., Ishimura, K., Ishisaki, Y., Isobe, N., Ito, M., Iwata, N., Kaastra, J., Kallman,

T., Kamae, T., Katagiri, H., Kataoka, J., Katsuda, S., Kawaharada, M., Kawai, N., Kawasaki, S., Khangaluyan, D., Kilbourne, C., Kinugasa, K., Kitamoto, S., Kitayama, T., Kohmura, T., Kokubun, M., Kosaka, T., Kotani, T., Koyama, K., Kubota, A., Kunieda, H., Laurent, P., Lebrun, F., Limousin, O., Loewenstein, M., Long, K., Madejski, G., Maeda, Y., Makishima, K., Markevitch, M., Matsumoto, H., Matsushita, K., McCammon, D., Miller, J., Mineshige, S., Minesugi, K., Miyazawa, T., Mizuno, T., Mori, K., Mori, H., Mukai, K., Murakami, H., Murakami, T., Mushotzky, R., Nakagawa, Y., Nakagawa, T., Nakajima, H., Nakamori, T., Nakazawa, K., Namba, Y., Nomachi, M., O'Dell, S., Ogawa, H., Ogawa, M., Ogi, K., Ohashi, T., Ohno, M., Ohta, M., Okajima, T., Ota, N., Ozaki, M., Paerels, F., Paltani, S., Parmar, A., Petre, R., Pohl, M., Porter, S., Ramsey, B., Reynolds, C., Sakai, S.-I., Sambruna, R., Sato, G., Sato, Y., Serlemitsos, P., Shida, M., Shimada, T., Shinozaki, K., Shirron, P., Smith, R., Sneiderman, G., Soong, Y., Stawarz, L., Sugita, H., Szymkowiak, A., Tajima, H., Takahashi, H., Takei, Y., Tamagawa, T., Tamura, T., Tamura, K., Tanaka, T., Tanaka, Y., Tanaka, Y., Tashiro, M., Tawara, Y., Terada, Y., Terashima, Y., Tombesi, F., Tomida, H., Tozuka, M., Tsuboi, Y., Tsujimoto, M., Tsunemi, H., Tsuru, T., Uchida, H., Uchiyama, Y., Uchiyama, H., Ueda, Y., Uno, S., Urry, M., Watanabe, S., White, N., Yamada, T., Yamaguchi, H., Yamaoka, K., Yamasaki, N., Yamauchi, M., Yamauchi, S., Yatsu, Y., Yonetoku, D., and Yoshida, A. (2010). The ASTRO-H Mission. In *Society of Photo-Optical Instrumentation Engineers (SPIE) Conference Series*, volume 7732 of *Society of Photo-Optical Instrumentation Engineers (SPIE) Conference Series*, page 0.

Tasse, C. (2014). Nonlinear Kalman filters for calibration in radio interferometry. *Astron. Astrophys.*, 566:A127.

Taylor, A. R. (2013). The Square Kilometre Array. In van Leeuwen, J., editor, *IAU Symposium*, volume 291 of *IAU Symposium*, pages 337–341.

Tegmark, M., Eisenstein, D. J., Strauss, M. A., Weinberg, D. H., Blanton, M. R., Frieman, J. A., Fukugita, M., Gunn, J. E., Hamilton, A. J. S., Knapp, G. R., Nichol, R. C., Ostriker, J. P., Padmanabhan, N., Percival, W. J., Schlegel, D. J., Schneider, D. P., Scoccimarro, R., Seljak,

U., Seo, H.-J., Swanson, M., Szalay, A. S., Vogeley, M. S., Yoo, J., Zehavi, I., Abazajian, K., Anderson, S. F., Annis, J., Bahcall, N. A., Bassett, B., Berlind, A., Brinkmann, J., Budavari, T., Castander, F., Connolly, A., Csabai, I., Doi, M., Finkbeiner, D. P., Gillespie, B., Glazebrook, K., Hennessy, G. S., Hogg, D. W., Ivezić, Ž., Jain, B., Johnston, D., Kent, S., Lamb, D. Q., Lee, B. C., Lin, H., Loveday, J., Lupton, R. H., Munn, J. A., Pan, K., Park, C., Peoples, J., Pier, J. R., Pope, A., Richmond, M., Rockosi, C., Scranton, R., Sheth, R. K., Stebbins, A., Stoughton, C., Szapudi, I., Tucker, D. L., vanden Berk, D. E., Yanny, B., and York, D. G. (2006). Cosmological constraints from the SDSS luminous red galaxies. *Physical Review D.*, 74(12):123507.

Tempel, E., Tago, E., and Liivamägi, L. J. (2012). Groups and clusters of galaxies in the SDSS DR8. Value-added catalogues. *Astron. Astrophys.*, 540:A106.

Thierbach, M., Klein, U., and Wielebinski, R. (2003). The diffuse radio emission from the Coma cluster at 2.675 GHz and 4.85 GHz. *Astron. Astrophys.*, 397:53–61.

Thompson, A. R., Moran, J. M., and Swenson, Jr., G. W. (2001). *Interferometry and Synthesis in Radio Astronomy, 2nd Edition*.

Tinker, J. L., Sheldon, E. S., Wechsler, R. H., Becker, M. R., Rozo, E., Zu, Y., Weinberg, D. H., Zehavi, I., Blanton, M. R., Busha, M. T., and Koester, B. P. (2012). Cosmological Constraints from Galaxy Clustering and the Mass-to-number Ratio of Galaxy Clusters. *Astrophys. J.*, 745:16.

Tortora, C., Napolitano, N. R., Saglia, R. P., Romanowsky, A. J., Covone, G., and Capaccioli, M. (2014). Evolution of central dark matter of early-type galaxies up to z $\sim$ 0.8. *Mon. Not. R. Astron. Soc.*, 445:162–174.

Treu, T. and Koopmans, L. V. E. (2004). Massive Dark Matter Halos and Evolution of Early-Type Galaxies to z ˜ 1. *Astrophys. J.*, 611:739–760.

Šuhada, R., Fassbender, R., Nastasi, A., Böhringer, H., de Hoon, A., Pierini, D., Santos, J. S., Rosati, P., Mühlegger, M., Quintana, H., Schwope, A. D., Lamer, G., Kohnert, J., and Pratt,

G. W. (2011). Exploring the galaxy cluster-group transition regime at high redshifts. Physical properties of two newly detected z $>$ 1 systems. *Astron. Astrophys.*, 530:A110.

Vacca, V., Murgia, M., Govoni, F., Feretti, L., Giovannini, G., Orrã[1], E., and Bonafede, A. (2010). The intracluster magnetic field power spectrum in Abell 665. *Astron. Astrophys.*, 514:A71.

van Weeren, R. J., Brüggen, M., Röttgering, H. J. A., and Hoeft, M. (2011a). Using double radio relics to constrain galaxy cluster mergers: a model of double radio relics in CIZA J2242.8+5301. *Mon. Not. R. Astron. Soc.*, 418:230–243.

van Weeren, R. J., Brüggen, M., Röttgering, H. J. A., Hoeft, M., Nuza, S. E., and Intema, H. T. (2011b). Radio continuum observations of new radio halos and relics from the NVSS and WENSS surveys. Relic orientations, cluster X-ray luminosity, and redshift distributions. *Astron. Astrophys.*, 533:A35.

van Weeren, R. J., Intema, H. T., Lal, D. V., Bonafede, A., Jones, C., Forman, W. R., Röttgering, H. J. A., Brüggen, M., Stroe, A., Hoeft, M., Nuza, S. E., and de Gasperin, F. (2014). The Discovery of a Radio Halo in PLCK G147.3-16.6 at z = 0.65. *Astrophys. J. Lett.*, 781:L32.

van Weeren, R. J., Intema, H. T., Röttgering, H. J. A., Brüggen, M., and Hoeft, M. (2011c). Low-frequency radio observations of the galaxy cluster CIZA J2242.8+5301 . *Mem. Societa Astronomica Italiana*, 82:569.

van Weeren, R. J., Röttgering, H. J. A., and Brüggen, M. (2011d). Diffuse steep-spectrum sources from the 74 MHz VLSS survey. *Astron. Astrophys.*, 527:A114.

van Weeren, R. J., Röttgering, H. J. A., Brüggen, M., and Hoeft, M. (2010). Particle Acceleration on Megaparsec Scales in a Merging Galaxy Cluster. *Science*, 330:347–.

van Weeren, R. J., Röttgering, H. J. A., Intema, H. T., Rudnick, L., Brüggen, M., Hoeft, M., and Oonk, J. B. R. (2012). The ”toothbrush-relic”: evidence for a coherent linear 2-Mpc scale shock wave in a massive merging galaxy cluster? *Astron. Astrophys.*, 546:A124.

Varenius, E., Conway, J. E., Martí-Vidal, I., Aalto, S., Beswick, R., Costagliola, F., and Klöckner, H.-R. (2014). The radio core structure of the luminous infrared galaxy NGC 4418. A young clustered starburst revealed? *Astron. Astrophys.*, 566:A15.

Vazza, F., Brüggen, M., Gheller, C., and Brunetti, G. (2012a). Modelling injection and feedback of cosmic rays in grid-based cosmological simulations: effects on cluster outskirts. *Mon. Not. R. Astron. Soc.*, 421:3375–3398.

Vazza, F., Brunetti, G., and Gheller, C. (2009a). Shock waves in Eulerian cosmological simulations: main properties and acceleration of cosmic rays. *Mon. Not. R. Astron. Soc.*, 395:1333–1354.

Vazza, F., Brunetti, G., Gheller, C., and Brunino, R. (2010a). Massive and refined: A sample of large galaxy clusters simulated at high resolution. I: Thermal gas and properties of shock waves. *New Astron.*, 15:695–711.

Vazza, F., Brunetti, G., Gheller, C., Brunino, R., and Brüggen, M. (2011a). Massive and refined. II. The statistical properties of turbulent motions in massive galaxy clusters with high spatial resolution. *Astron. Astrophys.*, 529:A17.

Vazza, F., Brunetti, G., Kritsuk, A., Wagner, R., Gheller, C., and Norman, M. (2009b). Turbulent motions and shocks waves in galaxy clusters simulated with adaptive mesh refinement. *Astron. Astrophys.*, 504:33–43.

Vazza, F., Dolag, K., Ryu, D., Brunetti, G., Gheller, C., Kang, H., and Pfrommer, C. (2011b). A comparison of cosmological codes: properties of thermal gas and shock waves in large-scale structures. *Mon. Not. R. Astron. Soc.*, 418:960–985.

Vazza, F., Gheller, C., and Brunetti, G. (2010b). The mixing and transport properties of the intra cluster medium: a numerical study using tracers particles. *Astron. Astrophys.*, 513:A32.

Vazza, F., Roediger, E., and Brüggen, M. (2012b). Turbulence in the ICM from mergers, cool-core sloshing, and jets: results from a new multi-scale filtering approach. *Astron. Astrophys.*, 544:A103.

Ventimiglia, D. A., Voit, G. M., Donahue, M., and Ameglio, S. (2008). Substructure and Scatter in the Mass-Temperature Relations of Simulated Clusters. *Astrophys. J.*, 685:118–127.

Venturi, T., Giacintucci, S., Brunetti, G., Cassano, R., Bardelli, S., Dallacasa, D., and Setti, G. (2007). GMRT radio halo survey in galaxy clusters at z = 0.2-0.4. I. The REFLEX sub-sample. *Astron. Astrophys.*, 463:937–947.

Venturi, T., Giacintucci, S., Dallacasa, D., Cassano, R., Brunetti, G., Bardelli, S., and Setti, G. (2008). GMRT radio halo survey in galaxy clusters at z = 0.2-0.4. II. The eBCS clusters and analysis of the complete sample. *Astron. Astrophys.*, 484:327–340.

Venturi, T., Giacintucci, S., Dallacasa, D., Cassano, R., Brunetti, G., Macario, G., and Athreya, R. (2013). Low frequency follow up of radio haloes and relics in the GMRT Radio Halo Cluster Survey. *Astron. Astrophys.*, 551:A24.

Venturi, T., Giovannini, G., and Feretti, L. (1990). High-sensitivity radio observations of the Coma cluster of galaxies. *Astron. J.*, 99:1381–1396.

Vermeulen, R. C. (2012). LOFAR, the low frequency array. In *Society of Photo-Optical Instrumentation Engineers (SPIE) Conference Series*, volume 8444 of *Society of Photo-Optical Instrumentation Engineers (SPIE) Conference Series*, page 2.

Vikhlinin, A., Kravtsov, A. V., Burenin, R. A., Ebeling, H., Forman, W. R., Hornstrup, A., Jones, C., Murray, S. S., Nagai, D., Quintana, H., and Voevodkin, A. (2009). Chandra Cluster Cosmology Project III: Cosmological Parameter Constraints. *Astrophys. J.*, 692:1060–1074.

Voit, G. M. (2005). Tracing cosmic evolution with clusters of galaxies. *Reviews of Modern Physics*, 77:207–258.

Völk, H. J., Aharonian, F. A., and Breitschwerdt, D. (1996). The Nonthermal Energy Content and Gamma-Ray Emission of Starburst Galaxies and Clusters of Galaxies. *Space Sci. Rev.*, 75:279–297.

Walsh, D., Carswell, R. F., and Weymann, R. J. (1979). 0957 + 561 A, B - Twin quasistellar objects or gravitational lens. *Nature.*, 279:381–384.

Wang, X., Hoag, A., Huang, K.-H., Treu, T., Bradač, M., Schmidt, K. B., Brammer, G. B., Vulcani, B., Jones, T. A., Ryan, Jr., R. E., Amorín, R., Castellano, M., Fontana, A., Merlin, E., and Trenti, M. (2015). The Grism Lens-amplified Survey from Space (GLASS). IV. Mass Reconstruction of the Lensing Cluster Abell 2744 from Frontier Field Imaging and GLASS Spectroscopy. *Astrophys. J.*, 811:29.

Weinberg, D. H. (1992). Reconstructing primordial density fluctuations. I - Method. *Mon. Not. R. Astron. Soc.*, 254:315–342.

Wells, D. C. (1985). NRAO's Astronomical Image Processing System (AIPS). In di Gesu, V., Scarsi, L., Crane, P., Friedman, J. H., and Levialdi, S., editors, *Data Analysis in Astronomy*, page 195.

Wen, Z. L. and Han, J. L. (2013). Substructure and dynamical state of 2092 rich clusters of galaxies derived from photometric data. *Mon. Not. R. Astron. Soc.*, 436:275–293.

Wetzel, A. R. and White, M. (2010). What determines satellite galaxy disruption? *Mon. Not. R. Astron. Soc.*, 403:1072–1088.

Wilkins, S. M., Bouwens, R. J., Oesch, P. A., Labbé, I., Sargent, M., Caruana, J., Wardlow, J., and Clay, S. (2016). Quantifying the UV-continuum slopes of galaxies to z $\sim$ 10 using deep Hubble+Spitzer/IRAC observations. *Mon. Not. R. Astron. Soc.*, 455:659–667.

Willis, J. P., Clerc, N., Bremer, M. N., Pierre, M., Adami, C., Ilbert, O., Maughan, B., Maurogordato, S., Pacaud, F., Valtchanov, I., Chiappetti, L., Thanjavur, K., Gwyn, S., Stanway, E. R., and Winkworth, C. (2013). Distant galaxy clusters in the XMM Large Scale Structure survey. *Mon. Not. R. Astron. Soc.*, 430:134–156.

Willson, M. A. G. (1970). Radio observations of the cluster of galaxies in Coma Berenices - the 5C4 survey. *Mon. Not. R. Astron. Soc.*, 151:1–44.

Wood-Vasey, W. M., Miknaitis, G., Stubbs, C. W., Jha, S., Riess, A. G., Garnavich, P. M., Kirshner, R. P., Aguilera, C., Becker, A. C., Blackman, J. W., Blondin, S., Challis, P., Clocchiatti, A., Conley, A., Covarrubias, R., Davis, T. M., Filippenko, A. V., Foley, R. J., Garg, A., Hicken, M., Krisciunas, K., Leibundgut, B., Li, W., Matheson, T., Miceli, A., Narayan, G., Pignata, G., Prieto, J. L., Rest, A., Salvo, M. E., Schmidt, B. P., Smith, R. C., Sollerman, J., Spyromilio, J., Tonry, J. L., Suntzeff, N. B., and Zenteno, A. (2007). Observational Constraints on the Nature of Dark Energy: First Cosmological Results from the ESSENCE Supernova Survey. *Astrophys. J.*, 666:694–715.

Xu, H., Li, H., Collins, D. C., Li, S., and Norman, M. L. (2010). Evolution and Distribution of Magnetic Fields from Active Galactic Nuclei in Galaxy Clusters. I. The Effect of Injection Energy and Redshift. *Astrophys. J.*, 725:2152–2165.

Xu, H., Li, H., Collins, D. C., Li, S., and Norman, M. L. (2011). Evolution and Distribution of Magnetic Fields from Active Galactic Nuclei in Galaxy Clusters. II. The Effects of Cluster Size and Dynamical State. *Astrophys. J.*, 739:77.

Young, A., Romero, C., Dicker, S., Mason, B. S., Mroczkowski, T., Reese, E. D., Sarazin, C. L., Sayers, J., Czakon, N. G., Devlin, M. J., Korngut, P., and Sievers, J. (2014). MUSTANG and MUSTANG 1.5: High-Resolution Measurements of the Sunyaev-Zel'dovich Effect in Galaxy Clusters. In *American Astronomical Society Meeting Abstracts #223*, volume 223 of *American Astronomical Society Meeting Abstracts*, page #208.02.

Yuan, Z. S., Han, J. L., and Wen, Z. L. (2015). The Scaling Relations and the Fundamental Plane for Radio Halos and Relics of Galaxy Clusters. *Astrophys. J.*, 813:77.

Zandanel, F., Pfrommer, C., and Prada, F. (2012). On the Physics of Radio Halos in Galaxy Clusters: Scaling Relations and Luminosity Functions. *ArXiv e-prints*.

Zeeman, E. C. (1977). *Catastrophe theory. Selected papers 1972-1977*.

Zheng, W., Postman, M., Zitrin, A., Moustakas, J., Shu, X., Jouvel, S., Høst, O., Molino, A., Bradley, L., Coe, D., Moustakas, L. A., Carrasco, M., Ford, H., Benítez, N., Lauer, T. R., Seitz,

S., Bouwens, R., Koekemoer, A., Medezinski, E., Bartelmann, M., Broadhurst, T., Donahue, M., Grillo, C., Infante, L., Jha, S. W., Kelson, D. D., Lahav, O., Lemze, D., Melchior, P., Meneghetti, M., Merten, J., Nonino, M., Ogaz, S., Rosati, P., Umetsu, K., and van der Wel, A. (2012). A magnified young galaxy from about 500 million years after the Big Bang. *Nature.*, 489:406–408.

Zhuravleva, I., Churazov, E., Kravtsov, A., and Sunyaev, R. (2012). Constraints on the ICM velocity power spectrum from the X-ray lines width and shift. *Mon. Not. R. Astron. Soc.*, 422:2712–2724.

Zhuravleva, I., Churazov, E., Sunyaev, R., Sazonov, S., Allen, S. W., Werner, N., Simionescu, A., Konami, S., and Ohashi, T. (2013). Resonant scattering in the Perseus Cluster: spectral model for constraining gas motions with Astro-H. *Mon. Not. R. Astron. Soc.*, 435:3111–3121.

Zitrin, A. and Broadhurst, T. (2009). Discovery of the Largest Known Lensed Images Formed by a Critically Convergent Lensing Cluster. *Astrophys. J. Lett.*, 703:L132–L136.

Zitrin, A., Broadhurst, T., Barkana, R., Rephaeli, Y., and Benítez, N. (2011). Strong-lensing analysis of a complete sample of 12 MACS clusters at z $>$ 0.5: mass models and Einstein radii. *Mon. Not. R. Astron. Soc.*, 410:1939–1956.

Zitrin, A., Meneghetti, M., Umetsu, K., Broadhurst, T., Bartelmann, M., Bouwens, R., Bradley, L., Carrasco, M., Coe, D., Ford, H., Kelson, D., Koekemoer, A. M., Medezinski, E., Moustakas, J., Moustakas, L. A., Nonino, M., Postman, M., Rosati, P., Seidel, G., Seitz, S., Sendra, I., Shu, X., Vega, J., and Zheng, W. (2013). CLASH: The Enhanced Lensing Efficiency of the Highly Elongated Merging Cluster MACS J0416.1-2403. *Astrophys. J. Lett.*, 762:L30.

ZuHone, J., Markevitch, M., and Brunetti, G. (2011a). Testing the connection between radio mini-halos and core gas sloshing with MHD simulations. *Mem. Societa Astronomica Italiana*, 82:632.

ZuHone, J. A., Markevitch, M., and Lee, D. (2011b). Sloshing of the Magnetized Cool Gas in the Cores of Galaxy Clusters. *Astrophys. J.*, 743:16.

Zwicky, F. (1933). Die Rotverschiebung von extragalaktischen Nebeln. *Helvetica Physica Acta*, 6:110–127.

Zwicky, F., Herzog, E., and Wild, P. (1968). *Catalogue of galaxies and of clusters of galaxies*.